

On Quantum Imaging with Time-Resolving Detector Arrays

Inauguraldissertation

der Philosophisch-naturwissenschaftlichen Fakultät
der Universität Bern

vorgelegt von

Manuel Unternährer

aus Romoos (LU)

Leiter der Arbeit:

Prof. Dr. André Stefanov

Institut für Angewandte Physik der Universität Bern

Originaldokument gespeichert auf dem Webserver der Universitätsbibliothek Bern



Dieses Werk ist unter einem Creative Commons Namensnennung-Keine kommerzielle Nutzung-Keine Bearbeitung 2.5 Schweiz Lizenzvertrag lizenziert. Um die Lizenz anzusehen, gehen Sie bitte zu <http://creativecommons.org/licenses/by-nc-nd/2.5/ch/> oder schicken Sie einen Brief an Creative Commons, 171 Second Street, Suite 300, San Francisco, California 94105, USA.

Copyright Notice

This document is licensed under the Creative Commons Attribution-Non-Commercial-No derivative works 2.5 Switzerland.

<http://creativecommons.org/licenses/by-nc-nd/2.5/ch/deed.en>

You are free:



to copy, distribute, display, and perform the work.

Under the following conditions:



Attribution. You must give the original author credit.



Non-Commercial. You may not use this work for commercial purposes.



No derivative works. You may not alter, transform, or build upon this work.

For any reuse or distribution, you must take clear to others the license terms of this work.

Any of these conditions can be waived if you get permission from the copyright holder.

Nothing in this license impairs or restricts the author's moral rights according to Swiss law.

The detailed license agreement can be found at:

<http://creativecommons.org/licenses/by-nc-nd/2.5/ch/legalcode.de>

Acknowledgements

Many people were involved in my journey without whom this thesis would not have been written. First of all, I would like to express my gratitude to André Stefanov for the supervision of this thesis in the Quantum Optics Group at the Institute of Applied Physics. During the work on a Master thesis project in his group, I learned to appreciate, on one hand, the physics of quantum optics and even more, on the other hand, André's calm and supporting nature. Giving me the opportunity to continue in a PhD thesis, I very much enjoyed this working atmosphere which allowed me to grow personally and professionally. Thank you very much for everything, André!

Special thanks go to Bänz Bessire. With my involvement in the SuperTwin project where he was already working on, I got the chance to work with him. I very much appreciated our experimental sessions in the lab and our extensive discussions on theory! This fruitful teamwork enriched my daily work tremendously. Thank you, Bänz, for sharing your knowledge and experience which guided me not only professionally.

Many thanks to Leonardo Gasparini who works in the SuperTwin collaboration and spent his sabbatical in Bern. Only his effort of developing the amazing detector adapted to our application made many of the here presented results possible. I very much enjoyed his elaborate and vivid explanations and patient answers to all of my questions!

I would also like to thank the other members of the quantum optics team, being my doctoral brothers Jos, Sacha and Stefan, for many interesting, fruitful discussions and their friendship which made the daily life at the university a much warmer place for me. Especially our very enjoyable lunch time and coffee break rituals I will always keep in best memory! Special thanks go to Stefan for motivating me to start my Master thesis in this group and introducing me into the lab and theory. Thanks also to my long-time office mates Jos and Maryam for their friendship, support and patience in stressful situations. Furthermore, I'd like to thank Thomas Feurer, the whole Laser Group and IAP for the very friendly and inspiring working environment.

I would like to thank my friends Christian, Agnes and Sandro for always being there for me. I'm grateful to have met my "physicist"-friends Erik, Lädi, Mike, Raphael, Sigi, and Stefan who made our years of study a marvelous time and certainly will lead to many future adventures! Thanks to my class mates Christa, Christoph, Damian, Florentin, Gregory, Luzius, Marc, and Sabina for so many hours we enjoyed together.

Finally, special thanks are dedicated to my parents Thomas and Edith who made it possible that I was able to discover and pursue my passion, and to my wonderful girlfriend Laura, my sister Karin and brother Marco. Without their love and support, this journey would not have been possible.

Contents

Acknowledgements	v
List of Abbreviations	xi
1 Introduction	1
2 Theoretical Framework	7
2.1 Classical Fourier Optics	7
2.1.1 Introduction	7
2.1.2 Linear System Theory	9
2.1.3 Elementary Optical Impulse Response Functions	9
2.1.4 Single Lens Near-Field Imaging	10
2.1.5 Far-Field Imaging	11
2.2 Fourier Optics of Quantum Fields	12
2.2.1 Introduction	12
2.2.2 Transformation of Field Operators	14
2.2.3 Field Correlation Functions	15
2.3 Field Intensity Correlation Measurements	16
2.3.1 Sample Averaging and Normalization	16
2.3.2 Discretization of Detector Arrays	18
2.3.3 Normal Ordered Photon Number Correlations	19
2.3.4 Example of Time-Stationary Sources	20
3 Light Sources	27
3.1 Two-Photon Source	27
3.1.1 Theory	27
3.1.2 Experimental Implementation	33
3.1.3 Characterization	34
3.2 Four-Photon Source	35
3.2.1 Theory	37
3.2.2 Experimental Implementation	40
3.2.3 Characterization	41
3.3 Pseudo-Thermal Light	44
3.3.1 Theory	44
3.3.2 Experimental Implementation	45
3.3.3 Characterization	46
3.4 Conclusion	48
4 Two-Photon Interferometry	51
4.1 Theory	51
4.1.1 Intensity Measurement	52
4.1.2 Second-Order Correlation Measurement	52
4.2 Self-Calibrating OLCR using Energy-Time Entangled Photons	54

4.2.1	Introduction	54
4.2.2	Classical Optical Low-Coherence Reflectometry	55
4.2.3	Quantum Optical Low-Coherence Reflectometry	56
4.2.4	Experimental Implementation	58
4.2.5	Results	59
4.2.6	Conclusion	62
4.3	Appendix	63
4.3.1	Single-Mode Coupling	63
4.3.2	Two-Photon Artifact in Intensity Measurements	66
5	Test and Characterization of Detector Arrays	67
5.1	SPADnet-I Sensor	68
5.1.1	Introduction	68
5.1.2	SPADnet-I sensor	70
5.1.3	Experiment	71
5.1.4	Results	73
5.1.5	Conclusions	77
5.1.6	Addendum to Publication	77
5.2	SuperEllen Sensor	79
5.2.1	Two-Photon Detection	81
5.2.2	Four-Photon Detection	89
5.2.3	Pseudo-Thermal Light Detection	95
5.2.4	Conclusion	99
6	Quantum Imaging	103
6.1	Theory	103
6.1.1	Near-Field Imaging	104
6.1.2	Far-Field Imaging	107
6.1.3	Object Reconstruction Algorithm	109
6.2	Experimental Results	110
6.2.1	Near-Field Imaging	111
6.2.2	Far-Field Imaging	116
6.3	Conclusion	119
7	Super-Resolution Quantum Imaging at the Heisenberg Limit	123
7.1	Preface	123
7.2	Introduction	124
7.3	Theory	125
7.4	Experiment	127
7.5	Discussion	131
7.6	Supplementary Material	132
7.6.1	Derivation of the OCM Imaging Equation	132
7.6.2	Incoherent OCM Imaging	134
7.6.3	OCM State Generation using SPDC	134
7.6.4	Standard Quantum Limit of Classically Correlated Photons	135
8	Conclusion	137
A	Derivation of Sampling Space Volume	139

B Implementation of the Correlation Algorithm	141
B.1 Measurement Data Correlation in C	141
B.2 Normalization and Symmetrization in Matlab	144
C Group Delay Dispersion Calculation with Zemax	147
D SuperEllen Technical Publication	149
Bibliography	155
Declaration	163
Curriculum Vitae	165

List of Abbreviations

[x]	Iverson bracket notation: $[x] = 1$ if x is true, $[x] = 0$ otherwise
Accidentals	Detection events which are not temporally correlated but occurred by chance together within a coincidence window
Crosstalk	Spurious detection events, a photon detection triggers a false detection event in a adjacent detector pixel
CW	Continuous Wave. Nearly monochromatic, non-pulsed light source
EM	Electromagnetic
FBK	Fondazione Bruno Kessler from Trento (Italy). Partner institution within the SuperTwin project
HL	Heisenberg Limit
IPNASB	Institute of Physics of the National Academy of Sciences of Belarus
MFrame	Million Frames
NLC	Nonlinear Crystal
OCM	Optical Centroid Measurement
OLCR	Optical Low Coherence Reflectometry
PDE	Photon Detection Efficiency
SHG	Second-Harmonic Generation. Nonlinear optical effect
Superframe	Packet of 64 frames treated as one measurement window
SuperTwin	European funded Horizon 2020 project
SPAD	Single Photon Avalanche Diode
SPDC	Spontaneous Parametric Down-Conversion. Nonlinear optical process to generate photon pairs
SQL	Standard Quantum Limit

Chapter 1

Introduction

In this thesis, we investigate possibilities of exploiting quantum imaging techniques for resolution improvements in microscopy beyond the diffraction limit. For their efficient implementation in applications, a newly developed sensor is presented and applied for the first time in quantum imaging experiments. Quantum correlations of light are analyzed for their potential improvement of image resolution in microscopy.

Investigation of the spatial structure of small objects is the main goal of microscopy. By illumination, this shape is imprinted onto the light via the spatial variation of the object's light transmission or reflection. With an appropriate imaging system, this imprint is replicated in a distant plane where the object shape can be remotely measured. Even for perfect, aberration-free imaging systems, spatial resolution is limited. This so-called diffraction limit was for the first time studied by Abbe in 1873 [1] and by Rayleigh in 1896 [2]. Their results show that the wavelength of the illumination and the size of the imaging system's entrance pupil give a fundamental limit on the spatial resolution: Two object points cannot be distinguished if their separation lies below this limit, even for arbitrarily large optical magnifications. In the case of optimal pupil size, a resolution of at most half a wavelength is attainable. Rayleigh's and Abbe's theoretical treatments laid the foundations for the modern Fourier optical description of imaging which will be used throughout this work [3].

While one possibility to improve resolution is minimizing the illumination wavelength by using ultra-violet light, Röntgen radiation or matter waves, e.g. in electron microscopy where 50 pm resolution can be achieved [4], this approach is not suitable for sensitive objects. Biological samples would be destroyed and hence could not be studied alive in their temporal development. Techniques which avoid this problem were developed [5]: Near-field scanning optical microscopy (NSOM) can surpass the Rayleigh limit and reach 20 nm resolution using visible light [6]. Its implementation is difficult and invasive not allowing measurement at a distance. Other approaches rely on the fluorescence of the object under investigation, i.e. self-emission of light by molecules which are previously excited. For instance in stimulated emission depletion (STED), the Rayleigh limit can in principle be fully circumvented [7]. The most recent and successful techniques, called PALM or STORM, rely on the sparsity of the emitting fluorophores in the object where single emitters can be identified [8, 9]. By statistical averaging and thereby precisely locating their positions, image resolution down to 2 nm was reported. A major drawback of these techniques is the needed fluorescence, i.e. that the object has to be prepared with fluorophores prior to microscopy.

Quantum imaging is a rather recent field of research [10–13]. While many works are investigating fundamental aspects of the quantum nature of light like intensity correlations in ghost imaging [11, 14], entanglement [15, 16], and multi-photon interference effects [17], a lot of techniques emerged which surpass the limits of classical imaging. In the line of quantum metrology, weak amplitude and phase objects can be measured with better

signal-to-noise ratio than classical shot noise allows [10, 13]. Quantum lithography aims at producing spatial structures beyond the diffraction limit by the use of multi-photon interference [18]. Quantum microscopy, or super-resolution quantum imaging, employs techniques to surpass the Rayleigh diffraction limit to obtain higher resolved images [12, 13].

Quantum microscopy uses particular types of illumination sources and, instead of intensity measurement as in classical imaging, multi-photon correlation measurements. For instance, it was shown that illumination with N spatially correlated photons and coincident detection, the resolution can be improved by \sqrt{N} beyond the Rayleigh limit [19]. This scaling with photon number is called standard quantum limit (SQL) [20]. It can be achieved with classically correlated photons and be explained by a statistical averaging effect. In contrast, improvements at the Heisenberg limit (HL) have the better scaling of N , an ultimate optimum [21]. In this case, the N -photon state, consisting of N quantum correlated photons at wavelength λ , shows effects which would be classically observed at wavelength λ/N , the de Broglie wavelength of the multi-photon state [22]. This effective reduction of the wavelength explains the N -fold improved spatial resolution. A few schemes were theoretically proposed to yield an improvement at the HL but are not attractive in applications due to the lack of high quality multi-photon transmitters [19] or preparation of the object with single photon emitters [23, 24]. Moreover, the unavailable scaling to higher N because of not yet existing efficient light sources with the particular properties hinder their application [25].

The mentioned quantum imaging schemes are relying on temporally and spatially resolved single photon detection. While many experiments employed scanning apertures, the resulting long measurement time, especially for higher photon number correlation measurements, is not tolerable for real applications. More recently, work on single-photon sensitive CCD and CMOS cameras which can be temporally gated improved these type of measurements considerably [26–30]. While these devices allow the measurement of coincident photons, only low fluxes with a low number of photons per exposed frame can be used in order to correctly assess the spatial correlations of photons. Low frame rates still prolong measurement time.

In this work, we present two newly developed 2D detector arrays which have sub-nanosecond time resolution for each individual single-pixel detection event and exceed the frame rates of cameras by several magnitudes. This allows for higher photon fluxes and thereby results in more efficient measurements. Glauber's field correlation functions are standard expressions to characterize the quantum field of light and are the main quantity of interest for the majority of quantum imaging experiments [31]. The raw sensor data has to be processed for inferring this quantity. We derive a general sensor data evaluation procedure for the measurement of arbitrary-order intensity correlation functions. For the given detectors, these results are worked out and efficient algorithms presented.

Relying on this measurement apparatus, quantum imaging experiments aiming at super-resolution are performed. Different standard correlated light sources are used for illumination while intensity correlation functions are measured. In this case, the physical improvement is expected to be at the SQL only [19, 32–34]. By employing object reconstruction algorithms, however, image resolution can in principle be arbitrarily improved only limited by noise [35, 36]. In contrast to standard computational microscopy methods like deconvolution [37], we apply the reconstruction on the full high-order correlation function of large dimensionality which potentially yields statistical advantages over the standard methods.

The above mentioned results of super-resolution at the HL are well known from quantum metrology where NOON-states exhibit features of the de Broglie wavelength in phase

measurements [13]. In this work, this characteristic signature is experimentally observed and exploited for interferometric length measurements. It seems to be a common misunderstanding that the illumination with entangled photon pairs is sufficient to yield imaging resolution improvements at the HL [13, 38], while it was shown that this only scales at the SQL [19]. No advantage due to entanglement is exploited in these schemes [39]. In an imaging context using entangled photons, the HL was only observed in the far-field of an object [17] and in the observation of interference fringes of plane waves [40, 41]. To the best of our knowledge, we present the first multi-mode generalization of these results, based on the seminal work of Tsang introducing optical centroid measurement [42], allowing for efficient, full visibility near-field imaging of object features with super-resolution at the HL.

The work of this thesis was performed in the Quantum Optics Group at the University of Bern. This group is a member of SuperTwin¹, a project funded by the European Union within the Future and Emerging Technology (FET) section of the Horizon 2020 program. The collaboration consists of nine institutes and companies across Europe. The goal of the project is the development of a new generation of microscopy technology. By employing quantum imaging schemes, the classical resolution limit of Rayleigh shall be surpassed. The key components of the planned microscope are the quantum light source, the detection unit, and the measurement data processing. Three project partners concentrate on the fabrication of a solid-state light source which is based on the physical effect of super-luminescence. This device is intended to provide an efficient source of photons with the correlations needed for super-resolution imaging. The above introduced directions of research are motivated by the group's responsibilities within the project. The test and characterization of newly developed detector arrays in quantum imaging experiments using standard quantum light sources allows to work out the specification for a next generation device. This is performed in close collaboration with the sensor developers and project partners at Fondazione Bruno Kessler (FBK). While the light source is not ready for its application, model quantum imaging experiments using standard sources of low photon number are designed and implemented. These allow delivering measurement data to the processing algorithm developers at the Institute of Physics of the Belarus National Academy of Science (IPNASB) for test and optimization of their approach.

This thesis is structured as follows: Chapter 2 provides a short introduction to quantum Fourier optics, allowing the description of imaging experiments in later chapters. Furthermore, sensor data processing is analyzed. Three different correlated light sources are implemented for the work of this thesis and are described and characterized in Chapter 3. The two-photon experiment of Chapter 4 demonstrates the de Broglie wavelength of a NOON-state in an interferometric metrology application. In Chapter 5, two time-resolving detector arrays are tested and characterized with the introduced light sources. Conclusions for a new sensor generation are worked out. The quantum imaging experiments of Chapter 6 provides measurement data to IPNASB's reconstruction algorithm. Relying on the chapters before, these experiments are described by the Fourier optics formalism, the different illumination sources are used, and the sensors and processing algorithms are applied for the measurement. Preliminary object reconstruction results are shown. Finally, Chapter 8 presents the theoretical and experimental results of super-resolution imaging at the HL. Detection is performed by one of the introduced sensor arrays.

¹See also project web page <http://www.supertwin.eu/>

The following publications are in preparation, have been submitted, or are published as a part of this thesis:

Published

- M. Unternährer, B. Bessire, L. Gasparini, D. Stoppa, and A. Stefanov, "Coincidence detection of spatially correlated photon pairs with a monolithic time-resolving detector array", *Optics Express* 24, 28829 (2016). Ref. [43].

M. Unternährer, B. Bessire, L. Gasparini, D. Stoppa, and A. Stefanov, "Coincidence detection of spatially correlated photon pairs with a monolithic time-resolving detector array", in *European CLEO Conference (2017)*, CD_10_1. Ref. [44].

This publication and conference paper is presented in Sec. 5.1. A.S., B.B., and M.U. devised the experiment which was implemented by M.U. and B.B. The manuscript is written by M.U. and B.B. with support from A.S. L.G., M.P., and D.S. developed the CMOS sensor array and driver software, M.U. the data acquisition and analysis software. A.S. supervised the project.

- L. Gasparini, B. Bessire, M. Unternährer, A. Stefanov, D. Boiko, M. Perenzoni, and D. Stoppa (2017), "SUPERTWIN: towards 100kpixel CMOS quantum image sensors for quantum optics applications", in *Proc. of SPIE*, Vol. 10111 (2017), 10111. Ref. [45].

This conference paper contains our work of Sec. 5.1 and the above mentioned publication. It is written by L.G., M.P., and D.S. with support from B.B., A.S. and M.U.

- L. Gasparini, M. Zarghami, H. Xu, L. Parmesan, M. Moreno Garcia, M. Unternährer, B. Bessire, A. Stefanov, D. Stoppa and M. Perenzoni, "A 32x32-pixels time-resolved single-photon image sensor with 44.64- μm pitch and 19.48% fill-factor with on-chip row/frame skipping features reaching 800 kHz observation rate for quantum physics applications", in *International Solid-State Circuits Conference, ISSCC'18 (IEEE, 2018)*, in press). Ref. [46].

This conference paper is presented in App. D. A.S., B.B. and M.U. devised the exemplary quantum experiment which was implemented by M.U., B.B. and L.G. The manuscript is written by L.G., M.P. and D.S. with support from A.S., B.B. and M.U. L.G., M.Z., H.X., L.P., M.M.G., D.S., and M.P. developed this new CMOS sensor array and characterized it. They also developed the driver software, while M.U. implemented the data acquisition and analysis software for the experiment. M.P. and A.S. supervised the project.

Submitted

- M. Unternährer, B. Bessire, L. Gasparini, M. Perenzoni, and A. Stefanov, "Super-Resolution Quantum Imaging at the Heisenberg Limit", arXiv:1712.02200 [quant-ph], (2018). Ref. [47].

This submitted manuscript is presented in Ch. 7. M.U. deduced the formalism and devised the experiment. M.U. and A.S. wrote the manuscript with support from B.B., while M.U. and B.B. implemented the experiment. L.G. and M.P. developed the CMOS sensor array and driver software, M.U. the data acquisition and analysis software. A.S. supervised the project.

In Preparation

- M. Unternährer and A. Stefanov, "Self-Calibrating Optical Low-Coherence Reflectometry using Energy-Time Entangled Photons", in preparation.

The work of this manuscript is presented in Ch. 4. A.S. and M.U. devised the experiment. M.U. implemented it and wrote this manuscript with support and under supervision from A.S.

- A. Mikhalychev, A. Sakovich, I. Karuseichyk, B. Bessire, M. Unternährer, A. Stefanov, and D. Mogilevtsev, "Piecewise Tomography: Optimizing Reconstruction of Multi-Parameter Systems", in preparation. Ref. [48].

This work is a collaboration with IPNASB. In Ch. 6, the theoretical approach of IPNASB and their preliminary results are discussed and our experimental data presented. A.S., B.B., and M.U. devised the experiments. M.U. and B.B. implemented it and performed the theoretical model calculations.

Chapter 2

Theoretical Framework

This chapter introduces the theoretical formalism which describes the transformation of the electromagnetic field by a general experimental setup. Furthermore, field measurements are modeled in this framework and allow to understand and predict experimental outcomes. Starting with classical optics allows to introduce the tools which can later be directly applied in the quantum treatment of the electromagnetic field.

In addition to this standard textbook theory, we analyze and describe the measurement of intensity correlation functions with detector arrays. These functions are the central quantity of interest for this thesis. Formal expressions for the processing of measurement data provided by the detectors are derived. Finally, an algorithm is proposed which allows for their fast implementation in software.

Results for general light sources and optical systems are derived in this chapter. These are applied to the concrete light sources introduced in Ch. 3 and used for the experiments of Chs. 4–7.

2.1 Classical Fourier Optics

Fourier optics uses the well elaborated tools of mathematical Fourier analysis to model and describe optical phenomena [3]. This framework relies on the theory and formalism of linear systems. The main concepts of Fourier optics and linear systems are introduced in the following. Thereby, concrete situations like field transmission through objects and lenses as well as free-space propagation are described within this theoretical framework. The optical setups of near- and far-field imaging, which are standard and extensively used in this thesis, can then be described and formalized. This allows to predict the outcomes of measurements in optical experiments using classical sources of light.

2.1.1 Introduction

In classical physics, the electromagnetic (EM) field is fully described by Maxwell's equations [3, 49]. For a given experimental setup and a classical light source, these equations determine the electric field vector

$$\mathbf{E}(\mathbf{r}, t)$$

at every spatial position $\mathbf{r} = (x, y, z)$ and time t . Outcomes of intensity measurements performed in this experiment are predicted by this physical model. For this work, detection is performed in free-space and the field is locally well approximated by transverse EM plane waves. Then, the magnetic field is fully determined by \mathbf{E} and leads to the intensity

$$I(\mathbf{r}, t) = \frac{\epsilon_0 c}{2} |\mathbf{E}(\mathbf{r}, t)|^2 \quad (2.1)$$

with the electric permittivity ε_0 and speed of light c in vacuum [3, 49, 50]. For the encountered situations of this work, we can assume the absence of free charges. We further assume aperture areas to be much larger than the wavelength and propagation of the EM field only through linear, isotropic, homogeneous, nondispersive and nonmagnetic media. Under these assumptions, Maxwell's equations reduce to a scalar wave equation which is satisfied by all vectorial components of the magnetic and electric field independently. It is therefore sufficient to model only the electric field for calculations of local intensities using Eq. (2.1). Moreover, for light source of one polarization mode only, the electric field is fully described by a scalar function whose behavior is determined by scalar diffraction theory [3].

For the description of coherent transmission of light and its Fourier analysis, it is of advantage to write this scalar function as sum of two complex conjugate quantities, the positive and negative frequency parts,

$$E(\mathbf{r}, t) = E^{(+)}(\mathbf{r}, t) + E^{(-)}(\mathbf{r}, t).$$

where $E^{(+)} = [E^{(-)}]^*$ and therefore the intensity $I \propto |E^{(+)}|^2$. Any electric field distribution can be decomposed into plane waves via a Fourier synthesis

$$E^{(+)}(\mathbf{r}, t) = \frac{1}{(2\pi)^4} \int d^3\mathbf{k} d\omega E^{(+)}(\mathbf{k}, \omega) e^{i\omega t - i\mathbf{k}\cdot\mathbf{r}}.$$

The angular frequency ω relates to the wavevector \mathbf{k} with the free-space dispersion relation [49]

$$|\mathbf{k}| = k = \sqrt{k_x^2 + k_y^2 + k_z^2} = \frac{\omega}{c}. \quad (2.2)$$

If this condition is met, the plane waves and therefore the synthesized $E^{(+)}(\mathbf{r}, t)$ fulfill the free-space Maxwell's equations and represent a physical solution. With light propagating mainly in z direction, we define the transverse position $\boldsymbol{\rho}$ and transverse wave vector \mathbf{q} as

$$\boldsymbol{\rho} = (x, y), \quad \mathbf{q} = (k_x, k_y).$$

This definition and the condition of the dispersion relation allows to write the free-space solution of the wave equations

$$E^{(+)}(\boldsymbol{\rho}, z, t) = \frac{1}{(2\pi)^3} \int d^2\mathbf{q} d\omega E^{(+)}(\mathbf{q}, \omega) e^{i\omega t - i\mathbf{q}\cdot\boldsymbol{\rho} - i\sqrt{k^2 - |\mathbf{q}|^2}z}. \quad (2.3)$$

This equation shows explicitly, that a given electric field at $z = 0$ also determines its distribution in all other z planes. For a reference plane Σ_1 , we can choose the coordinate system such that $z = 0$ and write

$$E_1^{(+)}(\boldsymbol{\rho}, t) = \frac{1}{(2\pi)^3} \int d^2\mathbf{q} d\omega E_1^{(+)}(\mathbf{q}, \omega) e^{i\omega t - i\mathbf{q}\cdot\boldsymbol{\rho}}. \quad (2.4)$$

The field in a plane Σ_2 of distance Δz can then be determined by concluding from Eq. (2.3) that the transformation $E_1^{(+)}(\mathbf{q}, \omega) \rightarrow E_2^{(+)}(\mathbf{q}, \omega) = E_1^{(+)}(\mathbf{q}, \omega) e^{-i\sqrt{k^2 - |\mathbf{q}|^2}\Delta z}$ yields with Eq. (2.4) the field $E_2^{(+)}(\boldsymbol{\rho}, t)$ in Σ_2 . This phase is called transfer function of the free-space propagation of distance Δz and is defined by

$$H_F(\mathbf{q}, \omega, \Delta z) := e^{-i\sqrt{k^2 - |\mathbf{q}|^2}\Delta z}. \quad (2.5)$$

2.1.2 Linear System Theory

The more general principle of linear system theory allows to model not only free-space propagation in a similar way, but arbitrary linear transformations of the electric field performed by optical systems. In the following we consider only wavelength preserving or, equivalently, time-invariant transformations which model time-stationary optical systems. They are characterized by their *impulse response function*

$$h(\boldsymbol{\rho}, \boldsymbol{\rho}', t - t').$$

The arguments of transverse position $\boldsymbol{\rho}'$ and time t' can be interpreted as inputs. For these values fixed, the impulse response function describes the field distribution at the output in the coordinates $\boldsymbol{\rho}$ and t . Having an input field $E_1^{(+)}$, the output therefore becomes

$$E_2^{(+)}(\boldsymbol{\rho}, t) = \int d^2\boldsymbol{\rho}' dt' E_1^{(+)}(\boldsymbol{\rho}', t') h(\boldsymbol{\rho}, \boldsymbol{\rho}', t - t'). \quad (2.6)$$

For multiple, successive transformations, this equation is applied recursively and allows the calculation of a total impulse response function.

For the case of *space-invariant* transformations, the impulse response function can be written as

$$h(\boldsymbol{\rho} - \boldsymbol{\rho}', t - t')$$

and Eq. (2.6) simplifies to the convolution

$$E_2^{(+)}(\boldsymbol{\rho}, t) = \int d^2\boldsymbol{\rho}' dt' E_1^{(+)}(\boldsymbol{\rho}', t') h(\boldsymbol{\rho} - \boldsymbol{\rho}', t - t') = (E_1^{(+)} * h)(\boldsymbol{\rho}, t). \quad (2.7)$$

Using the Fourier convolution theorem and the field's Fourier spectrum $E_1^{(+)}(\boldsymbol{q}, \omega)$ given in Eq. (2.4), it can be shown that this is equivalent to the identity

$$E_2^{(+)}(\boldsymbol{q}, \omega) = E_1^{(+)}(\boldsymbol{q}, \omega) H(\boldsymbol{q}, \omega) \quad (2.8)$$

in Fourier space, where the function $H(\boldsymbol{q}, \omega)$ is called *transfer function*. It is related to the impulse response function by the Fourier transform

$$H(\boldsymbol{q}, \omega) = \int d^2\boldsymbol{\rho} dt h(\boldsymbol{\rho}, t) e^{-i\omega t + i\boldsymbol{q}\cdot\boldsymbol{\rho}}.$$

and vice versa with an inverse Fourier transformation.

For simplicity but without loss of generality, we consider in the following monochromatic light at wavelength λ and therefore a wave vector magnitude $k = 2\pi/\lambda$ and angular frequency $\omega = kc$. This allows to remove the explicit ω dependence of the transfer functions and the time dependence of the impulse response functions.

2.1.3 Elementary Optical Impulse Response Functions

For the following elementary optical systems, impulse response functions are derived in [3, 38, 49, 50] and here put in a consistent form.

- The transfer function of *free-space propagation* was derived in Eq. (2.5). We impose the paraxial or Fresnel approximation which assumes only wavepackets travelling

mainly along the z -direction and therefore $|\mathbf{q}|^2 \ll k^2$. In this limit, the propagation transfer function can be approximated by

$$H_F(\mathbf{q}, \Delta z) = \exp\left(-ik\Delta z + i\frac{|\mathbf{q}|^2}{2k}\Delta z\right). \quad (2.9)$$

With an inverse Fourier transform, it can be shown that the space-invariant impulse response function reads

$$h_F(\boldsymbol{\rho}_1, \boldsymbol{\rho}_2, \Delta z) = h_F(\boldsymbol{\rho}_1 - \boldsymbol{\rho}_2, \Delta z) = \frac{ik}{2\pi\Delta z} \exp\left(-ik\Delta z - i\frac{k}{2\Delta z}|\boldsymbol{\rho}_1 - \boldsymbol{\rho}_2|^2\right). \quad (2.10)$$

- For the transmission through a *thin lens* of focal length f , it can be shown that the non-space-invariant impulse response function is given by

$$h_L(\boldsymbol{\rho}, \boldsymbol{\rho}') = \delta^{(2)}(\boldsymbol{\rho} - \boldsymbol{\rho}') \exp\left(i\frac{k}{2f}|\boldsymbol{\rho}|^2\right). \quad (2.11)$$

Using Eq. (2.6), this corresponds to a pure spatial phase factor.

- An *object aperture* of transmission amplitude $A(\boldsymbol{\rho})$ placed in the electric field, can be modeled with the impulse response function

$$h_A(\boldsymbol{\rho}, \boldsymbol{\rho}') = \delta^{(2)}(\boldsymbol{\rho} - \boldsymbol{\rho}') A(\boldsymbol{\rho}). \quad (2.12)$$

These set of impulse response functions are sufficient to describe the following imaging setups.

2.1.4 Single Lens Near-Field Imaging

Single lens near-field imaging is composed of the following intermediate steps: Starting from the initial object plane, the light is freely propagated for the distance s_o , a lens aperture $A(\boldsymbol{\rho})$ limits the size of the following lens, then a lens of focal length f refracts and transmits the field, and finally a free-space propagation to the image plane at the distance s_i is performed. The impulse response function of the total system can therefore be written in terms of the above defined elementary functions as

$$h_{NF}(\boldsymbol{\rho}_i, \boldsymbol{\rho}_o) = \int d^2\rho'_A d^2\rho_A d^2\rho_L h_F(\boldsymbol{\rho}_i, \boldsymbol{\rho}_L, s_i) h_L(\boldsymbol{\rho}_L, \boldsymbol{\rho}_A) h_A(\boldsymbol{\rho}_A, \boldsymbol{\rho}'_A) h_F(\boldsymbol{\rho}'_A, \boldsymbol{\rho}_o, s_o).$$

For near-field imaging, the thin lens imaging condition $1/f = 1/s_o + 1/s_i$ is fulfilled and by inserting Eqs. (2.9)–(2.12), we arrive at

$$h_{NF}(\boldsymbol{\rho}_i, \boldsymbol{\rho}_o) = \frac{-k^2}{(2\pi)^2 s_i s_o} e^{-ik(s_o + s_i)} \exp\left(-ik\frac{|\boldsymbol{\rho}_i|^2}{2s_i} - ik\frac{|\boldsymbol{\rho}_o|^2}{2s_o}\right) \tilde{A}\left(\frac{k\boldsymbol{\rho}_i}{s_i} + \frac{k\boldsymbol{\rho}_o}{s_o}\right).$$

The function $\tilde{A}(\mathbf{q})$ is given by the Fourier transform of the lens aperture $A(\boldsymbol{\rho})$. For a *circular aperture* of radius R and unity transmission

$$\tilde{A}(\mathbf{q}) = R^2 \frac{2J_1(R|\mathbf{q}|)}{R|\mathbf{q}|} = R^2 \text{somb}(R|\mathbf{q}|),$$

where J_1 is the first-order Bessel function and somb the hereby defined sombrero function, also known as Airy pattern. Using the imaging system magnification factor $m := s_i/s_o$, we can write in conclusion

$$h_{NF}(\boldsymbol{\rho}_i, \boldsymbol{\rho}_o) = \frac{-k^2 R^2}{(2\pi)^2 s_i s_o} e^{-ik(s_o+s_i)} \exp\left(-ik \frac{|\boldsymbol{\rho}_i|^2}{2s_i} - ik \frac{|\boldsymbol{\rho}_o|^2}{2s_o}\right) \text{somb}\left(\frac{Rk}{s_o} \left|\boldsymbol{\rho}_o + \frac{\boldsymbol{\rho}_i}{m}\right|\right). \quad (2.13)$$

For neglected prefactors and phase terms, this impulse response function reads

$$h_{NF}(\boldsymbol{\rho}_i, \boldsymbol{\rho}_o) = h_{NF}\left(\boldsymbol{\rho}_o + \frac{\boldsymbol{\rho}_i}{m}\right) = \text{somb}\left(\frac{Rk}{s_o} \left|\boldsymbol{\rho}_o + \frac{\boldsymbol{\rho}_i}{m}\right|\right) \quad (2.14)$$

and is therefore space-invariant after magnification and inversion/rotation. Applying Eq. (2.6), for each point source in the object plane at $\boldsymbol{\rho}_o$, a patch centered at $\boldsymbol{\rho}_i = -m\boldsymbol{\rho}_o$ whose shaped is given by the sombrero function is produced. Accordingly, h_{NF} is called *point-spread function* (PSF) and determines the resolution of the imaging system. In the optimal case of large R ,

$$h_{NF}(\boldsymbol{\rho}_o + \boldsymbol{\rho}_i/m) \xrightarrow{R \rightarrow \infty} \delta^{(2)}(\boldsymbol{\rho}_o + \boldsymbol{\rho}_i/m)$$

and the electric field in the object plane is fully replicated, in a magnified and rotated version, in the image plane.

The field transformation by single lens imaging described by Eq. (2.13) can be split into several steps: First, the multiplication of the field by a phase factor $\exp(-ik|\boldsymbol{\rho}_i|^2/2s_i)$ in the image plane. Second, the field transformation with the impulse response function $\text{somb}(Rk|\boldsymbol{\rho} - \boldsymbol{\rho}'|/s_o)$, or in general

$$h_2(\boldsymbol{\rho} - \boldsymbol{\rho}') = \tilde{A}\left(\frac{k(\boldsymbol{\rho} - \boldsymbol{\rho}')}{s_o}\right)$$

with the Fourier transform \tilde{A} of the lens aperture. Afterwards, the rotation, magnification by m , and finally the multiplication by the phase factor $\exp(-ik|\boldsymbol{\rho}_o|^2/2s_o)$ is performed.

The transformation h_2 shows explicitly space-invariance as introduced in Sec. 2.1.2. Therefore, it can be expressed in Fourier space by a transfer function which is here given by

$$H(\boldsymbol{q}) = A\left(\frac{s_o}{k} \boldsymbol{q}\right).$$

The lens aperture $A(\boldsymbol{\rho})$ plays therefore the role of a filter of transverse wave vectors as evident in the field transformation rule of Eq. (2.8). In cases of small enough object, all phase factors can be neglected. The only nontrivial transformation is then h_2 and the reduced image resolution is fully described by this filtering.

2.1.5 Far-Field Imaging

The far-field imaging is performed with the following steps: From the initial source plane the light is freely propagated for the distance d , a lens of focal length f and unlimited transverse size refracts and transmits the light, and finally a free-space propagation of distance

f to the far-field plane is performed. Therefore, the total impulse response function

$$h_{FF}(\boldsymbol{\rho}_f, \boldsymbol{\rho}_s) = \int d^2 \boldsymbol{\rho}'_L d^2 \boldsymbol{\rho}_L h_F(\boldsymbol{\rho}_f, \boldsymbol{\rho}_L, f) h_L(\boldsymbol{\rho}_L, \boldsymbol{\rho}'_L) h_F(\boldsymbol{\rho}'_L, \boldsymbol{\rho}_s, d).$$

Inserting the elementary response functions of Eqs. (2.9)–(2.12), we arrive at

$$h_{FF}(\boldsymbol{\rho}_f, \boldsymbol{\rho}_s) = \frac{ik}{2\pi f} e^{-ik(d+f)} e^{i\frac{k}{2f^2}(d-f)|\boldsymbol{\rho}_f|^2} e^{i\frac{k}{f}\boldsymbol{\rho}_f \cdot \boldsymbol{\rho}_s}. \quad (2.15)$$

For the case of $d = f$, this result simplifies to

$$h_{FF}(\boldsymbol{q}, \boldsymbol{\rho}_s) = \frac{ik}{2\pi f} e^{-ik2f} e^{i\boldsymbol{q} \cdot \boldsymbol{\rho}_s} \quad (2.16)$$

with the definition $\boldsymbol{q} := (k/f) \boldsymbol{\rho}_f$. Using Eq. (2.6), an input plane wave of wave vector \boldsymbol{q} , given by $E^{(+)}(\boldsymbol{\rho}) = \exp(-i\boldsymbol{q} \cdot \boldsymbol{\rho})$, is with this system focused to a single point at $\boldsymbol{\rho}_f = (f/k) \boldsymbol{q}$ in the far-field plane. And reversely, a point source in the input plane at $\boldsymbol{\rho}_s$ is being transformed to a plane wave at the output. In general, for the input field $E^{(+)}(\boldsymbol{\rho})$ we yield the Fourier transform $E^{(+)}(\boldsymbol{q})$ at the output far-field plane by identifying $\boldsymbol{q} = (k/f) \boldsymbol{\rho}_f$.

In contrast to the near-field case, the far-field lens is not modeled with a finite aperture. This comes from the fact that this lens can in principle be put arbitrary close to the object and thereby does not filter by its aperture. This becomes obvious in Eq. (2.15): Only a phase term occurs in the far-field plane for $d \neq f$, the response function is otherwise equal. In addition, the resolution in the object details depends on the measurable \boldsymbol{q} range. This is not depending on the lens aperture size and therefore not of interest for the investigation of resolution in this thesis.

2.2 Fourier Optics of Quantum Fields

In order to describe non-classical light sources, e.g. sources at a single photon level and exhibiting quantum correlations, the quantum description of the electromagnetic field is introduced in this section. The framework of Fourier optics presented in classical optics can be adapted to this quantum formalism. The previously discussed intensity measurements are here generalized to intensity correlations measurements. With this, the framework allows to model the outcomes of these correlation measurements with arbitrary experiment settings and light sources.

2.2.1 Introduction

In a quantum theoretical treatment of the EM field, under the same conditions as mentioned in Sec. 2.1 resulting in a scalar wave equation, the classical electric field $E(\boldsymbol{\rho}, t)$ has its analogue in the field operator [38, 51, 52]

$$\hat{E}(\boldsymbol{\rho}, t) = \hat{E}^{(+)}(\boldsymbol{\rho}, t) + \hat{E}^{(-)}(\boldsymbol{\rho}, t).$$

It represents field measurements in the transverse reference plane Σ . Being hermitian conjugates of each other $\hat{E}^{(+)} = [\hat{E}^{(-)}]^\dagger$, we can define similarly to Eq. (2.4)

$$\hat{E}^{(+)}(\boldsymbol{\rho}, t) := \frac{1}{(2\pi)^3} \int d^2 \boldsymbol{q} d\omega e(\omega) \hat{a}(\boldsymbol{q}, \omega) e^{i\omega t - i\boldsymbol{q} \cdot \boldsymbol{\rho}}. \quad (2.17)$$

The field operator normalization function is

$$e(\omega) = i\sqrt{\frac{\hbar\omega}{2(2\pi)^3\epsilon_0c}}$$

which establishes the correct units of the electric field. The photon annihilation operator \hat{a} removes a photon from the plane wave mode specified in its arguments and fulfills with its hermitian conjugate, the photon creation operator \hat{a}^\dagger , the commutation relations

$$[\hat{a}(\mathbf{q}, \omega), \hat{a}^\dagger(\mathbf{q}', \omega')] = \delta^{(2)}(\mathbf{q} - \mathbf{q}')\delta(\omega - \omega').$$

The photon number operator

$$\hat{n}(\mathbf{q}, \omega) := \hat{a}^\dagger(\mathbf{q}, \omega)\hat{a}(\mathbf{q}, \omega)$$

determines the number of photons present in the specified plane wave mode.

The physical state of the EM field is in this formalism represented as an abstract quantum state $|\Psi\rangle \in \mathcal{H}$ in the Hilbert space \mathcal{H} of all possible states [53]. The above mentioned operators act on these states and transform them within this space. The vacuum state $|0\rangle$ is normalized with respect to the inner product of the Hilbert space, denoted by the Dirac bracket notation $\langle\Phi|\Psi\rangle$, and represents the absence of any photonic excitation of the field

$$\langle 0|0\rangle = 1, \quad \hat{a}(\mathbf{q}, \omega)|0\rangle = 0, \quad \forall \mathbf{q}, \omega.$$

In a photon number or Fock basis, a N -photon state can be written as

$$|\Psi\rangle = C a^\dagger(\mathbf{q}_1, \omega_1) \dots a^\dagger(\mathbf{q}_N, \omega_N) |0\rangle = |\mathbf{q}_1, \omega_1; \dots; \mathbf{q}_N, \omega_N\rangle$$

with an appropriate normalization constant C . A general multi-photon state with a distribution in photon numbers is given with

$$|\Psi\rangle = \sum_{n=0}^{\infty} \int d^2\mathbf{q}_1 d\omega_1 \dots d^2\mathbf{q}_n d\omega_n \Lambda_n(\mathbf{q}_1, \omega_1; \dots; \mathbf{q}_n, \omega_n) \prod_{k=1}^n a^\dagger(\mathbf{q}_k, \omega_k) |0\rangle$$

where the n -photon wave functions Λ_n specify the distribution of the photons in the different plane wave modes.

Measurements outcomes are predicted by quantum expectation values [53]. Using the inner product of the Hilbert space, the expectation value of a general measurement of a quantity with corresponding operator \hat{M} for a given physical state $|\Psi\rangle$ is

$$\langle \hat{M} \rangle = \langle \Psi | \hat{M} | \Psi \rangle.$$

In analogy to the classical result in Eq. (2.1), the expectation value of the field intensity is given by

$$\langle \hat{I}(\boldsymbol{\rho}, t) \rangle = \frac{\epsilon_0 c}{2} \langle \hat{E}^{(-)}(\boldsymbol{\rho}, t) \hat{E}^{(+)}(\boldsymbol{\rho}, t) \rangle$$

In the following parts of this work, we are not interested in the intensity in its SI units of $[\text{W m}^{-2}]$, but in the flux density of photons $[\text{m}^{-2} \text{s}^{-1}]$. This allows to drop this last equation's prefactor and the field operator normalization $e(\omega)$. In this regime of photon counting, we get a simplified field operator

$$\hat{E}^{(+)}(\boldsymbol{\rho}, t) := \frac{1}{(2\pi)^{3/2}} \int d^2\mathbf{q} d\omega \hat{a}(\mathbf{q}, \omega) e^{i\omega t - i\mathbf{q}\cdot\boldsymbol{\rho}} \quad (2.18)$$

and accordingly its hermitian conjugate $\hat{E}^{(-)}(\boldsymbol{\rho}, t)$. They can be interpreted as a photon annihilation and creation operators in position-time coordinates with the commutation relations

$$[\hat{E}^{(+)}(\boldsymbol{\rho}, t), \hat{E}^{(-)}(\boldsymbol{\rho}', t')] = \delta^{(2)}(\boldsymbol{\rho} - \boldsymbol{\rho}') \delta(t - t'). \quad (2.19)$$

The expectation value of the photon flux density can now be written as

$$\langle \hat{I}(\boldsymbol{\rho}, t) \rangle = \langle \hat{n}(\boldsymbol{\rho}, t) \rangle,$$

where the photon number operator

$$\hat{n}(\boldsymbol{\rho}, t) := \hat{E}^{(-)}(\boldsymbol{\rho}, t) \hat{E}^{(+)}(\boldsymbol{\rho}, t) \quad (2.20)$$

is now defined in direct space.

2.2.2 Transformation of Field Operators

Having a prepared quantum state of the EM field, we want to predict measurement outcomes of an experiment. The optical setup can be classically characterized by its impulse response function $h(\boldsymbol{\rho}, \boldsymbol{\rho}', t - t')$ which transforms the classical electric field with Eq. (2.6), see Sec. 2.1. The electric field operator $\hat{E}_1^{(+)}$ which corresponds to measurements on the setup input plane Σ_1 transforms identically to the classical field [38, 51, 52]. Therefore, the operator which describes measurements at the output plane Σ_2 reads

$$\hat{E}_2^{(+)}(\boldsymbol{\rho}, t) = \int d^2\boldsymbol{\rho}' dt' \hat{E}_1^{(+)}(\boldsymbol{\rho}', t') h(\boldsymbol{\rho}, \boldsymbol{\rho}', t - t'). \quad (2.21)$$

Similarly, $\hat{E}^{(-)}$ can be transformed using the complex conjugate $[h(\boldsymbol{\rho}, \boldsymbol{\rho}', t - t')]^*$. The photon flux density is then $\hat{n}(\boldsymbol{\rho}, t) = \hat{E}_2^{(-)}(\boldsymbol{\rho}, t) \hat{E}_2^{(+)}(\boldsymbol{\rho}, t)$. This allows to calculate the flux density distribution in any plane and after any linear optical setup using the impulse response functions from Sec. 2.1.

The *Heisenberg picture* of quantum mechanics is here realized, as operators are transformed but the quantum states are stationary. Equivalent results are gained in a *Schrödinger picture* of an propagating wave function but stationary operators. This is possible in the case of states with fixed photon number N [38]. For non-unitary transformations, lower photon numbers arise which are not described by pure states anymore. Restricting or projecting to the N -photon state contribution allows even then the following procedure of wave function transformation: For a one-photon state

$$|\Psi\rangle = \int d^2\boldsymbol{\rho} dt \Psi_1(\boldsymbol{\rho}, t) \hat{E}_1^{(-)}(\boldsymbol{\rho}, t) |0\rangle$$

this effective wave function can be defined in the plane Σ_1 of the field operator $E_1^{(+)}$ with

$$\Psi_1(\boldsymbol{\rho}, t) = \langle 0 | \hat{E}_1^{(+)}(\boldsymbol{\rho}, t) | \Psi \rangle.$$

It fully characterizes the quantum field. Propagating the field from Σ_1 through a system with impulse response function $h(\boldsymbol{\rho}, \boldsymbol{\rho}', t - t')$, we get at the output plane Σ_2

$$\begin{aligned}
\Psi_2(\boldsymbol{\rho}, t) &= \langle 0 | \hat{E}_2^{(+)}(\boldsymbol{\rho}, t) | \Psi \rangle \\
&= \langle 0 | \int d^2 \boldsymbol{\rho}' dt' \hat{E}_1^{(+)}(\boldsymbol{\rho}', t') h(\boldsymbol{\rho}, \boldsymbol{\rho}', t - t') \int d^2 \boldsymbol{\rho}'' dt'' \Psi_1(\boldsymbol{\rho}'', t'') \hat{E}^{(-)}(\boldsymbol{\rho}'', t'') | 0 \rangle \\
&= \int d^2 \boldsymbol{\rho}'' dt'' \Psi_1(\boldsymbol{\rho}'', t'') h(\boldsymbol{\rho}, \boldsymbol{\rho}'', t - t'') \\
&= \langle 0 | \hat{E}_1^{(+)}(\boldsymbol{\rho}, t) \int d^2 \boldsymbol{\rho}' dt' \left(\int d^2 \boldsymbol{\rho}'' dt'' \Psi_1(\boldsymbol{\rho}'', t'') h(\boldsymbol{\rho}', \boldsymbol{\rho}'', t' - t'') \right) \hat{E}^{(-)}(\boldsymbol{\rho}', t') | 0 \rangle \\
&= \langle 0 | \hat{E}_1^{(+)}(\boldsymbol{\rho}, t) | \Psi_2 \rangle,
\end{aligned}$$

where we have used field operator propagation and the commutation relations of Eq. (2.19). Therefore, the same field characterizing result is yielded with a propagated field operator $\hat{E}_2^{(+)}$ and a fixed quantum state $|\Psi\rangle$ like with a transformed quantum state $|\Psi_2\rangle$ while using a fixed measurement operator $\hat{E}^{(+)} = \hat{E}_1^{(+)}$. For the normalized effective wave function of an N -photon state

$$\Psi(\boldsymbol{\rho}_1, t_1; \dots; \boldsymbol{\rho}_N, t_N) := \frac{1}{\sqrt{N!}} \langle 0 | \hat{E}^{(+)}(\boldsymbol{\rho}_1, t_1) \dots \hat{E}^{(+)}(\boldsymbol{\rho}_N, t_N) | \Psi \rangle,$$

the here derived transformation rule can be generalized to

$$\begin{aligned}
\Psi_2(\boldsymbol{\rho}_1, t_1; \dots; \boldsymbol{\rho}_N, t_N) &= \int d^2 \boldsymbol{\rho}'_1 dt'_1 \dots d^2 \boldsymbol{\rho}'_N dt'_N \Psi_1(\boldsymbol{\rho}'_1, t'_1; \dots; \boldsymbol{\rho}'_N, t'_N) \\
&\quad \times h(\boldsymbol{\rho}_1, \boldsymbol{\rho}'_1, t_1 - t'_1) \dots h(\boldsymbol{\rho}_N, \boldsymbol{\rho}'_N, t_N - t'_N). \quad (2.22)
\end{aligned}$$

The effective wave function transforms like the product of N classical fields [52].

2.2.3 Field Correlation Functions

Glauber showed in [31], that the coherence and correlation of the EM quantum field can be characterized by field correlation functions. For this work, we restrict to intensity correlations. This means, that the first-order correlation function

$$G^{(1)}(\boldsymbol{\rho}_1, t_1) = \langle \hat{E}^{(-)}(\boldsymbol{\rho}_1, t_1) \hat{E}^{(+)}(\boldsymbol{\rho}_1, t_1) \rangle$$

reduces to the intensity or flux density measurement in units $[\text{m}^{-2} \text{s}^{-1}]$. The second-order correlation function

$$G^{(2)}(\boldsymbol{\rho}_1, t_1; \boldsymbol{\rho}_2, t_2) = \langle \hat{E}^{(-)}(\boldsymbol{\rho}_1, t_1) \hat{E}^{(-)}(\boldsymbol{\rho}_2, t_2) \hat{E}^{(+)}(\boldsymbol{\rho}_1, t_1) \hat{E}^{(+)}(\boldsymbol{\rho}_2, t_2) \rangle$$

quantifies the spatial and temporal correlation of pairs of fluxes in units of $[\text{m}^{-4} \text{s}^{-2}]$. This can be generalized to a N th-order correlation function with

$$\begin{aligned}
G^{(N)}(\boldsymbol{\rho}_1, t_1; \dots; \boldsymbol{\rho}_N, t_N) &= \langle \hat{E}^{(-)}(\boldsymbol{\rho}_1, t_1) \hat{E}^{(-)}(\boldsymbol{\rho}_2, t_2) \dots \\
&\quad \dots \hat{E}^{(-)}(\boldsymbol{\rho}_N, t_N) \hat{E}^{(+)}(\boldsymbol{\rho}_1, t_1) \dots \hat{E}^{(+)}(\boldsymbol{\rho}_N, t_N) \rangle \quad (2.23)
\end{aligned}$$

in units of $[\text{m}^{-2N} \text{s}^{-N}]$. Using the photon number operator of Eq. (2.20), this can be equivalently written as

$$G^{(N)}(\rho_1, t_1; \dots; \rho_N, t_N) = \langle : \hat{n}(\rho_1, t_1) \dots \hat{n}(\rho_N, t_N) : \rangle \quad (2.24)$$

where $:$ denotes the normal ordering of the implicit field operators in the expression. This reorders the operators such that all $\hat{E}^{(-)}$ are left from all $\hat{E}^{(+)}$.

For the case of N -photon states, the N th-order correlation function is given by the effective wave function

$$G^{(N)}(\rho_1, t_1; \dots; \rho_N, t_N) = N! |\Psi(\rho_1, t_1; \dots; \rho_N, t_N)|^2$$

and transforms therefore according to Eq. (2.22). By construction, the intensity correlation function of Eq. (2.24) is symmetric under interchange of any of pair, or any permutation of all, of its spatial and temporal arguments

$$G^{(N)}(\rho_1, t_1; \dots; \rho_k, t_k; \dots; \rho_l, t_l; \dots; \rho_N, t_N) = G^{(N)}(\rho_1, t_1; \dots; \rho_l, t_l; \dots; \rho_k, t_k; \dots; \rho_N, t_N).$$

Reason is the indistinguishability of photons in any other degree of freedom than their point in space and time owing to the field operator commutation relations of Eq. (2.19).

The normal ordering procedure can be motivated with the following property: Only the normal ordered expectation value $G^{(N)}$ is proportional to the probability of a joint N -photon detection event. For a quantum state of maximum photon number M , we can therefore conclude that $G^{(N)} = 0$ for all $N > M$. This, its equivalence with the wave function for N -photon states and the corresponding transformation behavior, and the probability interpretation are key properties of the normal ordered field correlation function.

2.3 Field Intensity Correlation Measurements

In this thesis, the central measurement quantity of interest is the field correlation function introduced in Eq. (2.24). The following sections are dedicated to show how measurements can be performed and how measurement data are to be processed in order to be able to relate them to the formal, theoretical values of the correlation functions. For this, the first discussed continuous variable treatment is discretized in order to be applicable to concretely used sensor devices. These theoretical results are worked out for the case of a time-stationary source and a specific assumptions on the detector. Finally, an algorithm for calculating high-order correlation functions by efficiently processing the measurement data is presented. The here developed insights and techniques are extensively used in the experiments of Chs. 4–7.

2.3.1 Sample Averaging and Normalization

Eq. (2.24) defines the N th-order field correlation function as the quantum mechanical expectation value of a measurement operator consisting of a normal ordered product of photon number operators

$$G^{(N)}(\rho_1, t_1; \dots; \rho_N, t_N) = \langle : \hat{n}(\rho_1, t_1) \dots \hat{n}(\rho_N, t_N) : \rangle.$$

A measurement on a quantum state of the field at the given temporal and spatial arguments can only be performed once. In order to measure and estimate this theoretical expectation value, the statistical distribution in photon numbers has to be assessed in order to build an average. Therefore, many instances of the same quantum state are needed

for a good estimate of the value of the correlation function. An experiment needs to be designed to deliver these copies of the state which can then be measured. The average of many of these measurement outcomes yield an estimate of the desired quantum expectation value. This means for the measurement of the correlation function, that the sample average over the measured photon number outcomes $n(\boldsymbol{\rho}, t)$ converges to the theoretical value of the correlation function in the limit of large sample number N_S

$$\langle : n(\boldsymbol{\rho}_1, t_1) \dots n(\boldsymbol{\rho}_N, t_N) : \rangle_{\text{Sample}} \xrightarrow{N_S \rightarrow \infty} G^{(N)}(\boldsymbol{\rho}_1, t_1; \dots; \boldsymbol{\rho}_N, t_N). \quad (2.25)$$

The interpretation of normal ordering in this context will be given in Sec. 2.3.3.

Depending on the experiment, the individual instances of the quantum state are discriminated differently. The common feature of all implementations is the following: By introducing an abbreviation for the space-time coordinates of the correlation function

$$\mathbf{x}^{(N)} := (\boldsymbol{\rho}_1, t_1; \dots; \boldsymbol{\rho}_N, t_N) \in \mathbb{R}^{3N},$$

there are many $\mathbf{x}^{(N)}$ which yield on average the same value of the correlation function. This equality of space-time points can be captured by an equivalence relation denoted by \equiv . All $\mathbf{x}'^{(N)} \equiv \mathbf{x}^{(N)}$ yield the same theoretical value of the correlation function

$$G^{(N)}(\mathbf{x}^{(N)}) = G^{(N)}(\mathbf{x}'^{(N)}), \quad \text{if } \mathbf{x}'^{(N)} \equiv \mathbf{x}^{(N)}.$$

With this notation, a general sample averaging can be formally described with the sampling function

$$\Theta(\mathbf{x}^{(N)}, \mathbf{x}'^{(N)}) := \begin{cases} 1, & \text{if } \mathbf{x}^{(N)} \equiv \mathbf{x}'^{(N)}, \\ 0, & \text{otherwise.} \end{cases}$$

The sampling space volume of $G^{(N)}$ at a specific coordinate $\mathbf{x}^{(N)}$ is then given with

$$V(\mathbf{x}^{(N)}) := \int D\mathbf{x}'^{(N)} \Theta(\mathbf{x}^{(N)}, \mathbf{x}'^{(N)}), \quad (2.26)$$

where we integrate over all coordinates using $D\mathbf{x}'^{(N)} = d^2\rho'_1 dt'_1 \dots d^2\rho'_N dt'_N$. In the limit of large enough volume, this sampling space is sufficient and representative for the estimation of parameters of the statistical distribution. The parameter of an average value needed in Eq. (2.25), can be estimated using the sample average over the measurements

$$G^{(N)}(\mathbf{x}^{(N)}) = \frac{1}{V(\mathbf{x}^{(N)})} \int D\mathbf{x}'^{(N)} [: n(\boldsymbol{\rho}'_1, t'_1) \dots n(\boldsymbol{\rho}'_N, t'_N) :] \Theta(\mathbf{x}^{(N)}, \mathbf{x}'^{(N)}). \quad (2.27)$$

The normal ordered outcomes of photon flux density measurements are denoted by $[: n(\boldsymbol{\rho}'_1, t'_1) \dots n(\boldsymbol{\rho}'_N, t'_N) :]$, see Sec. 2.3.3. Thanks to the normalization by the sampling space volume, this quantity yields the original units of $[\text{m}^{-2N} \text{s}^{-N}]$.

For a concrete example of sample averaging, one might conceive spatial parallel input of the quantum state copies. More often, the delivery is in temporal sequence. One example are *time-stationary* light sources which emit continuously and whose correlation function exhibit the symmetry

$$G^{(N)}(\boldsymbol{p}_1, t_1; \dots; \boldsymbol{p}_N, t_N) = G^{(N)}(\boldsymbol{p}_1, t_1 + t; \boldsymbol{p}_N, t_N + t), \quad \forall t.$$

This is given for CW pumped spontaneous parametric down-conversion or pseudo-thermal light used in later chapters. The sampling function can then be written as

$$\Theta(\mathbf{x}^{(N)}, \mathbf{x}'^{(N)}) = \left(\prod_{k=2}^N \delta((t_1 - t'_1) - (t_k - t'_k)) \right) \left(\prod_{l=1}^N \delta^{(2)}(\boldsymbol{\rho}_l - \boldsymbol{\rho}'_l) \right)$$

With this and Eq. (2.27), the sample average is therefore given by the time average

$$G^{(N)}(\mathbf{x}^{(N)}) = \frac{1}{V(\mathbf{x}^{(N)})} \int dt [: n(\boldsymbol{\rho}_1, t_1 + t) \dots n(\boldsymbol{\rho}_N, t_N + t) :].$$

For a *pulsed* source operation of pulse period T_p , it is possible to formalize the sample average similarly and one arrives at

$$G^{(N)}(\mathbf{x}^{(N)}) = \frac{1}{V(\mathbf{x}^{(N)})} \sum_k [: n(\boldsymbol{\rho}_1, t_1 + kT_p) \dots n(\boldsymbol{\rho}_N, t_N + kT_p) :].$$

2.3.2 Discretization of Detector Arrays

For a model of the measurement, we first have to specify the geometrical detection characteristics. The measurement is to be performed in a plane Σ , which is transverse to the light propagation direction z . The transverse position in this plane is denoted by $\boldsymbol{\rho} = (x, y) \in \Sigma$. For the spatial resolution of the measurement, many individual detectors are needed. Assume that an array of single photon detectors, hereafter referred to as *pixels*, are placed in the plane Σ . Each pixel is identified by its coordinate index $\boldsymbol{p} \in \mathbb{N}^2$ and has a sensitive surface $A_p \subset \Sigma$ of area A . This divides the plane Σ and introduces the discrete pixel coordinate \boldsymbol{p} , while area is measured in units of A . Similarly, the measurement of time is performed in units of Δt and discretized in intervals $[t, t + 1]$ which are identified by $t \in \mathbb{N}$.

For a specific pixel \boldsymbol{p} with optimal detection efficiency in a time interval t , the number of detection events is given by the incident photon flux. We can model the measurement of the number of detection events with the photon number operator of this pixel and time interval

$$\hat{n}(\boldsymbol{p}, t) := \int_{A_p} d^2\boldsymbol{\rho} \int_t^{t+1} dt' \hat{n}(\boldsymbol{\rho}, t')$$

using the flux density operator $\hat{n}(\boldsymbol{\rho}, t)$ of Eq. (2.20). In these discrete coordinates, we can define the N th-order correlation function

$$G^{(N)}(\boldsymbol{p}_1, t_1; \dots; \boldsymbol{p}_N, t_N) := \langle : \hat{n}(\boldsymbol{p}_1, t_1) \dots \hat{n}(\boldsymbol{p}_N, t_N) : \rangle \quad (2.28)$$

in units of $[A^{-N} \Delta t^{-N}]$. Note the equality

$$G^{(N)}(\boldsymbol{p}_1, t_1; \dots; \boldsymbol{p}_N, t_N) = \int_{A_{p_1}} d^2\boldsymbol{\rho}_1 \int_{t_1}^{t_1+1} dt'_1 \dots \int_{A_{p_N}} d^2\boldsymbol{\rho}_N \int_{t_N}^{t_N+1} dt'_N G^{(N)}(\boldsymbol{\rho}_1, t'_1; \dots; \boldsymbol{\rho}_N, t'_N)$$

which explicitly shows the discretization of the correlation density of Eq. (2.24). From this theoretical density which can be calculated for specific experimental situations, we can therefore calculate the quantity which corresponds to the measurement. This equation illustrates the need of small enough pixels and time intervals in order to resolve the physical correlation function. Otherwise, temporal or spatial features are averaged out.

The formalism described above for sample averaging and normalization gets now a discrete form. The generalized coordinate is

$$\mathbf{x}^{(N)} := (\mathbf{p}_1, t_1; \dots; \mathbf{p}_N, t_N) \in \mathbb{N}^{3N}.$$

The sampling function $\Theta(\mathbf{x}^{(N)}, \mathbf{x}'^{(N)})$ is equally defined on this coordinate, while the sampling space volume of Eq. (2.26) becomes

$$V(\mathbf{x}^{(N)}) = \sum_{\mathbf{x}'^{(N)}} \Theta(\mathbf{x}^{(N)}, \mathbf{x}'^{(N)}), \quad (2.29)$$

and the sample average of Eq. (2.27) is now

$$G^{(N)}(\mathbf{x}^{(N)}) = \frac{1}{V(\mathbf{x}^{(N)})} \sum_{\mathbf{x}'^{(N)}} [: n(\mathbf{p}'_1, t'_1) \dots n(\mathbf{p}'_N, t'_N) :] \Theta^{(N)}(\mathbf{x}^{(N)}, \mathbf{x}'^{(N)}). \quad (2.30)$$

This discrete average results in units of $[A^{-N} \Delta t^{-N}]$.

2.3.3 Normal Ordered Photon Number Correlations

A general intensity correlation function defined in Eq. (2.28) can be easily measured for $(\mathbf{p}_1, t_1) \neq (\mathbf{p}_2, t_2) \dots \neq (\mathbf{p}_N, t_N)$. In this case, all implicit field operators do commute thanks to the commutation relations of Eq. (2.19) and the normal ordering is not needed

$$G^{(N)}(\mathbf{p}_1, t_1; \dots; \mathbf{p}_N, t_N) = \langle \hat{n}(\mathbf{p}_1, t_1) \dots \hat{n}(\mathbf{p}_N, t_N) \rangle, \text{ if } (\mathbf{p}_1, t_1) \neq \dots \neq (\mathbf{p}_N, t_N). \quad (2.31)$$

The expectation value is gained by sample averaging over many measurements, as discussed in Sec. 2.3.1. Every individual measurement outcome $n(\mathbf{p}_1, t_1) \dots n(\mathbf{p}_N, t_N)$ is simply the product of the total number of photons $n(\mathbf{p}, t)$ measured in the corresponding pixels and time intervals.

If a coordinate appears multiple times in the argument of $G^{(N)}$, the normal ordering of field operators constitutes a different measurement value. Every coordinate pair (\mathbf{p}, t) appearing m -times can then be replaced by

$$: (\hat{n}(\mathbf{p}, t))^m : = \prod_{k=0}^{m-1} (\hat{n}(\mathbf{p}, t) - k) \quad (2.32)$$

where the normal ordering vanishes for the right expression. This is shown straightforwardly by rearranging the normal ordered field operators using their commutation relations. Therefore, we have to incorporate this rule of processing the measured photon numbers depending on their coordinate multiplicity m . The normal ordered measurement outcome

$$[: n(\mathbf{p}_1, t_1) \dots n(\mathbf{p}_N, t_N) :]$$

used in sample averaging of Sec. 2.3.1 can therefore be expressed in terms of the measured photon numbers $n(\mathbf{p}, t)$ accordingly.

For the simple case of a second-order correlation function $G^{(2)}$, we get the following result. With the measurement of the photon numbers $n(\mathbf{p}, t)$, we identify the normal ordered

measurement outcome for the sample averaging procedure with

$$[:n(\mathbf{p}_1, t_1) n(\mathbf{p}_2, t_2):] = \begin{cases} n(\mathbf{p}_1, t_1) n(\mathbf{p}_2, t_2), & \text{if } (\mathbf{p}_1, t_1) \neq (\mathbf{p}_2, t_2), \\ n(\mathbf{p}_1, t_1) (n(\mathbf{p}_1, t_1) - 1), & \text{if } (\mathbf{p}_1, t_1) = (\mathbf{p}_2, t_2). \end{cases}$$

2.3.4 Example of Time-Stationary Sources

This section uses the previously derived general results and applies them to the specific, often encountered case of time-stationary light sources where the temporally correlated signal is of interest. This is the case for the spontaneous parametric down-conversion and pseudo-thermal light introduced in Ch. 3 and used in Chs. 4–7. Characteristics of the detector arrays used in later chapters are taken into account. This results in explicit expressions for correlation function estimation using measured data. Analytic expression for the sampling space volume are derived. A correlation algorithm is presented which implements the results efficiently and allows the calculation of intensity correlation functions of arbitrary orders.

Detector Assumptions

In order to get concrete results, characteristics of a detector have to be fixed. Here we assume the measurement in fixed temporal windows, hereafter referred to as *frames*, consisting of $T_F \in \mathbb{N}$ time intervals. The correlation analysis is performed within this frame. All frames correspond to measurements of the same quantum state, see the equivalence defined in Sec. 2.3.1. The acquisition of many frames is therefore used for sample averaging and improvement of statistics.

The detector pixels do not resolve photon numbers. An individual pixel only provides the presence or absence of a detection event for every time interval within the frame, which means $n(\mathbf{p}, t) \in \{0, 1\}$. With this, the rule of Eq. (2.32) for processing the measurement outcomes to get the normal ordered result yields zero if any (\mathbf{p}, t) coordinate pair of $G^{(N)}$ has multiplicity $m > 1$. Therefore, this part of correlation space is not measurable, the device gives no information. In order to get an accurate sample average, this non-sampled regions have to be accounted for in the sampling function and accordingly results in a reduced sampling space volume. If this is implemented, the sample average only considers coordinates with multiplicity $m = 1$ and we can drop therefore any normal ordering and use the simple product of photon numbers, see Eq. (2.31). In order to be able to measure the correlation function correctly despite this detector limitation, we have to make sure that contributions $n(\mathbf{p}, t) > 1$ can be neglected by appropriately choosing the source's parameters, detector pixel size and time interval duration.

Spatio-Temporal Second-Order Correlation

Restricting to the second-order correlations, time-stationary sources exhibit the symmetry $G^{(2)}(\mathbf{p}_1, t_1; \mathbf{p}_2, t_2) = G^{(2)}(\mathbf{p}_1, t_1 + t; \mathbf{p}_2, t_2 + t)$ as used for sample averaging in Sec. 2.3.1. Therefore, the function

$$G^{(2)}(\mathbf{p}_1, \mathbf{p}_2, \Delta t), \quad \text{with } \Delta t := t_2 - t_1,$$

fully characterizes the correlations. For its measurement, we can define the sampling function

$$\Theta_{\Delta}(\Delta t; t_1, t_2) := \begin{cases} 1, & \text{if } \Delta t = t_2 - t_1, \\ 0, & \text{otherwise.} \end{cases}$$

In order to account for the above discussed detector assumptions leading to not measurable space, we introduce an additional function removing this space with

$$\Theta_{\text{meas.}}(\mathbf{p}_1, t_1; \mathbf{p}_2, t_2) := \begin{cases} 0, & \text{if } (\mathbf{p}_1, t_1) = (\mathbf{p}_2, t_2), \\ 1, & \text{otherwise.} \end{cases}$$

We arrive at the total sampling function

$$\Theta(\mathbf{p}_1, \mathbf{p}_2, \Delta t; \mathbf{p}'_1, t'_1; \mathbf{p}'_2, t'_2) := \Theta_{\Delta}(\Delta t; t'_1, t'_2) \Theta_{\text{meas.}}(\mathbf{p}'_1, t'_1; \mathbf{p}'_2, t'_2) \delta_{\mathbf{p}_1, \mathbf{p}'_1} \delta_{\mathbf{p}_2, \mathbf{p}'_2} \quad (2.33)$$

with the Kronecker δ notation to make the pixel coordinates match because no spatially averaging takes place.

With the results of the detector assumptions discussion and this sampling function, the normal ordering can be dropped. Using Eq. (2.30), Eq. (2.33), and a number N_F of acquired frames, the coincident correlation function can be estimated with

$$G^{(2)}(\mathbf{p}_1, \mathbf{p}_2, \Delta t) = \frac{1}{V(\mathbf{p}_1, \mathbf{p}_2, \Delta t)} \sum_{k=1}^{N_F} \sum_{t_1=1}^{T_F} \sum_{t_2=1}^{T_F} n_k(\mathbf{p}_1, t_1) n_k(\mathbf{p}_2, t_2) \times \Theta_{\Delta}(\Delta t; t_1, t_2) \Theta_{\text{meas.}}(\mathbf{p}_1, t_1; \mathbf{p}_2, t_2). \quad (2.34)$$

The index k runs over all frames, while $n_k(\mathbf{p}, t)$ denotes the therein measured photon numbers. This expression can be used in a measurement data processing algorithm.

With Eq. (2.29), Eq. (2.33), and taking into account the number of frames N_F , the sampling space volume can be evaluated to

$$V(\mathbf{p}_1, \mathbf{p}_2, \Delta t) = N_F \sum_{t_1=1}^{T_F} \sum_{t_2=1}^{T_F} \Theta_{\Delta}(\Delta t; t_1, t_2) \Theta_{\text{meas.}}(\mathbf{p}_1, t_1; \mathbf{p}_2, t_2) = \begin{cases} 0, & \text{if } \mathbf{p}_1 = \mathbf{p}_2 \wedge \Delta t = 0, \\ N_F(T_F - |\Delta t|), & \text{otherwise.} \end{cases} \quad (2.35)$$

These results are used in Ch. 5. In Sec. 5.1.6, an illustrated example of the normalization is shown in a concrete situation with acquired measurement data.

Coincident Spatial High-Order Correlation

The memory for storage of a correlation function increases exponentially with the order N . Even at a moderate number of pixels, this exceeds practical limits very fast. For that reason, only spatial correlations of temporally coincident events are considered in the following. The coincidence is given by a time window of length $T_c \in \mathbb{N}$ and has to be adapted to the specific source's correlation time. A natural choice of temporal windowing is the maximum time separation and allows to define the sampling function in the

temporal coordinates $\mathbf{t}^{(N)} := (t_1, \dots, t_N)$

$$\Theta_{T_c}(\mathbf{t}^{(N)}) := \begin{cases} 1, & \text{if } \max_{k,l} |t_k - t_l| \leq T_c, \\ 0, & \text{otherwise.} \end{cases} \quad (2.36)$$

In order to account for the above discussed detector assumptions leading to not measurable space, we introduce an additional function removing this space with

$$\Theta_{\text{meas.}}(\mathbf{x}^{(N)}) := \begin{cases} 0, & \text{if } \exists k, l : k \neq l \wedge (\mathbf{p}_k, t_k) = (\mathbf{p}_l, t_l), \\ 1, & \text{otherwise.} \end{cases} \quad (2.37)$$

Using $\mathbf{p}^{(N)} := (\mathbf{p}_1, \dots, \mathbf{p}_N)$, this yields the total sampling function

$$\Theta(\mathbf{p}^{(N)}, \mathbf{x}'^{(N)}) := \Theta_{T_c}(\mathbf{t}'^{(N)}) \Theta_{\text{meas.}}(\mathbf{x}'^{(N)}) \delta_{\mathbf{p}^{(N)}, \mathbf{p}'^{(N)}} \quad (2.38)$$

with the Kronecker δ notation to make all discrete pixel indices $\mathbf{p}^{(N)}$ and $\mathbf{p}'^{(N)}$ match. The input coordinates $\mathbf{x}'^{(N)}$ of the measurement data are in space and time, while the output coordinates $\mathbf{p}^{(N)}$ of the resulting correlation function are in space only.

With the results of the detector assumptions discussion and this sampling function, the normal ordering can be dropped. Using Eq. (2.30), Eq. (2.38), and a number N_F of acquired frames, the coincident correlation function can be estimated with

$$G^{(N)}(\mathbf{p}^{(N)}) = \frac{1}{V(\mathbf{p}^{(N)})} \sum_{k=1}^{N_F} \sum_{t_1=1}^{T_F} \cdots \sum_{t_N=1}^{T_F} n_k(\mathbf{p}_1, t_1) \dots n_k(\mathbf{p}_N, t_N) \\ \times \Theta_{T_c}(\mathbf{t}^{(N)}) \Theta_{\text{meas.}}(\mathbf{x}^{(N)}). \quad (2.39)$$

The index k runs over all frames, while $n_k(\mathbf{p}, t)$ denotes the therein measured photon numbers. This expression can be used in a measurement data processing algorithm. While the sums are computationally expensive already at moderate correlation order, frame length and pixel number, sparse density of detection events allow for optimizations, see the proposed algorithm below.

With Eq. (2.29), Eq. (2.38), and taking into account the number of frames N_F , the sampling space volume is given by

$$V(\mathbf{p}^{(N)}) = N_F \sum_{t_1=1}^{T_F} \cdots \sum_{t_N=1}^{T_F} \Theta_{T_c}(\mathbf{t}^{(N)}) \Theta_{\text{meas.}}(\mathbf{x}^{(N)}). \quad (2.40)$$

Given a correlation algorithm evaluating the sums of Eq. (2.39), direct comparison of the equations show that the volume can be computed using this algorithm for input data with $n(\mathbf{p}, t) = 1$ for all \mathbf{p} and t . While the volume only needs to be computed once, it is very time-intensive for numerical computation. An analytic solution is therefore desirable.

Analytic Expression for Sampling Space Volume

The specific choice of the coincidence windowing function $\Theta_{T_c}^{(N)}$ in Eq. (2.36) allows a analytic evaluation of the sampling space volume in Eq. (2.40). The only factor introducing the dependence of the volume on specific pixel coordinates \mathbf{p} is $\Theta_{\text{meas.}}(\mathbf{x}^{(N)})$ which removes

contributions of (\mathbf{p}, t) pairs of higher multiplicities $m > 1$. Summing over all t , this has the consequence that $V(\mathbf{p}^{(N)})$ is only dependent on the multiplicities of its \mathbf{p} coordinates and not on its specific values.

The multi-coordinate vector $\mathbf{p}^{(N)} = (\mathbf{p}_1, \dots, \mathbf{p}_N)$ is categorized for its coordinate multiplicities with the multiplicity vector

$$m^{(N)} = m^{(N)}(\mathbf{p}^{(N)}) := (m_1, \dots, m_N), \quad \text{with } m_k \in \mathbb{N}_0 \text{ and } \sum_k m_k = N.$$

The ordering of the individual multiplicities m_k is of no relevance and for this reason not specified. The special case $m^{(N)}(\mathbf{p}, \mathbf{p}, \dots, \mathbf{p}) = (N, 0, 0, \dots, 0)$, while for all distinct coordinates $m^{(N)}(\mathbf{p}_1, \dots, \mathbf{p}_N) = (1, 1, \dots, 1)$ and unit multiplicities are given. Please note that m_k denotes here the multiplicities of the spatial coordinate only, as opposed to the multiplicity m defined above for the pairs (\mathbf{p}, t) .

The sampling space volume in the time interval $t = 1, \dots, T$ only restricted by the measurable region can be shown to yield

$$V_m(m^{(N)}, T) := \sum_{t_1=1}^T \cdots \sum_{t_N=1}^T \Theta_{\text{meas.}}(\mathbf{x}^{(N)}) = \prod_{k=1}^N \frac{T!}{(T - m_k)!} \quad (2.41)$$

which reduces to T^N for unit multiplicities where the full space was measurable. The total sampling space volume, further restricted by the coincidence window T_c and frame length T_F , can be quantified with this intermediate step as

$$V(\mathbf{p}^{(N)}) = \left([T_F - T_c] V_m(m^{(N)}, T_c + 1) - [T_F - T_c - 1] V_m(m^{(N)}, T_c) \right) N_F. \quad (2.42)$$

In the limit of large frame duration $T_F \gg T_c$, the volume is proportional to T_F . If the coincidence window is of comparable size, the frame boundaries introduce significant corrections. These analytic expressions are derived in App. A.

Algorithm for Coincident Spatial High-Order Correlation

For calculation of the coincident correlation function $G^{(N)}(\mathbf{p}^{(N)})$ with the measurement data using Eq. (2.39), computationally expensive sums have to be evaluated at every point in the large space of function arguments $\mathbf{p}^{(N)}$. The algorithm 1 implements these sums in an efficient way using the following improvements:

- Measurement data is not provided to the algorithm with an array representing all entries of $n(\mathbf{p}, t) \in \{0, 1\}$. Instead, the set $Data = \{(\mathbf{p}_1, t_1), \dots\}$ of detection events at the corresponding pixel and time are more efficient for sparse events and serve as input. In other words, the set is defined by: $n(\mathbf{x}) = 1 \Leftrightarrow \mathbf{x} \in Data$.
- The expression summed over in Eq. (2.39) is not evaluated explicitly. The algorithm only considers non-vanishing summands, i.e. with sampling function $\Theta \neq 0$ and measurements $n(\mathbf{p}_k, t_k) \neq 0$.
- The correlation function's symmetry under permutation of its arguments is exploited. This avoids calculating the same result $N!$ times. This symmetry, formally described

in Sec. 2.2.3, is established for the algorithm output in one step after the main task of measurement data processing (line 17).

- A recursive method is used to calculate arbitrary correlation orders in one run (line 33).

A concrete implementation of the algorithm, here described in pseudo-code, is presented in Appendix B using Matlab and C. The algorithm can be checked for consistency by using detection event input data with $n(\boldsymbol{\rho}, t) = 1$ for all $\boldsymbol{\rho}$ and t . In this case, the sums in $G^{(N)}$ of Eq. (2.39) are equal to the sampling space volume V of Eq. (2.40) and therefore $G^{(N)}(\boldsymbol{p}^{(N)}) = 1$ at every $\boldsymbol{p}^{(N)}$ and every order N . This is the case for this implementation.

Algorithm 1 Calculate coincident correlation functions $G^{(N)}(\mathbf{p}^{(N)})$, $N = 1, \dots, N_{\max}$.

Input: Detection event data in *Data*, maximal correlation order N_{\max} , coincidence window length T_c

```

1: global variables
2:    $t, p$ , arrays ▷ time and position of detection events
3:    $t_s$  ▷ current coincidence window start time
4:    $x$ , array ▷ positions of events in current coinc. window
5:    $G^{(N)}$ ,  $N = 1, \dots, N_{\max}$ , arrays ▷ correlation functions
6: end global variables

7: initialize all  $G^{(N)}$  to zero
8: for all  $frm \in Data$  do ▷ go through all frames
9:   read arrays  $(t, p)$  from  $frm$  ▷ time and pixel position pairs
10:  sort  $(t, p)$  for increasing time  $t$ 
11:  UPDATEGN(1,1) ▷ start at correlation order  $N = 1$  with first event
12: end for
13: for  $N = 1, \dots, N_{\max}$  do
14:  initialize  $G_{\text{out}}^{(N)}$  to zero
15:  for all  $x \in \{1, \dots, p_{\max}\}^N$  do ▷ over all coordinates of  $G^{(N)}$ 
16:    for all  $i \in \text{permutations}(1, \dots, N)$  do ▷ symmetrize in position arguments
17:       $G_{\text{out}}^{(N)}(x) \leftarrow G_{\text{out}}^{(N)}(x) + G^{(N)}(x(i_1), \dots, x(i_N))$ 
18:    end for
19:     $G_{\text{out}}^{(N)}(x) \leftarrow G_{\text{out}}^{(N)}(x) / V(x)$  ▷ normalize with  $V(\mathbf{p})$  from Eq. (2.42)
20:  end for
21:  write  $G_{\text{out}}^{(N)}$  to output
22: end for

23: procedure UPDATEGN( $N, k_0$ ) ▷ updates  $G^{(N)}$  using data  $(t, p)$ , start at index  $k_0$ 
24:  for  $k = k_0, \dots, \text{length}(t)$  do ▷ loop over detection events
25:    if  $N = 1$  then
26:       $t_s \leftarrow t(k)$  ▷ set coincidence window start
27:    else if  $t(k) - t_s > T_c$  then
28:      return ▷ cancel if out of coincidence window
29:    end if
30:     $x^{(N)} \leftarrow p(k)$  ▷ update position array
31:     $G^{(N)}(x(1), \dots, x(N)) \leftarrow G^{(N)}(x(1), \dots, x(N)) + 1$ 
32:    if  $N < N_{\max}$  then
33:      UPDATEGN( $N + 1, k + 1$ ) ▷ next correlation order by recursion
34:    end if
35:  end for
36: end procedure

```

Chapter 3

Light Sources

Various classical and quantum sources of light are used throughout this thesis. This chapter provides their theoretical description, the documentation of the experimental implementations and their characterization.

3.1 Two-Photon Source

In the following, the theoretical description of two-photon state generation in different approximations is discussed. A concrete experimental implementation of a two-photon source is presented. Its output is verified and characterized by appropriate measurements.

The here developed source is used for detector array tests in Ch. 5 and in quantum imaging experiments of Ch. 6. These rely on the spatial correlation of the emitted photon pairs. An adapted version of this source will be separately derived for optical centroid measurement in Ch. 7. In two-photon interferometer experiments of Ch. 4, the temporal correlations of this source are relevant while only one single spatial mode is used.

3.1.1 Theory

The generation of two-photon states, or photon pairs, relies here on spontaneous parametric down-conversion (SPDC). It is a nonlinear optical process [54] and is experimentally exploited by directing a beam of light, called pump, in an optically nonlinear crystal (NLC) which in turn emits photon pairs at the doubled pump wavelength. SPDC is a very weak interaction mediated by the optical properties of the NLC between the pump and emission modes. The relevant property is the response of the dielectric polarization density \mathbf{P} of the NLC medium to an external electrical field \mathbf{E} . The electrical susceptibility χ relates these quantities with

$$(\mathbf{P})_i = \sum_j \chi_{ij}^{(1)} (\mathbf{E})_j + \sum_{j,k} \chi_{ijk}^{(2)} (\mathbf{E})_j (\mathbf{E})_k + \dots$$

for the vectorial components $i, j, k \in \{1, 2, 3\}$ [54]. $\chi^{(N)}$ is therefore a tensor which here appears in tensor products with the electric field. Non-vanishing second-order susceptibilities $\chi^{(2)}$ exist for crystal lattices without point symmetry.

For incident light waves $E(t) = e^{i\omega t}$, the second-order part produces terms with polarization $P \propto \chi^{(2)} e^{2i\omega t}$ and emits a corresponding electric field oscillating at double frequency. This process is known as second-harmonic generation (SHG) and can be described classically [54]. SPDC can be seen as inverse process to SHG, or more generally to sum frequency generation. Its weak interaction in comparison to SHG comes about due to its non-stimulated but spontaneous nature. This allows the generation of individual photons and needs a quantum description.

Quasi-Phase Matching

In order to build up a strong enough two-photon signal, the interaction volume of the modes in the NLC is to be maximized and can be achieved by long NLCs. Every pump illuminated point in the NLC is a source of the two-photon amplitude. In order to get a high amplitude of their coherent sum at the output, the sources have to be in phase. This so called phase matching can be achieved by different means. The method of quasi-phase matching, originally developed for SHG [55], can be adopted for SPDC. Along the light propagation axis of the NLC, the crystal domains are periodically rotated by 180° and introduce a modulation of the second-order susceptibility and thereby of the phase of the two-photon amplitude. These periodically poled NLCs are used in the following.

Assuming the same single polarization for pump and generated fields reduces the relevant second-order susceptibility tensor to a scalar. With this, quasi-phase matching of periodically poled crystals is modeled with

$$\chi^{(2)}(z) = \chi_0^{(2)} \text{sign}(\cos(2\pi z/G))$$

varying along the optical propagation direction z with the poling period G . The effective nonlinearity of the crystal $d_{\text{eff}} = \frac{1}{2}\chi_0^{(2)}$. In a Fourier series, we can rewrite

$$\chi^{(2)}(z) = \frac{2\chi_0^{(2)}}{\pi} \sum_{m=-\infty}^{\infty} \frac{\sin(\frac{1}{2}m\pi)}{m} e^{ik_m z}, \quad k_m := \frac{2\pi m}{G}. \quad (3.1)$$

Phase matching will only be given for one term in this sum. For highest efficiency, the maximum amplitude of first-order $m = 1$ quasi-phase matching is desirable. If the corresponding needed poling period G is not available for manufacturing, higher orders can be considered.

Two-Photon State of Type-0 SPDC

In 1985, the two-photon quantum state of SPDC was analytically elaborated by Mandel and Hong for monochromatic pump, a single spatial emission mode, and for the first time taking into account the geometry of the NLC [56]. Keller and Rubin generalized this result in 1997 to pulsed pump fields [57]. The spatial degrees of freedom of SPDC emission with monochromatic but transversally shaped pump beams were formalized by Monken et al. in 1998 [58].

Considering all temporal and spatial degrees of freedom for pump and SPDC emission, results are derived in [51]. SPDC of *type-0* is assumed where all involved field's polarizations are identical. Furthermore, quasi-phase matching is implemented in the formalism. The here presented steps follow the more detailed derivation in [51].

The quantum theoretical description of SPDC is presented in the following. The pump field originates from a laser source and can therefore be represented as coherent state. Moreover, the weak SPDC process does not perturb this strong field significantly and can therefore be treated as a classical field which is undepleted. Similarly as the electric fields introduced in Sec. 2.1, it can be written as in positive and negative frequency part with

$$E_p(\mathbf{r}, t) = E_p^{(+)}(\mathbf{r}, t) + E_p^{(-)}(\mathbf{r}, t) = \mathcal{E}^{(+)}(\boldsymbol{\rho}, z, t) e^{i\omega_{cp}t} + \text{c. c.}$$

using the center pump frequency ω_{cp} and the slowly varying envelope $\mathcal{E}^{(+)}(\boldsymbol{\rho}, z, t)$ of the pump pulse. The transverse coordinate $\boldsymbol{\rho} = (x, y)$ is defined in a plane Σ at z normal to the propagation direction of the light.

In the following, fields are defined in the dielectric medium of the crystal. Therefore, the field operators have to take into account the material's refractive index $n(\omega)$. This results in an adapted normalization function of the free-space field operators of Sec. 2.2

$$e(\omega) = i\sqrt{\frac{\hbar\omega}{(2\pi)^3 2\varepsilon_0 c (n(\omega))^2}}$$

while the wave vectors in the crystal obey the dispersion relation

$$|\mathbf{k}| = k_c(\omega) = \sqrt{k_x^2 + k_y^2 + k_z^2} = \frac{\omega}{c} n(\omega). \quad (3.2)$$

The nonlinear interaction between the pump and the SPDC emission modes can be described by the time dependent interaction Hamiltonian

$$\hat{H}_{\text{int}}(t) = \frac{2\varepsilon_0}{3} \int_{V_{\text{NLC}}} d^3\mathbf{r} \chi^{(2)}(z) \hat{E}(\mathbf{r}, t) \hat{E}(\mathbf{r}, t) E_p(\mathbf{r}, t)$$

where the integration volume is performed over the NLC volume. Invoking the rotating wave approximation, terms can be neglected and the Hamiltonian simplified to

$$\hat{H}_{\text{int}}(t) = \frac{2\varepsilon_0}{3} \int_{V_{\text{NLC}}} d^3\mathbf{r} \chi^{(2)}(z) \hat{E}^{(-)}(\mathbf{r}, t) \hat{E}^{(-)}(\mathbf{r}, t) E_p^{(+)}(\mathbf{r}, t) + \text{h. c.} \quad (3.3)$$

The output of the SPDC process can be calculated in the interaction (or Dirac) picture by the formal solution of the Schrödinger equation

$$|\Psi(t)\rangle = \mathcal{T} \exp\left(\frac{1}{i\hbar} \int_{t_0}^t dt' \hat{H}_{\text{int}}(t')\right) |\Psi(t_0)\rangle \quad (3.4)$$

where time ordering of the Hamiltonians in the evaluation of the exponential is imposed by symbol \mathcal{T} and an input state $|\Psi(t_0)\rangle$ is given for the emission modes. With the vacuum state as input $|\Psi(t_0)\rangle = |0\rangle$, the Dyson series of Eq. (3.4) allows to write the first-order perturbation theory result [53]

$$|\Psi(t)\rangle = |0\rangle - \frac{i}{\hbar} \int_{t_0}^t dt' \hat{H}_{\text{int}}(t') |0\rangle$$

As the interaction only occurs during the time interval of the pump pulse implicitly specified in $E_p(\mathbf{r}, t)$ (or equivalently the coherence time for CW pump), the integration boundaries can be extended to $t_0 \rightarrow -\infty$ and $t \rightarrow \infty$.

A cuboid shaped NLC of length L is assumed with its input surface in plane $z = -L$ and the end surface in plane $z = 0$. If the transverse pump beam size in the crystal $E_p(\mathbf{r}, t)$, $\mathbf{r} \in V_{\text{NLC}}$, is smaller than the transverse crystal dimensions, the latter can be extended to infinity for calculations. First-order quasi-phase matching for the term $m = 1$ is assumed while the other are neglected, see Eq. (3.1). Then, the resulting field state reads

$$|\Psi\rangle = |0\rangle + \int d^2\mathbf{q}_i d\omega_i d^2\mathbf{q}_s d\omega_s \Lambda(\mathbf{q}_i, \omega_i, \mathbf{q}_s, \omega_s) a^\dagger(\mathbf{q}_i, \omega_i) a^\dagger(\mathbf{q}_s, \omega_s) |0\rangle \quad (3.5)$$

with the photon creation operators $a^\dagger(\mathbf{q}, \omega)$ and the two-photon wave function [51]

$$\Lambda(\mathbf{q}_i, \omega_i, \mathbf{q}_s, \omega_s) = -\frac{4i\varepsilon_0\chi_0^{(2)}Le(\omega_i)e(\omega_s)}{3\hbar\pi(2\pi)^6n(\omega_i)n(\omega_s)}\mathcal{E}^{(+)}(\mathbf{q}_i + \mathbf{q}_s, \omega_i + \omega_s - \omega_{cp}) \times \text{sinc}\left(\frac{1}{2}\Delta k_z L\right) \exp\left(-i\Delta k_z \frac{L}{2}\right). \quad (3.6)$$

The longitudinal wave vector mismatch is

$$\Delta k_z = \sqrt{k_c^2(\omega_i) - |\mathbf{q}_i|^2} + \sqrt{k_c^2(\omega_s) - |\mathbf{q}_s|^2} - \sqrt{k_c^2(\omega_i + \omega_s) - |\mathbf{q}_i + \mathbf{q}_s|^2} + \frac{2\pi}{G} \quad (3.7)$$

where the dispersion relation of Eq. (3.2) determines wave vector magnitudes $k_c(\omega)$.

The generated photon pair is entangled because the two-photon function is not factorizable into subsystems of the two photons

$$\Lambda(\mathbf{q}_i, \omega_i, \mathbf{q}_s, \omega_s) \neq f(\mathbf{q}_i, \omega_i)g(\mathbf{q}_s, \omega_s).$$

The annihilation of one pump photon in the process is not modeled in this approximation, but a full quantum model would confirm the interpretation of one pump photon being converted into a pair of photons. Energy and transverse momentum conservation of the process is explicit in the arguments of the pump field $\mathcal{E}^{(+)}$ in Eq. (3.6). The generated photon pair's energy sum is equally distributed as one photon of the pump. The same applies to the transverse wave vector sum.

The phase matching function $\text{sinc}(x) = \sin(x)/x$ determines the efficiency of pair generation via the phase mismatch $\frac{1}{2}\Delta k_z L$ in its argument. By appropriately choosing the crystal poling period G , the phase mismatch can be minimized for the generation of photon pairs into a emission cone of selected angle and a corresponding energy splitting ratio [59]. We optimize for *collinear* emission in this work which maximizes the photon emission in $\mathbf{q} = 0$ direction along the optical axis of the pump beam. The energy splitting ration is then close to *frequency-degenerate* emission where $\omega_s = \omega_i = \frac{1}{2}\omega_{cp}$.

Spatio-Temporal Factorization

We assume a pump field which factorizes

$$\mathcal{E}^{(+)}(\mathbf{q}, \omega) = \mathcal{E}_q^{(+)}(\mathbf{q})\mathcal{E}_\omega^{(+)}(\omega).$$

Filtering the SPDC emission in a narrow bandwidth around the frequency degenerate case, the wave vector mismatch is nearly constant over the frequency range and the two-photon wave function factorizes to good approximation into

$$\Lambda(\mathbf{q}_i, \omega_i, \mathbf{q}_s, \omega_s) = \Lambda(\mathbf{q}_i, \mathbf{q}_s)\mathcal{E}_\omega^{(+)}(\omega_i + \omega_s - \omega_{cp})f(\omega_i)f(\omega_s). \quad (3.8)$$

with the filter transmission amplitude $f(\omega)$ and the spatial two-photon wave function

$$\Lambda(\mathbf{q}_i, \mathbf{q}_s) := \Lambda(\mathbf{q}_i, \frac{1}{2}\omega_{cp}, \mathbf{q}_s, \frac{1}{2}\omega_{cp}).$$

This factorization in wave vector and frequency leads, with a Fourier transform to direct space, to a factorization in position $\boldsymbol{\rho}$ and time t . Therefore, correlations between spatial and temporal degrees of freedom are absent in this limit.

Under certain conditions, an optical system with an impulse response function (see Sec. 2.1.2) factorizes into temporal and spatial components

$$h(\boldsymbol{\rho}, \boldsymbol{\rho}', t - t') = h_s(\boldsymbol{\rho}, \boldsymbol{\rho}') h_t(t - t').$$

This is for example the case for a 4-f imaging system. In good approximation, it is also valid for single lens near- and far-field systems of Eq. (2.13) and Eq. (2.16) under the assumption of a narrow-band spectrum determined by filter $f(\omega)$. In this case, the second-order correlation function, defined in Ch. 2, of the SPDC state, described by Eq. (3.8), propagated through this system factorizes

$$G^{(2)}(\boldsymbol{\rho}_1, t_1; \boldsymbol{\rho}_2, t_2) = G^{(2)}(\boldsymbol{\rho}_1, \boldsymbol{\rho}_2) G_t^{(2)}(t_1, t_2). \quad (3.9)$$

In the special case of a monochromatic pump $\mathcal{E}_\omega^{(+)}(\omega) = \delta(\omega - \omega_{cp})$, this temporal part of the SPDC state is given by

$$G_t^{(2)}(t_1, t_2) = G_t^{(2)}(t_1 - t_2) = |(\tilde{f} * h_t)(t_1 - t_2)|^2$$

with the Fourier transform $\tilde{f}(t)$ of the bandpass filter transmission $f(\omega)$ and the convolution with the temporal impulse response function $h_t(t)$ of the optical system. It depends on time differences only. Therefore, detection can occur at any time but is temporally correlated by a correlation time given by the bandwidth of the used filter.

The limit of spatio-temporal factorization is assumed in the following and allows to consider the spatial correlation function independently of the temporal degrees of freedom.

Monochromatic Plane Wave Pump Approximation

A simpler expression of the derived two-photon state is possible for the case of a monochromatic pump field with a collimated beam of sufficient radius to be locally in the crystal well approximated by a plane wave. The latter is the case for a Gaussian beam with a Rayleigh length longer than the NLC length L . Assuming a pump of a frequency is ω_{cp} aligned to the optical axis z , it is approximated by a plane wave with $\mathbf{q} = 0$ given by

$$\mathcal{E}^{(+)}(\mathbf{q}, \omega) = \delta^{(2)}(\mathbf{q}) \delta(\omega - \omega_{cp}).$$

By defining a relative frequency $\Omega := (\omega_i - \omega_s)/2$ and $\mathbf{q} := \mathbf{q}_i = -\mathbf{q}_s$, the quantum state of Eq. (3.5) becomes

$$|\Psi\rangle = |0\rangle + \int d^2\mathbf{q} d\Omega \Lambda(\mathbf{q}, \Omega) a^\dagger(\mathbf{q}, \frac{1}{2}\omega_{cp} + \Omega) a^\dagger(-\mathbf{q}, \frac{1}{2}\omega_{cp} - \Omega) |0\rangle. \quad (3.10)$$

The two-photon wave function reads in this simplified case

$$\Lambda(\mathbf{q}, \Omega) = \Lambda(|\mathbf{q}|, \Omega) = C(\Omega) \operatorname{sinc}\left(\frac{1}{2}\Delta k_z L\right) \exp\left(-i\Delta k_z \frac{L}{2}\right). \quad (3.11)$$

where we absorbed the prefactors of Eq. (3.6) into the function $C(\Omega)$. It exhibits a circular symmetry in \mathbf{q} as expected from the rotation symmetry of the physical situation. The wave

vector mismatch is given by

$$\Delta k_z = \sqrt{k_c^2(\frac{1}{2}\omega_{cp} + \Omega) - |\mathbf{q}|^2} + \sqrt{k_c^2(\frac{1}{2}\omega_{cp} - \Omega) - |\mathbf{q}|^2} - k_c(\frac{1}{2}\omega_{cp}) + \frac{2\pi}{G}$$

This approximation does not model the finite transverse extension of the pump beam. A further observation is the perfect anti-correlation in momentum and frequency of the emitted photons as apparent in Eq. (3.10). This is a consequence of energy and momentum conservation and the narrow bandwidth of the pump in these degrees of freedom.

Using the spatio-temporal factorization limit from above, we get the spatial two-photon wave function

$$\Lambda(\mathbf{q}) = \Lambda(\mathbf{q}, \Omega = 0).$$

Far-Field Correlations

A second-order correlation function in the far-field, using a lens of focal length f , is calculated in the following for the quantum state of Eq. (3.10). As apparent in the definition of the correlation function in Eq. (2.23), we have to transform the free-space field operator of Eq. (2.18) with the far-field impulse response function of Eq. (2.16) using the transformation rule in Eq. (2.21). Furthermore, employing the factorization property discussed for Eq. (3.9) by spectrally filtering, this yields the spatial correlation function

$$G^{(2)}(\mathbf{q}_1, \mathbf{q}_2) = C |\Lambda(\mathbf{q}_1, \mathbf{q}_2)|^2.$$

We use the position to wave vector relation $\mathbf{q} = (k/f)\boldsymbol{\rho}$ in the far-field plane and all constants are absorbed into C .

In monochromatic plane wave pump approximation, we get

$$G^{(2)}(\mathbf{q}_1, \mathbf{q}_2) = C \delta^{(2)}(\mathbf{q}_1 + \mathbf{q}_2) |\Lambda(\mathbf{q}_1)|^2 \quad (3.12)$$

which can be interpreted as spatial perfectly anti-correlated photon pairs within the circular symmetric wave vector emission spectrum $|\Lambda(\mathbf{q})|^2$. The pump propagation direction, here assumed to be along $\mathbf{q} = 0$, determines the center point of symmetry.

Near-Field Correlations

A near-field measurement with a lens is described by the impulse response function of Eq. (2.13). The ideal case of a large lens diameter is chosen because we are interested in the actual emission of the source, without modification by the limitations of the optical system. The transfer function becomes a delta function as shown in Sec. 2.1.4. This single lens imaging system allows to measure correlation functions in different planes. With a free propagation using the transfer function Eq. (2.5), the spatial correlation function in an object plane at any position z is given by

$$G^{(2)}(\boldsymbol{\rho}_1, \boldsymbol{\rho}_2, z) = \left| C \int d^2\mathbf{q}_i d^2\mathbf{q}_s \Lambda(\mathbf{q}_i, \mathbf{q}_s) e^{-iz\sqrt{k^2-|\mathbf{q}_i|^2}} e^{-iz\sqrt{k^2-|\mathbf{q}_s|^2}} e^{i(\mathbf{q}_i \cdot \boldsymbol{\rho}_1 + \mathbf{q}_s \cdot \boldsymbol{\rho}_2)/m} \right|^2$$

which is essentially a Fourier transform of the propagated two-photon wave function. The wave vector magnitude k is given by the free-space dispersion relation $k = \frac{1}{2}\omega_{cp}/c$. An optical magnification m is assumed.

In monochromatic pump approximation, this equation reduces to

$$G^{(2)}(\boldsymbol{\rho}_1, \boldsymbol{\rho}_2, z) = G^{(2)}(\Delta\boldsymbol{\rho}, z) = \left| C \int d^2\boldsymbol{q} \Lambda(\boldsymbol{q}) e^{-2iz\sqrt{k^2-|\boldsymbol{q}|^2}} e^{i\boldsymbol{q}\cdot\Delta\boldsymbol{\rho}/m} \right|^2 \quad (3.13)$$

and is only depending on the relative position $\Delta\boldsymbol{\rho} := \boldsymbol{\rho}_1 - \boldsymbol{\rho}_2$. An infinite transverse extension is given in this approximation. Inserting $\Lambda(\boldsymbol{q}) = \Lambda(\boldsymbol{q}, \Omega = 0)$ from Eq. (3.11), using the results of its wave vector mismatch, and defining $k_c := k_c(\frac{1}{2}\omega_{cp})$, we get without the Fourier transform and constants

$$\text{sinc}\left(\frac{1}{2}\Delta k_z L\right) \exp\left(-i\frac{L}{2}\sqrt{k_c^2-|\boldsymbol{q}|^2} - iz\sqrt{k^2-|\boldsymbol{q}|^2}\right)^2.$$

By employing the paraxial approximation of the free-space propagator as in Eq. (2.9), we arrive at

$$\text{sinc}\left(\frac{1}{2}\Delta k_z L\right) \exp\left(i\frac{L}{2}\frac{|\boldsymbol{q}|^2}{2k_c} + iz\frac{|\boldsymbol{q}|^2}{2k}\right)^2$$

where constant phases were omitted. With the dispersion relations Eq. (2.2) and Eq. (3.2), in the plane at

$$z = z_0 := -\frac{L}{2n(\frac{1}{2}\omega_{cp})}, \quad (3.14)$$

the exponential function with quadratic phases in \boldsymbol{q} vanish. In this plane, the two-photon wave function is therefore a real function and the corresponding Fourier transform of Eq. (3.13) yields the narrowest correlation in $\Delta\boldsymbol{\rho}$ due to this Fourier limited wave function. Reminding us that in the derivation of the SPDC two-photon state we have chosen the coordinate system where $z = 0$ is at output surface of the NLC, the image plane at z_0 coincides with central plane in the crystal as we have to take into account the refractive index of the material in propagation [49].

3.1.2 Experimental Implementation

The NLC is a periodically poled KTiOPO_4 (PPKTP) crystal with a poling period of $G \approx 3.51 \mu\text{m}$ and a length of $L = 5 \text{ mm}$. For the selected type-0 SPDC, the material's nonlinear coefficient $d_{eff} = 15.6 \text{ pm/V}$ [60]. For the two-photon state calculation with Eq. (3.6), the wavelength dependent index of refraction $n(\omega)$ is needed. This is modeled by a Sellmeier equation [49], whose coefficients for KTP are experimentally determined in reference [61]. The crystal temperature is influencing $n(\omega)$ and yields a correction term to the Sellmeier equation which is experimentally found in [62]. Thermal expansion, which influences the poling period, is also given in this reference. The NLC is temperature stabilized within 0.01°C . This allows to modify the phase matching and is here set for collinear emission [59].

The optical setup is shown in Fig. 3.1. The pump source is a grating-stabilized CW diode laser. It emits a polarized, collimated beam at $\lambda_{cp} = 405 \text{ nm}$ with a bandwidth of 2 MHz at 30 mW power. With a $\lambda/4$ and $\lambda/2$ plate, the beam is linearly polarized. A telescope consisting of two lenses focuses the light to a Gaussian beam of waist radius $w_0 = 240 \mu\text{m}$. Its Rayleigh length of 447 mm is much larger than L and justifies the plane wave approximation. The NLC is centered on the beam waist position.

The above discussed spatio-temporal factorization is given in good approximation with the used emission bandpass filter (F2) transmitting $810 \pm 5 \text{ nm}$. Numerical analysis shows only negligible variation of the phase mismatch in this spectral region. This

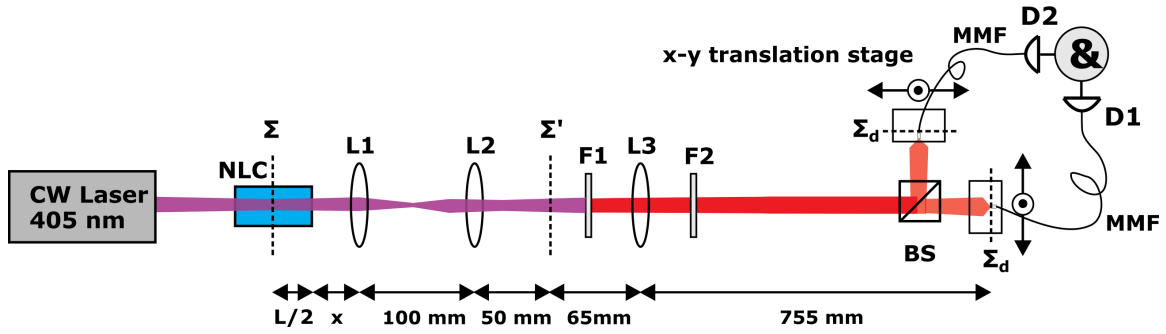


FIGURE 3.1: Two-photon light source. Photon pairs are generated in SPDC in the NLC. A longpass filter (F1) blocks the pump, the bandpass filter (F2) transmits 810 ± 5 nm and selects the nearly frequency-degenerate emission. The central crystal plane Σ is 1:1 imaged with the telescope (L1, L2, $f = 50$ mm) to the output plane Σ' . Here the field is ready for measurement and manipulation. For characterization of the source, the lens L3 ($f = 60$ mm) images Σ' onto the detection plane Σ_d . Two multi-mode fiber coupled detectors scan transverse positions and detect photon pairs in coincidence.

validates the treatment of the spatial degrees of freedom only and the assumption of frequency degenerate emission in the following. In the filtered spectral range, a total of 2 nW SPDC light is generated.

A 4- f 1:1 imaging system of two $f = 50$ mm lenses replicates the electric field of the crystal center plane Σ in the output plane Σ' . Taking into account the refractive index $n(810 \text{ nm}) = 1.84$, Eq. (3.14) yields the effective position $z_0 = -1.36$ mm of this plane. The NLC to lens distance x in Fig. 3.1 is therefore $x = f + z_0 = 48.64$ mm. This makes the central plane, which is of interest due to its strong spatial correlation as discussed above, available for measurement and manipulation. The here calculated value of x is experimentally validated in Sec. 5.1 to yield the minimal correlation length.

3.1.3 Characterization

In order to characterize this source depicted in Fig. 3.1, the output plane Σ' is imaged with magnification $m = 11.6$ by a single lens (L3, $f_3 = 60$ mm) to the detector plane Σ_d . A beam splitter cube separates photon pairs to two different detectors. These are coupled to multi-mode fibers of $50 \mu\text{m}$ diameter whose bare fiber tips are on motorized x - y stages scanning the Σ_d plane. Detectors are single photon counters based on silicon avalanche diodes (Perkin Elmer SPCM-AGR-14). Detection events are timestamped with a time-to-digital converter (IDQ TDC id800) with 81 ps time resolution. The crystal temperature is set to 25°C .

The real-time evaluation of this timestamp data is performed with a LabView program. It allows to count coincidences, i.e. event pairs with a relative time difference in a window of $T_c = 2$ ns. The resulting number of coincidence events at detector positions $\rho_1, \rho_2 \in \Sigma_d$ is given by the second-order correlation function with

$$C(\rho_1, \rho_2) = \int_{A_1} d^2\rho'_1 \int_{A_2} d^2\rho'_2 \int_{-\infty}^{\infty} dt_1 \int_{t_1 - T_c/2}^{t_1 + T_c/2} dt_2 \frac{1}{2} G^{(2)}(\rho'_1, t_1; \rho'_2, t_2)$$

with the fiber core aperture areas $A_1, A_2 \subset \Sigma_d$ and the beam splitter ratio introducing a reduction of the signal. With the normalization procedure presented in Sec. 2.3, this quantity allows to get $G^{(2)}$ in appropriate units.

Background light, dark counts and other sources of noise produce detection events and lead to *accidental* coincidence events. As the SPDC light source is expected to exhibit a

temporally correlated signal within the coincidence window, accidentals can be estimated by measuring pair events at a delay $\Delta t \gg T_c$ where no correlation signal is expected

$$C_{acc}(\rho_1, \rho_2) = \int_{A_1} d^2\rho'_1 \int_{A_2} d^2\rho'_2 \int_{-\infty}^{\infty} dt_1 \int_{t_1+\Delta t-T_c/2}^{t_1+\Delta t+T_c/2} dt_2 \frac{1}{2} G^{(2)}(\rho'_1, t_1; \rho'_2; t_2).$$

Therefore, the accidental corrected counts $C_{corr} := C - C_{acc}$ only include the temporally correlated part of the signal.

Near-Field Correlation, Poling Period Determination

Fig. 3.2 shows the measurement results. The 1D and 2D detector position scans in panel (a) and (b) show strong spatial correlation, as expected from Eq. (3.13). Single count rates in panel (d) show a flat behavior modulated by the pump beam shape. A cross-section of (b) is shown in panel (c), where a correlation length of the photon pairs of $330 \mu\text{m}$ FWHM can be determined. In the source output plane Σ' , this corresponds to $27.6 \mu\text{m}$.

Using Eq. (3.13) of $G^{(2)}(\Delta\rho)$ in monochromatic plane wave pump approximation, the measurement data fit in Fig. 3.2(c) determines the crystal poling period to $G = (3.51108 \pm 0.00004) \mu\text{m}$, which is the only free parameter of the model. The sub-nanometer confidence interval of the fit can be explained by the fact that the measurement is very sensitive to changes in G . Even at this scale, the SPDC emission along the crystal consisting of more than one thousand periods adds up a considerable phase difference and leads to a measurable modification of the correlation function.

The fit of G is very sensitive to the assumed pump wavelength λ_{cp} . Within a nanometer range of this value, we always find an appropriate G which fits the data. If λ_{cp} cannot be determined to sub-nanometer precision, we can treat G as an effective poling period under the assumption of a coarsely determined, but fixed wavelength λ_{cp} .

Far-Field Correlation, NLC Temperature Scan

As shown in Sec. 2.1.5, a lens can be used to perform measurements in the far-field. For this, the lens L3 in the setup of Fig. 3.1 is replaced with a focal length $f_3 = 500 \text{ mm}$ and is placed in distance f_3 in front of the detection plane Σ_d . For detection, two $105 \mu\text{m}$ fibers are used in the following for higher count rates. The longer correlation length in comparison with the near-field measurements from above is fully resolved by this larger fiber aperture, see Fig. 3.3(a). As expected from Eq. (3.12), anti-correlated emission of photon pairs is measured. A crystal temperature of 26°C is used.

By varying the crystal temperature, its refractive index can be slightly tuned. This allows to change the phase matching. The single count rates in Fig. 3.3(b) show the distribution in photon pair emission angles for different temperatures. Collinear emission is favored at 26°C .

3.2 Four-Photon Source

The here presented four-photon source is implemented for its application in detector array testing of Ch. 5, where the capability of newly developed devices in the measurement of ultra-fast higher order correlation is to be demonstrated. Furthermore, it is considered for quantum imaging, but not realized up to this date.

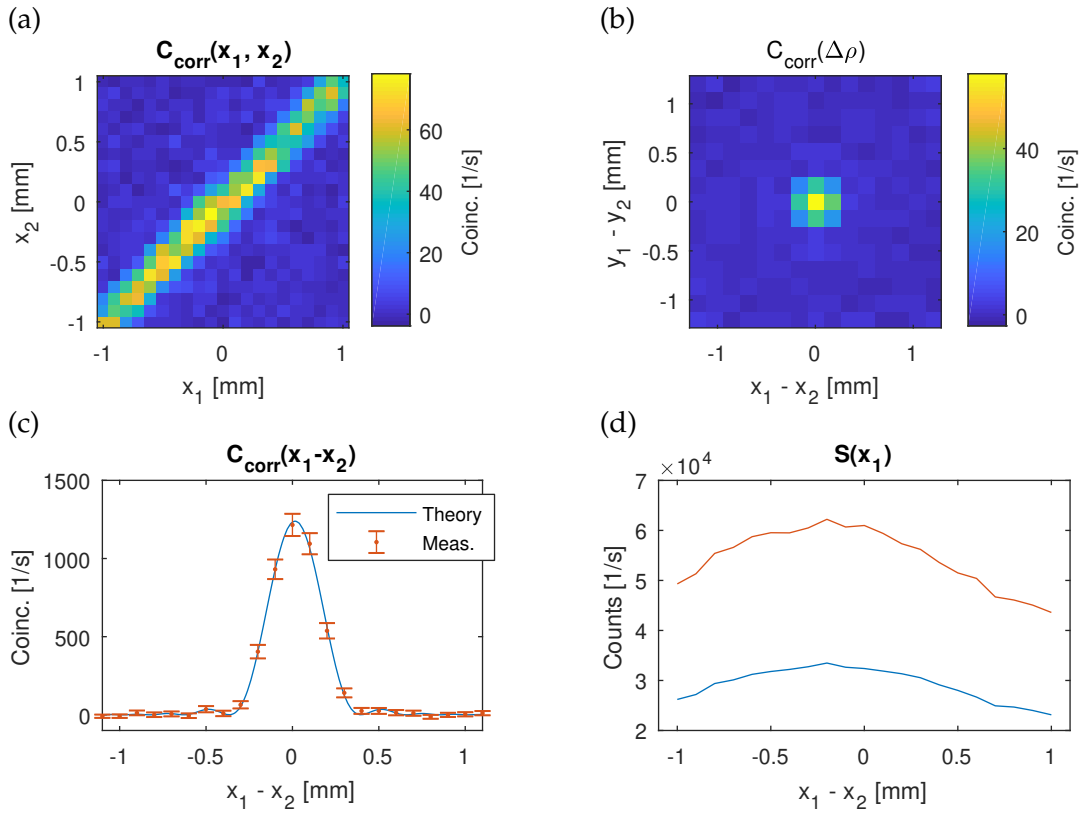


FIGURE 3.2: Near-field measurement of the SPDC two-photon source. Accidental corrected 1D (a) and 2D (b) coincidences in dependence of (relative) detector positions. The correlation width in (c), showing 2σ errors, is fitted to the theoretical model and yields a poling period $G = 3.51108 \mu\text{m}$. Single count rates in (d) are shown for both detectors.

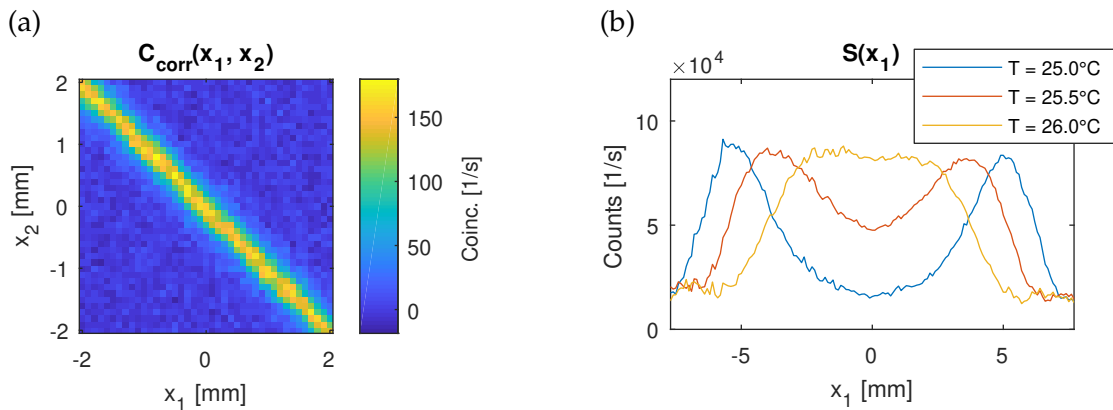


FIGURE 3.3: Far-field measurement of the SPDC two-photon source. (a): Accidental corrected coincidences in dependence of the detector positions. (b): Single count rates at different crystal temperatures T .

3.2.1 Theory

In order to realize a source generating four-photon states, the SPDC process described in Sec. 3.1 is here considered for stronger pump fields. This results in non-negligible double-pair generation and is theoretically analyzed in the following.

Four-Photon State in Type-0 SPDC

Multi-photon pair generation in SPDC was first studied in 1999 by Ou et. al [63]. This theoretical analysis only considers temporal degrees freedom. Taking into account spatial dimensions as well, a discrete spatial mode model is put forward and analyzed in [64, 65]. Continuing with the results of Sec. 3.1 for two-photon SPDC, a SPDC four-photon state including spatial degrees of freedom can be derived in the following.

Eq. (3.4) describes the quantum state of the SPDC emission modes after the interaction. The approximation of this expression using first-order perturbation theory yielded the two-photon state output. Considering in addition second order, the output state reads

$$|\Psi\rangle = |0\rangle + |\Psi_2\rangle + |\Psi_4\rangle \quad (3.15)$$

with the vacuum contribution and the two-photon state $|\Psi_2\rangle$ given in Eq. (3.5). The new contribution is with second-order perturbation theory [53]

$$|\Psi_4\rangle = -\frac{1}{\hbar^2} \int_{-\infty}^{\infty} dt \int_t^{\infty} dt' \hat{H}_{\text{int}}(t') \hat{H}_{\text{int}}(t) |0\rangle$$

where the time ordering required in Eq. (3.4) is fulfilled. The interaction Hamiltonian given in Eq. (3.3) can be separated into $\hat{H}_{\text{int}} = \hat{H}_{\text{int}}^{(-)} + \hat{H}_{\text{int}}^{(+)}$ with

$$\hat{H}_{\text{int}}^{(-)}(t) = \frac{2\varepsilon_0}{3} \int_{V_{\text{NLC}}} d^3\mathbf{r} \chi^{(2)}(z) \hat{E}^{(-)}(\mathbf{r}, t) \hat{E}^{(-)}(\mathbf{r}, t) E_p^{(+)}(\mathbf{r}, t)$$

and its hermitian conjugate accordingly. With this, we can write the four photon contribution

$$|\Psi_4\rangle = -\frac{1}{2\hbar^2} \int_{-\infty}^{\infty} dt \hat{H}_{\text{int}}^{(-)}(t) \int_{-\infty}^{\infty} dt' \hat{H}_{\text{int}}^{(-)}(t') |0\rangle.$$

The contribution to the vacuum state comes from a down- and again up-converted photon pair and is not considered in the following. The commuting operators allowed to rewrite the time ordered integral. Using the result of Eq. (3.5), we conclude that

$$|\Psi_4\rangle = \frac{1}{2} \int dx_1 dx_2 dx_3 dx_4 \Lambda(x_1, x_2) \Lambda(x_3, x_4) a^\dagger(x_1) a^\dagger(x_2) a^\dagger(x_3) a^\dagger(x_4) |0\rangle \quad (3.16)$$

with the abbreviation $x_k := (\mathbf{p}_k, \omega_k)$ and the two-photon wave function $\Lambda(\mathbf{q}_i, \omega_i, \mathbf{q}_s, \omega_s)$ of Eq. (3.6). This can be identified as a four-photon state and is a generalization of the result in [63]. Despite its factorization into two pairs, it shows correlation between these due to photon bunching or, equivalently, stimulated emission effects [63, 64].

The wave function's linear dependence on the pump electric field results in a quadratic dependence of this four-photon state. High pump intensities are therefore needed to make this contribution a relevant part of the total quantum state. This is achieved by employing pulsed pump fields which allow for high peak intensities.

Temporal Mode Number

Photon bunching, i.e. the effect of enhanced probability of photon emission in one mode given that photons are already present in that mode [66], is implicitly present in the state of Eq. (3.16) and is quantitatively analyzed below. It is responsible for the correlation of the two pairs which would otherwise be fully independent. For high visibility of spatial correlation, a number of temporal modes close to unity is required [63–65, 67]. The per pulse probability to emit a four-photon state is given by

$$P_4 = \frac{(P_2)^2}{2}(1 + \chi) \quad (3.17)$$

with the visibility $\chi \in [0, 1]$ and the two-photon emission probability P_2 [64]. The absence of photon bunching with $\chi = 0$ corresponds to a purely Poissonian emission statistics, i.e. of two independent two-photon emissions. At optimal $\chi = 1$, photon bunching allows a doubling of the emission probability. This is the case if both photon pairs are emitted in the same spatial and temporal mode pairs. Therefore, detection must be able to distinguish between different modes in order to achieve the full visibility. While the needed spatial resolution of the detection is moderate, electronic detectors are much slower than the coherence time of generated photons, the time scale of the modes, even for narrow-band filtered SPDC emission. As these temporal modes cannot be resolved in a pulse, the only possibility to achieve high visibility is to minimize the number of emitted temporal modes.

The maximum visibility $\chi = 1/M$ relates inversely proportional to the number of temporal modes M in the case of slow detectors. Furthermore, heuristic arguments show for Gaussian filters and pulses

$$\chi = \frac{r}{\sqrt{1 + r^2}}, \quad r := \frac{\Delta_p}{\Delta_f},$$

with the filter frequency transmission bandwidth Δ_f and pump pulse bandwidth Δ_p [67]. By selecting a broad pump (short pulse) and a narrow filter, the high r value results in a low mode number where high visibility is achievable.

Fedorov derived analytically the temporal emission modes of SPDC [68]. This result is more rigorous than the above as it takes into account dispersion effects. On the other hand, it does not consider the filtering of the emission spectrum. A numerical analysis of the temporal mode number in the concrete experimental situation gives clarity: A model of the pump pulse $\mathcal{E}^{(+)}(t)$ allows to explicitly calculate the temporal two-photon wave function. Assuming spatio-temporal factorization discussed in Sec. 3.1, it is sufficient to analyze one spatial mode. In case of collinear emission, the spectral wave function is therefore given with

$$\Lambda(\mathbf{q}_i = 0, \omega_i, \mathbf{q}_s = 0, \omega_s) f(\omega_s) f(\omega_i).$$

Its Schmidt decomposition allows to determine the temporal or, equivalently, the spectral modes. Then, the Schmidt number yields the effective number of temporal modes emitted after filtering [51]. This will be done in Sec. 3.2.2 using the concrete experimental parameters.

In the following, a single temporal mode per pulse is assumed. It is therefore sufficient to consider the spatial degrees of freedom only.

Spectral Signal-Idler Separation

Setting at the SPDC output a bandpass filter not symmetrically for frequency-degenerate emission but at some off-center wavelength, only one photon of a pair generated in SPDC is transmitted due to their frequency anti-correlation explicit in the two-photon wave function in Eq. (3.6). This distinguishability of the photons is formally implemented by assigning an index $k \in \{s, i\}$, corresponding to signal and idler, to the photon creation and annihilation operators. With temporal mode assumption from above, we now have a single temporal mode for the signal and one for the idler photons. These operators obey the commutation relation

$$[\hat{a}_k(\mathbf{q}), \hat{a}_{k'}^\dagger(\mathbf{q}')] = \delta_{k,k'} \delta^{(2)}(\mathbf{q} - \mathbf{q}'), \quad k, k' \in \{s, i\}.$$

Following the SPDC derivations with this, the two-photon state of Eq. (3.5) reads

$$|\Psi_2\rangle = \int d^2\mathbf{q}_i d^2\mathbf{q}_s \Lambda(\mathbf{q}_i, \mathbf{q}_s) a_i^\dagger(\mathbf{q}_i) a_s^\dagger(\mathbf{q}_s) |0\rangle$$

and the four-photon state of Eq. (3.16) accordingly. Due to this distinguishability, it is therefore possible to measure correlation functions of only the signal photons with

$$G_s^{(1)}(\mathbf{q}_1) := \langle \Psi | \hat{a}_s^\dagger(\mathbf{q}) \hat{a}_s(\mathbf{q}) | \Psi \rangle$$

and higher orders accordingly.

Far-Field Correlations

Using a far-field system of Sec. 2.1.5 after the emitting crystal, a fourth-order correlation function in the far-field plane reads

$$G^{(4)}(\mathbf{q}_1, \mathbf{q}_2, \mathbf{q}_3, \mathbf{q}_4) = 16 |\Lambda(\mathbf{q}_1, \mathbf{q}_2)\Lambda(\mathbf{q}_3, \mathbf{q}_4) + \Lambda(\mathbf{q}_1, \mathbf{q}_3)\Lambda(\mathbf{q}_2, \mathbf{q}_4) + \Lambda(\mathbf{q}_1, \mathbf{q}_4)\Lambda(\mathbf{q}_2, \mathbf{q}_3)|^2.$$

Due to the experimental difficulty of measuring this quantity, simplified measurements are considered. In the following, we assume that the generated four-photon state is given by two pairs as derived in Eq. (3.16). Knowing the two-photon state from theory and experiment, see Sec. 3.1, the correlations between the two photon pairs is the only unknown property of the four-photon state. Under these assumptions, it is sufficient to measure a second-order correlation function to characterize the source. These are derived in the following.

For spectral signal-idler separation with an asymmetric bandpass filter as discussed above, the probability to generate a photon pair, equaling the probability to measure on signal photon P_{1s} , is given by the first-order correlation function or intensity of the signal field and can be calculated to be

$$P_{1s} = G_s^{(1)}(\mathbf{q}) := \langle \Psi | a_s^\dagger(\mathbf{q}) a_s(\mathbf{q}) | \Psi \rangle = \int d^2\mathbf{q}_i |\Lambda(\mathbf{q}, \mathbf{q}_i)|^2 + \mathcal{O}(\Lambda^4).$$

The first order term originates from the two-photon state $|\Psi_2\rangle$ which dominates the generation rate. Higher order terms are neglected in the following. The probability to have two pairs in a pulse, equaling the probability to measure two signal photons P_{2s} , is then given

by the second-order correlation function of the signal field

$$\begin{aligned} P_{2s} &= G_s^{(2)}(\mathbf{q}_1, \mathbf{q}_2) := \langle \Psi | a_s^\dagger(\mathbf{q}_1) a_s^\dagger(\mathbf{q}_2) a_s(\mathbf{q}_2) a_s(\mathbf{q}_1) | \Psi \rangle \\ &= G_s^{(1)}(\mathbf{q}_1) G_s^{(1)}(\mathbf{q}_2) + \left| \int d^2 \mathbf{q}_i \Lambda^*(\mathbf{q}_1, \mathbf{q}_i) \Lambda(\mathbf{q}_2, \mathbf{q}_i) \right|^2 = \mathcal{A} + \mathcal{E} \end{aligned} \quad (3.18)$$

and originates from the four-photon state $|\Psi_4\rangle$ only. This is the results of [63] in spatial degrees of freedom. The first summand \mathcal{A} can be interpreted as accidental event or spontaneous emission of two pairs, while the second term \mathcal{E} describes the excess rate due to photon bunching or stimulated emission. Its integral quantifies the overlap of the emission modes of two pairs given the detection positions for the signal photons. We can conclude

$$P_{2s} = (P_{1s})^2 (1 + \chi), \quad \chi = \frac{\mathcal{E}}{\mathcal{A}} \in [0, 1].$$

For optimal overlap at $\mathbf{q}_1 = \mathbf{q}_2$ we get $\mathcal{A} = \mathcal{E}$ and a visibility $\chi = 1$. This is the case if we measure the double-pair generation in the same spatial and temporal mode as stated above. This equality directly corresponds to Eq. (3.17), where the degenerate case of a single detection mode $\mathbf{q}_1 = \mathbf{q}_2$ needs the Poissonian prefactor with $P_{2s} = \frac{1}{2} G_s^{(2)}(\mathbf{q}, \mathbf{q})$.

3.2.2 Experimental Implementation

The experimental setup for generation of four-photon states is shown in Fig. 3.4. A Ti:Sa femtosecond laser emits pulses at 791 nm with 6.5 nm FWHM bandwidth and approx. 200 fs pulse width, a repetition rate of 85 MHz and 700 mW average power. With lens L_1 ($f_1 = 200$ mm), it is focused to a beam waist radius of 50 μm in a first NLC. Via second-harmonic generation (SHG) in this crystal of 1 mm length, pulses in UV at 395.5 nm are generated. An average UV power of 35 mW is achieved. The 4-f lens configuration (L_2 and L_3 , $f = 50$ mm) images these pulses into the second NLC. Filters (F) transmit UV only and remove laser light at a suppression ratio better than 10^{-15} . NLC₂ is 2 mm long and generates photon pairs in type-0 SPDC. The lens L_4 ($f_4 = 75$ mm) produces this source's far-field distribution in plane Σ_{FF} . This plane is imaged to the sensor plane Σ'_{FF} with L_5 ($f_5 = 150$ mm) where a magnification $m = 0.31$ is realized. A narrow bandpass filter (BP) transmits 1.2 nm FWHM at 795 nm. Its central frequency is tuneable by tilting of the filter for transmission. It is adjusted to transmit both photons of a generated SPDC pair in nearly frequency-degenerate emission at 791 nm.

Both NLCs are periodically poled KTiOPO₄ (PPKTP) crystals with a poling period of $G \approx 3.17 \mu\text{m}$ yielding phase-matching for collinear type-0 SPDC. The material's properties of optical non-linearity [60] and temperature dependent index of refraction [61, 62] are the same as in Sec. 3.1.2. Each crystal is temperature stabilized to 0.1°C.

The narrow-band filter BP enforces a low number of emitted temporal modes and allows to observe photon bunching effects at good visibility, see Sec. 3.2.1. Assuming a Fourier-limited pulse emitted by the laser with mentioned spectrum, numerically solving the coupled-wave equation of the SHG process in the periodically poled crystal in plane-wave approximation determines the electric field of the output pulse [54]. This yields a UV pulse width of 1.5 ps FWHM at 0.3 nm FWHM bandwidth. As an input to the SPDC process, a temporal mode number of M can be calculated using the procedure outlined above. It yields $M = 2.1\text{--}2.4$, depending on SPDC phase-matching.

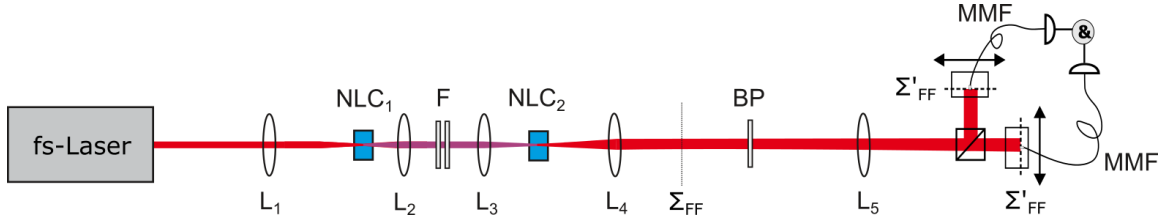


FIGURE 3.4: Experimental setup for the 4-photon generation. A Ti:Sa femtosecond laser emits pulses at 791 nm which is converted to 395.5 nm via second-harmonic generation in NLC₁. This UV pulses are imaged with the 4-f lens configuration (L_2 and L_3) into the second NLC₂. Filters (F) only transmit UV. SPDC in NLC₂ generates photon pairs. The lens L_4 produces the SPDC far-field distribution in Σ_{FF} . This plane is imaged onto the sensor with L_5 . A narrow bandpass filter (BP) only transmits photons at the central frequency of 791 nm. Fiber-coupled detectors on motorized stages allow to measure $G^{(2)}$ for source characterization.

3.2.3 Characterization

In order to characterize the light source depicted in Fig. 3.4, the source's output plane Σ_{FF} is imaged with magnification $m = 0.31$ by a single lens (L_5 , $f = 150$ mm) to the detector plane Σ'_{FF} . A first- and second-order correlation function is measured in this plane: A beam splitter cube separates photons to two different detectors. These are coupled to multi-mode fibers of $105 \mu\text{m}$ diameter whose bare fiber tips are on motorized stages scanning the detector plane in horizontal x direction. Detectors are single photon counters based on silicon avalanche diodes (Perkin Elmer SPCM-AGR-14). Detection events are timestamped with a time-to-digital converter (IDQ TDC id800) with 81 ps time resolution. The crystal temperature of NLC₁ is set to 47°C . Collinear SPDC emission, assessed with a CCD camera in the detector plane, is achieved for NLC₂ at the temperature of 44°C .

The real-time evaluation of this timestamp data is performed with a LabView program. It allows to count coincidences, i.e. event pairs with a relative time difference in a window of $T_c = 2$ ns which are assumed to originate from the same pulse. The thereby measured coincidence event rate at detector positions $\rho_1, \rho_2 \in \Sigma_d$ is given by the second-order correlation function with

$$C^{0p}(\rho_1, \rho_2) := \int_{A_1} d^2\rho'_1 \int_{A_2} d^2\rho'_2 \int_{-\infty}^{\infty} dt_1 \int_{t_1 - T_c/2}^{t_1 + T_c/2} dt_2 \frac{1}{2} G^{(2)}(\rho'_1, t_1; \rho'_2; t_2)$$

with the fiber core aperture areas $A_1, A_2 \subset \Sigma_d$ and the beam splitter ratio introducing a reduction of the signal. In addition, the coincidences between two successive pulses are measured. Given the pulse separation $T_p = 12$ ns, this rate can be expressed as

$$C^{1p}(\rho_1, \rho_2) := \int_{A_1} d^2\rho'_1 \int_{A_2} d^2\rho'_2 \int_{-\infty}^{\infty} dt_1 \int_{t_1 + T_p - T_c/2}^{t_1 + T_p + T_c/2} dt_2 \frac{1}{2} G^{(2)}(\rho'_1, t_1; \rho'_2; t_2).$$

Pump Power Dependence

The measured dependence of the coincidences signal on the pump power is shown Fig. 3.5. The fibers are adjusted to collect collinear emission at $q = 0$ in the far-field plane Σ'_{FF} . Different spectral filtering settings are used in the following.

The bandpass filter BP is tuned for symmetric, frequency-degenerate emission around 791 nm. Therefore, a coincident event within a pulse C^{0p} can be originating either from two photons of the same or from different pairs. As the single pair generation dominates at low pump power, its linear dependence on the pump intensity apparent in Eq. (3.6) is reflected in C^{0p} . This behavior is validated with the linear fit in in Fig. 3.5(a). Coincidences

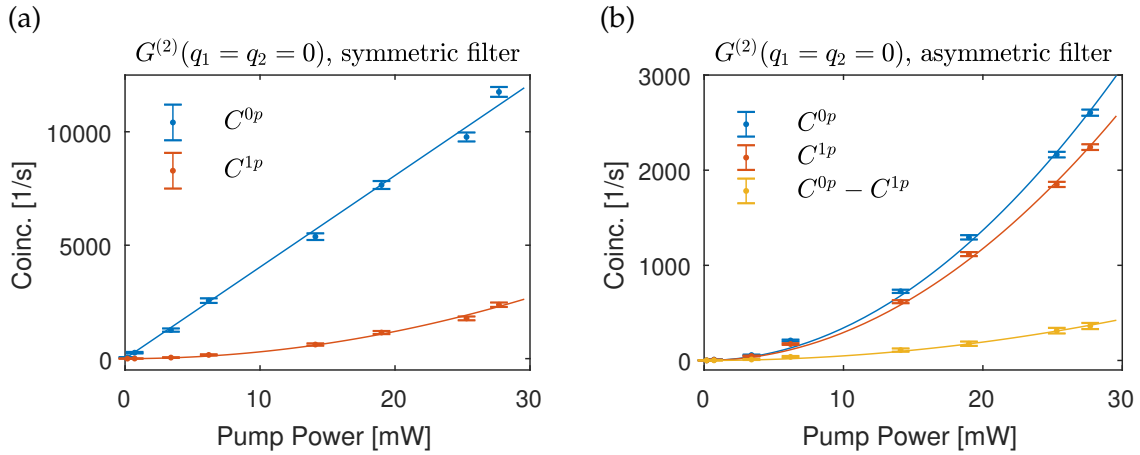


FIGURE 3.5: Measured coincidence rate for collinear emission of the four-photon source in dependence on the average power of the pump pulse. The bandpass filter (BP) centered symmetrically around 791 nm (a) allows detection of both photons of a pair. Detuning it to approx. 793 nm in (b) only transmits signal photons. Coincidences of detection events within a pulse C^{0p} and between successive pulses C^{1p} are shown. The excess $C^{0p} - C^{1p}$ is due to photon bunching. Purely linear and quadratic fits and Poisson 2σ errors are shown.

between successive pulses C^{1p} are between independent pairs. Their probability is $(P_2)^2$ with the pair emission probability P_2 . The resulting quadratic dependence on pump power is verified in Fig. 3.5(a).

By tuning the bandpass filter BP for asymmetric transmission at approx. 793 nm, only one photon of a generated pair can be detected. Coincidences within a pulse C^{0p} are therefore originating from different pairs and is theoretically described by the double pair generation probability $P_{2s} \propto C^{0p}$ in Eq. (3.18). As expected from this equation, the rate scales quadratically with pump power and is confirmed with the fit in Fig. 3.5(b). Coincidences between successive pulses C^{1p} would be described by a generalized Eq. (3.18) taking into account multiple pulses. Then, the lack of temporal mode overlap leads to $C^{1p} \propto P_{2s} = (P_{1s})^2$ and therefore models the independent emission of pairs.

The excess $C^{0p} - C^{1p}$ is due the photon bunching and can be identified as the term \mathcal{E} in Eq. (3.18). By calculating $\chi = C^{0p}/C^{1p} - 1$, a value of the bunching visibility $\chi = 0.18 \pm 0.02$ across all pump powers can be determined. This value is smaller than the theoretical expectation of $\chi = 1/M \approx 0.4$ but can be explained by different sources of uncorrelated light causing accidental detection events and a not thoroughly characterized pump pulse leading to an inaccurate estimate of the temporal mode number.

Spatial Correlation

Fig. 3.6 shows the spatial correlation produced by the photon bunching effect by visualizing the excess $C^{0p} - C^{1p}$. Panel (a) and (c) uses a symmetric bandpass filter (BP) at 791 nm where both photon of a pair are transmitted. The strong anti-diagonal is the expected two-photon signal, see Sec. 3.1.2. Four-photon generation produces the faint diagonal correlation, which is only visible in the used logarithmic scale. Panel (c) uses a NLC temperature of 40°C for slightly non-collinear emission.

For panel (b), the asymmetric setting of the BP filter at 793 nm only transmits signal photons. The two-photon correlation is therefore suppressed, only photon bunching is visible. The diagonal allows to calculate the bunching visibility $\chi = C^{0p}/C^{1p} - 1$ in dependence of x separation, see panel (d). Again, a peak visibility of $\chi = 0.18$ is measured. A Gaussian fit yields a FWHM of 0.26 ± 0.03 mm, while the theoretical value with Eq. (3.18)

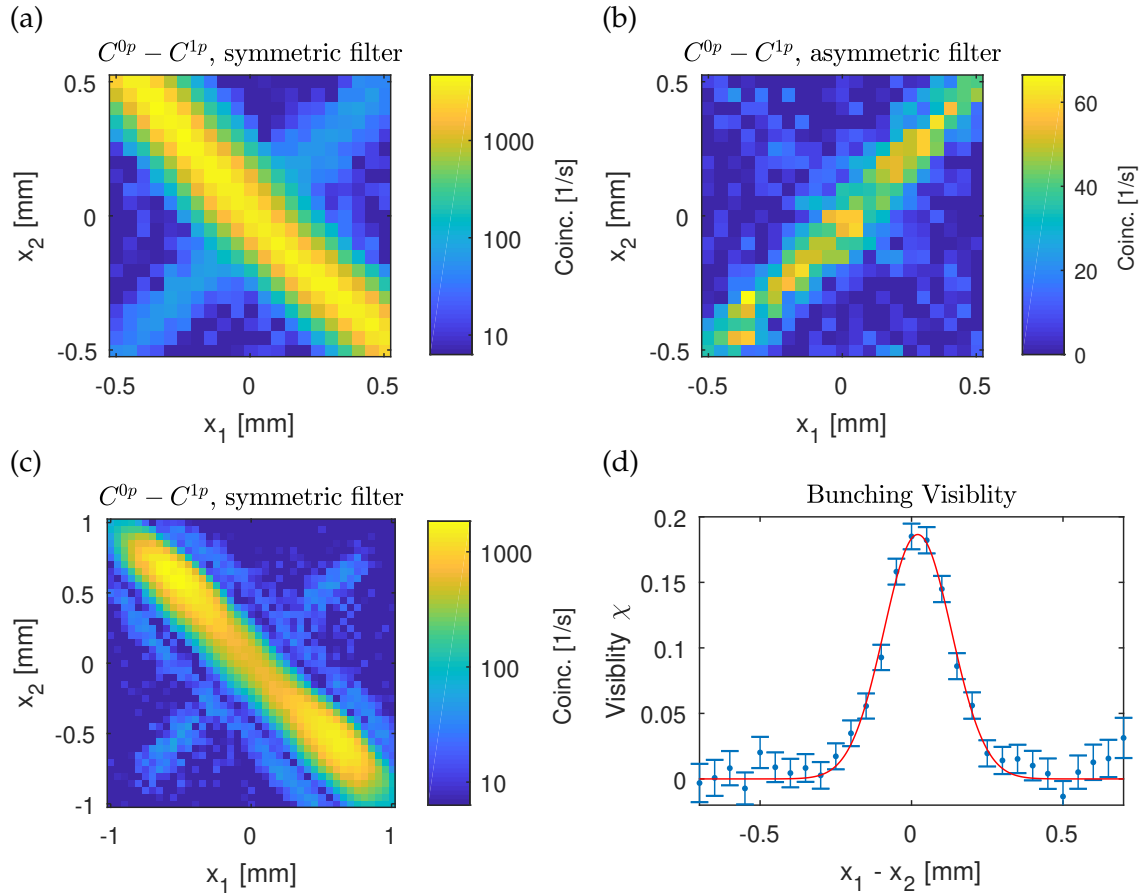


FIGURE 3.6: Measured excess coincidence rates $\mathcal{E} = C^{0p} - C^{1p}$ at 25 mW pump power. Collinear emission is present in (a) and (b), while slightly non-collinear in (c) is due to NLC temperature change. The bandpass filter (BP) is centered at 791 nm in (a) and (c), while in (b) it is set to 793 nm only showing the photon bunching signal. Note the logarithmic scale of (a) and (d). Panel (d) shows the bunching visibility of the measurement in (b) and 1σ errors with a Gaussian fit.

and the experimental settings is given by 0.20 mm. This discrepancy is due to the detection fiber diameter of 0.105 mm which does not allow to resolve correlation width.

The correlated signal verifies the generation of four-photon states according to the theoretical expectation.

3.3 Pseudo-Thermal Light

Thermal light can be generated by classical means like incandescent lamps. Therefore, the problem of low detection rates of the above described weak sources is solved by its almost arbitrary intensity. While it does not provide entangled photon states, it nevertheless exhibits interesting spatial and temporal correlations which allow to test detector arrays for high-order correlation measurement in Ch. 5. It is also applied for quantum imaging in Sec. 6, where it allows to improve image resolution due its the well known statistics.

3.3.1 Theory

The statistics and coherence of thermal light is fully described by field correlation functions. We assume in the following the measurement within the correlation time of the thermal source and can therefore restrict to a time independent description. The quantum state of thermal light is given by a density operator

$$\hat{\rho} = \sum_{\{n_k\}} P(\{n_k\}) |\{n_k\}\rangle \langle\{n_k\}|$$

with the summation over the photon numbers n_k of all modes plane wave \mathbf{k} . Their distribution is given by the Bose-Einstein statistic

$$P(\{n_k\}) = \prod_k \frac{\langle n_k \rangle}{(1 + \langle n_k \rangle)^{(1+n_k)}} = \prod_k p(n_k)$$

which factorizes into a product of separated mode distributions [66]. The density matrix is fully diagonal and reflects the absence of any coherence or correlation between the modes.

Instead of the here used Fock basis, the density operator can be expressed in a coherent state basis [69]. Then, the corresponding distributions p are Gaussian and P is in general a multivariate normal distribution. Isserlis' theorem for Gaussian moments, or Wick's theorem, states that a correlation function of any order can then be expressed in terms of first-order correlations. With the first-order field correlation function

$$G^{(1)}(\boldsymbol{\rho}_1, \boldsymbol{\rho}_2) = \langle \hat{E}^{(-)}(\boldsymbol{\rho}_1) \hat{E}^{(+)}(\boldsymbol{\rho}_2) \rangle \quad (3.19)$$

related to the before defined intensity correlation function by $G^{(1)}(\boldsymbol{\rho}) = G^{(1)}(\boldsymbol{\rho}, \boldsymbol{\rho})$, the second-order correlation function for thermal light reads

$$\begin{aligned} G^{(2)}(\boldsymbol{\rho}_1, \boldsymbol{\rho}_2) &= \langle \hat{E}^{(-)}(\boldsymbol{\rho}_1) \hat{E}^{(-)}(\boldsymbol{\rho}_2) \hat{E}^{(+)}(\boldsymbol{\rho}_1) \hat{E}^{(+)}(\boldsymbol{\rho}_2) \rangle \\ &= \langle \hat{E}^{(-)}(\boldsymbol{\rho}_1) \hat{E}^{(+)}(\boldsymbol{\rho}_1) \rangle \langle \hat{E}^{(-)}(\boldsymbol{\rho}_2) \hat{E}^{(+)}(\boldsymbol{\rho}_2) \rangle \\ &\quad + \langle \hat{E}^{(-)}(\boldsymbol{\rho}_1) \hat{E}^{(+)}(\boldsymbol{\rho}_2) \rangle \langle \hat{E}^{(-)}(\boldsymbol{\rho}_2) \hat{E}^{(+)}(\boldsymbol{\rho}_1) \rangle \\ &= G^{(1)}(\boldsymbol{\rho}_1) G^{(1)}(\boldsymbol{\rho}_2) + |G^{(1)}(\boldsymbol{\rho}_1, \boldsymbol{\rho}_2)|^2. \end{aligned} \quad (3.20)$$

The second term

$$\Delta G^{(2)}(\boldsymbol{\rho}_1, \boldsymbol{\rho}_2) := |G^{(1)}(\boldsymbol{\rho}_1, \boldsymbol{\rho}_2)|^2 = |\langle \hat{E}^{(-)}(\boldsymbol{\rho}_1) \hat{E}^{(+)}(\boldsymbol{\rho}_2) \rangle|^2 \quad (3.21)$$

can be interpreted as photon bunching leading to an increased two-photon probability in comparison to coherent light where this contribution is absent. Higher-order $G^{(N)}$ can be expressed in $G^{(1)}(\rho_1, \rho_2)$ accordingly [38, 70]. Their maximal bunching is given for

$$G^{(N)}(\rho, \dots, \rho) = N! |G^{(1)}(\rho, \rho)|^N$$

leading to a normalized N th-order correlation function $g^{(N)} = N!$. An increase of $N!$ in coincidence signal is expected for thermal light in comparison to coherent light where Poissonian statistics governs the photon numbers [38].

Thermal light propagated through a linear optical system exhibits again thermal statistics [66]. Therefore, it is sufficient to calculate the propagated first-order coherence which fully characterizes all other correlation orders. For this, the electric field operators in Eq. (3.19) are transformed by the system's impulse response function by applying Eq. (2.21).

Far-Field Correlations of a Ground Glass Disc

The correlation time of real thermal sources like incandescent lamps is very short. This makes an experiment very difficult because a measurement apparatus needs to resolve this time scale in order to see the spatial correlations described above. It is possible to prolong correlation time by narrow-band filtering, but at the cost of a strongly reduced signal. A more convenient approach is to use pseudo-thermal light which artificially generates light with the same statistics.

The pseudo-thermal source is implemented in the following with a rotating ground glass disk (GDD) [71, 72]. Its pattern of small feature size imprints random phases onto an incident illumination beam. It can be shown, that the transmitted light's correlation functions obey thermal statistics [38]. Furthermore, the correlation time is freely adjustable: With the rotation frequency of the disk ν , the radial position r of the illuminating beam, and the beam size w we can determine the characteristic field correlation time

$$t_c \approx \frac{w}{2\pi r \nu}.$$

The advantage of using the far-field of a GDD for the source output is that the field correlation length, or speckle size, is independent of surface details (roughness, correlation length) of the disc. Furthermore, in contrast to the disk's near-field, where the rotations of the disk produce correlation artifacts due to moving speckles, the far-field better agrees to the theoretical model of truly thermal light. A single lens of focal length f can be used to obtain a far-field plane, as described in Sec. 2.1.5. This lens has the further benefit, that the light is not spherically diverging, as it is emanating from the GDD, but collimated. A laser of wavelength λ and Gaussian beam radius w illuminates the GDD. If the disk's feature size is sufficiently small, resulting in phase randomization with a correlation length much smaller than w , the first-order correlation function in the far-field plane can be shown to read

$$G^{(1)}(\rho_1, \rho_2) = I_0 e^{-(\rho_1 - \rho_2)^2 / 2l_c^2}, \quad l_c = \frac{f\lambda}{\pi w}, \quad (3.22)$$

with the average intensity I_0 and correlation length l_c . Therefore, l_c is easily adjustable by the beam radius w of the illumination. This coherence length corresponds to the size of speckles which are visible in the instantaneous intensity distribution.

3.3.2 Experimental Implementation

Fig. 3.7 shows the experimental setup. A CW laser beam at $\lambda = 405$ nm is focused by lens L1 onto the GDD. A Gaussian beam radius of $w = 240$ μm is incident at the radial position

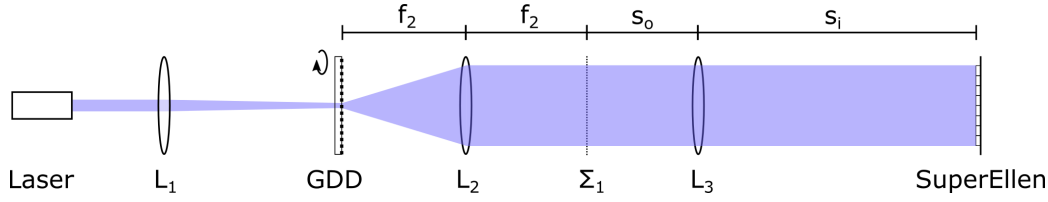


FIGURE 3.7: Source of pseudo-thermal light. The rotating ground glass disk (GDD) is illuminated by a laser and produces a random speckle pattern. With lens L_2 , the far-field plane Σ_1 of the disk is obtained. It constitutes the source output. For characterization of the light, this plane is imaged with lens L_3 to the SuperEllen detector array.

$r = 20$ mm of the disk. Lens L_2 of focal length $f_2 = 75$ mm establishes the far-field plane of the disk in Σ_1 which serves as output plane. The opaque GDD is mounted on a DC motor where rotation speeds up to 4000 rpm (rotations per minute) are possible.

3.3.3 Characterization

For characterization of the light in output plane Σ_1 , it is imaged by lens L_3 ($f = 150$ mm) into the detector plane. The detector SuperEllen is a 32×32 pixels time-resolving silicon photon detector based on SPAD arrays. The pixel pitch (separation distance) is $44.67 \mu\text{m}$. It is fully introduced in Sec. 5.2 where we demonstrate its capability to measure high-order correlation functions using the theoretical results of Sec. 2.3. The sensor is applied here for measurements, while technical details are avoided and postponed for discussion in Ch. 5.

The implemented pseudo-thermal light source using a CW laser constitutes a time-stationary source. With the measurement data of the sensor, the results of Sec. 2.3.4 allow to gain the intensity $G^{(1)}(\mathbf{p})$ and the second-order correlation function

$$G^{(2)}(\mathbf{p}_1, \mathbf{p}_2, \Delta t), \quad \Delta t := t_1 - t_2, \quad (3.23)$$

at the pixel coordinates $\mathbf{p} = (x, y)$, $x, y \in \{1, \dots, 32\}$.

Temporal Correlation and Spatial Artifacts

An imaging magnification $m = s_i/s_o = 1$ from Σ_1 to the detector is chosen for the following measurements. The illumination beam radius is here changed to $w = 150 \mu\text{m}$. The data of Eq. (3.23) provided by the detector acquisition allows to determine a correlation function

$$G^{(2)}(\Delta \mathbf{p}, \Delta t) := \sum_{\mathbf{p}} G^{(2)}(\mathbf{p}, \mathbf{p} + \Delta \mathbf{p}, \Delta t), \quad \Delta \mathbf{p} := \mathbf{p}_1 - \mathbf{p}_2.$$

In order to assess the correlation time, single-pixel correlation $\Delta \mathbf{p} = 0$ is considered in the following and enforces the measurement within the correlation length l_c only. At a disk rotation speed of 1000 rpm, Fig. 3.8(a) shows a width of the correlation peak of $50 \mu\text{s}$ FWHM (theory $t_c \approx 70 \mu\text{s}$), while at the reduced value of 300 rpm in Fig. 3.8(b) a width of $140 \mu\text{s}$ FWHM is measured (theory $t_c \approx 240 \mu\text{s}$). In the latter case, a bunching visibility of 1.74 can be determined while the theory predicts 2, see Eq. (3.20). This discrepancy can be explained by regularities of the GDD leading to biased statistics, not considered polarization effects [69], or background light increasing the uncorrelated signal at higher Δt and thereby reducing the visibility.

With the above defined $G^{(2)}(\Delta \mathbf{p}, \Delta t)$, it is possible to analyze how distant pixel correlate in time. Subtracting the constant background, persisting at larger Δt , allows to isolate bunching term $\Delta G^{(2)}$ of Eq. (3.20). Fig. 3.9 shows this for different horizontal and vertical

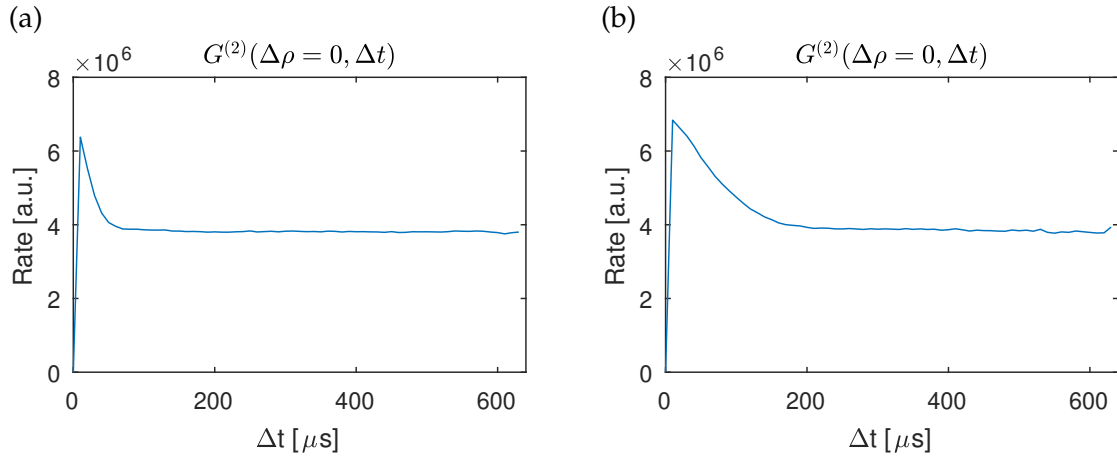


FIGURE 3.8: Temporal second-order correlation function for pseudo-thermal light. A GDD rotation speed of 1000 rpm is chosen in (a) and 300 rpm in (b). Only correlations within the same pixel $\Delta\rho = 0$ are considered, where $\Delta t = 0$ is not available by the detector.

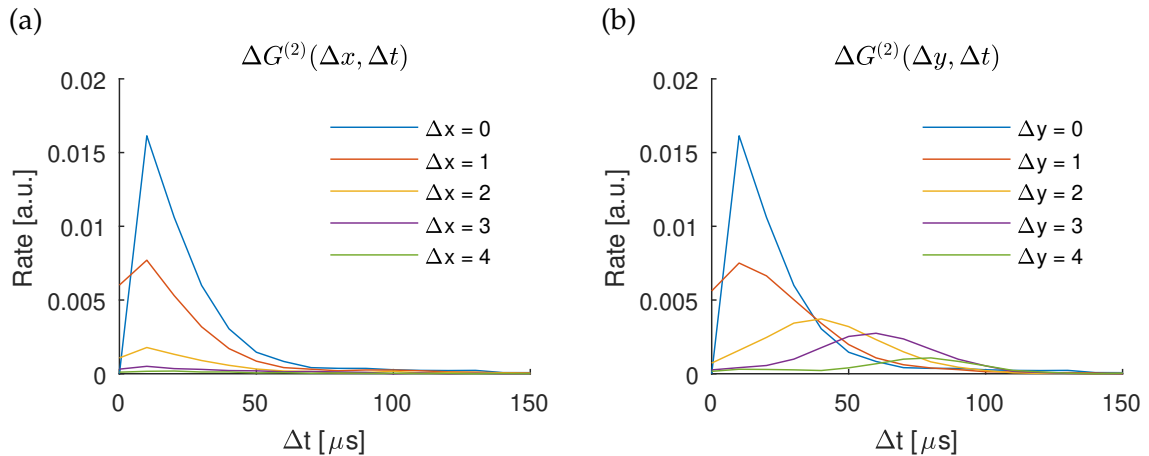


FIGURE 3.9: Measured excess correlation function $\Delta G^{(2)}$ for horizontally (a) and vertically (b) separated pixels at different distances. A temporal shift of correlation with distance is observed in (b) and corresponds to the movement of speckles.

separations. While for horizontal shift Δx in panel (a) only the expected decrease in the magnitude for larger separation is visible, vertical shifts in (b) show a moving correlation peak. It was verified that the direction of this spatio-temporal correlation coincides with the direction of the movement of the GDD relative to the optical axis. We observe therefore a moving speckle pattern. In a near-field arrangement, the same magnitude at all Δy would be expected, while in this far-field case it decreases fast with separation. While theory does not show moving speckles in far-field, this might be due to imperfect alignment of the far-field plane.

This observed spatio-temporal correlations can be avoided in measurements by appropriately selecting the coincidence window. If it is short enough at around $10\text{-}30\ \mu\text{s}$, these unwanted contributions can be temporally suppressed as explicit in Fig. 3.9. A longer window effectively elongates the correlation width, analyzed in the following, in the direction of speckle movement.

Spatial Correlation

The spatial correlation are measured in a slightly different setup. A magnification of $m = 1.96$ is realized and the original source's illumination beam radius $w = 250 \mu\text{m}$ is present. A GDD speed of 1000 rpm is set and a coincidence window $T_c = 40 \mu\text{s}$ is chosen for the evaluation of spatial correlation. Thereby, only events of $\Delta t \leq T_c$ are considered. This yields the temporally coincident, spatial correlation function

$$G^{(2)}(\mathbf{p}_1, \mathbf{p}_2) := \sum_{\Delta t=0}^{T_c} G^{(2)}(\mathbf{p}_1, \mathbf{p}_2, \Delta t),$$

by using the raw measurement data of Eq. (3.23), see also Sec. 2.3.4 for a discussion on coincidence and measurement data processing. This is identified as the theoretical second-order correlation function of Eq. (3.20) measured within the correlation time. Therefore, it is possible to subtract the accidental background, being the first term in this equation and estimated by the measured intensities $G^{(1)}$, and get the excess correlation $\Delta G^{(2)}$.

In order to assess the correlation length l_c , the background corrected, averaged, relative correlation function

$$\Delta G^{(2)}(\Delta \mathbf{p}) := \sum_{\mathbf{p}} G^{(2)}(\mathbf{p}, \mathbf{p} + \Delta \mathbf{p}) - G^{(1)}(\mathbf{p})G^{(1)}(\mathbf{p} + \Delta \mathbf{p})$$

is shown in Fig. 3.10. The x cross-section in panel (b) shows a fitted correlation length of $68 \mu\text{m}$, corresponding to $l_c = 35 \mu\text{m}$ in the output plane Σ_1 , while the theoretical value is $38 \mu\text{m}$ by using Eq. (3.22). This discrepancy can be explained by possible imperfect far-field alignment as discussed above, or the insufficient characterization of the profile of the illumination beam.

Fig. 3.11(a) shows the measured intensity distribution. While high dark-count pixels form a foreground pattern, the background shows an inhomogeneous illumination. This is also verified in Fig. 3.11(b) with the coincidence signal of a pixel with itself

$$\Delta G^{(2)}(\mathbf{p}, \mathbf{p}) := \sum_{\mathbf{p}} G^{(2)}(\mathbf{p}, \mathbf{p}) - G^{(1)}(\mathbf{p})G^{(1)}(\mathbf{p}).$$

This source inhomogeneity is given by regularities of the GDD. Further means of phase randomization would be required in order to get rid of these artifacts. In the correlation length measurements above, the procedure to get $\Delta G^{(2)}(\Delta \mathbf{p})$ averages out these spatial intensity variations.

Note that a third-order correlation measurement of the source is performed in Fig. 5.28 on page 99 where it verifies the detector and processing software. This data nicely agrees to the theoretical model of the pseudo-thermal source. The inhomogeneity of the source is there averaged out by only considering relative position and summing over all pixels triplets.

3.4 Conclusion

In this chapter, three different light source were theoretically described, experimentally implemented and characterized. The two-photon source shows the photons spatial correlation and anti-correlation in near-field and far-field respectively. At a total power of a few nanowatt, a photon flux of approx 10^9 ph/s is generated. In single photon detection experiments like sensor test and imaging, this is sufficient.

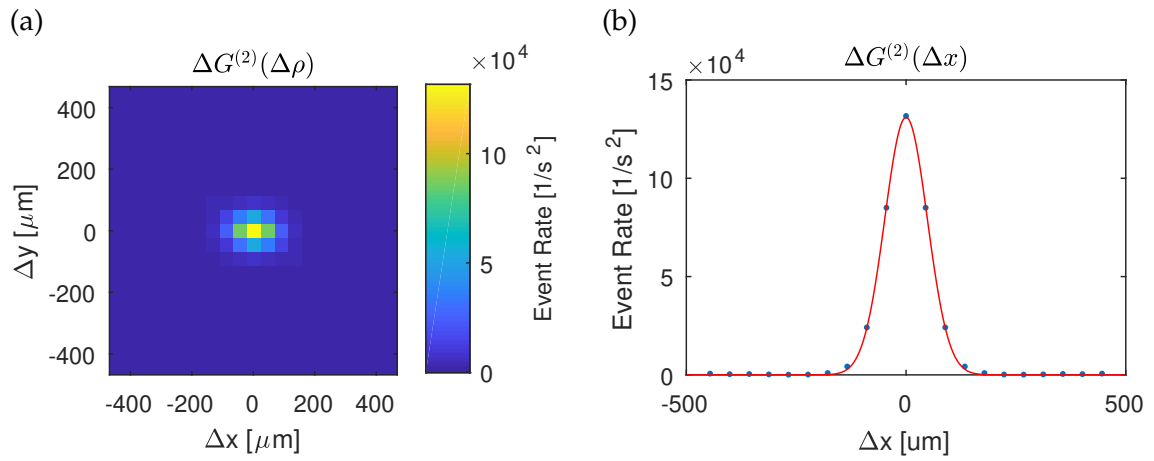


FIGURE 3.10: Measured spatial correlation of the pseudo-thermal source. A cross-section of (a) is shown in (b) with a Gaussian fit yielding a correlation length of $68 \mu\text{m}$ in the detector plane.

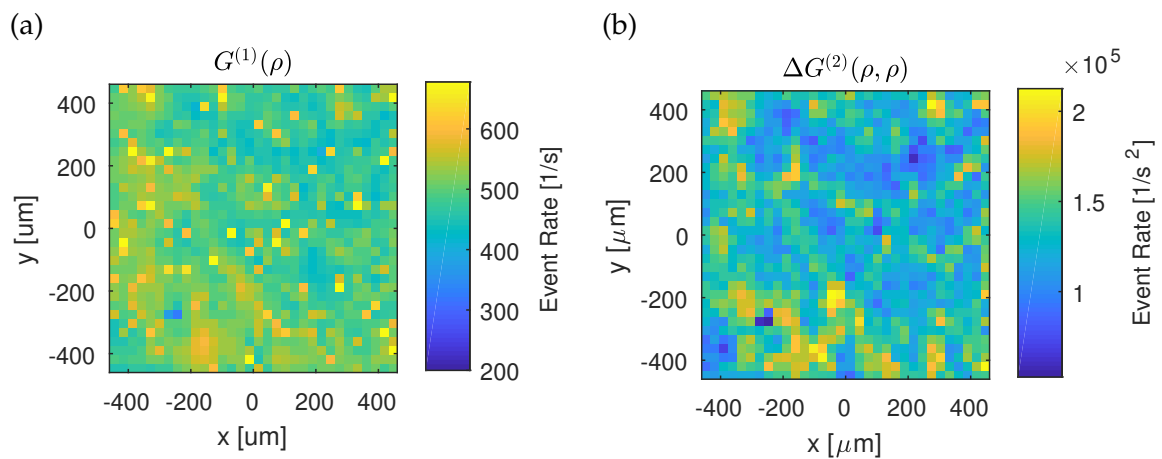


FIGURE 3.11: Measurements of the pseudo-thermal source. The intensity distribution (a) and the excess second-order correlation (b) of pixels with itself.

The four-photon source generates a similar flux of pairs, but the rate of double-pair generation is measured to be a few dozens to hundreds per second. For less optimal detectors than used in this chapter, with low detection efficiency and more noise, this very low flux will be difficult to measure. While stronger pump power would increase the four-photon rate, damaging the crystals is already a problem at the current power. Scaling the source to higher rates is difficult with the given means. In order to generate not only weakly correlated but truly entangled multi-photon states, higher-order non-linearity are to be considered.

The thermal light source allows almost arbitrary intensities as it is not restricted by a weak interaction process for generation. Furthermore, the thermal statistics is not changed by low detection efficiencies and can be compensated by increasing the source intensity. This will allow the use of non-optimal detectors and verification of data processing in high-order correlation measurements in later chapters.

While the discussed light sources are used within this thesis in the following, they are, together with their appropriate measurement system and software for real-time analysis and post-process evaluation, ready to be used in possible future experiments.

Chapter 4

Two-Photon Interferometry

This chapter investigates correlations in the spectral degrees of freedom of the SPDC two-photon source introduced in Sec. 3.1. While the available detectors neither resolve the spectrum nor the correlation time of the emitted photon pairs, an interferometer output nevertheless shows distinct signatures of these correlation in appropriate measurements. The specific signal features arising in correlation measurements are utilized in an application for interferometric length measurement. This experiment is implemented and analyzed for its accuracy.

The observed effect of two-photon interference shows oscillations periods corresponding to half the photon's wavelength, the de Broglie wavelength of the photon pair. This effect is studied in theory and experiment. Thanks to these insights, a spatial multi-mode case can be constructed in Ch. 7 allowing for super-resolved images.

4.1 Theory

The formal description of an interferometer in the quantum optical framework of Ch. 2 is introduced in the following. A Michelson interferometer, shown in Fig. 4.1, is described by its transfer function

$$H_I(\mathbf{q}) = \frac{1}{2} (H_F(\mathbf{q}, z) + H_F(\mathbf{q}, z + c\tau))$$

with the free-space propagation H_F from Eq. (2.9), the optical path length z from input Σ_1 to output Σ_2 through the fixed arm, and the time delay τ introduced in the scanning arm. The obvious interpretation is that the field at the output is resulting from a linear superposition of the two possible paths.

In plane Σ_2 , a single-mode detection in a Gaussian mode $G(\mathbf{q}) := \exp(-w_0^2 |\mathbf{q}|^2 / 4)$ with waist radius w_0 at position z in front of Σ_2 is realized. Then, the corresponding mode field operator is

$$\hat{M}^{(+)}(\omega) = \int d^2\mathbf{q} G(\mathbf{q}) H_F^*(\mathbf{q}, z) H_I(\mathbf{q}) \hat{E}_1^{(+)}(\mathbf{q}, \omega)$$

expressed in the propagated field operator $E_1^{(+)}$ in Σ_1 . See also Eq. (4.7) of Sec. 4.3 for discussion on SPDC fiber coupling. For a Gaussian of sufficiently large waist w_0 , we can approximate

$$G(\mathbf{q}) H_F^*(\mathbf{q}, z) H_I(\mathbf{q}) = \frac{1}{2} G(\mathbf{q}) (1 + H_F^*(\mathbf{q}, z) H_F(\mathbf{q}, z + c\tau)) \approx \frac{1}{2} G(\mathbf{q}) (1 + e^{i\omega\tau}).$$

This is valid if the difference in path length $c\tau$ is much smaller than the Rayleigh length $z_R = \pi w_0^2 / \lambda$ of the Gaussian beam [49]. If this is not the case, the Gouy phase introduces

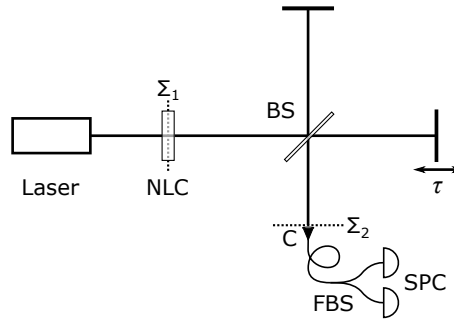


FIGURE 4.1: Michelson interferometer consisting of a beam splitter (BS) and two arms where one introduces a relative time delay τ . Photon pairs are produced in the nonlinear crystal (NLC) and detected in the Gaussian mode of a single mode fiber using a collimator (C). A fiber beam splitter (FBS) connects two single photon counters (SPC) which allow to measure second-order correlations $G^{(2)}$.

a correction to this approximation. Furthermore, reduced coupling efficiency becomes relevant. In the following we assume $c\tau \ll z_R$ and therefore

$$\hat{M}^{(+)}(\omega) = \frac{1}{2} \int d^2\mathbf{q} G(\mathbf{q}) \left(1 + e^{i\omega\tau}\right) \hat{E}_1^{(+)}(\mathbf{q}, \omega). \quad (4.1)$$

4.1.1 Intensity Measurement

A SPDC state is generated in plane Σ_1 . With Eq. (4.1) and the monochromatic plane wave pump approximation, see Sec. 3.1.1 and its fiber coupling in Sec. 4.3, the total single photon detection rate in the detection mode measured by a wavelength insensitive detector

$$R^{(1)}(\tau) = \int d\Omega G_M^{(1)}(\Omega) = \int d\Omega S(\Omega) + \text{Re} \left\{ e^{i\omega_c\tau} \int d\Omega S(\Omega) e^{i\Omega\tau} \right\} \quad (4.2)$$

with the central emission frequency ω_c and the spectral power density

$$S(\Omega) = \int d^2\mathbf{q} |G(\mathbf{q}) \Lambda(\mathbf{q}, \Omega)|^2$$

where the two-photon wave function $\Lambda(\mathbf{q}, \Omega)$ is used. Eq. (4.2) is equivalent to the result of the output intensity with classical light of the given spectral power density. $R^{(1)}(\tau)$ is given by a oscillating function at frequency ω_c which is modulated by the slowly varying envelope given by the Fourier transform of $S(\Omega)$. Therefore, the measurement of $R^{(1)}(\tau)$ allows to extract this envelope and, via an inverse Fourier transform, the spectral power density coupled into the fiber. This is the Wiener–Khinchin theorem, applied on the field auto-correlation realized by the interferometer and is used in Fourier-transform spectroscopy.

4.1.2 Second-Order Correlation Measurement

If detectors neither resolves the wavelength spectrum nor are fast enough to resolve the correlation time of the photon pairs, the only quantity which can be measured is the coincidence rate given by

$$R^{(2)} = \int d\omega_1 d\omega_2 G^{(2)}(\omega_1, \omega_2) \stackrel{!}{=} \int dt_1 dt_2 G^{(2)}(t_1, t_2).$$

This quantifies the overall two-photon probability at the output port.

For the case of the SPDC input state in plane wave approximation, see Sec. 3.1.1 and its fiber coupling in Sec. 4.3, and the Michelson interferometer formalized in Eq. (4.1), the coincidence rate of two wavelength insensitive detectors coupled to the detection mode can be derived to read

$$R^{(2)}(\tau) = \int d\Omega G^{(2)}(\Omega) = \frac{1}{4} \int d\Omega S_2(\Omega) \left| (1 + e^{i(\omega_c + \Omega)\tau})(1 + e^{i(\omega_c - \Omega)\tau}) \right|^2 \quad (4.3)$$

with the two-photon spectral power density

$$S_2(\Omega) = \left| \int d^2\mathbf{q} G(\mathbf{q}) G(-\mathbf{q}) \Lambda(\mathbf{q}, \Omega) \right|^2.$$

The coincidence rate $R^{(2)}(\tau)$ can be separated into different contributions of interference effects. By writing the factor

$$\begin{aligned} \left| (1 + e^{i(\omega_c + \Omega)\tau})(1 + e^{i(\omega_c - \Omega)\tau}) \right|^2 &= \left| 1 + e^{i(\omega_c - \Omega)\tau} + e^{i(\omega_c + \Omega)\tau} + e^{2i\omega_c\tau} \right|^2 \\ &= |A_{11} + A_{12} + A_{21} + A_{22}|^2 \end{aligned}$$

in terms of implicitly defined amplitudes A_{ij} corresponding to the propagation paths where one photon took arm i and the other arm j . Evaluating the squared modulus, we arrive at

$$|A_{11}|^2 + |A_{12}|^2 + |A_{21}|^2 + |A_{22}|^2 + A_{11}A_{22}^* + (A_{11} + A_{22})(A_{12}^* + A_{21}^*) + A_{12}A_{21}^* + \text{c.c.}$$

Interference occurs between two possibilities, described by their amplitudes, in which the same final state can result. Then, total interference signal

$$R^{(2)}(\tau) = R_0^{(2)} + R_{\text{HOM}}^{(2)}(\tau) + R_{\text{SPI}}^{(2)}(\tau) + R_{\text{TPI}}^{(2)}(\tau)$$

is given by the contributions of

- *Hong-Ou-Mandel interference*: The terms A_{12} and A_{21} describe the splitting of the photon pair into two arms. Both possibilities interfere in $A_{12}A_{21}^*$ with each other and yield

$$R_{\text{HOM}}^{(2)}(\tau) = 2 \text{Re} \{ M(2\tau) \}, \quad M(\tau) = \frac{1}{4} \int d\Omega S_2(\Omega) e^{i\Omega\tau}.$$

This is a slowly varying signal without a fast carrier oscillation.

- *Single-photon interference*: The terms $(A_{11} + A_{22})(A_{12}^* + A_{21}^*)$ describe the interference between the two possible path of one photon only, while the second photon has a definite path without interference possibility. This is made clear with the example $A_{11}A_{12}^* = |A_1|^2 A_1A_2^*$ with the single photon amplitudes A_i . The total contribution reads

$$R_{\text{SPI}}^{(2)}(\tau) = 8 \text{Re} \left\{ M(\tau) e^{i\omega_c\tau} \right\}.$$

It is oscillating at ω_c with a slowly varying envelope given by $M(\tau)$. Visibility vanishes for τ larger than the single-photon coherence time defined by the spectrum $S(\Omega)$.

- *Two-photon interference*: The term $A_{11}A_{22}^*$ corresponds to the propagation of both photons together in the same arm. Interference between both arms yield the

$$R_{\text{TPI}}^{(2)}(\tau) = 2 \operatorname{Re} \left\{ M(0) e^{2i\omega_c\tau} \right\}.$$

This is a pure sinusoidal oscillation of frequency is $2\omega_c$. Full visibility to large τ is given, due to the long two-photon coherence time of the SPDC state inherited from the pump field coherence time.

The single-photon and two-photon interference effects are experimentally investigated in the following. In the context of the concrete application of low-coherence reflectometry, the conventions in notation already established in literature are used and lead to slightly adapted expressions.

4.2 Self-Calibrating Optical Low-Coherence Reflectometry using Energy-Time Entangled Photons

Manuel Unternährer and André Stefanov

Institute of Applied Physics, University of Bern, 3012 Bern, Switzerland

Optical coherence tomography (OCT) or, equivalently, optical low-coherence reflectometry (OLCR) exploits coherence properties of light to measure a sample's partial reflection layers with a resolution in axial direction. It is a standard tool in medicine and biomedical applications [73]. Abbourady et al. showed in theory and experiment that the transition from a classical broadband light source to a quantum light can be beneficial [74, 75]. The frequency correlated photon pairs emitted by SPDC source allows for the compensation of the sample's chromatic dispersion and thereby undisturbed axial resolution. Their SPDC emission geometry was non-collinear, while it was later shown that the same signal can be recovered in a collinear system [76].

Based on these results, we make use of the two-photon interference signal for precise length measurement. Aiming not at applications with dispersive material but surfaces separated by free-space, the proposed scheme allows the position measurement with interferometric precision relative to a fixed laser wavelength due to the simultaneous short and very long coherence times of SPDC light in first- and second-order correlation measurements respectively.

4.2.1 Introduction

OLCR is capable of determining the positions of fully and partially reflective surfaces (e.g. layered samples, fibers, mirrors). To do so, the sample is inserted in one arm of a Michelson interferometer while the length of the other arm is scanned. Using a classical broadband light source, the interferometer output only shows interference oscillations if the arms are balanced within the short coherence time of the source. Therefore, the relative position between different surfaces can be determined within an error given by the resolution and linearity of the delay stage position feedback in the scanning arm.

We propose to replace the classical broadband light source by a photon pair source with energy-time entangled photons. Its single photon spectrum is broadband, giving rise to the same interferometer intensity output as for the classical source. The total energy of the photon pair is narrow-band due to entanglement. Its two-photon interference, visible in coincident photon detections, has therefore a long coherence time and is visible all

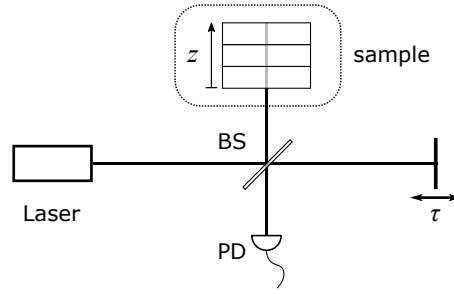


FIGURE 4.2: Classical OLCR setup. The Michelson interferometer consists of a beamsplitter (BS), a reference arm with delay τ and a sample arm with multiple reflective layers. A broadband laser serves as illumination. The reference arm is scanning τ and thereby measuring the positions z of reflecting layers in a sample.

over the scanning range. The well-defined oscillation period allows to establish a position scale independent of the delay stage position feedback. This self-calibrating feature permits to measure distances between surfaces in terms of multiples of the wavelength of a narrowband laser. Sub-wavelength precision can be achieved by proper signal processing and assumptions about the chromatic dispersion properties of the surfaces and media. In our experimental implementation, the measurement of a distance of 0.28 mm between two mirrors is shown to be reproducible within 1.6 nm standard deviation. Furthermore, this measurement method is verified to have a nearly perfect linearity over different magnitudes of distance ranges.

4.2.2 Classical Optical Low-Coherence Reflectometry

A standard OLCR setup is depicted in Fig. 4.2. A Michelson interferometer geometry is used with a broadband light source for illumination. The sample object in one arm, consisting of reflective surfaces, is measured by scanning the mirror position which introduces a temporal delay τ in the reference arm. Measuring the intensity $I(\tau)$ at the interferometer output with the photodiode PD allows to identify the positions of reflective surfaces, as the following treatment will show.

A sample object to be measured by OLCR can be characterized by a transfer function $H(\omega)$ which determines its reflection properties. In the case of n partially reflecting surfaces, neglecting multiple reflections, it reads

$$H(\omega) = \sum_{j=1}^n r_j e^{i\omega\tau_j} \quad (4.4)$$

with reflection amplitudes $r_j \in [0, 1]$ and introduced time delays τ_j . The surfaces are either stacked but partially reflective, or fully reflective but cover only a part of the light beam (detection mode). Assuming free-space propagation without optically dense or dispersive media between surfaces, the temporal delays are related to the sample surface positions z_j by

$$\tau_j = \frac{2z_j}{c}$$

with the speed of light c .

A broadband light source with central frequency ω_0 is characterized by the spectral power density $S(\Omega)$ which is defined in terms of the relative frequency $\Omega := \omega - \omega_0$. The

power measured at the interferometer output is given by [74]

$$I(\tau) = \Gamma_0 + 2 \operatorname{Re} \left\{ \Gamma(\tau) e^{-i\omega_0\tau} \right\}$$

depending on the time delay $\tau = 2d/c$ introduced in the reference arm of length d . Γ_0 is a constant self-interference term depending on the sample $H(\omega)$ and light source $S(\omega)$. The cross-interference between sample- and reference-arm reads

$$\Gamma(\tau) = \int d\Omega H(\omega_0 + \Omega) S(\Omega) e^{-i\Omega\tau}.$$

With the assumptions made for Eq. (4.4) and surface separations larger than the coherence time of the light source, we can rewrite

$$I(\tau) = I_0 + \sum_{j=1}^n r_j f(\tau - \tau_j) \quad (4.5)$$

with the single surface interferometer response

$$f(\tau) = 2 \operatorname{Re} \{ s(\tau) e^{-i\omega_0\tau} \}$$

where the envelope $s(\tau)$ is the inverse Fourier transform of $S(\Omega)$. The even function $f(\tau)$ is therefore the source electric field temporal auto-correlation. It is peaking at $\tau = 0$ and has a width given by the coherence time of the source. A broad spectrum or low coherence time yields therefore narrow interferometer oscillations centered around every surface position.

In order to reconstruct the surface positions z_j from the measurement of $I(\tau)$, a digital signal autocorrelation can be performed in a post-processing step with

$$A(\Delta\tau) = \int d\tau I(\tau) I(\tau + \Delta\tau) = A_0 + \sum_{i,j} r_i r_j \int d\tau f(\tau) f(\tau + \Delta\tau + \tau_j - \tau_i).$$

It shows very distinct peaks at every $\Delta\tau_{ij} := \tau_i - \tau_j$ due to the fact that $f(\tau)$ has a narrow envelope given by the coherence time and that it is oscillatory at a period of one wavelength. The evaluation of the peaks of this auto-correlation determine the position differences at sub-wavelength precision via $z_i - z_j = \Delta\tau_{ij}/2c$. This method shows high robustness against noise in the measurement of $I(\tau)$ because noise, which is uncorrelated with the reference arm position d (e.g. constant background or shot noise), averages out by performing the auto-correlation $A(\Delta\tau)$ as this involves all measurement points $I(\tau)$ for every $\Delta\tau$.

In this measurement using a classical light source, a motorized delay stage with calibrated position d reading is essential. Length measurements are relying on its accuracy.

4.2.3 Quantum Optical Low-Coherence Reflectometry

In quantum optical low-coherence reflectometry (QOLCR), we show in the following how a narrow-band laser wavelength can serve as length reference and thereby replaces the delay stage's calibration. Instead of the broadband laser, a type-0 spontaneous parametric down-process (SPDC) two-photon pair source is used in the following. The joint quantum state of the down-converted photon pair, generated with a narrow band laser at frequency

ω_p pumping SPDC, is given by

$$|\Psi\rangle = \int d\Omega \Lambda(\Omega) |\omega_0 + \Omega, \omega_0 - \Omega\rangle$$

where $\Omega := \omega - \omega_0$ is the relative frequency with respect to the central emission frequency $\omega_0 = \omega_p/2$ [74]. See also the full introduction of this light source in Sec. 3.1. Therefore, pairs of photons are emitted frequency anti-correlated around ω_0 . The joint spectral amplitude $\Lambda(\Omega)$ can be assumed to be a normalized, even function and leads to the joint spectral density $S(\Omega) = |\Lambda(\Omega)|^2$. Both photons are emitted into the same polarization mode and, due to collinear emission [76], into the same spatial mode which is selected by the detection. These degrees of freedom are implicitly treated and not labeled in the quantum state.

With this as the light source in the Michelson interferometer, an intensity measurement $I(\tau)$ at the output port yields exactly the classical result of Eq. (4.5) with the down-conversion spectrum $S(\Omega)$ used.

In a second-order correlation measurement, new features arise. As derived in [76], the two-photon coincidence rate measured at the output port, using a beam splitter and two detectors, is given by

$$M(\tau) = M_0 + 2 \operatorname{Re}\{M_1(2\tau)\} + 4 \operatorname{Re}\{M_2(\tau) e^{-i\omega_0\tau}\} + 2 \operatorname{Re}\{M_3 e^{-i2\omega_0\tau}\} \quad (4.6)$$

at a reference arm delay τ . The interference terms $M_1(2\tau)$ and $M_2(\tau)$, corresponding to Hong-Ou-Mandel and single-photon interference, are slowly varying at the time scale of the first-order coherence time corresponding to the width of the Fourier transform of the spectrum $S(\Omega)$. The last term describes two-photon interference (TPI) and is sinusoidally oscillating at double central frequency ω_0 with a constant amplitude M_3 . This term is originating from the interference of amplitudes where both photons take either the reference or the sample arm and is given by $M_3 = \int d\Omega H(\omega_0 + \Omega) H(\omega_0 - \Omega) S(\Omega)$ [76]. In the case of reflecting surfaces with no dispersive media as assumed in Eq. (4.4) and the total light source power S_0 , we arrive at

$$M_3 = S_0 \sum_{j=1}^n r_j^2 e^{-i2\omega_0\tau_j}$$

which is usually a non-zero constant. Only for very specific reflection coefficients r_j and separations τ_j it vanishes. In this equation, we made the simplifying assumption that the reflecting surfaces are spaced by much more than the first-order coherence time or, equally, the two-photon correlation time. This suppresses cross-interference terms between different sample surfaces at two-photon level. In contrast to the first-order interference fringes in $I(\tau)$ which are only visible close to a sample surface position, the TPI oscillations in $M(\tau)$ are equally present all over the measurement range of τ due to the long two-photon coherence time inherited from the pump laser.

Self-Calibration Signal Processing

In an interferometer scan, the real value τ at a measurement point is not known. An approximate value τ' is assumed to be provided by the measurement apparatus. For instance, it can be measured by a coarse motor encoder of the reference arm mirror position d by $\tau' = 2d/c$, or in a fixed motor speed setting by $\tau' = 2vt/c$ with measurement time t and velocity v .

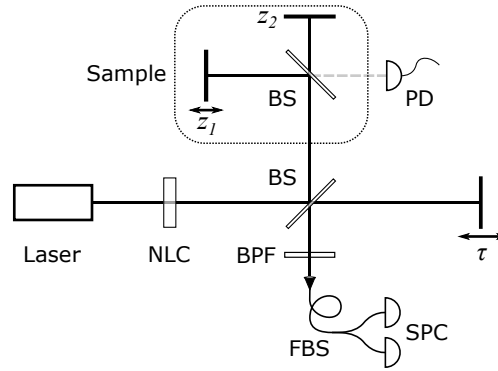


FIGURE 4.3: Quantum OLCR setup. SPDC light produced in a CW pumped non-linear crystal (NLC) is inserted into a Michelson interferometer consisting of: Beamsplitter (BS), band-pass filter transmitting SPDC at 810 nm (BPF), fiber beamsplitter (FBS), single photon counters (SPC) and scanning reference arm with delay τ . The sample consists of two surfaces at positions z_1 and z_2 , whose relative distance is interferometrically locked to the pump wavelength using a control loop with photodiode (PD) feedback measuring pump laser light (dashed line).

In a QOLCR measurement, coincidences $M(\tau')$ are being measured simultaneously with $I(\tau')$ while the reference arm is scanned over all the measurement range of τ' . As obvious from Eq. (4.6), the TPI is well separated from the others in terms of oscillation frequency. It can be extracted from $M(\tau')$ in a post-processing step by applying a digital high-pass filter. Its very well defined and narrow oscillation frequency $2\omega_0 = \omega_p$ inherited from the SPDC pump laser serves as a position reference signal.

By knowing the exact value of ω_p , the extracted signal $\text{TPI}(\tau') = 2 \text{Re}\{M_3 e^{i\omega_p\tau(\tau')}\}$ allows with a fitting procedure (e.g. using peak finding and interpolation) to get the relation

$$\tau' = \tau'(\tau)$$

between the exact τ value and its coarse measurement τ' . From the measured classical intensity signal $I(\tau')$, a calibrated signal

$$I_c(\tau) = I(\tau'(\tau))$$

is defined on the exact, calibrated scale τ . Applying the autocorrelation procedure shown in section 4.2.2 on $I_c(\tau)$, measurements of the surface distances are independent of the approximate length measurement but are directly linked to the known wavelength of the pump laser.

4.2.4 Experimental Implementation

The QOLCR setup is shown in Fig. 4.3. A non-linear, periodically poled KTP crystal is used in type-0, collinear SPDC. It is pumped by a grating stabilized diode laser of 30 mW power at $\lambda_p = 405 \text{ nm}$ with less than 2 MHz bandwidth and a collimated beam of 1 mm radius. The laser wavelength is locked to an etalon cavity. A lock-in amplifier and integrating control-loop regulates the laser cavity length on the maximum of an etalon interference fringe. This establishes a long-time wavelength stability.

In the reference arm, a standard motorized delay stage (Thorlabs PT1-Z8) is used. A retro-reflecting corner-cube mirror guarantees pointing stability during the scan in the presence of mechanical stage imprecisions resulting in tilting, because a stable mode overlap between reference and sample arm is needed for constant interference visibility. The

delay stage is driven at constant speed of 500 nm/s while the detectors measure continuously.

The detection uses a single mode fiber with an adjustable collimator. The detection mode is therefore nearly Gaussian and its waist of 0.2 mm radius is positioned at the crystal center and aligned to the pump beam for maximal coincidence signal [33], see also Sec. 4.3.1. The used reference arm scanning range of 0.3 mm introduces in the detection mode a negligible Gouy phase corresponding to 0.12 nm position shift. A 50:50 fiber beam splitter distributes the interferometer output to two fiber-coupled avalanche diode single photon counting modules. An electric coincidence circuit with 10 ns coincidence window is used to detect photon pairs. The counts are read at a rate of 100 Hz corresponding to a resolution of 5 nm in delay arm position at the mentioned velocity.

The sample consists of two reflecting surfaces whose distance is to be measured. As depicted in Fig. 4.3, the surfaces are mirrors behind the two output ports of a beamsplitter. One mirror is fixed at distance z_2 , the other at z_1 is on a nano-positioner with 30 μm range and sub-nanometer accuracy (MCL Nano-OP30). Using the pump light incident into the sample arm, the relative position between the mirrors $z_1 - z_2$ is interferometrically locked to the pump wavelength. A control-loop measures the pump intensity at sample beam-splitter output port with the photodiode PD and regulates the nano-positioner accordingly. Different surface distances can be realized by changing the controller set-point.

4.2.5 Results

A continuous OLCR scan of the reference arm length d is performed while measuring intensity $I(\tau)$ and second-order coincidence $M(\tau)$, see Fig. 4.4. The two fringe envelopes of $I(\tau)$ correspond to the surfaces of the sample while almost no interference is visible in between. $M(\tau)$ shows single-photon interference fringes at the surface positions, a Hong-Ou-Mandel feature centered between them, and the TPI signal which is recovered in all regions by applying a digital band-pass filter, see also the magnified regions in Fig. 4.5. In the lower left figure, distortions of the TPI are present in the single-photon interference regions as the latter is not fully suppressed by the filter. In the upper right figure, a unexpected regular oscillation in the intensity $I(\tau)$ is visible and can be explained by a two-photon detection artifact, see Sec. 4.3.2.

The regular TPI is used for realizing the calibrated reference arm position d scale. The correction of this calibrated scale to the motor stage encoder are shown in Fig. 4.6. The auto-correlation of $I(\tau)$ for identifying the surface distance $z_1 - z_2$ is given in Fig. 4.7. A parabolic fit of the envelope helps to identify the central peak uniquely which allows to determine the distance $z_1 - z_2 = \Delta d = 0.280228$ mm.

In order to quantify the measurement precision, 70 successive measurements are performed for a fixed sample. The measured average surface distance is $z_1 - z_2 = 0.284459$ mm. The distribution histogram of the measured values are shown in Fig. 4.8 which shows a standard deviation of 1.6 nm. Four outliers at one wavelength shift, due to misidentification of the auto-correlation peak, are ignored.

By changing the sample surface distance with variation of the position z_1 using the nano-positioner, the linearity of the measurement method is studied. Fig. 4.9 shows the stepwise increase of z_1 . Single measurements are performed and the above determined standard deviation used to indicated measurement error. With step sizes of 5 nm, 202.5 nm and 2025 nm, we observe very good linearity over the full range with deviations of less than 7 nm from ideal values indicated by lines of unit slope. The 5 nm steps are realized by changing the set-point of the sample control loop according to the theoretical response

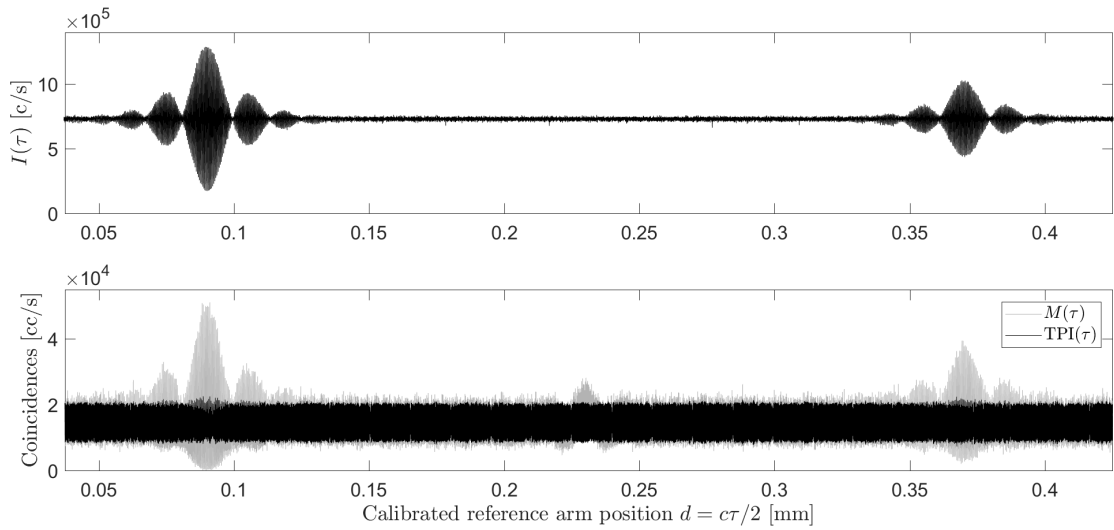


FIGURE 4.4: OLCR scan with intensity (top) and second-order coincidence (bottom) measurements. In the intensity signal, the two sample surfaces produce interference fringes only for reference arm positions d in their vicinity. The coincidence signal $M(\tau)$ and the extracted two-photon interference $TPI(\tau)$ are shown. The position scale d is calibrated using TPI .

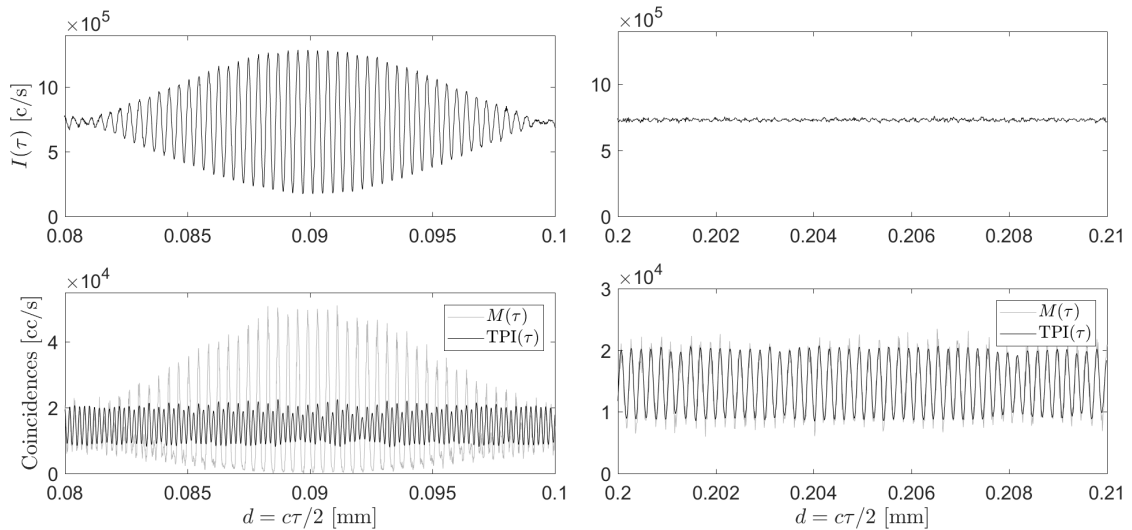


FIGURE 4.5: OLCR scan with intensity (top) and second-order coincidence (bottom) measurements. Two magnified regions of Fig. 4.4. Also in the presence intensity fringes and single-photon interference in the signal $M(\tau)$ (left), a TPI signal can be extracted by band-pass filtering. In the absence of intensity fringes (right), TPI is still visible. The position scale d is calibrated using TPI .

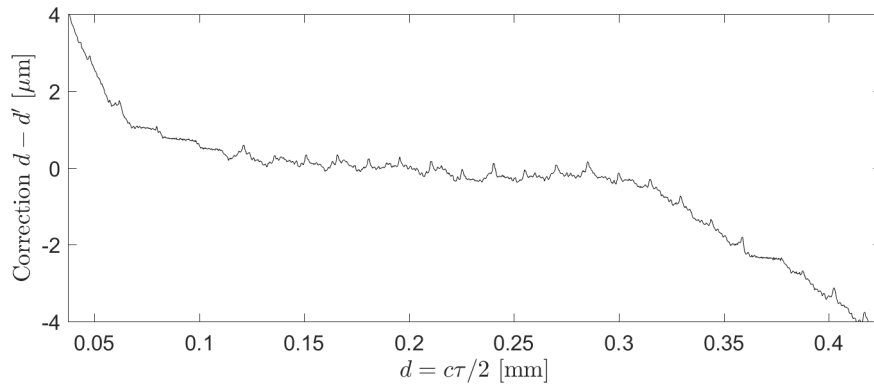


FIGURE 4.6: Correction of the motor stage position encoder d' to the TPI calibrated position d .

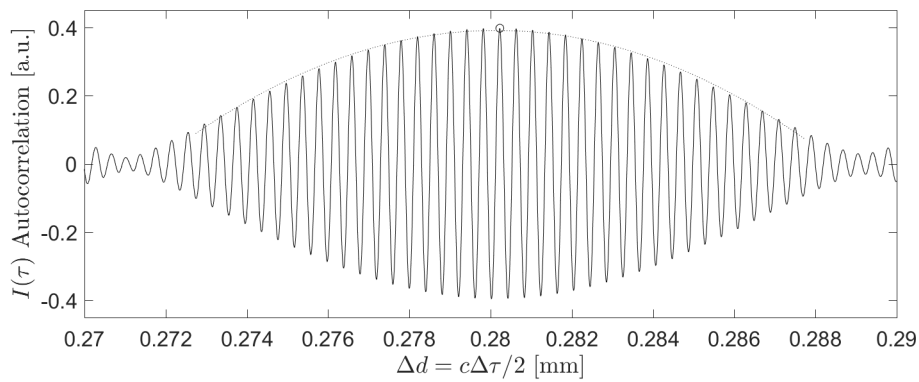


FIGURE 4.7: Auto-correlation of measured $I(\tau)$ from Fig. 4.4. A parabolic fit (dashed) serves for identification of the central peak (circle) at $\Delta d = 0.280228$ mm.

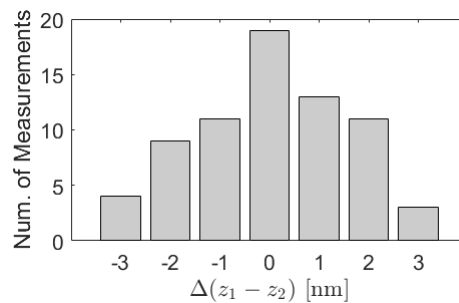


FIGURE 4.8: Distribution of the deviation $\Delta(z_1 - z_2)$ of the measured sample surface distance from the average value $z_1 - z_2 = 0.284459$ mm. 70 independent measurements are performed on the same sample. Ignoring 4 outliers at 405 nm shift, the standard deviation is 1.6 nm.

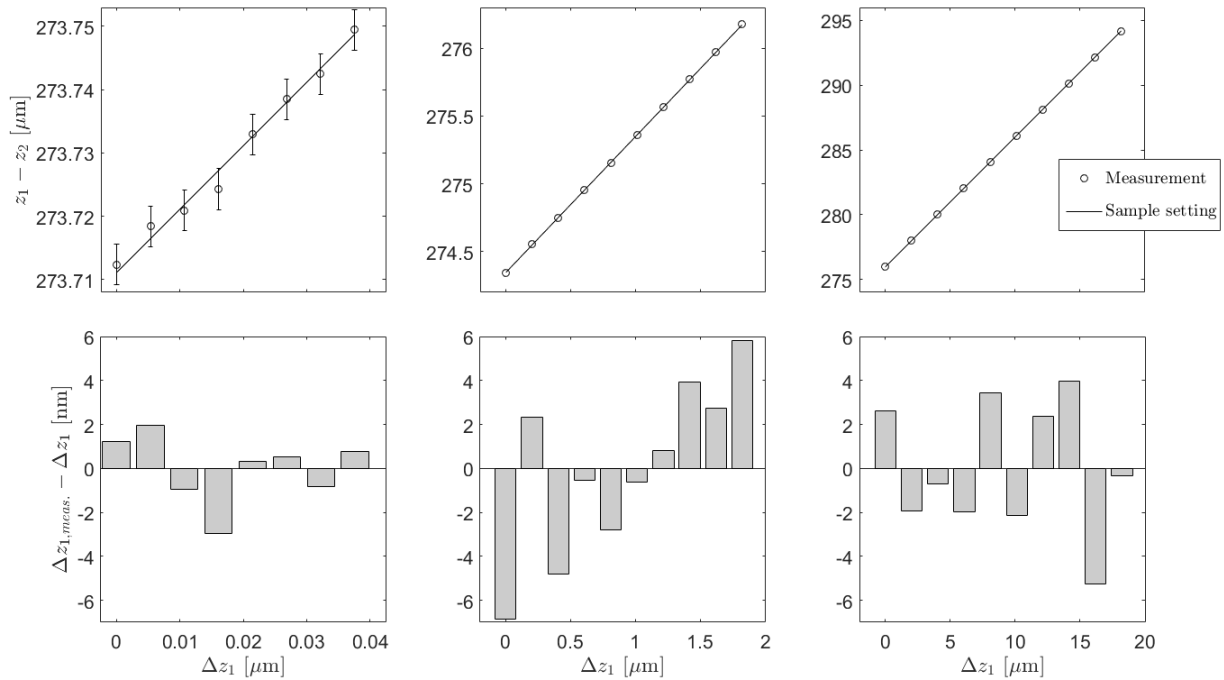


FIGURE 4.9: Linearity analysis of the QOLCR method. The distance $z_1 - z_2$ is measured for different sample settings (top row), where z_1 is varied in steps of 5 nm steps (left), 202.5 nm (middle) and 2025 nm (right). The expected linearity of unit slope is shown (lines). Sample averages and 2σ sample errors are shown. Bottom row: Corresponding deviations of the average measurements from the expected values.

of the interferometric feedback signal. The two larger steps are multiples of the oscillation period $\lambda_p/2$ and use the same, constant controller set-point after the nano-positioner performed this step.

4.2.6 Conclusion

The QOLCR experiment shows very high precision for length measurement. Despite the wavelength of 810 nm and only one measurement per 5 nm, a measurement precision of 1.6 nm was demonstrated. This can be understood in terms of the implicit averaging happening in the auto-correlation procedure for finding the distances. Even better results are expected for faster measurement acquisition. The imperfections of the delay stage were successfully detected and compensated by the interferometric signal present in second-order correlation measurement.

The proposed scheme is potentially very robust against background light: The two-photon interference signal is temporally strongly correlated. An uncorrelated background can be removed by estimating it with coincidence measurement of events with a time difference. In a implementation using classical light sources, temporal correlations are only achieved with more technical effort. Furthermore, the reference oscillation and the classical OLCR signal are well separable by the measurement and transmitted in the same spectral bandwidth and spatial mode. This allows to reduce background with appropriate spectral band filtering. In a classical scheme where an additional narrow-band laser would provide the reference oscillation, this signal would have to be spectrally separated from the broadband light for proper discrimination by detection and thereby more complex spectral filtering and distribution to detectors needed.

The investigation of linearity in Fig. 4.9 can also be seen from a different, more fundamental perspective: As the sample distance is locked to the pump wavelength, the variation of the sample length is measured in multiples of this wavelength. The good linearity of the TPI based length measurement indirectly validates the theoretical model of SPDC where the two-photon phase evolves identically to the pump laser field in free-space propagation. In the scans of Fig. 4.9, this is validated to a relative precision of approx. 10^{-4} .

The coincidence signal of Eq. (4.6) is only depending on the spectral density $S(\Omega) = |\Lambda(\Omega)|^2$ but not any phases of the two-photon wave function Λ . This implies that no entanglement can be relevant: It would be destroyed by phase randomization while the coincidence signal stays the same. A source of classically frequency anti-correlated photon pairs would be sufficient in this experiment. Using two polarization modes of classical coherent light with random but anti-correlated frequencies and one detector per polarization would again yield the same intensity and correlation signal. For other schemes proposed in literature for quantum coherence tomography [74–76], this replacements by classical sources is possible as well. Only if strong temporal correlation is required, e.g. for background suppression in ultra-fast coincidence detection, and at the same time a very well defined summed frequency for an accurate length reference, entanglement can surpass classical limits.

In conclusion, the proposed scheme for interferometric length measurement showed advantages by using quantum light. For real applications, however, these would not compensate the drawback of low photon flux of currently available sources. Nevertheless, the technique might provide a solution for measurements in very specific environments of high background noise and at the same time very high requirements on interferometric precision.

4.3 Appendix

For SPDC two-photon source in a bulk crystal introduced in Sec. 3.1, single-mode coupling is studied for the optimized experimental implementation of a two-photon interferometer. Expressions of higher-order correlations functions are derived. Furthermore, detector signal artifacts due to multi-photon states are explained. Group delay dispersion calculation is derived App. C but shows no relevance for the here presented experiment.

4.3.1 Single-Mode Coupling

Coupling of light to a single-mode fiber is classically described by an overlap integral [49]. In a quantum field formalism and a plane wave mode basis, it has its analogue in fiber mode field operator

$$\hat{M}^{(+)}(\omega) := \int d^2\mathbf{q} E_M^{(-)}(\mathbf{q}, \omega) \hat{E}^{(+)}(\mathbf{q}, \omega) \quad (4.7)$$

with the field operator $\hat{E}^{(+)}$ of Sec. 2.2 and the negative frequency part of the classical electrical field distribution $E_M^{(-)}$ of the fiber mode [66]. Both are defined in a detection plane Σ_d . Restricting to photon counting as done in Eq. (2.18), $\hat{M}^{(+)}$ can be interpreted as annihilation operator of a photon in the fiber mode. The creation operator $\hat{M}^{(-)}$ is defined similarly.

A good approximation of a fiber mode is the Gaussian beam [49]. It is fully characterized by its beam waist radius w_0 and waist position z_0 . The electric field distribution in a plane Σ_d at position z is given by

$$E_M^{(+)}(\mathbf{q}, \omega) = G(\mathbf{q}) H_F(\mathbf{q}, z - z_0) \quad (4.8)$$

with the Gaussian beam $G(\mathbf{q}) := \exp(-\omega_0^2 |\mathbf{q}|^2/4)$ and the free-space transfer function H_F from Eq. (2.9). We approximated the fiber mode to be independent of the wavelength which is valid for a small spectral bandwidth.

For a free propagation, we can conclude that a detection fiber in plane Σ_d at position z leads to the corresponding measurement operator

$$\begin{aligned}\hat{M}^{(+)}(\omega) &= \int d^2\mathbf{q} G(\mathbf{q}) H_F^*(\mathbf{q}, z - z_0) H_F(\mathbf{q}, z) \hat{E}_0^{(+)}(\mathbf{q}, \omega) \\ &= \int d^2\mathbf{q} G(\mathbf{q}) H_F^*(\mathbf{q}, -z_0) \hat{E}_0^{(+)}(\mathbf{q}, \omega)\end{aligned}\quad (4.9)$$

where the electric field operator $\hat{E}_d^{(+)} = H_F(\mathbf{q}, z) \hat{E}_0^{(+)}$ in Σ_d is expressed as a propagated $\hat{E}_0^{(+)}$ from plane at $z = 0$. The equation shows that the detection mode of the fiber can be propagated backwards to the source at $z = 0$. The overlap integral with the local field distribution of source and detection mode is invariant in the selection of the plane. A consequence is also that it is sufficient to characterize the detection mode in any plane. Fiber collimators or other optics do not have to be taken into account if a backwards propagated detection mode beam is experimentally characterized in front of such optics.

Correlation Functions

The field intensity in the fiber mode is given by the first-order correlation function

$$G_M^{(1)}(\omega) = \langle \hat{M}^{(-)}(\omega) \hat{M}^{(+)}(\omega) \rangle.$$

A second-order correlation function is accordingly

$$G_M^{(2)}(\omega_1, \omega_2) = \langle \hat{M}^{(-)}(\omega_1) \hat{M}^{(-)}(\omega_2) \hat{M}^{(+)}(\omega_1) \hat{M}^{(+)}(\omega_2) \rangle.$$

For the SPDC two photon state of Eq. (3.5), this reads

$$G_M^{(1)}(\omega) = \int d^2\mathbf{q}_s d\omega_s \left| 2 \int d^2\mathbf{q}_i E_M^{(-)}(\mathbf{q}_i, \omega) \Lambda(\mathbf{q}_i, \omega, \mathbf{q}_s, \omega_s) \right|^2$$

and

$$G_M^{(2)}(\omega_1, \omega_2) = \left| 2 \int d^2\mathbf{q}_s d^2\mathbf{q}_i E_M^{(-)}(\mathbf{q}_i, \omega_1) E_M^{(-)}(\mathbf{q}_s, \omega_2) \Lambda(\mathbf{q}_i, \omega_1, \mathbf{q}_s, \omega_2) \right|^2.$$

SPDC Two-Photon Coupling

For the case of a SPDC two-photon state given in Eq. (3.5)

$$|\Psi\rangle = \int d^2\mathbf{q}_i d\omega_i d^2\mathbf{q}_s d\omega_s \Lambda(\mathbf{q}_i, \omega_i, \mathbf{q}_s, \omega_s) a^\dagger(\mathbf{q}_i, \omega_i) a^\dagger(\mathbf{q}_s, \omega_s) |0\rangle,$$

the measurement of one photon in the fiber mode projects the second photon into the state

$$\hat{M}^{(+)}(\omega) |\Psi\rangle = \int d^2\mathbf{q}_s d\omega_s \left(2 \int d^2\mathbf{q}_i E_M^{(-)}(\mathbf{q}_i, \omega) \Lambda(\mathbf{q}_i, \omega, \mathbf{q}_s, \omega_s) \right) a^\dagger(\mathbf{q}_s, \omega_s) |0\rangle.$$

For SPDC in monochromatic plane wave pump approximation we have

$$|\Psi\rangle = \int d^2\mathbf{q} d\Omega \Lambda(\mathbf{q}, \Omega) a^\dagger(\mathbf{q}, \omega_c + \Omega) a^\dagger(-\mathbf{q}, \omega_c - \Omega) |0\rangle \quad (4.10)$$

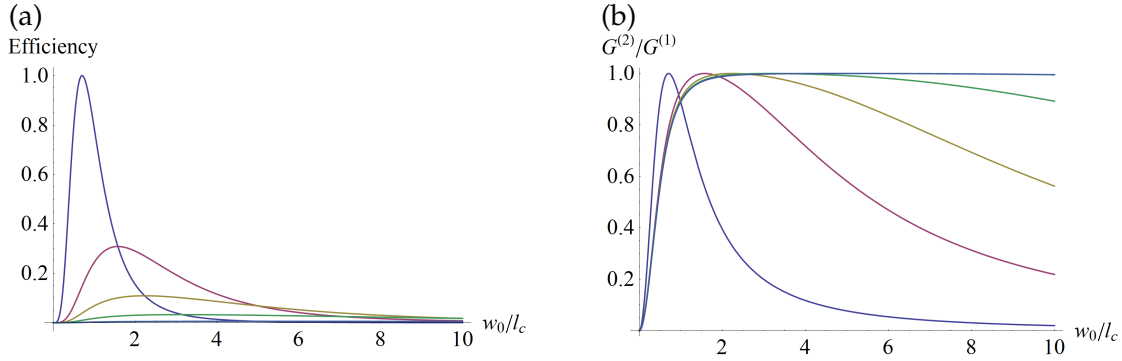


FIGURE 4.10: Double-Gaussian model for two-photon fiber coupling. (a): Two-photon coupling efficiency in dependence of the detection waist w_0 relative to correlation length l_c . Different pump waists $w_p/l_c = 1, 5, 10, 20, 50$ in decreasing order of efficiency, are used. (b): The ratio of single to coincidence counts in dependence of w_0/l_c . The same pump waists are used again.

with the relative frequency $\Omega := \omega - \omega_c$ and central emission ω_c as shown in Sec. 3.1.1. For this state,

$$\hat{M}^{(+)}(\Omega) |\Psi\rangle = 2 \int d^2\mathbf{q} E_M^{(-)}(\mathbf{q}, \Omega) \Lambda(\mathbf{q}, \Omega) a^\dagger(-\mathbf{q}, -\Omega) |0\rangle.$$

For a wave function $\Lambda(\mathbf{q}, \Omega)$ which is nearly constant over the \mathbf{q} acceptance of detection mode $E_M^{(+)}(\mathbf{q}, \Omega)$, the single photon state reduces to

$$\hat{M}^{(+)}(\Omega) |\Psi\rangle = 2\Lambda(\bar{\mathbf{q}}, \Omega) \int d^2\mathbf{q} E_M^{(-)}(\mathbf{q}, \Omega) a^\dagger(-\mathbf{q}, -\Omega) |0\rangle.$$

Therefore, the photon is projected into the complex conjugated and 180° rotated detection mode. This corresponds in the interpretation of the Klyshko advanced-wave picture to a mirror-like reflection of the two emitted photon modes from the flat plane wave pump [77].

In order to couple this second photon into the same mode, the two-photon detection probability

$$G_M^{(2)}(\Omega, -\Omega) = \|\hat{M}^{(+)}(-\Omega) \hat{M}^{(+)}(\Omega) |\Psi\rangle\|^2 = \left| 2\Lambda(\bar{\mathbf{q}}, \Omega) \int d^2\mathbf{q} E_M^{(-)}(-\mathbf{q}, -\Omega) E_M^{(-)}(\mathbf{q}, \Omega) \right|^2$$

is to be maximized. For Gaussian beam given above, this integral is maximal for a vanishing free propagation term and therefore the Gaussian beam waist position $z_0 = 0$ at the central plane of the crystal. Furthermore, the detection mode needs to be well aligned to the optical axis along $\mathbf{q} = 0$ defined by the pump beam: The rotation property $\mathbf{q} \rightarrow -\mathbf{q}$ reduces the overlap integral for non-symmetric $E_M^{(-)}$.

Analytical SPDC Coupling Model

A more general analysis without the assumption of a plane wave pump is possible. For Gaussian beam pumped SPDC in a narrow bandwidth around the central emission wavelength, the spatial two-photon state can be well approximated by a double-Gaussian wave function

$$\Lambda(\mathbf{q}_s, \mathbf{q}_i) = \exp\left(-\frac{(\mathbf{q}_s + \mathbf{q}_i)^2 w_p^2}{4} - \frac{(\mathbf{q}_s - \mathbf{q}_i)^2 l_c^2}{4}\right)$$

with the pump beam waist radius w_p and transverse correlation length l_c of the photon pairs [78]. The latter is mainly determined by the SPDC crystal length. For a Gaussian detection mode of waist radius w_0 , single and coincidence count rates can be calculated with the above defined correlation functions. Fig. 4.10(a) shows the two-photon coupling efficiency which is fully characterized by the ratios w_0/l_c and w_p/l_c . Optimal efficiency is gained for $w_0 = l_c = w_p$, i.e. for vanishing spatial entanglement or, equivalently, single spatial mode emission. In a concrete implementation with two detectors, the ratio of single to coincidence events is of importance. While a strong coincidence signal is beneficial, at the same time a low background of uncorrelated single events is desirable for low accidental rate and thereby good statistics. Fig. 4.10(b) shows this ratio for the same parameter range. The point of optimal two-photon coupling efficiency shows here strong sensitivity to w_0 . It has to be accurately set to the correlation length which is to be determined. Choosing a larger pump beam waist allows for more robust ratio nearly independent of the correlation length.

In conclusion, for an insensitive high singles to coincidences ratio, the pump beam waist w_p , correlation length l_c and detection mode waist w_0 should satisfy

$$l_c < w_0 < w_p.$$

This motivates the use of collimated pump beams with large radii where the conclusions from the discussion above with the plane wave pump assumption apply. A drawback of large pump waists is the sensitivity of the coincidence rate on detection mode tilt, see the rotation/mirror property of plane waves pumps discussed above. In contrast to the narrow-band analysis done here, broad spectrum coupling of SPDC is investigated in [33] where the optimization is not towards alignment sensitivity or singles to coincidences ratios but the absolute coincidence rate and thereby arrive at different conclusions.

4.3.2 Two-Photon Artifact in Intensity Measurements

For single mode coupled detection, the intensity measurement is described by $G^{(1)} = \langle \hat{n} \rangle$ with the photon number operator $\hat{n} = M^{(-)} M^{(+)}$, see also Sec. 2.2. For multiple photon simultaneously incident, an analog photodiode is able to generate the corresponding proportional signal and is therefore accurately modeled by $G^{(1)}$. A single photon counter (SPC) is blind to a second photon arriving within the detectors dead-time. SPDC photon pairs with a correlation time around 100 fs are not resolved by such a device. The detector therefore generates the same signal for an incident one- or two-photon state.

That means that the photon number operator \hat{n} does not correspond to the measurement a SPC is performing. One can construct the operator

$$\hat{n}' := \frac{3}{2} \hat{n} - \frac{1}{2} \hat{n}^2$$

which satisfies for the photon number (Fock) states $|n\rangle$: $\hat{n}' |0\rangle = 0$, $\hat{n}' |1\rangle = 1 |1\rangle$ and $\hat{n}' |2\rangle = 1 |2\rangle$. Hence, this new operator's eigenvalues correspond to the SPC output behavior for up to two-photon states.

We can conclude, that the detection rate of a SPC for maximally two-photon states is given by $R^{(1)} = \langle \hat{n}' \rangle$. Therefore, the measurement shows a contribution \hat{n}^2 which would otherwise only be measured in a second-order correlation measurement.

Chapter 5

Test and Characterization of Detector Arrays

Any quantum imaging scheme relies not only on the possibility to generate but also to detect quantum states of light. The relevant features are expected in temporal and spatial correlations of the photons. Therefore, it is of highest importance to be able to detect these efficiently and adequately process the detector data. While different camera technologies based on CCD or CMOS exist for the measurement of temporally correlated photons, their bottleneck are the restriction to low photon fluxes and their low frame rates for data read out. Furthermore, they are rather complex technical devices. Potential improvements in measurement time, as well as the need for less expensive and simpler devices in possible applications are the main driving forces for introduction of a new sensor technology in quantum imaging.

Fondazione Bruno Kessler (FBK), a collaboration partner within the SuperTwin project, is specialized in the development of single-photon sensitive detector pixel arrays with high temporal resolution. In contrast to the above mentioned devices, every pixel provides the temporal information for every detection event individually and allows for more general temporal correlation measurements. Their very high frame rate surpass the mentioned camera solution by several magnitudes. Manufactured in a integrated circuit in CMOS technology, they become inexpensive in production of larger units. Two detector arrays, SPADnet-I and the newly, specifically for quantum imaging experiments developed SuperEllen, are here presented, tested and characterized in an exemplary experiment using different sources.

Key sensor characteristic for a quantum imaging experiments are the following: Photon detection efficiency is given by the used sensor technology's detection probability and the realized fill-factor, i.e. the percentage of light sensitive area which is reduced due to the data processings electronics and clocks. The measurement duty-cycle, the percentage of time during which the detector is able to measure, is limited by the amount of data than can be transmitted to a computer. The dark count rate, false detection events are due to thermal noise and imperfect pixels. And finally crosstalk, i.e. spurious events triggered by the detection event of an adjacent detector pixel. These figures strongly influence the possible advantage over existing measurement solutions. They are discussed in the following and determined for the sensors.

The theoretical results of Ch. 2 for correlation function measurements are implemented for the two detectors. Spatial correlations are measured for the two-photon source, the four-photon source, and the pseudo-thermal light introduced in Ch. 3. Due to these well known sources, given by well established theoretical models and our prior measurements using standard detectors, the acquired measurement results allow the characterization of the detectors arrays in the following.

5.1 SPADnet-I Sensor

This section consists of the publication [43] in Optics Express of 2016. It introduces the SPADnet-I detector array, formerly developed for medical applications by FBK, and shows its ability to measure a spatial second-order correlation function of temporally correlated photon pairs. Experiences and results of this work went into the specification for the development of the next generation sensor SuperEllen which is specifically designed for quantum imaging experiments.

Coincidence detection of spatially correlated photon pairs with a monolithic time-resolving detector array

Manuel Unternährer,¹ Bänz Bessire,¹
Leonardo Gasparini,² David Stoppa,² and André Stefanov¹

¹ *Institute of Applied Physics, University of Bern, 3012 Bern, Switzerland*

² *Fondazione Bruno Kessler FBK, 38122 Trento, Italy*

Abstract. We demonstrate coincidence measurements of spatially entangled photons by means of a multi-pixel based detection array. The sensor, originally developed for positron emission tomography applications, is a fully digital 8×16 silicon photomultiplier array allowing not only photon counting but also per-pixel time stamping of the arrived photons with an effective resolution of 265 ps. Together with a frame rate of 500 kfps, this property exceeds the capabilities of conventional charge-coupled device cameras which have become of growing interest for the detection of transversely correlated photon pairs. The sensor is used to measure a second-order correlation function for various non-collinear configurations of entangled photons generated by spontaneous parametric down-conversion. The experimental results are compared to theory.

5.1.1 Introduction

The non-linear interaction of spontaneous parametric down-conversion (SPDC) has become a pervasive process to obtain spatially entangled two-photon states used in experiments addressing fundamental properties of quantum mechanics as well as practical applications [79]. Double-slit induced interference patterns using transversely entangled photons were studied in [80–83]. Continuous variable entanglement in the spatial degrees of freedom of the photon pairs was demonstrated in [28, 29, 84, 85] and transverse entanglement in ghost imaging has been shown to create a spatially resolved image of an object carried by a photon which did not interact with the object itself [86–89]. Finally, due to their inherent high-dimensionality, the transverse degrees of photons are also a primary resource to perform quantum information tasks. Entangled d -dimensional qudit states were implemented using transverse spatial correlations [90], in a discrete set of orbital angular momentum modes in [91–95] or in the intensity profile of Hermite- or Laguerre-Gauss modes [96–98]. Transverse correlation based protocols for quantum key distribution and teleportation were realized in [99] and proposed in [100].

By doing so, the detection of transverse photon correlations has been subjected to change in the last few years. Past experiments resolved these correlations by scanning apertures in front of single photon detectors while measuring a position dependent correlation function. Such detection schemes were deployed from the very first experiment investigating the spatio-temporal properties of SPDC photons [101], to the concept of ghost imaging [102] and to the early detection of Einstein-Podolsky-Rosen (EPR) correlations in the transverse position and momentum of the entangled photons [15].

However, to overcome the time consuming scanning process, parallel detection by multi-pixel arrays has become the preferred method to record coincidences of spatially entangled photons. Thereby, as conventional charge-coupled device cameras (CCDs) cannot work in the photon-counting regime, mainly due to readout-noise, and are not capable of sub-nanosecond time resolution, optical and electrical amplification schemes are used. In both of these systems, time resolution for coincidence detection is determined by the shutter/gating time or pulsing of the light source. Electrical amplification is implemented by electron-multiplying CCDs (EMCCDs) where an amplifier stage, using avalanche diodes, enhances the collected photoelectrons before the output amplification and analog-to-digital conversion. The accompanying drawbacks are the costly cooling needed and the large gating time window of the order of microseconds [27]. Because of the latter, low SPDC fluxes were used to investigate spatial correlations [27], photon statistics [26] and EPR-type entanglement [28, 29] by means of EMCCDs. Further, an absolute calibration of an EMCCD was performed in [30] using spatially entangled photon states. The optical amplification approach uses an image intensifier, consisting of a photocathode, a multi-channel plate and a phosphor screen, in front of a CCD. By reversing the voltage on the photocathode, intensifiers can be gated for sub-nanosecond time windows and therefore are not relying on low fluxes or pulsed sources. Such intensified charge-coupled devices were used to study spatial correlations in SPDC [103, 104], spatial entanglement [105, 106] and ghost imaging [107, 108].

A different type of sensor array is used in [109]. This hybrid detector is a CMOS integrated circuit developed for electron detection in particle physics and is used in combination with a photomultiplier. It exhibits a high spatial resolution given by 256×256 pixels which stores the time of the first detection event in a frame with a resolution of 10 ns. Coincidence measurements with SPDC light allowed to determine its detection efficiency. Further, a monolithic array of single-photon avalanche diodes (SPADs) based on CMOS technology is used in [110] to spatially resolve second-order intensity correlations in order to measure temporal correlation functions of classical light. Recently, several other SPAD-based CMOS sensors have been reported for time-resolved single-photon applications such as: fluorescence lifetime imaging [111], time-resolved fluorescence spectroscopy [112] or 3D time-of-flight imaging [113, 114]. These SPAD-based sensors are good potential candidates for coincidence detection of spatially correlated photon pairs, however, they suffer from very low fill factors [111, 113], time-coincidence detection capability longer than 0.6 ns [111–113], acquisition frame rates below 160 kHz [111–114], limited spatial resolution of the 2D pixel array arrangement [111, 112]. The state-of-the-art in terms of spatial resolution for a SPAD-based sensor is represented by [115] that reports a QVGA $8\text{-}\mu\text{m}$ pixel pitch with 26.8% fill factor, however its time-resolving performance is in the order of nanoseconds and not fully reported yet while the sensor frame rate is of 16 kfps.

In this work, we demonstrate coincidence detection of spatially correlated photon pairs by means of the SPADnet-I sensor, a 8×16 pixel single photon detector based on CMOS-technology [116]. SPADnet-I converts the SPAD signal from the analog to the digital domain at pixel level, thus avoiding spurious correlations due to inductive wire coupling. The SPADnet-I pixels are individually equipped with time-to-digital converters (TDCs). This allows for per-pixel timestamping of the detected photons with 265 ps resolution. Furthermore, the detector frame rate of 500 kfps outperforms conventional CCD based camera systems by at least three orders of magnitude and surpasses the frame rates of the aforementioned SPAD-based CMOS sensors in [111–115]. The here presented fill factor of 42.6% moreover exceeds the fill factors presented in [110, 111, 113, 115]. By means of non-classical light states generated by continuous wave SPDC we demonstrate the ability of the here presented sensor to measure a second-order correlation function for various non-collinear propagation modes of the photons. Thereby, we compare the experimental

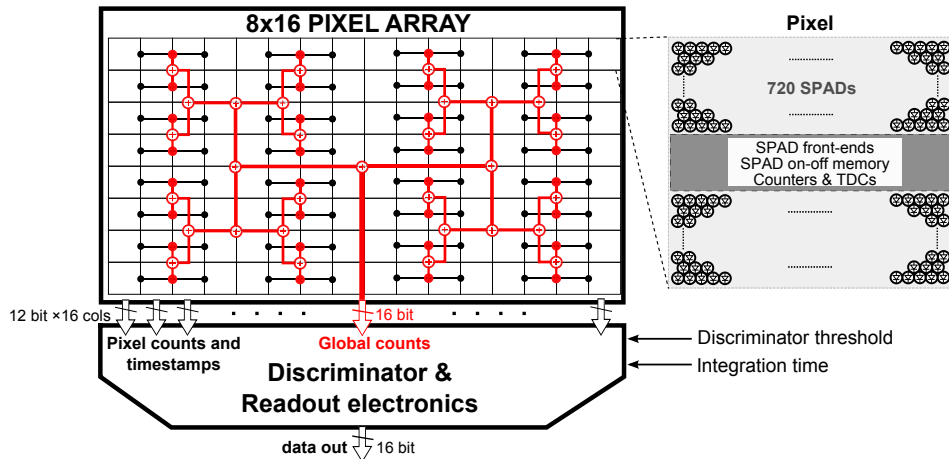


FIGURE 5.1: Architecture of the SPADnet-I sensor. It includes an 8×16 array of pixels, each including 720 SPADs, photon counters and TDCs. A tree of adders is distributed across the array to calculate the number of triggering SPADs at 100 MHz. Additional logic units are present at the periphery of the array for event discrimination and data readout. Operations are synchronous with a global clock.

results to theoretical predictions.

5.1.2 SPADnet-I sensor

SPADnet-I is a fully digital silicon photonic device based on SPAD arrays implemented in a 130 nm CMOS technology. It consists of an 8×16 array of pixels of $610.5 \times 571.2 \mu\text{m}^2$ area, for a total size of $9.85 \times 5.45 \text{ mm}^2$. Each pixel contains 720 SPADs of circular shape with a diameter of $16.87 \mu\text{m}$, the electronics required to count photons and two 12-bit TDCs each having a nominal time resolution of 65 ps. SPAD detection time jitter as well as electronic jitter reduces the effective resolution to 265 ps. The SPADs can be individually enabled and disabled due to a dedicated programmable 1-bit memory cell. This is typically done for those exhibiting a high dark count rate (DCR), i.e. a high rate of avalanche events induced by thermal generation or tunnelling rather than photon detection. A photon detection efficiency (PDE) of 19% is achieved at the design wavelength of 450 nm, whereas at the wavelength of 810 nm used in this work a PDE of 1.1% is reported [116].

The sensor is synchronous with a global clock signal that can be operated at up to 100 MHz. For every clock bin, each pixel generates a photon count (number of the SPADs triggered in the current bin) and one photon timestamp of the first photon detected in the bin. At the same rate, a distributed network of adders computes the number of photons detected globally. Fig. 5.1 shows the architecture of the chip.

SPADnet-I has been specifically designed for gamma ray monitoring in positron emission tomography (PET) applications and includes additional logic for this purpose [116]. In a PET system, sensors are coupled to crystal scintillators that convert gamma photons into bursts of visible photons. The capability of recording the photon arrival time with a relatively high spatial resolution (with respect to analog silicon photo-multipliers), in conjunction with a high fill factor (with respect to other CMOS SPAD arrays with per-pixel time-stamping capabilities) of 42.6% makes SPADnet-I suitable for quantum optics applications. In this context, the sensor is read out using an external trigger at a fixed rate of up to 250 kHz limited by readout time, see Fig. 5.2. Every data acquisition provides for all pixels the timestamps of two consecutive clock bins. Therefore, 8×16 maps of photon timestamps (hereinafter referred to as *frames*) are generated at up to 500 kfps. A timestamp

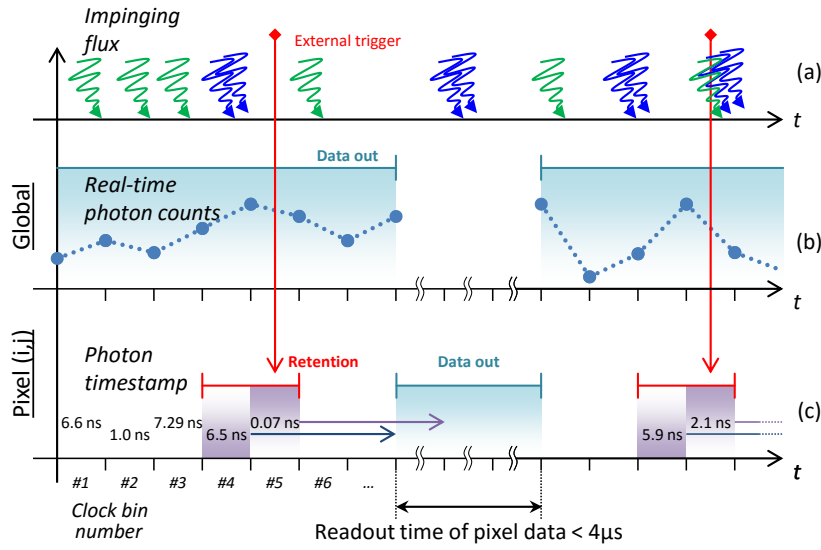


FIGURE 5.2: Timing diagram of the SPADnet-I sensor operation with example data, adapted to quantum optics experiments, looking for coincident photons (blue arrows in *a*). During standard operation (clock bins #1-#3) each pixel generates photon counts (not shown) and timestamps (*c*) at the clock rate, while the sensor streams out the number of photons globally detected (*b*, light blue area). When the external trigger is provided (vertical red arrows) each pixel retains the photon time-stamps (*c*, purple areas), the stream of global counts is interrupted and data are read out of the chip (*c*, light blue area). Then the process starts over again. The sensor is read out at the maximum frame rate limited by readout time.

is an integer TDC code which is thereby measured in TDC units of 65 ps. The measurement or exposure time of one frame is given by the period of the global clock signal.

Crosstalk events are spurious, simultaneous detection events between pixels. Since the digital signal handling at pixel level prevents electrical crosstalk, mainly photonic crosstalk is expected: light emitted in a SPAD avalanche event leads to secondary detection events in neighbouring pixels. The temporal and spatial correlation of these events will be present in the following measurements.

5.1.3 Experiment

The experimental setup is depicted in Fig. 5.3. Spatially entangled photon pairs are created by degenerated type-0 SPDC in a 12 mm long KTiOPO_4 (PPKTP) non-linear crystal (NLC) pumped by a quasi-monochromatic laser operating at $\lambda_{p,c} = 405 \text{ nm}$ with a power of 33 mW. The pump (p) beam is focused into the middle of the NLC with a beam waist of $w_p = 0.25 \text{ mm}$. The residual pump beam is afterwards filtered out by a longpass filter and a subsequent bandpass filter transmits photons at 810 nm with central frequency $\omega_c = \omega_{p,c}/2$. The corresponding biphoton state can be derived by perturbation theory under the assumption of a classical plane-wave pump field and a fixed central frequency ω_c . The first-order order correction to the vacuum state then reads

$$|\Psi\rangle = \int d^2q \Lambda(\mathbf{q}, -\mathbf{q}) |1_{\mathbf{q}}\rangle_s |1_{-\mathbf{q}}\rangle_i, \quad (5.1)$$

where $\mathbf{q} = (q_x, q_y)$ denotes the transverse momentum of the signal (s) and idler (i) photon [79]. The transverse joint momentum amplitude $\Lambda(\mathbf{q}, -\mathbf{q})$ governs the phase matching condition of the SPDC process and is, for the approximations used to derive Eq. (5.1),

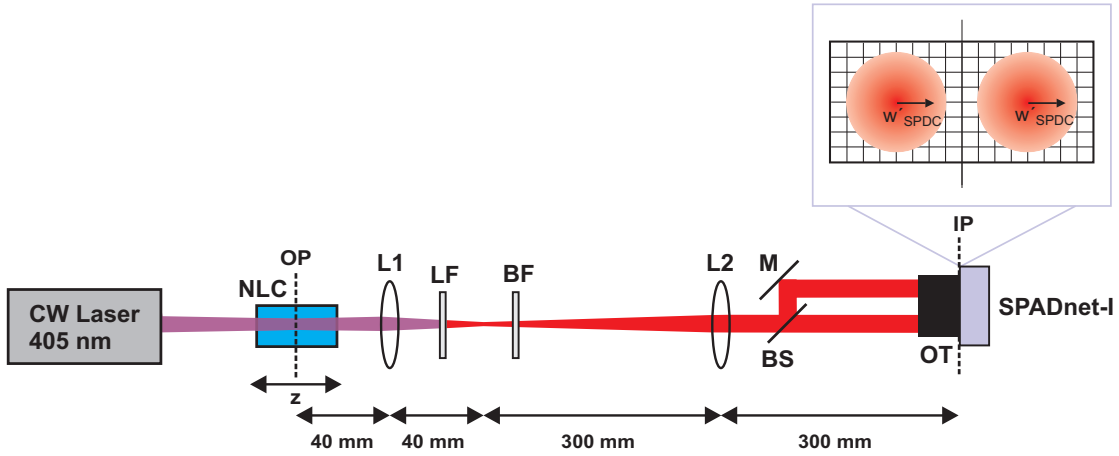


FIGURE 5.3: Experimental setup. CW continuous wave pump laser at 405 nm, NLC non-linear crystal movable in z -direction, L1 lens ($f_1 = 40$ mm), LF longpass filter to reject the residual of the pump, BF bandpass filter (810 nm, 10 nm FWHM), L2 lens ($f_2 = 300$ mm), BS 50:50 plate beam splitter, M mirror (the distance between BS and M is 2 cm), OT optically opaque tube to reduce the effect of stray light, SPADnet-I sensor. The telescope (L1, L2) provides a magnification of $m = 8$ from the object plane (OP) to the imaging plane (IP). The inset shows the arrangement of the two beams on the sensor surface. The magnified beam waist is $w'_{SPDC} \approx 2$ mm and covers about 3 pixels in radius.

explicitly given by

$$\Lambda(\mathbf{q}, -\mathbf{q}) \propto \text{sinc} \left\{ \frac{1}{2} \left[\Delta k_z(\mathbf{q}, -\mathbf{q}, \omega_c, T) + \frac{2\pi}{G} \right] L \right\} \quad (5.2)$$

with the NLC length L and poling period G . The phase mismatch $\Delta k_z(\mathbf{q}, -\mathbf{q}, \omega_c, T) = k_s(\mathbf{q}, \omega_c, T) + k_i(-\mathbf{q}, \omega_c, T) - k_p(0, 2\omega_c, T)$ includes the dispersion characteristics of the NLC through its temperature dependent Sellmeier equation [117]. The minor additional temperature dependence of Λ due to thermal length expansion of G and L is negligible in our configuration. In the experiment, the crystal temperature is stabilized to $\pm 0.01^\circ\text{C}$ and allows to modify Eq. (5.2) for collinear and non-collinear emission. Additionally, the crystal position can be varied in z -direction by means of a manually driven linear stage. We experimentally determined a poling period of $G = 3.511 \mu\text{m}$ in a separate measurement with fibre coupled detectors where the dependence of the near-field coincidence rate on the NLC temperature T was measured.

In order to better separate the effective coincidence signal from unwanted crosstalk between adjacent pixels we split the entangled photon beam into two beams which are then arranged next to each other on the detector. Additionally, this allows to detect coincidence events between photons which are spatially separated below the size of a single pixel. To image the entangled photons from the object plane to the SPADnet-I sensor such that the two adjacent beams cover a large area on the sensor without overlapping we choose a telescope system using two lenses with focal lengths $f_1 = 40$ mm and $f_2 = 300$ mm. The measured magnification factor is $m = 8$. The SPDC photon pairs are spatially distributed across the transverse pump profile and thus for their waist w_{SPDC} it holds that $w_{SPDC} \approx w_p$. Given the magnification of the used telescope, this leads to a beam waist of the entangled pairs of $w'_{SPDC} = mw_{SPDC} \approx 2$ mm at the imaging plane which coincides with the active surface of the sensor. Therefore, the magnified beam waist of the SPDC photons covers about 3 pixels in radius in each half of the sensor (Fig. 5.3). The beam

separation itself is performed by means of a 50:50 plate beam splitter and a mirror in front of the imaging plane. The length difference of 2 cm of the reflected beam defocuses the image only to a small extent and is unobservable in our measurements due to the limited spatial resolution of the sensor given by the pixel size. Additionally, the active area of the sensor is shielded with an optically opaque tube to reduce the detection of stray light. The flux of entangled photons impinging on the detector is 2.1 nW which corresponds to 8.6×10^9 ph/s. Finally, the sensor is connected to a PC via Ethernet and data gathering is performed using LabView.

Coincidence events between distant pixels are described by a second-order correlation function

$$G^{(2)}(\Delta\mathbf{q}, z) \propto \left| \int d^2q \Lambda(\mathbf{q}, -\mathbf{q}) H_s(\mathbf{q}, z) H_i(-\mathbf{q}, z) \exp(-i\mathbf{q} \Delta\mathbf{q}/m) \right|^2, \quad (5.3)$$

where $\Delta\mathbf{q} = \mathbf{q}_1 - \mathbf{q}_2 = (\Delta x, \Delta y)$ denotes the distance between the transverse positions \mathbf{q}_1 and \mathbf{q}_2 . Further, m is the magnification factor of the imaging system. The transfer function H_j , $j \in \{s, i\}$, describes an additional free space propagation of the signal (idler) photon along a distance z which is equivalent to move the crystal in $-z$ direction (Fig. 5.3). The corresponding transfer function in paraxial approximation is given by

$$H_j(\mathbf{q}, z) = \exp \left[-ikz + \frac{iz}{2k} |\mathbf{q}|^2 \right], \quad (5.4)$$

where $k = \omega_c/c$. Note that by our specific choice of coordinates, $z = 0$ mm fixes the object plane in the middle of the NLC.

5.1.4 Results

In the following measurements, the SPADnet-I clock signal is operated at 100 MHz leading to a measurement time of 10 ns per frame. The frame readout rate is set to 330 kfps. This corresponds to measurement duty cycle of $330 \text{ kHz} \times 10 \text{ ns} = 0.33\%$. If not stated otherwise, the acquired data consists of 5.4 M frames corresponding to 1.3 GB raw binary data which could be acquired in 16 seconds given the mentioned frame rate. At this data rate ($\sim 0.5 \text{ Gbit/s}$), the limited computational performance of the PC for the real time analysis prolongs the measurement to 45 seconds due to dropped and thereby lost frame data. The effective measurement time of 5.4 M frames, during which the sensor acquires time-resolved detection events, is $5.4 \text{ M} \times 10 \text{ ns} = 54 \text{ ms}$. To reduce the dark counts, 50% of the highest DCR SPADs are disabled. Crosstalk between pixels is suppressed by further turning off SPADs in the boundary region between two pixels, leaving a gap of $\sim 70 \mu\text{m}$ between them. In total, a fraction of 36% of all SPADs are used in the subsequent measurements.

Single photon detection

Figure 5.4(a) shows the spatially resolved total number of single photon detection events at maximal SPDC power. The shown maximal photon detection number of the order of 10^5 per pixel leads to a maximum of 0.02 registered events per pixel and per frame. Taking into account all pixels we measure an average of 0.56 events per frame. Figure 5.4(b) depicts a distribution of the number of detection events N per frame where it can be seen that 55% of the frames contain no event. By taking into account all intervals with $N \geq 1$ we obtain a total number of 3.07 M single photon detection events. Measuring the same

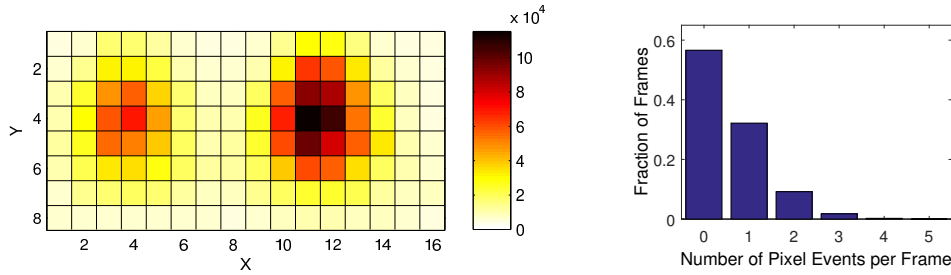


FIGURE 5.4: Single photon counting events. Panel (a) depicts the sensor pixel array with the number of detection events per pixel. A total of 3.07 M events are registered in 5.4 M frames. The intensity of the left hand beam is slightly degraded due to the non-perfect 50:50 behaviour of the beam splitter. Panel (b) shows the distribution of the total number of detection events in a frame.

number of frames without any incident light, a total of 427 k dark count events are registered. They are homogeneously distributed across all pixels. Per frame, this translates to an average of 0.08 events in total and a maximum of 0.0006 events per pixel. At the mentioned incident photon flux, the detection number corrected for dark counts, and effective acquisition time, the photon detection efficiency (PDE) is 0.57%, or 1.6% if we correct for the amount of disabled SPADs. This is slightly higher than the PDE of 1.1% at 810 nm reported by [116]. The DCR of all pixels is 7.9 Mcps.

Coincidence detection

All intervals with $N \geq 2$ in Fig. 5.4(b) are considered to evaluate coincidence events. A histogram of the time differences between all events within every frame is shown in Fig. 5.5. A coincident detection of a photon pair is expected to appear at small time differences Δt due to a coherence time of the entangled photons of about 500 fs. The histogram reveals, on top of a linear background of accidentals, a peaked signal with a FWHM of 6 TDC units which corresponds to ~ 390 ps. From pixel-to-pixel, the FWHM variation of the TDC unit of 64.56 ps is ± 1.90 ps. For the 10 ns frame interval, the largest TDC code is 155 and thus the average time uncertainty of an event is $155/2 \times 1.90$ ps ≈ 150 ps. Together with the detector timing jitter of 265 ps FWHM, this leads to the measured spread of a time difference of $(2(265 \text{ ps})^2 + 2(150 \text{ ps})^2)^{1/2} \approx 430$ ps FWHM.

The linear, triangular background originates from independent, i.e. uncorrelated, sources which are dark counts and photons from different pairs. Their detection time is uniformly distributed in the measurement window. The distribution of the time difference between two of these uncorrelated events is therefore given by the convolution of two uniform distributions, leading to the triangular shape. By linear fitting and extrapolation, the accidental events can be removed from the signal of real coincidences (Fig. 5.5, solid line). The following results are obtained with a coincidence window $\Delta t = [-4, 4]$ of 9 TDC units width and removed accidentals.

The accidental corrected signal in Fig. 5.5 contains not only photon pair coincidences but crosstalk events between neighbouring pixels as well. To experimentally confine the crosstalk and to demonstrate temporal resolution, we increase the optical path delay between the right and the left beam incident on the sensor from 20 mm to 300 mm. The photon pair detection is therefore expected at $\Delta t = 15$ TDC units. The effective temporal resolution limited by jitter and TDC variations together with still a high amount of crosstalk events at this Δt leads to a masked coincidence signal (Fig. 5.6, blue line). Suppressing crosstalk by only considering events of pixels in the left half with those on the right half of

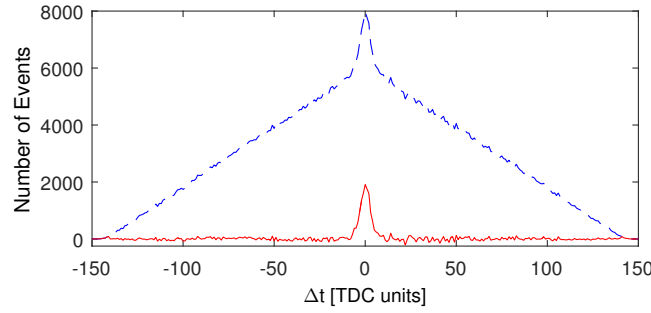


FIGURE 5.5: Histogram of the time difference Δt between all events within every frame. Photon pair detections are expected at $\Delta t = 0$ TDC units. The raw data (dashed line) shows a linear background of accidental events which are also present in a coincidence window around $\Delta t = 0$ TDC units. These accidental events are removed by linear fitting and extrapolation (solid line). 1 TDC unit ≈ 65 ps.

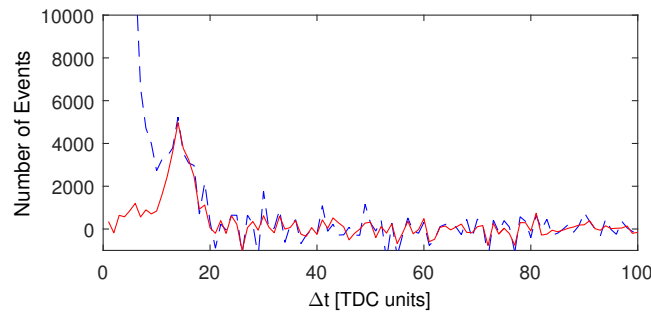


FIGURE 5.6: Histogram of the time difference Δt between all events within each frame. One beam incident on the sensor is delayed by 300 mm and photon pair detections are expected at $\Delta t = 15$ TDC units. Coincidences between all pixels are considered in the dashed line where the crosstalk events at $\Delta t = 0$ TDC units rise to 4×10^4 events. In order to suppress these, only coincidences between the left half with the right half of the sensor array are taken into account in the solid line. Accidentals are removed in both graphs as shown in Fig. 5.5 and 54 M frames are evaluated.

the sensor (Fig. 5.6, red), a peak at $\Delta t = 13$ TDC units with 5 units FWHM is visible. The path delay of 300 mm corresponding to 1 ns delay would lead to a TDC code difference of 15 units. A systematic difference of the TDC unit between pixels on the left half of the sensor with pixels on the right half explains this discrepancy.

Spatial correlations

We now spatially resolve the coincidence events in relative distances between two pixels using the difference coordinates $(\Delta x, \Delta y)$ in units of pixels (Fig. 5.7(a)). The experimental configuration is such that $z = 0$ mm, i.e. the object plane coincides with the middle of the NLC, and the phase matching temperature is kept fix at $T = 25^\circ\text{C}$. For $\Delta x = 8$ pixels, which corresponds to the horizontal distance between the two beams, a narrow pixel correlation is observed. By means of the aforementioned values for z and T , the second-order correlation function of Eq. (5.3) consistently shows a photon pair correlation width smaller than one pixel (Fig. 5.7(b)). A total of 2,372 events are registered in this region. This comes close to the theoretical value of 3,770 events which would be expected at the above measured PDE, the beam splitter ratio and the given photon flux. The discrepancy can be explained by losses in the optical setup which results in single photons without its partner.

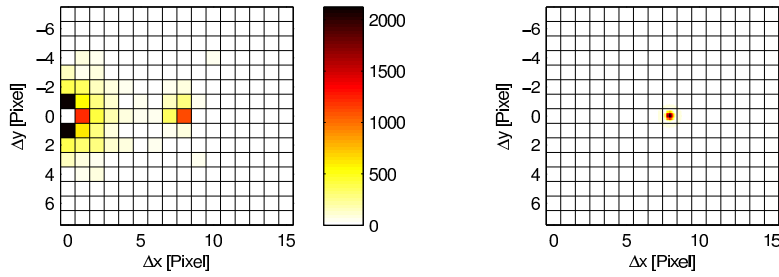


FIGURE 5.7: Second-order correlation function $G^{(2)}(\Delta\mathbf{q}, 0)$ of coincidence events in measurement (a) and theory (b). The NLC temperature is 25°C , a coincidence window of 9 TDC units is used and accidentals are removed.

The region centered at $\Delta x = 0$ pixels comprises the coincidence events within each beam individually and includes a total of 11,176 events. The photon pair correlation width of less than one pixel measured at $\Delta x = 8$ pixels suggests, that photon pairs not separated by the beam splitter will be incident on the same pixel and therefore rarely lead to coincidence events between adjacent pixels. Hence, the central region is expected to show considerably less events, especially at a separation of $\Delta x \geq 2$. Therefore, most of the coincidence events have to be attributed to crosstalk between neighbouring pixels. A measurement with uncorrelated, classical light of similar power showed a comparable amount of events in this region (7,880 counts) and supports this conclusion.

In order to suppress crosstalk events, the same procedure as in Section 5.1.4 is applied. A path delay of 300 mm between the left and the right beam temporally separates crosstalk and photon pair detection events. The second-order correlation function in Fig. 5.8(a) shows strongly suppressed events around $\Delta x = 0$ in comparison to the measurement in Fig. 5.7(a). The path delay leads to a defocussing and thereby enlarges the correlation function which results in a slightly broader correlation peak.

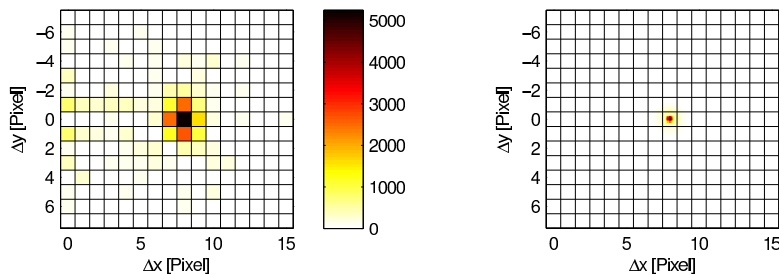


FIGURE 5.8: Second-order correlation function $G^{(2)}(\Delta\mathbf{q}, 0)$ of events with $\Delta t = 13 \pm 4$ TDC units in measurement (a) and theory (b). One beam is delayed by 300 mm. Due to temporal separation of the coincidence signal and crosstalk, the latter expected around $\Delta x = 0$ is suppressed (Fig. 5.7(a)). The NLC temperature is 25°C , accidentals are removed and 54 M frames are evaluated.

The second-order correlation function shown in Fig. 5.7(b) has a width of approximately 0.3 mm at FWHM which is not resolvable by a pixel of 0.6 mm size. However, according to Eq. (5.3), the correlation function starts to broaden while moving the central plane of the NLC out of focus using the z degree of freedom shown in Fig. 5.3. In addition, lowering the crystal temperature T allows to modify the SPDC phase matching from collinear to non-collinear emission of photon pairs which has a similar effect on the correlation function as changing the crystal's z -position. By using 54 M frames for better statistics (corresponding to 540 ms effective measurement time acquired in 165 s), Fig. 5.9

and Fig. 5.10 show experimental results in comparison with Eq. (5.3) for different settings of z and T . As above, crosstalk is minimized by considering only coincident events of the left half with the right half of the sensor. In order to measure the correlation function in a plane, no path difference is introduced between the left and the right beam to temporally separate crosstalk as before. Because of that, crosstalk of the same magnitude is present in all measurements in the region of small Δx . Its relative strength increases the weaker the signal density gets from the first to the third column.

5.1.5 Conclusions

In this work, we demonstrate a high signal-to-noise ratio measurement of the spatial second-order correlation function of a high flux SPDC light source by means of a monolithic, fully digital and high temporal resolution SPAD pixel-array. The data acquisition time of the here presented measurements is below 3 minutes. Therefore, despite the low measurement duty cycle of 0.33%, the simultaneous measurement on all pixels outweighs conventional scanning experiments in terms of mechanical complexity and in measurement time. This is even more the case for multi-photon experiments where higher photon numbers are involved. With the given 128 pixels and second-order correlation measurements, a time reduction factor of $128^2 \times 0.33\% = 54$ is realized compared to a single pixel scanning experiment with optimal duty cycle.

At a PDE of 0.57% at 810 nm and a total DCR of 7.9 Mcps over all pixels, a high rate of accidental coincidence events originating from single photons and dark count events are expected. The photon arrival time resolution of 265 ps allows to realize a small coincidence window which keeps accidentals at a minimum. The remaining accidentals can be estimated very accurately and removed in a post-processing step.

The presented measurement of the second-order correlation function is currently only possible by splitting the photon pair and imaging it onto two distant parts of the sensor. Otherwise, pixel crosstalk would have superimposed and, to a large extent, masked the signal. Since the digital signal handling prevents electrical crosstalk events, the observed crosstalk, over distances of more than 100 μm , has to be mainly of photonic origin. Light emitted in SPAD avalanche events is reflected back by the glass surface of the chip and thereby leads to secondary detection events. Preliminary measurements with a sensor of the same type having no glass surface on top support this hypothesis.

The sensor is currently not optimized for quantum imaging experiments, neither for the used wavelength and, compared to the sensors presented in [111–115], shows a considerably high DCR. Nevertheless, it showed the potential of a planned next generation sensor where a higher pixel density, a higher PDE and a better measurement duty cycle is desirable in order to further reduce the measurement time. The latter can be achieved by a higher frame rate or, to avoid unfeasible high data rates, by a frame readout triggered by multi-pixel events. To avoid the splitting into individual photon beams in future experiments, particular efforts will be put onto the reduction of crosstalk. This will pave the way for fast, higher photon number imaging experiments and applications.

5.1.6 Addendum to Publication

The here presented results demonstrate the advantages of the technology. Its parallel detection, thanks to the pixel array, allows a considerable speedup in measurement time. Furthermore, it opens the way for the measurement of higher-order spatially correlation function in the following for a new detector. The temporal resolution does not resolve the photon correlation time, but allows a minimal coincidence window and thereby a good

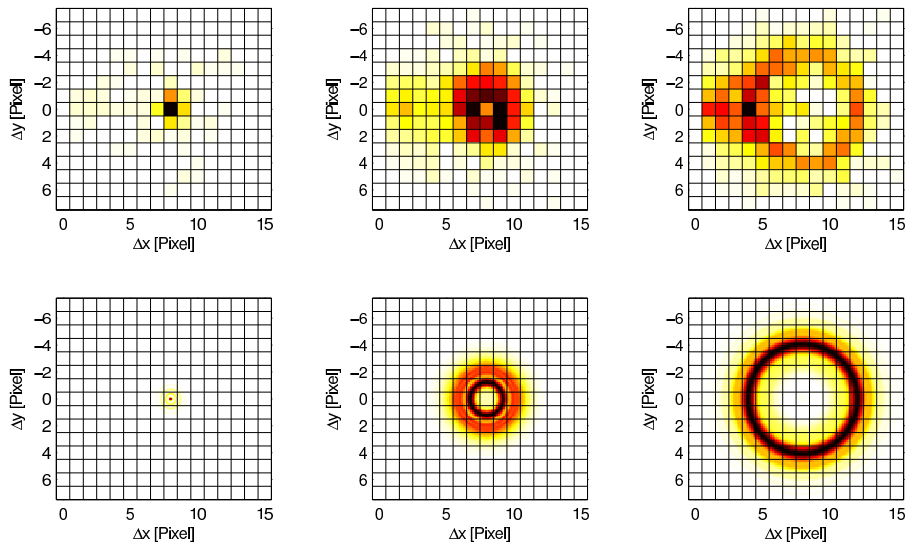


FIGURE 5.9: Measurements (upper row) and theory (lower row) of the second-order correlation function $G^{(2)}(\Delta\mathbf{q}, z)$ for different crystal positions $z = 0, 5, 10$ mm and a fixed crystal temperatures $T = 23^\circ\text{C}$. Pixel crosstalk is present at small Δx and superimposes the light's coincidence signal. Every measurement consists of 54 M frames. A coincidence window of 9 TDC units is used and accidentals are removed.

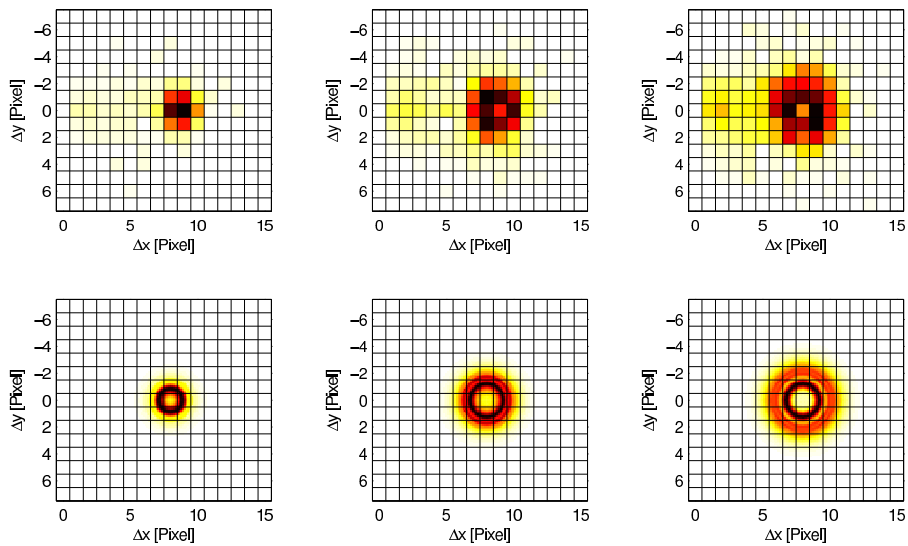


FIGURE 5.10: Measurements (upper row) and theory (lower row) of the second-order correlation function $G^{(2)}(\Delta\mathbf{q}, z)$ for fixed crystal position $z = 5$ mm and different crystal temperatures $T = 25, 24, 23^\circ\text{C}$. Pixel crosstalk is present at small Δx and superimposes the light's coincidence signal. Every measurement consists of 54 M frames. A coincidence window of 9 TDC units is used and accidentals are removed. Note that in the first two measurements, the beam distance is slightly higher due to realignment.

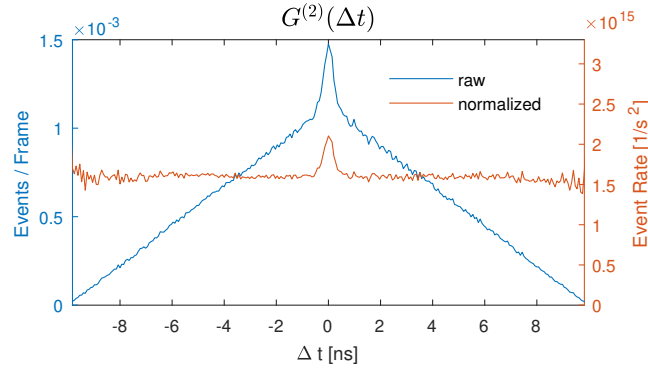


FIGURE 5.11: Histogram of the time difference Δt between all events within a frame. In contrast to the figures shown in Sec. 5.1, the normalization of the raw sensor data by the sampling space volume results in a flat background and a narrow correlation peak. Insufficient statistics (low sampling space volume) at large Δt explain the noisy regions.

rejection of uncorrelated background. Residual accidentals can be well estimated and removed thanks to the access to the full temporal correlation distribution. This is a clear advantage in comparison to gated detectors.

The theoretical results for the measurement and normalization of correlation functions, developed in Sec. 2.3, were not yet acquired at the time of the preparation of this manuscript. As seen in Fig. 5.11, the normalization of the raw detector data in Eq. (2.34) with the sampling space volume of Eq. (2.35) removes the pyramidal shape. The latter is an artifact of the finite observation window of a frame. Therefore we arrive at a proper $G^{(2)}(\Delta t)$ measurement, where only detection efficiencies, temporal and spatial resolution limit the observation.

As expected, a flat background with a peak around $\Delta t = 0$ is given for $G^{(2)}(\Delta t)$. For removal of accidental events, the above used and in Sec. 5.1.4 described method of linear fitting becomes here a fit of the constant background. Accordingly, this allows to estimate the number of uncorrelated events within the coincidence window.

5.2 SuperEllen Sensor

SuperEllen is a 32×32 pixels, time-resolving silicon photon detector based on SPAD arrays implemented in a 150 nm CMOS technology [46], see Fig. 5.12. It was developed within the SuperTwin project by FBK after the aforementioned experiments with SPADnet-I, as an intermediate development step towards the finally envisioned detector array of larger size of up to 256×256 pixels. The time resolving capability is implemented with several technologies in different sections of the same chip for the purpose of evaluation. Hereafter we will only use the sensor based on a time-to-digital converter.

This sensor has a pixels pitch of $44.67 \mu\text{m}$ and a total sensitive area of $1.4 \times 1.4 \text{ mm}^2$. Similarly to SPADnet-I in Sec. 5.1, it contains for every pixel a dedicated time-to-digital converter (TDC) which timestamps the first detection event at 205 ps resolution within a frame of exposure time of up to 50 ns. Using on-chip features for reading empty rows or frames, an observation rate of 800 kHz is achieved leading to a measurement duty-cycle of 3.6%. The photon detection efficiency (PDE) reaches 5% at 400 nm and 0.8% at 810 nm. At room temperature, the median dark count rate per pixel is below 1 kHz over the whole pixel population. Despite these type of devices exist since 2009 [118], their use in quantum optics applications were limited by low fill-factor (1-5%). Only recently it was possible to

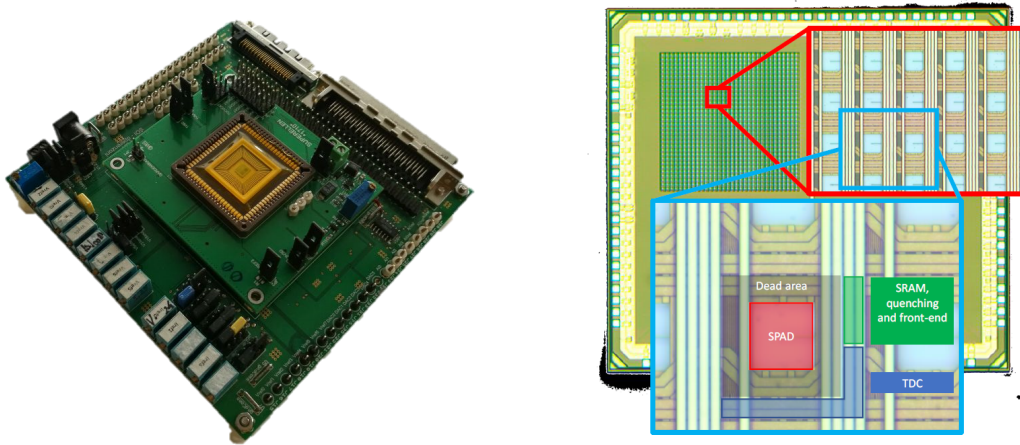


FIGURE 5.12: SuperEllen Detector. The sensor board with the chip in its center (left) and a micrograph of the chip zooming into a single pixel (right).

achieve 19.48% allowing higher detection efficiencies. The full technical publication [46] of the sensor is shown in App. D.

Many device parameters are set in soft- and hardware, among them the SPAD bias voltage. It is applied to each diode and influences the PDE and the dark count rate, as investigated below. A TDC control voltage determines the TDC clock speed and thereby the linearity of the timestamp code in comparison to actual time. The sensor is operated at room temperature of 21°C. SuperEllen acquires frames at a rate of 600 kfps and a frame exposure time of 30 ns is used.

The hardware is equipped with a sensor controller and read out board based on a FPGA. It is connected to a computer using USB 3.0 interface, where a driver implemented in C allows the integration into LabView. This software is developed by FBK and provides a continuous stream of the detected events and their timestamps. Events belonging to the same frame can therefore be represented by a 32×32 map of detection timestamps, hereafter referred to as *frames*. Therefore, the sensor provides the measured photon numbers

$$n(\boldsymbol{\rho}, t) \in \{0, 1\}, \quad \text{with } \boldsymbol{\rho} \in \{(x, y) | x, y \in \{1, \dots, 32\}\}, \quad t \in \mathbb{N},$$

at all pixel indices $\boldsymbol{\rho}$ and times t , measured in TDC units of 205 ps, within a frame. Sec. 2.3 describes how to generally process this data in order to arrive at the field intensity correlation functions. For the given time-stationary source and the concrete detector characteristic, Sec. 2.3.4 worked out the general results in this specific case. A LabView subroutine, implementing the result of Eq. (2.34), allows for real-time calculation and visualization of the second-order correlation function

$$G^{(2)}(\boldsymbol{\rho}_1, \boldsymbol{\rho}_2, \Delta t)$$

for pixel indices $\boldsymbol{\rho}$ and relative time differences $\Delta t := |t_1 - t_2|$. Optimizing the LabView acquisition for speed performance, real-time calculation and visualization of $G^{(2)}$ without reducing the sensor frame rate is possible. This allows fast and convenient optimization of the optical setup. Higher-order correlations are evaluated in a post-processing step using the saved raw event data stream as discussed below.

In the following, SuperEllen is tested in real experimental situations. First, the experiment with SPDC photon pairs already used in Sec. 5.1 is repeated for this detector. The results allow to evaluate the temporal and spatial resolution, its detection efficiency and to optimize electrical parameters. Furthermore, for approaching the SuperTwin goal of

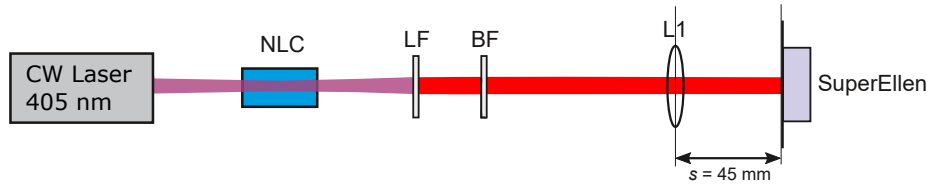


FIGURE 5.13: Experimental setup for the two-photon measurement with SuperEllen. A 30 mW CW laser pumps a non-linear crystal (NLC), the pump beam is filtered using a longpass (LF), the SPDC emission is spectrally limited with a bandpass filter (BF) centered at 810 nm and 10 nm FWHM transmission. The lens L_1 of focal length $f_{L1} = 45$ mm is used for measuring the far-field of the source.

measuring ultrafast higher-order correlations, a SPDC four-photon state is experimentally generated and validated. The test results with SuperEllen will serve as source for the specification of the development of a next generation sensor.

5.2.1 Two-Photon Detection

The experimental setup used in the following is depicted in Fig. 5.13. The two-photon source introduced in Sec. 3.1 is used: Spatially entangled photon pairs are created by degenerated type-0 SPDC in a 5 mm long KTiOPO_4 (PPKTP) non-linear crystal (NLC) pumped by a quasi-monochromatic laser operating at $\lambda_p = 405$ nm with a power of 33 mW. The pump (p) beam is focused into the NLC with a beam radius of 0.25 mm. The pump beam is afterwards filtered out by a longpass filter, a subsequent bandpass filter with 10 nm FWHM transmits photons at 810 nm with central frequency $\omega_c = \omega_p/2$. The generated biphoton state can be derived by perturbation theory under the simplified assumption of a classical plane-wave pump field and a fixed central frequency ω_c and is given in Eq. (3.11). In this experiment we use an NLC of length $L = 5$ mm at a temperature $T = 25.5^\circ\text{C}$ set for phase-matching the collinear, frequency-degenerate emission, see also Sec. 3.1. A total power of 0.45 nW is emitted and incident on the sensor. Using a lens of focal length $f_{L1} = 45$ mm and a lens to detector distance $s = f_{L1}$ allows to measure the far-field correlation of the SPDC source. As derived in Eq. (3.12), this is given by the second-order correlation function

$$G^{(2)}(\rho_1, \rho_2) \propto \delta(q_1 + q_2) |\Lambda(q_1)|^2, \quad q_i = \frac{k}{f_{L1}} \rho_i, \quad i \in \{1, 2\}, \quad (5.5)$$

with the wave vector $k = \omega_c/c$ and the biphoton wave function $\Lambda(q_1, -q_1)$ given in Eq. (3.11). Perfect anti-correlation in position is given in plane-wave approximation, while the circularly symmetric wave function limits the emission radius through the SPDC phase-matching. The emitted and transmitted bandwidth through the bandpass filter (BF) allows a pair correlation time below 1 ps and cannot be resolved by the detector – perfect temporal coincidence of the pairs can be assumed. This temporal degree of freedom can be shown to factorize with the spatial correlations of the biphoton state for the given generation parameters and validates the simplification of monochromatic emission and the treatment of the spatial degrees of freedom only, see also discussion in Sec. 3.1.1.

Eq. (5.5) exhibits only anti-correlated photon detection events, or equally a fixed centroid position whose center is defined by the optical axis of the pump beam. Spatial correlations in other regions of the $G^{(2)}$ space are not of photonic origin and can be considered as detector artifacts, e.g. crosstalk. This allows for good discrimination between detected signal and spurious detector events biasing the measurement data.

The SuperEllen sensors uses in the following a TDC control voltage of 2.89 V which determines the clock speed of the TDCs. While for an ideal TDC the generated time codes increase linearly with the measured time interval, deviations can occur in real implementations. By using uncorrelated light, every fourth TDC code appears in a measured occurrence histogram strongly underrepresented and therefore corresponds to a much shorter time interval. This pattern can be explained by the TDC architecture, see also App. D. The removal of every fourth code is applied in the following and results in a smooth, uniform TDC code distribution representing equal time intervals. A SPAD bias voltage of 21.8 V (at 17.8 V threshold) is used if not otherwise mentioned.

Measurement

For this measurement, we acquire 26 million frames (MFrames). The intensity measurement $G^{(1)}$ is shown in Fig. 5.14(a). Detection events are measured at a rate of $R_{\text{tot}} = 0.64$ events/frame. The circular biphoton beam is weakly visible under the pattern of pixels with high dark count rate. Neglecting the spatial information of detection events by evaluating

$$G^{(2)}(\Delta t) = \frac{1}{2} \sum_{\rho_1, \rho_2} G^{(2)}(\rho_1, \rho_2, \Delta t), \quad (5.6)$$

the temporal correlation is shown in Fig. 5.14(b). With the given observation windows of 30 ns and the maximal Δt value, a TDC unit time step of 245 ps is determined. The raw data (dotted line) is a histogram of event occurrences, while the normalized plot represents $G^{(2)}$ in proper physical units without the detector artifact of a linear decreasing trend due to the finite observation window, see Sec. 5.1.6 and Sec. 2.3. The background of accidentals A can be estimated by averaging $G^{(2)}(\Delta t)$ over the region $\Delta t = 4$ to 20 ns. Removing A from the signal, only temporally correlated events survive (blue line). A correlation feature of approx. 1 ns width can be observed.

A coincidence window of $T_c = 1$ ns corresponding to 4 TDC units is used for selection of temporally correlated events only. With the estimated accidental rate $A(\rho_1, \rho_2)$ for every pixel pair, the accidental corrected spatial correlation function

$$G^{(2)}(\rho_1, \rho_2) := \sum_{\Delta t=0}^{T_c} G^{(2)}(\rho_1, \rho_2, \Delta t) - A(\rho_1, \rho_2) \quad (5.7)$$

and is depicted in Fig. 5.15. A linear pixel index $p = 1, \dots, 1024$ is used for visualization of this otherwise 4-D object. Two features are prominent: Correlation between adjacent pixels are shown on the diagonal and have to be attributed to pixel crosstalk, see below. The anti-diagonal shows correlations between pixel pairs with fixed centroid position and is therefore the expected photonic signal. Using a comparison with the theoretical variance of the signal, the regular rectangular background pattern is shown to consist mainly of statistical noise due to accidentals. The spatial correlation function $G^{(2)}(\rho_1, \rho_2)$ is used in the following for further analysis.

Photonic Signal and Detection Efficiency

The biphoton light signal can be made more directly accessible by observing the distribution of the centroid position $\rho_+ := (\rho_1 + \rho_2)/2$ of detected events. From the measurement, we acquire this statistic by calculating

$$G^{(2)}(\rho_+) := \frac{1}{2} \sum_{\rho_1, \rho_2} [\rho_1 + \rho_2 = 2\rho_+] G^{(2)}(\rho_1, \rho_2)$$

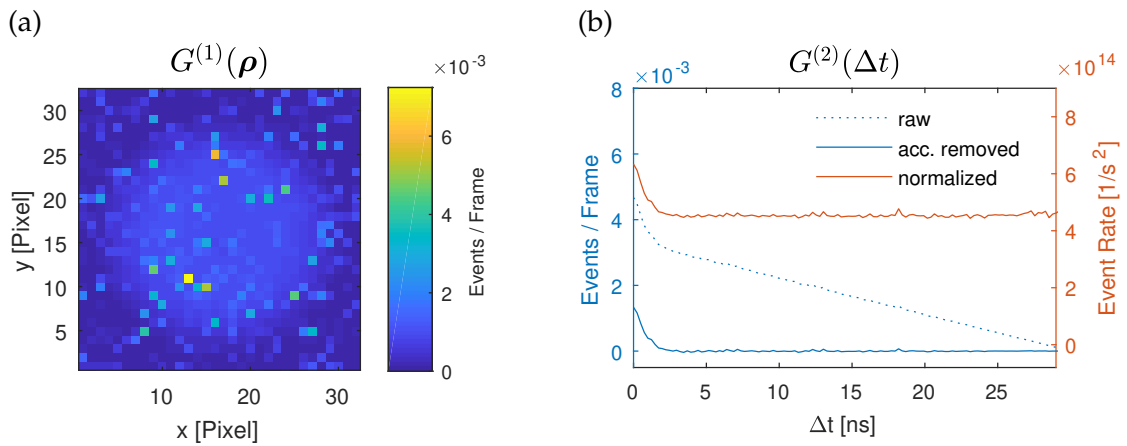


FIGURE 5.14: In the intensity measurement $G^{(1)}(\rho)$ (a), pixels with high dark count rate appear as noise on top of the faint, circular biphoton beam. The temporal second-order correlation $G^{(2)}(\Delta t)$ (b) is accumulated over all pixels. The detection event counts are shown in raw form, after removal of uncorrelated accidentals and with normalization.

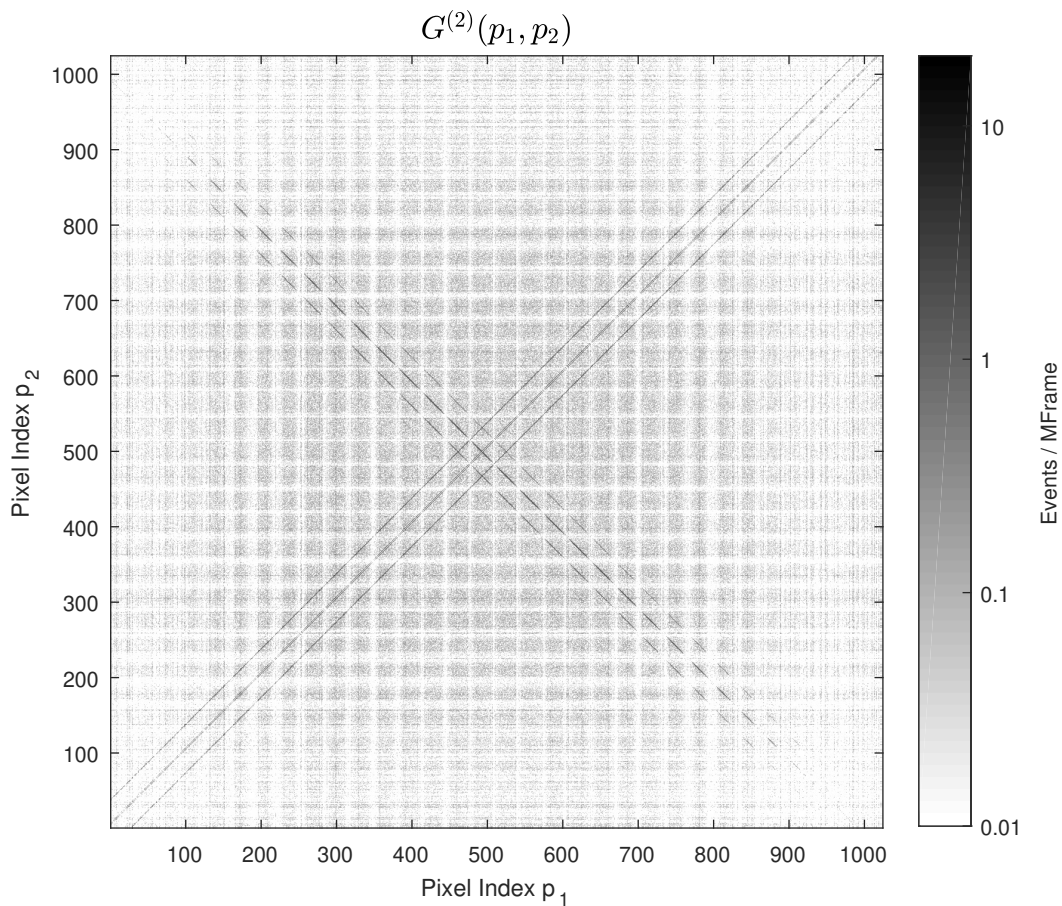


FIGURE 5.15: Full spatial correlation function $G^{(2)}(\rho_1, \rho_2)$ between every pixel pair corrected for accidentals and in logarithmic scale. The $32 \times 32 = 1024$ pixels are addressed by their linear index $p = 1, \dots, 1024$. The diagonal and off-diagonal at 32 pixels displacement are correlations of pixels with their horizontally and vertically adjacent neighbors. The anti-diagonal signal is the expected biphoton correlation. Statistical noise from subtracted accidental events remains as background.

using the Iverson bracket notation for sampling: $[x] = 1$ if x is true, $[x] = 0$ otherwise. The prefactor compensates for the fact that the interchange of the arguments in $G^{(2)}(\rho_1, \rho_2)$ is physically indistinguishable and constitutes the same event, which would have been counted twice in the summation. The result is shown in Fig. 5.16(a). A prominent, almost only one pixel spanning centroid peak is visible. A total of

$$R_{\text{Signal}} = 0.83 \times 10^{-3} \text{ Events/Frame}$$

are registered with a centroid within a 3×3 pixel region. By considering the anti-correlated pairs $G^{(2)}(\rho, -\rho)$ where $-\rho$ denotes the anti-correlated partner of ρ , pixels contributing to the signal can be visualized in Fig. 5.16(b). This shows the extension of the $\Lambda(\rho)$ function of Eq. (5.5). For reference, Fig. 5.16(c) and (d) show a measurement at a detuned NLC Temperature of 23°C which exhibits non-collinear emission. Note, that these two-photon distributions do not have to be visible in the intensity measurement. In this case, a potentially present single-photon contribution, or background like dark counts as in Fig. 5.14(a), could mask the two-photon term.

With the given incident power of photon pairs and assuming no other losses in the optical setup, a photon flux of $\Phi = 1.8 \times 10^9$ ph/s is given. In the 30 ns time of the exposure of a frame, we expect therefore 54 photons or 27 pairs incident. As the biphoton detection rate depends on the PDE η and flux Φ with $R_{\text{Signal}} = \eta^2 \Phi / 2$, using the mentioned total number of detected pair events, the photon detection efficiency

$$\eta = 0.56 \text{ \%}.$$

This value comes close to the PDE of 0.8% measured with classical light in device characterization experiments performed by FBK.

A comparison of the measurement histogram $G^{(2)}(\rho_1, \rho_2, \Delta t)$ with and without accidental subtraction yields the number of accidentals in the chosen coincidence window. Here we measure

$$R_{\text{Acc}} = 14.8 \times 10^{-3} \text{ Events/Frame}$$

summed over all pixels pairs. The rather low detection efficiency allows to make the assumption, that most of the detection events are uncorrelated without a partner. This allows to infer R_{Acc} from the singles count rate R_{tot} . Using TDC units of $dt = 245$ ps, the frame exposure time is $T_{\text{frm}} \cdot dt = 30$ ns and we get

$$R_{\text{Acc}} = \frac{1}{2} \sum_{t_1=1}^{T_{\text{frm}}} \sum_{t_2=1}^{T_{\text{frm}}} [|t_1 - t_2| \leq T_c] \left(\frac{R_{\text{tot}}}{T_{\text{frm}}} \right)^2.$$

The prefactor can be either interpreted as originating from Poisson statistics, or equivalently from the indistinguishability of events of interchanged time arguments similar as discussed above. This yields a theoretical value of 14.7×10^{-3} events per frame closely agreeing to the measured value.

Pixel Crosstalk

Crosstalk are undesirable, spurious detection events: A single detection event, triggered by dark count or a photon, triggers a nearby pixel. This detector artifact is temporally correlated and can therefore not be removed with the method of accidental subtraction. Due to the digital signal processing within a pixel, electrical crosstalk can be excluded. Optical crosstalk must be present: The physical process of the charge avalanche in a triggering SPAD is creating photons which in turn can be detected by other pixels via reflection from

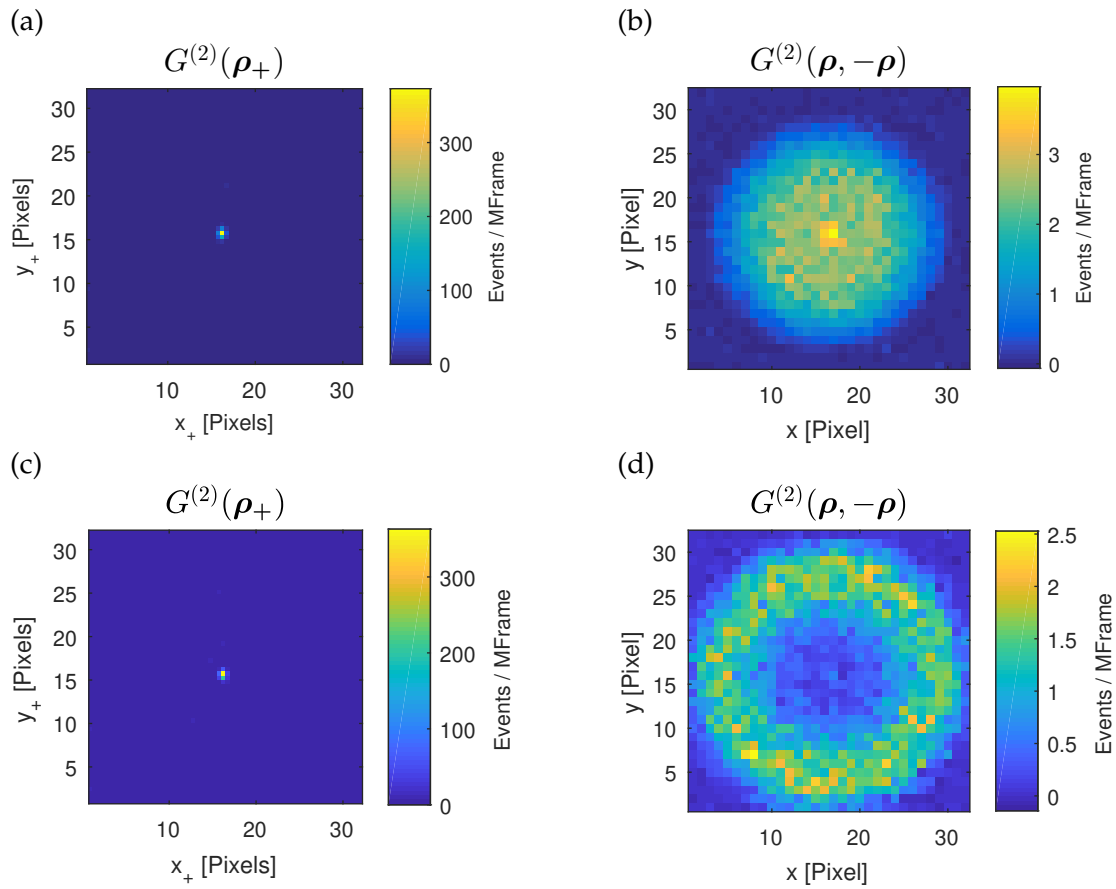


FIGURE 5.16: Second-order measurements with the SPDC biphoton source. (a) and (c): Correlation in the centroid variable $\rho_+ = (\rho_1 + \rho_2)/2$. The anti-correlation peak expected from theory is measured. (b) and (d): Visualization of the pixels contributing to the anti-correlation signal. The NLC temperature is detuned in (c) and (d) for non-collinear SPDC emission.

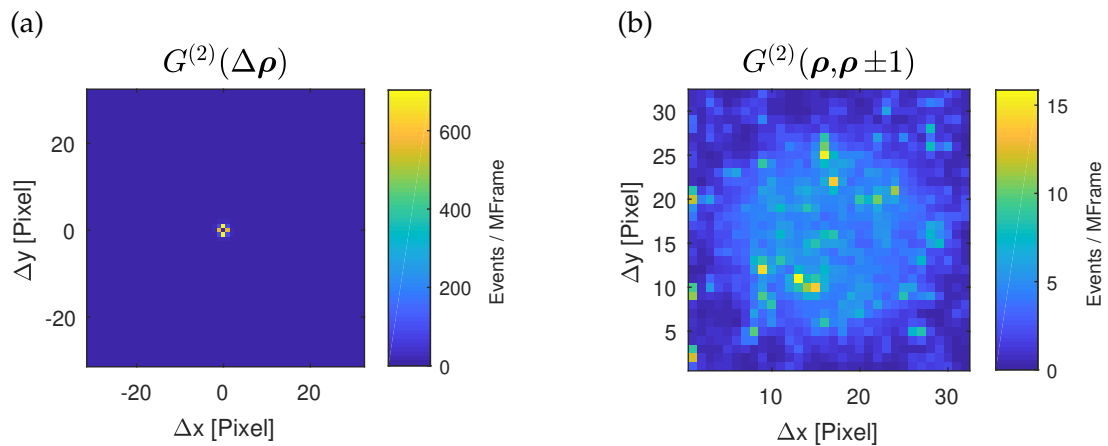


FIGURE 5.17: (a): Correlation function in variable $\Delta\rho = (\rho_1 - \rho_2)$. The correlation peak is due to crosstalk between adjacent pixels. Pixel self-correlation at $\Delta\rho = 0$ cannot be measured. (b): Visualization of the pixels contributing to the correlated signal. Events between directly adjacent pixels are considered.

the sensor surface glass, or even by short distance propagation in the chip. The amount of crosstalk is analyzed in the following.

Similarly as the photonic signal, detector pixel crosstalk can be measured by considering the distribution $G^{(2)}(\Delta\rho)$ of the position difference coordinate $\Delta\rho = \rho_1 - \rho_2$, see Fig. 5.17(a). Because only the first pixel detection event in a frame is registered, no events occur at $\Delta\rho = 0$. The distribution shows clearly the nearest-neighbor crosstalk is most relevant. Because detections at $\Delta\rho$ and $-\Delta\rho$ are physically identical and not distinguishable, the point symmetry of $G^{(2)}(\Delta\rho)$ arises. This means that a total of

$$R_{\text{Xtalk}} := \frac{1}{2} \sum_{\Delta\rho} [|\Delta\rho| \leq 1] G^{(2)}(\Delta\rho) = 1.42 \times 10^{-3} \text{ Events/Frame}$$

crosstalk events are recorded within one pixel separation. With the total photon detection rate of $R_{\text{tot}} = 0.64$ events/frame, this yields an average crosstalk probability of

$$p_{\text{Xtalk}} = \frac{R_{\text{Xtalk}}}{R_{\text{tot}}} = 0.22\%$$

Every single detection event induces with this probability an immediate crosstalk event in one of its neighbors.

With a similar approach as above, the pixels contributing to nearest-neighbor crosstalk can be identified. For this, we calculate

$$G^{(2)}(\rho, \rho \pm 1) := \sum_{\rho_2} [|\rho - \rho_2| \leq 1] G^{(2)}(\rho, \rho_2)$$

and is depicted in Fig. 5.17(b).

Time Resolution

In order to evaluate the performance of individual TDCs, the time correlation between simultaneously triggered pixels can be used. This is the case for anti-correlated pixel pairs ρ and $-\rho$. Therefore, $G^{(2)}(\rho, -\rho, \Delta t)$ should show temporal correlation which is indeed present in the measurement of Fig. 5.18. In (a), the 30 pixel pairs of highest statistics are selected and show a correlation feature of less than 0.5 ns. In the histogram (b), all anti-correlated pairs are used and the width of the temporal correlation peak is evaluated by calculating to distance from the first to the third quartile of the cumulative event distribution in order to be robust against possibly shifted peaks. This can occur for a TDC pair where one is running faster than the other. While equal time codes should be produced for coincident photons in the ideal case, this unequal clocks will produce a correlation maximum at non-zero time code difference Δt .

SPAD Bias Voltage

Increasing the SPAD bias voltage allows to improve the PDE of the detector, but at the same time increases the dark count rate. A higher PDE is also expected to increase crosstalk probability, see the optical model discussed above. For best device performance and signal to noise ratios, optimal value of this voltage should be set depending on the measurement and light conditions.

Table 5.1 provides the PDE η , dark count rate R_{DC} and crosstalk probabilities p_{Xtalk} at different voltages. Using the determined PDE η , the known incident photon flux Φ and the measured rate of photon detection events R_{tot} , a dark count rate $R_{\text{DC}} = R_{\text{tot}} - \eta\Phi$ can be calculated. This value is provided at different bias voltages.

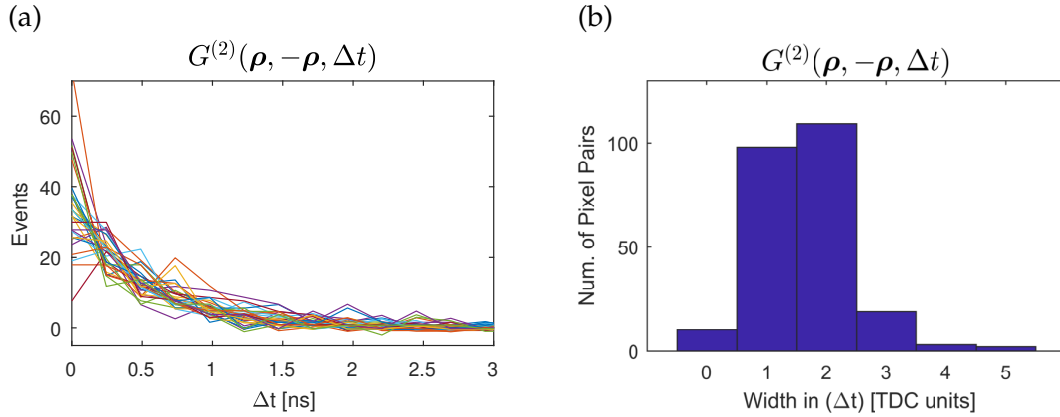


FIGURE 5.18: (a): Temporal correlation of anti-correlated pixel pairs located at ρ and $-\rho$ measuring the biphoton signal, 30 high statistics pairs are shown. (b): Histogram of the width of correlation peaks of all anti-correlated pixels pairs in TDC units of 245 ps.

SPAD Bias Voltage [V]	19.6	19.7	19.8	20.0	20.1	20.2	21.8
R_{tot} [Events/Frame]	0.31	0.32	0.33	0.36	0.37	0.38	0.56
R_{DC} [Events/Frame]	0.22	0.22	0.23	0.26	0.26	0.27	0.41
R_{Signal} [10^{-3} Events/Frame]	0.31	0.34	0.37	0.42	0.45	0.47	0.86
R_{Acc} [10^{-3} Events/Frame]	3.48	3.70	3.94	4.69	4.95	5.23	11.35
R_{Xtalk} [10^{-3} Events/Frame]	0.19	0.23	0.25	0.33	0.35	0.40	1.30
PDE η [%]	0.34	0.36	0.37	0.39	0.41	0.42	0.56
p_{Xtalk} [%]	0.06	0.07	0.07	0.09	0.09	0.10	0.22
p_{Xtalk}/η [1]	0.18	0.20	0.20	0.23	0.23	0.25	0.41

TABLE 5.1: Measurement with SPDC biphoton light at different SPAD bias voltages. A 1 ns coincidence window is used for second-order correlation. Only 98% of all pixels with lowest dark count rate are considered. Shown quantities: The singles detection rate R_{tot} , dark counts R_{DC} , biphoton signal R_{Signal} , accidentals R_{Acc} , crosstalk R_{Xtalk} , PDE η , and crosstalk probability p_{Xtalk} . The PDE and R_{DC} are inferred quantities as calculated in the main text.

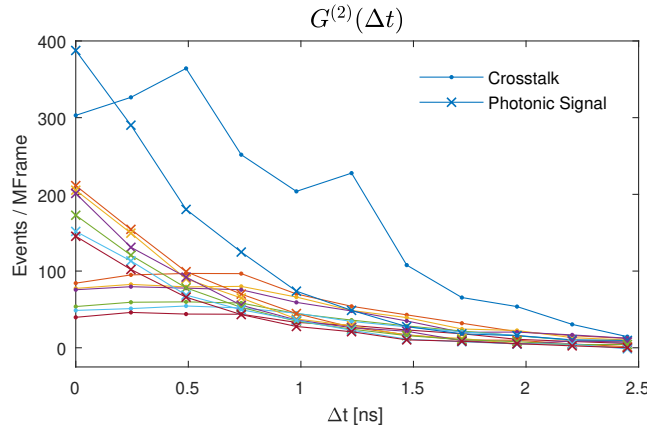


FIGURE 5.19: Measurement of temporal correlation of crosstalk events (dots) and biphoton signal (crosses) at different SPAD bias voltages (colors). In increasing order of signal strength, the voltages are 19.6, 19.7, 19.8, 20.0, 20.1, 20.2, and 21.8 V.

The temporal correlation of crosstalk and the biphoton signal within the small peaking region summed over all pixels pairs can be measured by evaluating

$$G_{\text{Signal}}^{(2)}(\Delta t) := \sum_{\rho_1, \rho_2} [|\rho_1 + \rho_2| \leq 1] G^{(2)}(\rho_1, \rho_2, \Delta t), \quad (5.8)$$

$$G_{\text{Xtalk}}^{(2)}(\Delta t) := \sum_{\rho_1, \rho_2} [|\rho_1 - \rho_2| \leq 1] G^{(2)}(\rho_1, \rho_2, \Delta t). \quad (5.9)$$

This results are shown in Fig. 5.19 for different bias voltages.

Discussion

The physical photon pair correlation time of less than 1 ps is broadened to approx. 1 ns in the measurement. Despite the TDC resolution of 245 ps, this can be explained by the following factors: (i) Electrical jitter of the signal from the SPAD to the TDC (in SPADnet-I 265 ps), and (ii) pixel-to-pixel deviation in TDC clock rate. The former is present twice in $G^{(2)}(\Delta t)$ because two measurements are needed for the relative time. The latter introduces an apparent shift in the time stamp between two pixels and broadens the correlation peak. On the other hand, the analysis of individual pixel pairs showed a very good temporal correlation in the order of two TDC units. This comes close to the optimal case and indicates that a proper characterization and calibration of each TDC would decrease the width of the correlation peak in Fig. 5.14(b).

A very homogeneous distribution of the pixels contributing in the photonic signal in Fig. 5.16(b) verifies the uniformity of the pixels in detection efficiency and TDC clock speed within the frame exposure time and used coincidence window. Furthermore, the crosstalk sources in Fig. 5.17(b) show peaks for high dark count rate pixels in comparison to Fig. 5.14(a), and is increased in the region of incident light. This is in agreement with the assumption of a crosstalk probability per detection event triggered by light or dark counts.

The influence of the SPAD bias voltage is considerable, see Tab. 5.1. The PDE is almost increased by a factor of two within 2 V increase but introduces a higher amount of crosstalk. Dark counts R_{DC} , PDE η and crosstalk probability p_{Xtalk} can be verified to grow in good approximation linearly with the bias voltage change over the investigated range. By observing the ratio p_{Xtalk}/η which also exhibits near linearity with the bias voltage change,

the crosstalk probability increases disproportionately faster than the PDE. Using the optical crosstalk model of emitted photons in a triggered SPAD avalanche described above, the increase in its strength is not only due to better PDE and thereby higher sensitivity to these photons. An increase of photons emitted in the avalanche process, linear in bias voltage change, would explain the excess.

One source of statistical uncertainty in the measured data is the Poisson shot noise of the signal depending on the PDE, but the main contribution comes from accidentals whose shot noise is still present after accidental removal. These accidentals and their noise can be decreased by setting a smaller coincidence window which would be possible with better temporal resolution. The source of accidentals are temporally uncorrelated events which are dark counts and single photons without detection of its partner. Reducing dark counts or increasing PDE would improve signal to noise ratio.

A systematic bias in the measurement data is introduced with crosstalk. At a crosstalk probability of similar magnitude as the PDE at high bias voltage (see Tab. 5.1), a crosstalk signal as strong as the photonic signal is expected. Reducing the bias voltage can improve this ratio by a factor of 5 at the cost of more accidental noise due to lower PDE. As seen in Fig. 5.19, crosstalk shows a less pronounced temporal correlation than the photonic signal. This might hint to the possibility of discriminating between these two if an even better temporal resolution could be established. A different approach would be the characterization and modeling of the crosstalk between all pixels. This would allow for a removal of the crosstalk signal.

In conclusion, the detector is suitable for measurements of biphoton correlation. At the given photon detection efficiency of 0.56%, a measurement duty-cycle of 3.6%, a relatively strong photon pair beam with a flux of 1.8×10^9 ph/s, and a well confined correlation feature which nicely discriminates from crosstalk, a second-order correlation function with similar statistics as presented here can be measured within a few minutes of measurement time. Having the mentioned parameters fixed, photon correlations which are less confined in the $G^{(2)}(\rho_1, \rho_2)$ space than here (c.f. Fig. 5.15) will have a lower signal density in this space but a constant noise background due to accidentals. These will therefore need longer acquisitions in order to achieve the same signal to noise ratio.

5.2.2 Four-Photon Detection

In order to demonstrate the sensor's capability to measure higher-order correlation, the light source generating four-photon states introduced in Sec. 3.2 is used in this experiment in exactly the same configuration, but detection is performed by SuperEllen. This light source was characterized with $G^{(2)}$ measurements of the generated four-photon state using scanning fiber detectors. Similarly to this, before a four-photon detection in a $G^{(4)}$ measurement is considered, a $G^{(2)}$ showing correlations of two out of four photons should be performed here. Identical results as for these source characterization experiments are expected. A comparison of SuperEllen's detection rates with this reference will then allow to estimate possible four-photon detection rates and corresponding measurement times.

The experimental setup is shown in Fig. 5.20. We repeat the introduction of Sec. 3.2: A Ti:Sa femtosecond laser emits pulses at 791 nm with 6.5 nm FWHM bandwidth, approx. 200 fs pulse width, a repetition rate of 85 MHz and 700 mW average power. With lens L_1 ($f_1 = 200$ mm), it is focused to a beam waist radius of $50 \mu\text{m}$ in a first NLC. Via second-harmonic generation in this NLC₁ of 1 mm length, pulses in UV at 395 nm are generated with a pulse width of approx. 1 ps. An average UV power of 35 mW is achieved. The 4-f configuration (L_2 and L_3 , $f = 50$ mm) images these pulses into the second NLC. Filters (F) transmit UV and remove laser light at a suppression ratio better than 10^{-15} . The second NLC₂ of 2 mm length generates photon pairs in SPDC. Multiple generated pairs in the

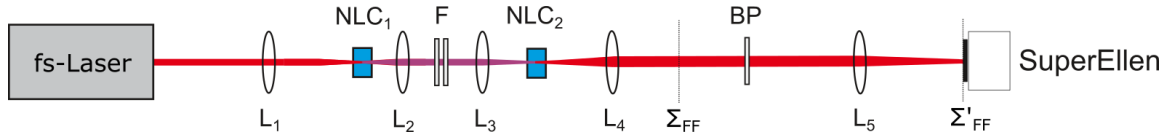


FIGURE 5.20: Experimental setup for the four-photon generation and measurement with SuperEllen detector. A Ti:Sa femtosecond laser emits pulses at 791 nm which is converted to 395 nm via second-harmonic generation in NLC₁. This UV pulses are imaged with the 4-f lens configuration (L_2 and L_3) into the second NLC₂. Filters (F) only transmit UV. SPDC in NLC₂ generates photon pairs. The lens L_4 produces the SPDC far-field distribution in Σ_{FF} . This plane is imaged onto the sensor with L_5 . A narrow bandpass filter (BP) only transmits photons at the central frequency of 791 nm.

same pulse can constitute a genuine four-photon state. The lens L_4 ($f_4 = 75$ mm) produces this source's far-field distribution in plane Σ_{FF} . This plane is imaged onto the sensor with L_5 ($f_5 = 150$ mm) where a magnification $m = 0.31$ is realized. A narrow bandpass filter (BP) transmits 1 nm FWHM at 791 nm. Its central frequency is tuned by tilting of the filter for transmission of the both photons of a generated SPDC pair in nearly frequency-degenerate emission. This filter enforces a low number of detected temporal modes and allows to observe photon bunching effects at high visibility, see Sec. 3.2.

SuperEllen is operated with 45 ns frame exposure time. The SPAD bias voltage is set to 20 V. This lower value than above reduces crosstalk which is favorable for the following measurements, see Sec. 5.2.1. A coincidence window $T_c = 0.6$ ns is used which Fig. 5.19 shows to be long enough to detect coincident photons without signal loss at the given bias voltage. The TDC control voltage is set to 2.35 V which FBK advised to use for more linear TDC operation.

Second-Order Correlation Measurements

The correlation function is obtained from the sensor data as described above in Sec. 5.2.1 in the case of a two-photon source. A total of 4.4×10^9 frames are acquired in approx. 3 hours. The described real-time sensor data processing avoids the storage of the large amount of raw data for these frame numbers, only the second-order correlation histogram $G^{(2)}(\rho_1, \rho_2, \Delta t)$ of fixed size is saved. An average of $R_{\text{tot}} = 0.54$ events/frame are detected.

The light source emits pulses at a separation of approx. 12 ns. This is well resolved by the TDCs within a frame and allows SuperEllen, despite its asynchronous frame acquisition, to distinguish between consecutive pulses via the detection time difference Δt statistics of the second-order correlation function. Fig. 5.21(a) shows $G^{(2)}(\Delta t)$ over all pixels, formally defined above in Eq. (5.6). Despite the better long-time linearity of the TDC with the new control voltage setting advised by FBK, the TDC codes are not equally represented and therefore do not correspond to equal time steps. A pattern period of four TDC codes can be observed and is also explainable by the TDC architecture, see App. D. Averaging over four codes results in the much smoother Fig. 5.21(b). Using the frame exposure time of 45 ns and the maximal TDC codes, an average TDC unit step of 200 ps can be determined. The normalized $G^{(2)}(\Delta t)$ shows consecutive pulses at the expected separation and a strong uncorrelated background. This is removed by the above described accidental background estimation, where the region of $\Delta t = 4$ to 8 ns is used and no signal but uncorrelated background is expected.

The temporally coincident spatial correlation function $G^{(2)}(\rho_1, \rho_2)$, formally defined in Eq. (5.7), is calculated with the coincidence window of $T_c = 0.6$ ns and with accidental events estimated in the mentioned region of Δt . In order to suppress the crosstalk signal

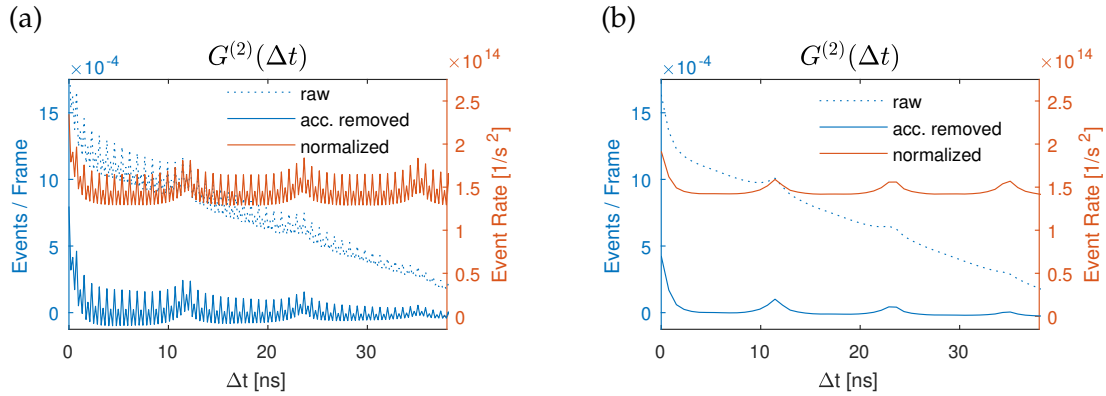


FIGURE 5.21: Temporal second-order correlation function using the four-photon source summed over all pixels. (a) shows non-uniform TDC behavior, which can be corrected by averaging over every TDC codes in (b). Consecutive pulses are visible.

discussed above in Sec. 5.2.1, a dark reference measurement of blocked light source is performed. A total of 1.4×10^9 frames are acquired for this, yielding the accidental corrected, spatial correlation function $G_{\text{xtalk}}^{(2)}(\rho_1, \rho_2)$ consisting only of the crosstalk signal. In the following, corrected correlation functions $G^{(2)} = G_{\text{meas}}^{(2)} - G_{\text{xtalk}}^{(2)}$, using the measured $G_{\text{meas}}^{(2)}$, are evaluated. This procedure removes crosstalk initiated by dark counts, but photon detection events causing crosstalk will still be present.

This accidental and crosstalk correction results in the spatial $G^{(2)}(\rho_1, \rho_2)$, see Fig. 5.22. The SPDC signal is mainly on the anti-diagonal of anti-correlating pixels. The crosstalk removal described above strongly suppresses the diagonal signal strength in comparison to Fig. 5.15.

Fig. 5.23(a) shows the two-photon centroid distribution. It is identically calculated like the same figure in Sec. 5.2.1. A pointing instability of the pump laser causes the horizontal elongation. At a total photonic coincidence signal

$$R_{\text{Signal}} = 0.122 \times 10^{-3} \text{ Events/Frame}$$

in a 5×5 pixel region of the centroid, the total crosstalk is

$$R_{\text{Xtalk}} = 0.037 \times 10^{-3} \text{ Events/Frame}$$

at nearest neighbor level. In comparison to Sec. 5.2.1, much less crosstalk is present at a similar single count rate. This is explained by a factor of 10 reduction due to the mentioned crosstalk reference subtraction and almost a factor of 3 due to lower SPAD bias voltage, see Tab. 5.1. The pixels contributing to the centroid peak are shown in Fig. 5.23(b).

Two-Photon Bunching Signal

In order to simplify analysis in the following, measurement data is reduced to 1-D. Furthermore, the measurements will be directly comparable to the 1-D scans of the source characterization in Sec. 3.2. The 1-D correlation function is given by

$$G^{(2)}(x_1, x_2) := \sum_{y_1, y_2} G^{(2)}(\rho_1, \rho_2).$$

Fig. 5.24(a) shows this data. The anti-diagonal shows a strong anti-correlation feature expected from the detection of two photons of the same pair. The diagonal comprises

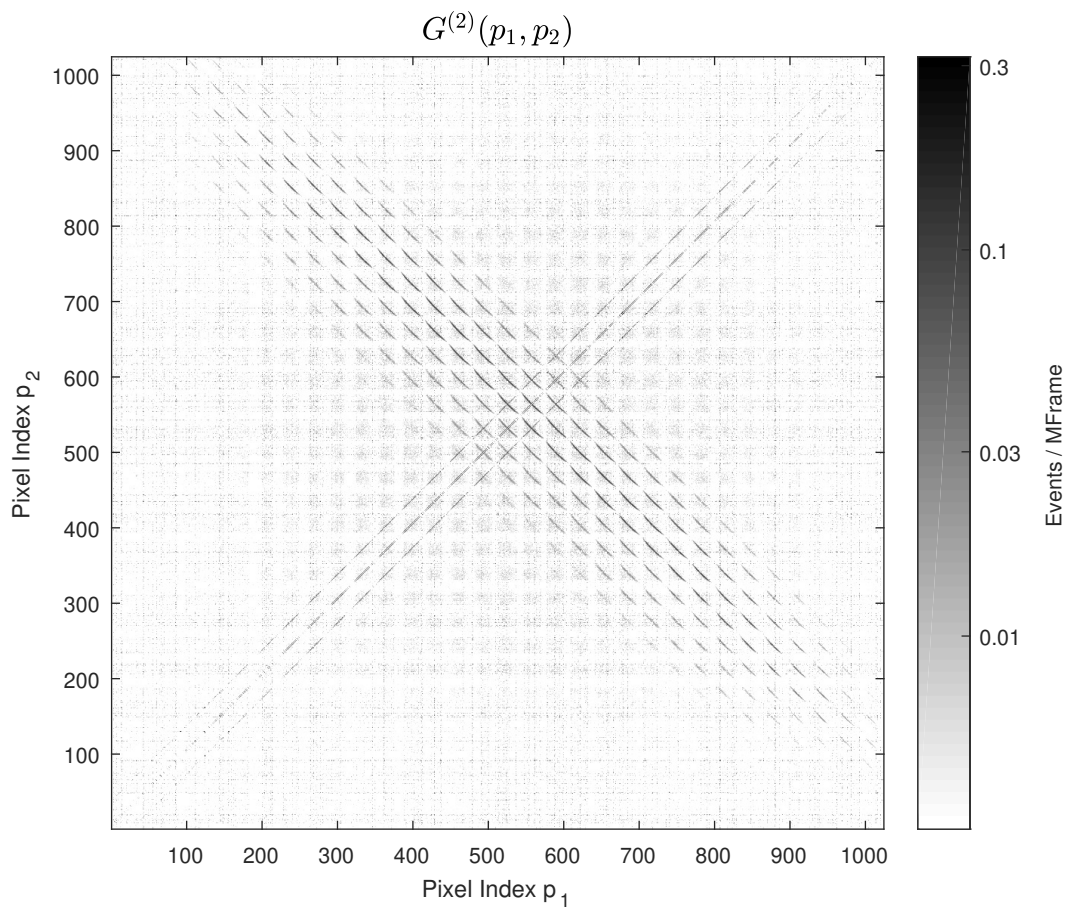


FIGURE 5.22: Full spatial correlation function $G^{(2)}(\rho_1, \rho_2)$ between every pixel pair corrected for accidentals and in logarithmic scale. The four-photon source is used. The $32 \times 32 = 1024$ pixels are addressed by their linear index $p = 1, \dots, 1024$. Accidentals are removed. Crosstalk initiated by dark counts is removed by the subtraction of a reference dark measurement.

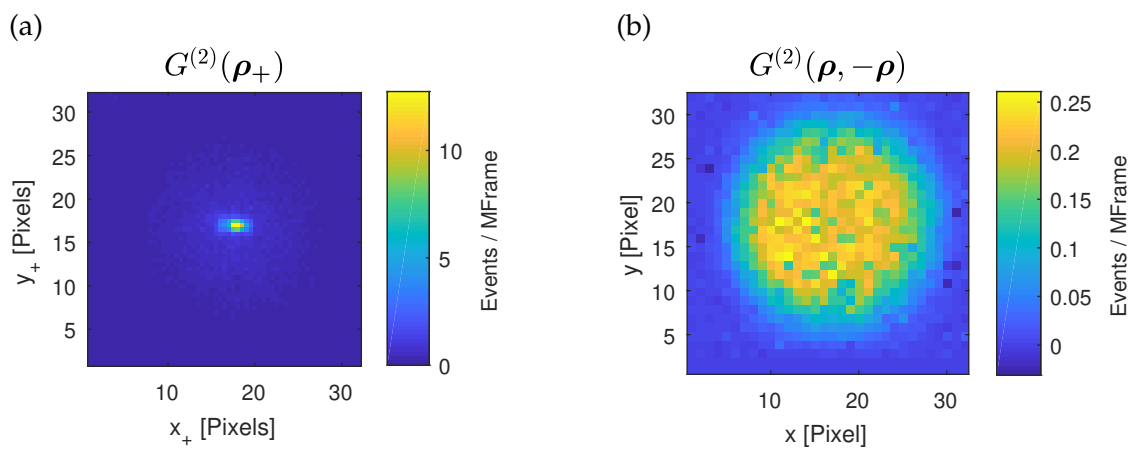


FIGURE 5.23: Second-order measurements with the four-photon source. (a): Correlation in centroid variable $\rho_+ = (\rho_1 + \rho_2)/2$. (b): Visualization of the pixels contributing to the anti-correlation signal.

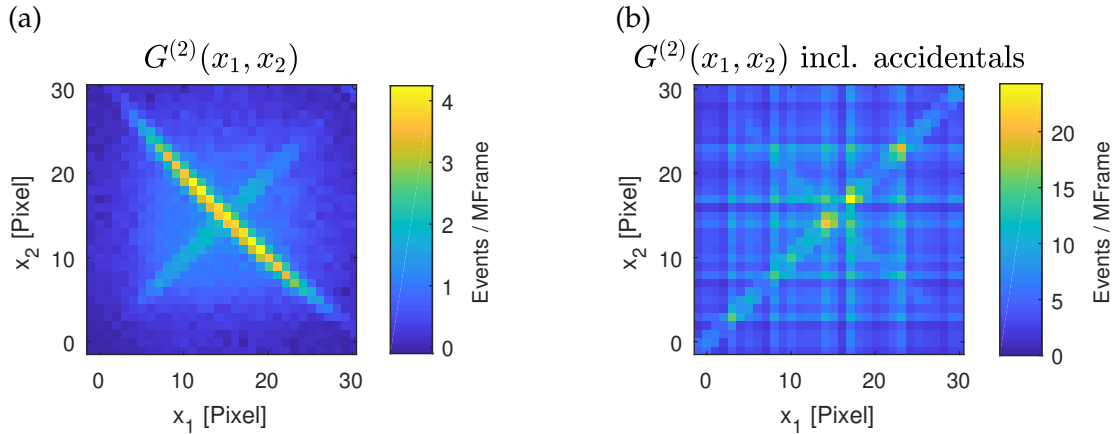


FIGURE 5.24: Second-order measurements with the four-photon source, evaluated in 1-D x -position correlation only and summed over all pixel rows. Accidentals are subtracted in (a), but present in (b) for error estimation.

residual crosstalk and might include two-photon detection from different pairs showing x -correlation due to photon bunching effects. Fig. 5.24(b) shows the same data, but with accidentals present which is useful for estimation of the measurement error in the following.

In Fig. 5.24(a), the anti-diagonal shows a two-photon correlation detection rate of approx. $G_{\text{TPC}}^{(2)} = 4 \times 10^{-6}$ events/frame. In comparison, the fiber coupled detectors showed there 4000 coincidences/s, while the correlated bunching signal was 50 coincidences/s in Fig. 3.6(b). This ratio can be used to estimate the expected rate of bunching event with SuperEllen to be $G_{\text{bunch}}^{(2)} = 50/4000 \cdot G_{\text{TPC}}^{(2)} = 0.05 \times 10^{-6}$ events/frame. This very weak signal is masked by the crosstalk on the diagonal of the data which shows 40 times higher magnitude.

The statistical shot-noise of the measurement is determined in the following and allows to estimate the measurement time needed for a signal-to-noise ratio (SNR) which would allow to see the bunching signal. The data of Fig. 5.24(a) is accidental subtracted. The mean value of these uncorrelated accidental events A can be well estimated using the fitting method, see Sec. 5.1.6, but their statistical noise will still be present in the data after subtraction of their estimated mean $\langle A \rangle$. The standard deviation of the measured values

$$\text{Std} \left(G^{(2)} \right) = \sqrt{G^{(2)} + \langle A \rangle}$$

where Poisson statistics for signal and accidentals is assumed. The accidental uncorrected event number $G^{(2)} + \langle A \rangle$ is given in Fig. 5.24(b). The bunching signal appearing on the diagonal would therefore yield an error of

$$\text{Std} \left(G_{\text{bunch}}^{(2)} \right) \approx 4 \times 10^{-3} \text{ Events} / \sqrt{\text{Frame}}.$$

In order to achieve a minimal $\text{SNR} = \sqrt{N_{\text{frm}}} G_{\text{bunch}}^{(2)} / \text{Std}(G_{\text{bunch}}^{(2)}) = 1$, a total of $N_{\text{frm}} = 6.4 \times 10^9$ frames would have to be acquired corresponding to three hours of measurement. This is a very optimistic estimate, as the needed removal of the strong crosstalk signal, see discussion below, would further degrade statistics.

By using the measurements of Sec. 3.2 with detection rates, its measurement parameters (fiber diameter and PDE) and SuperEllen's specifications (PDE, dark counts, pixel size and number) given in Sec. 5.2.1, the expected detection rates and their statistics can

be theoretically estimated. Using the optimistic median dark count value of 300 Hz/pixel and summation over the all pixel rows for enhancements of the statistics, a $\text{SNR} = 1$ can be reached below one minute of measurement time for the correlations on the anti-diagonal $G^{(2)}(x, -x)$ of two photons of the same pair. The bunching signal $G^{(2)}(x, x)$ requires 8 hours for the same SNR. This is in rough agreement with the results above where crosstalk is neglected as well.

Four-Photon Detection Rates

The detection of a real four-photon event of two pairs showing bunching can be estimated by

$$G^{(4)}(x, x, -x, -x) \approx G^{(2)}(x, x) \eta^2.$$

The rate of generated and detected bunching events is $G^{(2)}(x, x)$ determined for the source in Sec. 3.2.2. Given such a event, two detections are needed at $-x$ each with PDE η for the measurement of the fourth-order correlation. Only a total detection rate of one four-photon event per 30 minutes is expected. The crosstalk problem would be even more important to address and would considerably prolong the measurement time. At this fourth-order measurement and the given sensor parameters, accidentals are very weak and are not relevant anymore for statistics. Shot-noise is dominated by the signal itself.

Discussion

The temporal resolution of SuperEllen is demonstrated again, now with a pulsed source. Using the new TDC control voltage, a better average TDC unit of 200 ps is achieved. Long-time linearity (integrated non-linearity) is shown by FBK for this setting. Nevertheless, the TDC codes do not represent uniform time steps anymore. A more complicated procedure of calibrating the TDCs could compensate this artifact. But for the determination of coincidence and accidental estimation at a small coincidence window, more important than long-time linearity and a short TDC unit is the uniformity in TDC steps (differential non-linearity). It has to be reconsidered to go back to the older setting which showed better performance in that respect in Sec. 5.2.1.

The measurements with the four-photon source shows good agreement with the fiber scanning experiments of Sec. 3.2 at the level of detection of two photons belonging to the same pair. Correlations between photons of different pairs was not possible to measure. While the amount of frames needed for a minimal SNR is considerable, it could be achieved within several hours measurement time, although the instability of the setup, mainly in terms of intensity, would make it challenging to realize. Despite the applied means of crosstalk suppression, residual crosstalk masks the potential region of the photon bunching with a 40 times stronger signal which cannot be separated from each other. One possibility to solve this problem is to magnifying the far-field plane and increase the correlation length of the bunching signal beyond the crosstalk signal. This would further reduce the weak signal and was therefore not considered. The other possibility is the crosstalk characterization of all pixel pairs which would allow to remove of this signal at the cost of again increased statistical noise, see accidental noise discussion above. The success of this approach would depend on the temporal stability of crosstalk, which for example dark count rates of SPADs is not given.

In conclusion, this detector is not suitable for the measurement the very weak source of less than a few dozens coincidences per second in the bunching signal. As it does not allow for second-order correlation measurements, it is even less suited at higher orders. The main reason is the limited PDE at the given wavelength and the low photon flux of the source.

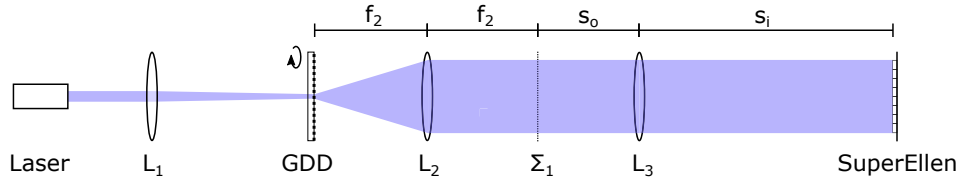


FIGURE 5.25: Experimental setup for the pseudo-thermal light generation and measurement with SuperEllen detector. A CW laser is focused onto a rotating ground glass disk (GDD). With the lens L_2 , the source's far-field distribution is given in plane Σ_1 . This is imaged with L_3 to the measurement plane of the SuperEllen detector.

5.2.3 Pseudo-Thermal Light Detection

The main goal of this section is to show the ability of SuperEllen to measure high-order correlation functions. This is achieved by avoiding the problems of the last section using pseudo-thermal light, see Sec. 3.3. First, this source is of almost arbitrary intensity. Second, the statistics of the light is not influenced by a low PDE and can be fully compensated by increasing the source intensity. Third, a longer correlation time of dozens of microseconds allows the measurement of pixel self correlation by correlating multiple consecutive frames. Furthermore, it is possible to discriminate signal from crosstalk due to their measurable difference in correlation time. The here used wavelength for thermal light is much more optimal and shows a more than six fold increased PDE of the sensor.

For the following measurements, data is acquired in packets of 64 consecutive frames. The readout time determines the fixed frame separation. For temporal information, the TDCs are neglected but only the frame position is used. Within a packet, hereafter referred to as *superframe*, pixels are correlated among each other. The detector therefore provides the photon numbers

$$n(\boldsymbol{\rho}, t) \in \{0, 1\}, \quad \text{with } \boldsymbol{\rho} \in \{(x, y) \mid x, y \in \{1, \dots, 32\}\}, \quad t \in \{1, \dots, 64\},$$

for all pixel positions $\boldsymbol{\rho}$ and times t , measured in units of approx. $10 \mu\text{s}$, within a superframe. Sec. 2.3 describes how to generally process this data in order to arrive at the field intensity correlation functions. For the given time-stationary source and the concrete detector characteristic, Sec. 2.3.4 worked out the general results in this specific case.

Temporal Second-Order Correlation Measurement

In order to measure a second-order correlation function $G^{(2)}(\boldsymbol{\rho}_1, \boldsymbol{\rho}_2, \Delta t)$, the sensor data $n(\boldsymbol{\rho}, t)$ is processed with Eq. (2.34) and Eq. (2.35). A LabView subroutine allowing for its real-time calculation and visualization simplifies setup alignment.

The measurement is performed with the experimental setup shown in Fig. 5.25. As introduced in Sec. 3.3, a CW laser at 405 nm is focused with L_1 to a beam radius of $w_p = 150 \mu\text{m}$ on the ground glass disk (GDD) at a radial position of $r = 2 \text{ cm}$. The disk is rotating at 1000 rpm and produces the pseudo-thermal light. The lens L_2 with $f_2 = 75 \text{ mm}$ produces the far-field distribution in the plane Σ_1 . This plane is imaged with lens L_3 of focal length $f_3 = 150 \text{ mm}$ onto the SuperEllen sensor. With the object and image distance s_o and s_i , the magnification $m = s_i/s_o = 1$ is set.

A total of 13 M frames (200 k superframes) are acquired with an average of 4.95 detection events per frame. By using correlations between all pixels for $G^{(2)}(\Delta t)$ as given in Eq. (5.6), the temporal correlation of Fig. 5.26(a) is measured. Accidental subtraction as performed for the previous light sources does remove the flat background at large Δt . For

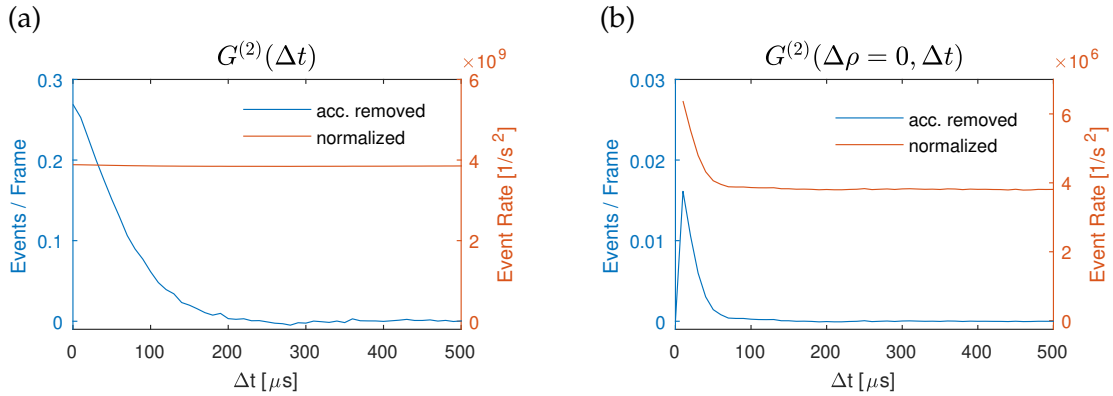


FIGURE 5.26: Temporal second-order correlation function for thermal light. Graph (a) takes into account all pixels correlations, while (b) only considers correlations of a pixels with itself.

the case of thermal light and $G^{(2)}$, this essentially isolates the $\Delta G^{(2)}$ term which is responsible for the correlation peak, see Eq. (3.20). Here, an almost flat correlation line is given with a weak peak on top of roughly $60 \mu\text{s}$ width. As explicit in the $\Delta G^{(2)}(\rho_1, \rho_2, \Delta t)$ term for thermal light, temporal correlations are only expected for pixels within the correlation length. Only considering correlations of the pixels with themselves, which are measurable for superframes at nonzero time separation, we can evaluate

$$G^{(2)}(\Delta\rho = 0, \Delta t) := \frac{1}{2} \sum_{\rho} G^{(2)}(\rho, \rho, \Delta t).$$

This yields Fig. 5.26(b) and gives a much higher visibility of the correlation peak. The ratio of the peak to the flat background is theoretically 2, but is here measured to be 1.67. Reasons can be a imperfect source because of not considered polarization effects or regularities in the ground glass disk. Furthermore, the peak value at $\Delta t = 0$ is for pixel self-correlation $\Delta\rho = 0$ still not measurable and would increase this value closer the theoretical expectation.

The relevant correlation time is given in Fig. 5.26(b) and is approx. $20 \mu\text{s}$. The discrepancy between to aforementioned correlation time is due to the movement of speckles across the sensor, see Sec. 3.3.3. Distant pixel pairs with $|\Delta\rho| > 0$ can be shown to be correlated at a time delay and therefore broaden the overall correlation peak in Fig. 5.26(a).

Spatial Higher-Order Correlation Measurements

For the measurement of higher order correlations, temporally correlated events are considered and only the spatial information retained as discussed in Sec. 2.3.4. Using Eq. (2.39) and Eq. (2.42), correlation functions can be expressed in the sensor data $n(\rho, t)$. This is efficiently implemented in the algorithm of Sec. 2.3.4 which yields the temporal coincident spatial correlation function

$$G^{(N)}(\rho_1, \dots, \rho_N).$$

This N th-order correlation function needs for storage an amount of memory which is scaling with m^N where m are the number of pixels. For the given $m = 1024$, it is already impractical to store the full correlation function for $N \geq 3$. The fact that thermal light shows the non-trivial correlations for pixel within the correlation length, it is sufficient to store only a part of the full function. The correlation function

$$G^{(N)}(\rho_1, \Delta\rho_2, \dots, \Delta\rho_{N-1}), \quad \Delta\rho_k := \rho_k - \rho_1,$$

is in terms of memory much less expensive if we only save $|\Delta\rho| < d$. Here, the memory scales with $m d^{2(N-1)}$ which is more compact for processing and storage.

For the measurements, the setup of Fig. 5.25 is slightly adapted: A pump beam radius of $w_p = 250 \mu\text{m}$ on the ground glass disk and a magnification of $m = 1.96$ for the imaging of lens L_3 are used. For these settings, a correlation time of $100 \mu\text{s}$ can be measured at the detector. The coincidence window should be chosen slightly smaller than the correlation time to have good visibility of the bunching signal which would be otherwise be averaged out. On the other hand, a smaller window lowers the statistics and is therefore undesirable. A coincidence window of $T_c = 40 \mu\text{s}$ is set. For memory saving, we restrict the coordinate $|\Delta\rho| \leq 10$ for $N = 1$ and 2, and $|\Delta\rho| \leq 4$ for $N = 3$ and 4. This already yields several hundreds of megabytes correlation data for one measurement.

A total of 20 M frames are acquired. The measurements are shown in Fig. 5.27. Panels (a-d) are measured with the described optical setup, for (e-h) the imaging lens L_3 was limited in its diameter in order to observe a longer correlation length by the enlarged PSF of the optical system, see Sec. 2.1.4. Comparing (b) and (c) shows that calculating the bunching signal $\Delta G^{(2)} = G^{(2)} - G^{(1)}G^{(1)}$ removes the uncorrelated background noise (mostly dark counts), see Sec. 3.3. The smoother signal in (e) is due to the larger speckles in this lens configuration which smooths non-optimal regularities of the ground glass disk. $\Delta G^{(2)}(\Delta\rho)$ shows in (d) and (f) the correlation length, and as expected from theory it drops to zero at far enough $\Delta\rho$. The third- and fourth-order correlations in (g) and (h) are noisy due to shot noise statistics, but show as expected a similar pattern as seen in (e).

For a more quantitative evaluation of a measurement, a third-order correlation is directly compared to theory in Fig. 5.28. A similar analysis is shown in [119]. The imaging lens L_3 is not limited but uses its 25 mm full diameter. The correlations are analyzed in one spatial dimension x , while $y_1 = y_2 = y_3$. The analysis in relative distances $\Delta x_2 := x_2 - x_1$ and $\Delta x_3 := x_3 - x_1$ effectively produces a projection of the 3D space of $G^{(3)}(x_1, x_2, x_3)$ onto a plane with normal vector $(1, 1, 1)$. Furthermore, the constant background, and with it uncorrelated events, are removed by subtraction of $(G^{(1)})^3$. This correlation function can be calculated from the measurement by

$$\Delta G^{(3)}(\Delta x_2, \Delta x_3) := \frac{1}{V} \sum_{\rho_1, \rho_2, \rho_3} [\Delta x_2 = x_2 - x_1 \wedge \Delta x_3 = x_3 - x_1 \wedge y_1 = y_2 = y_3] \\ \left(G^{(3)}(\rho_1, \rho_2, \rho_3) - G^{(1)}(\rho_1)G^{(1)}(\rho_2)G^{(1)}(\rho_3) \right)$$

where the sampling space volume

$$V(\Delta x_2, \Delta x_3) = \sum_{\rho_1, \rho_2, \rho_3} [\Delta x_2 = x_2 - x_1 \wedge \Delta x_3 = x_3 - x_1 \wedge y_1 = y_2 = y_3]$$

is the normalization in order to get a proper average of all the available pixel triplets of the given relative distances on the sensor. The theoretical model uses the thermal $G^{(1)}$ and $G^{(3)}$ from Sec. 3.3 and is analyzed by the same method. A theoretical correlation length given by Eq. (3.22) is used.

Discussion

The measurements of the pseudo-thermal light source show a spatially inhomogeneous emission. This can be attributed to regularities of the ground glass disk which are biasing the statistics. Despite this imperfection, the temporal and spatial correlations were demonstrated using SuperEllen. The formal development for correlation measurement

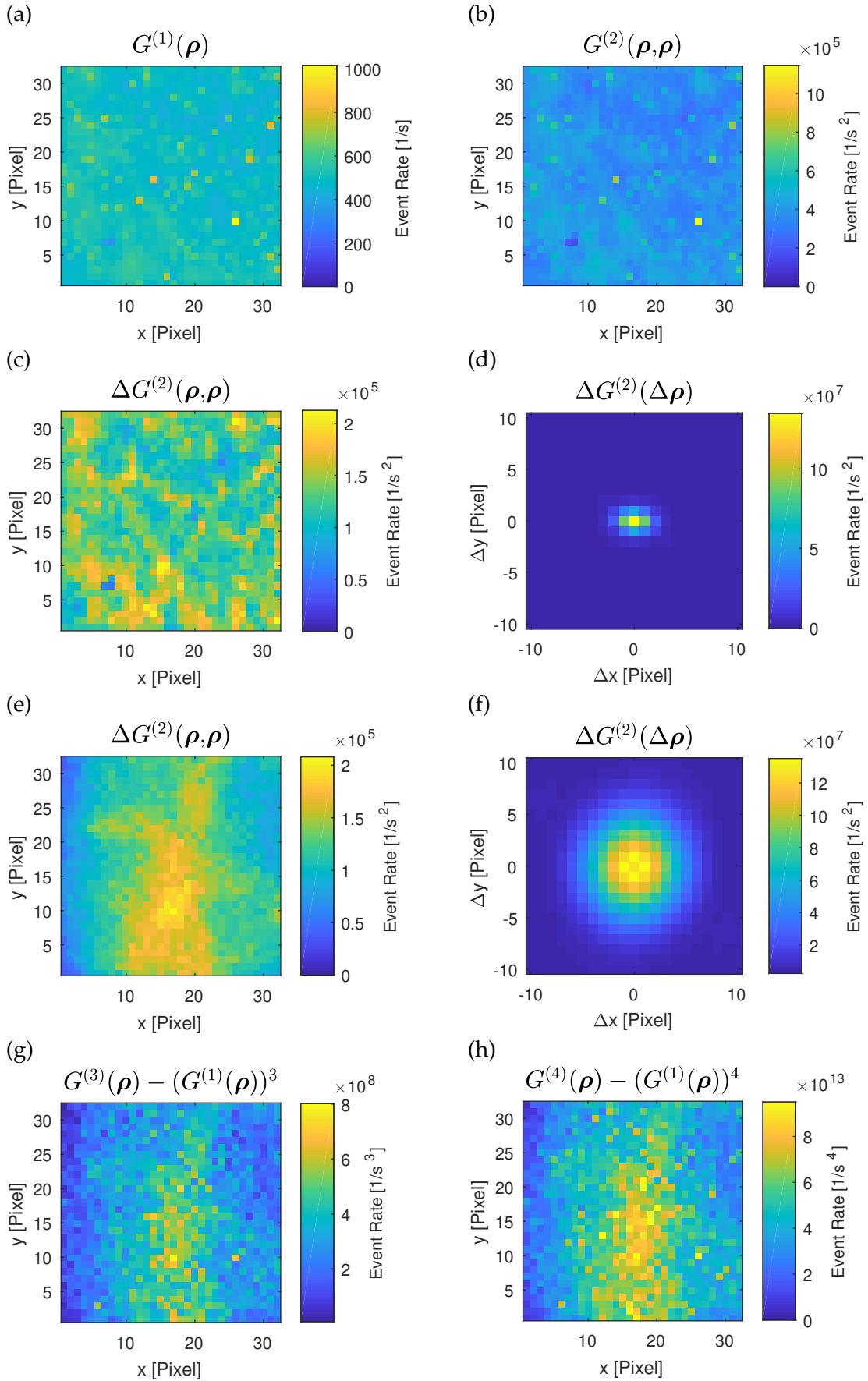


FIGURE 5.27: High-order correlation measurements of a pseudo-thermal source. (a-d) used a large lens diameter for imaging, in (e-h) the lens diameter was limited to 0.6 mm. With exception of (d) and (f), single-point correlation of pixels with themselves are shown. The source's inhomogeneity is responsible for the non-uniform distributions.

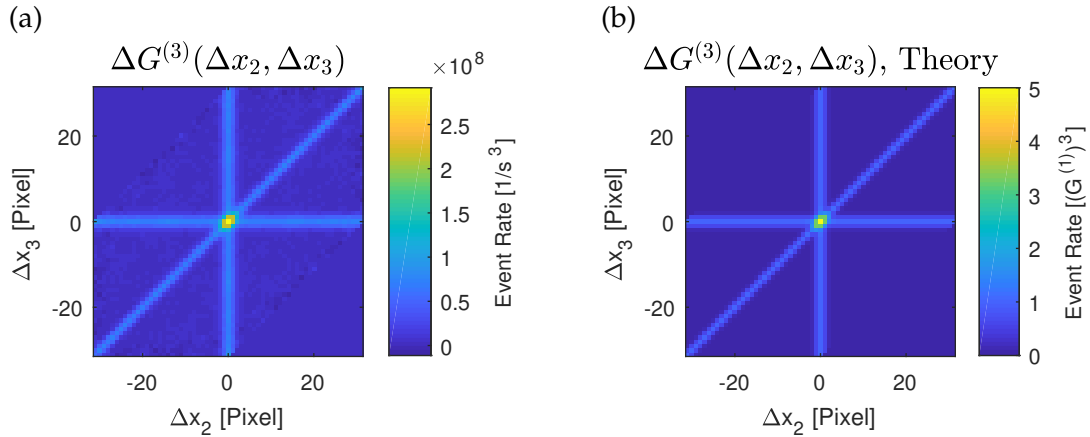


FIGURE 5.28: Spatial third-order correlation function of thermal light with removed background in measurement (a) and theory (b). Only one dimensional x position correlation in $\Delta x_2 = x_2 - x_1$ and $\Delta x_3 = x_3 - x_1$ is considered while $y_1 = y_2 = y_3$.

and its normalization developed in Sec. 2.3 is here applied. The success in removal of uncorrelated background with $G^{(N)} - (G^{(1)})^N$ verifies the proper signal normalization with these procedures in practice. Even more convincingly, Fig. 5.28 of measured and processed data shows a very good agreement to theoretical expectations.

SuperEllen is not developed for the long correlation time of pseudo-thermal light. By neglecting the TDC's detection event timing and only using the frame index for temporal information, SuperEllen is certainly not fully used. For this case without TDC, a different sensor architecture with less readout time providing a higher frame rate or long time exposure but photon number resolution (e.g. CCDs) would be possible and more efficient. Nevertheless, this section demonstrated the possibility of the measurement of a higher-order correlation function with SuperEllen and will be used extensively in Ch. 6 for imaging.

5.2.4 Conclusion

The first measurements with SPADnet-I sensor clearly demonstrated the usefulness of the technology for quantum imaging experiments. Its main advantages are spatially parallel event detection by its pixel array, and the high temporal resolution with the fast TDCs. This allows the measurement of spatial intensity correlation functions of temporally correlated sources, as demonstrated for photon pairs. The temporal resolution was not able to resolve the correlation time of the photons, but allowed a small coincidence window. This reduced accidental background to a minimum. Furthermore, in contrast to a gated detector, having access to the full temporal information permits the estimation and subtraction of accidental background events within the coincidence window. This technique makes it robust to background light and dark count events of the detector. Problems spotted during the evaluation of this sensor technology was related to low PDE, low duty-cycle and crosstalk.

Despite the sensor exhibits a rather high dark count noise and a background due to low detection efficiency, the measurement of temporal correlated signals was possible by the removal of the uncorrelated noise. While the proposed procedure nicely works to recover the correlated signal, this noise subtraction would spoil any attempt to verify entanglement in appropriate experiments [120]. Nevertheless, applications not relying on this aspect can benefit from the sensor technology.

SuperEllen was developed after these experiences and many of the challenges are addressed. The number of pixels and the duty-cycle are tenfold increased. Because crosstalk and PDE are depending on the CMOS manufacturing technique, they are still of similar magnitude. For the measurements performed here using ultra-fast correlated photons, these were the main limitation. For improving crosstalk, technical means in the sensor development are considered: Trenches in the chip architecture providing optical isolation between the pixels. A different approach could be the characterization and modeling of the crosstalk behavior which would allow the subtraction in a post-processing step. This works under the assumption of a time stable behavior. For very weak sources like the four-photon source or for higher-order correlations, the currently given PDE does not allow good statistics in an acceptable amount of measurement time.

In case of a continuously emitting source, the improvement factor in measurement time by using the sensor array in comparison to scanning detectors can be quantified by

$$\frac{m^N}{N!} \eta^N \eta_{\text{duty}}$$

with the correlation order N , number of pixels and detector positions m , PDE η and duty cycle η_{duty} of the array. Ideal scanning detectors with optimal PDE and duty cycle are assumed and detector repositioning time neglected in this comparison. For SuperEllen in a second order correlation measurement $N = 2$, this evaluates to unity and corresponds therefore to a vanishing improvement. For $N = 3$ and $N = 4$, an improvement of 3 and 7 is found respectively. For low correlation order, the technology loses its superiority in the given situations in comparison to a scanning experiment. For a pulsed source, an external gating would improve the effective duty cycle and thereby considerably increase the advantage. Furthermore, higher pixel number in a next generation sensor can strongly increase this factor of time saving. In the procedure of setup alignment of quantum imaging experiments, however, not statistics but fast, real-time visualization of the correlation function is of importance. Then, the sensor is superior due to the here not considered repositioning overhead not allowing fast update rates in scanning.

As discussed in Sec. 5.1, the time correlated detection with gated EMCCD and ICCD cameras is possible at very high detection efficiency [27, 28]. While these devices show a much lower frame rate compared to SuperEllen, their pixel number, detection efficiency, low noise and optimal duty cycle compensates this drawback. For the here used quantum light's wavelength, where CMOS shows reduced detection efficiency, the current generation of CMOS sensor array technology is not superior to these cameras for detection of coincident photons. But in contrast to these CCD devices, the detector arrays are not restricted to coincidence measurements. Thanks to the TDCs, more temporal information is accessible allowing for the observation of more general temporal correlations useful in other application, see below. In addition, the very high frame rate of up to 800 kHz allows to study fast processes not available to cameras. In contrast to complex CCD systems which have to be cooled below -75°C [27], the sensor arrays are technically much simpler and inexpensive giving advantages in possible implementations.

For a next generation sensor, a higher PDE is most desirable. This is the quantity with highest influence on the quality and speed of a measurement due to its exponential dependence on the order of measured correlation. For applications with (pseudo-)thermal light, PDE and very high temporal resolution is not critical while a higher frame would improve measurement statistics.

SuperEllen and its following generation has many advantages in other applications. Its inexpensive fabrication in CMOS technology would allow for its use in consumer devices. For instance in quantum random number generation, the measurement of the two

degrees of freedom of space and time of a quantum source serve as random variables and are available with the detector array. Thereby, it is possible to generate higher bit rates than the traditional single spatial mode approaches. For high photon flux measurements of a single spatial mode distributed over the sensor, the parallel and independent pixels can be used multiplexed as one effective detector of a very high maximal count rate and vanishing dead-time. Imaging in 3D using time-of-flight measurement is possible with an appropriate illumination source [121]. As a generalization of the experiment shown in Ch. 4, spatially resolved quantum low-coherence reflectometry (QOLCR) imaging could be realized.

SuperEllen is applied in a quantum imaging experiments in two chapters. In Ch. 7, it is used for the measurement of second-order correlation functions of the two-photon source. The fact that the signal to be acquired is present in pixels of large separation avoids the crosstalk problem. Nevertheless, several hours of measurement are needed due to the low PDE and low photon flux density of the source. In Ch. 6, pseudo-thermal light is used in the here described manner for the measurement of higher-order correlation functions. The strength of the signal in comparison to crosstalk and the independence of the light's statistics on the PDE allows for efficient measurements.

Chapter 6

Quantum Imaging

As introduced in Ch. 1, the spatial resolution in classical imaging is fundamentally limited by the Rayleigh or diffraction limit. In order to overcome this restriction, a source of entangled photon pairs as well as thermal light is employed for illumination while intensity correlation functions are measured. Near- and far-field imaging is considered. As known from literature, this approach yields a resolution improvement of $\sqrt{2}$ for near-field and 2 for far-field imaging if no data post-processing is performed. In addition to this direct imaging, a reconstruction algorithm is here applied on the full high dimensional correlation function which allows to yield further enhancements in image resolution beyond the mentioned improvements.

This chapter presents the theoretical description well known in literature and our experimental results of imaging with the quantum and thermal light source introduced in Ch. 3 for illumination. Furthermore, the measurement devices introduced in Ch. 5 are applied. This work serves as model experiments within the SuperTwin project and are devised to show the advantage of using the non-standard light sources and measurement techniques in order to improve spatial image resolution in microscopy applications. For the time being, the planned source of quantum light, developed within SuperTwin, is not yet available. The experiments are used for the test of the measurement devices and the object reconstruction algorithm which is developed by our project partners from the B.I. Stepanov Institute of Physics of the National Academy of Sciences of Belarus (IPNASB). This algorithm is planned to be later applied in imaging with the developed quantum source of light. IPNASB's theoretical approach and preliminary reconstruction results are presented in the following together with our measurements.

6.1 Theory

A general Fourier optics description of imaging with entangled photon in different geometries was studied by Abouraddy et al. [52]. Shih gives an overview of imaging with entangled and thermal light [11]. While more fundamental aspects related to quantum correlation motivated these works, Giovannetti et al. studied the improvement in spatial resolution by using an entangled light source [19]. For thermal light illumination, this is done in [34, 122]. Its similarity to imaging with entangled photons, also explicit in our following results, is explored in [123, 124]. Motivated by these insights, the following results are derived from the fundamentals of Ch. 2 and the properties of the light sources in Ch. 3.

In the following, imaging of rather large objects using low resolution imaging systems are theoretically analyzed. While their experimental implementation is not competitive in a microscopy application, they allow to demonstrate the spatial resolution advantage by direct comparison of the non-standard illumination sources and measurement techniques to classical schemes.

As imaging is only expected to yield high resolution in a focal plane, we restrict in the following treatment to 2-D object apertures without axial extension. This object, whose shape is to be measured by the imaging apparatus, can be described by an amplitude aperture function $A(\boldsymbol{\rho})$ in transverse coordinates $\boldsymbol{\rho} = (x, y)$. Illuminating it with light, the impulse response function of apertures in Eq. (2.12) and the transformation of field operators in Eq. (2.21) show that the electric field operator after the aperture in the object plane

$$\hat{E}_o(\boldsymbol{\rho}, t) = \int d^2\boldsymbol{\rho}' h_A(\boldsymbol{\rho}, \boldsymbol{\rho}') \hat{E}(\boldsymbol{\rho}', t) = A(\boldsymbol{\rho}) \hat{E}(\boldsymbol{\rho}, t)$$

given an illuminating field $\hat{E}(\boldsymbol{\rho}, t)$. The goal of any imaging system is to measure this spatially modulated field distribution, with the imprinted object shape, at a distance. Different approaches to this are considered in the following.

6.1.1 Near-Field Imaging

In near-field imaging, the field distribution given with $\hat{E}_o(\boldsymbol{\rho}, t)$ is replicated in a distant plane, where its spatial structure can be measured in a intensity measurement of a standard camera. The use of a single lens for imaging introduced in Sec. 2.1.4 for replicating the electric field. A detector in the object plane probes therefore the corresponding electric field

$$\hat{E}_i(\boldsymbol{\rho}_i, t) = \int d^2\boldsymbol{\rho}_o h_{\text{NF}}(\boldsymbol{\rho}_i, \boldsymbol{\rho}_o) \hat{E}_o(\boldsymbol{\rho}_o, t)$$

with the impulse response function of the near-field setup h_{NF} . By using its explicit expression from Eq. (2.13), we get

$$\hat{E}_i(\boldsymbol{\rho}_i, t) = C \int d^2\boldsymbol{\rho}_o \exp\left(-ik \frac{|\boldsymbol{\rho}_o|^2}{2s_o}\right) \text{somb}\left(\frac{Rk}{s_o} \left|\boldsymbol{\rho}_o + \frac{\boldsymbol{\rho}_i}{m}\right|\right) \hat{E}_o(\boldsymbol{\rho}_o, t) \quad (6.1)$$

with the illumination light wave vector magnitude $k = 2\pi/\lambda$, lens diameter R , focal length f , object to lens distance s_o , and magnification m . All constants and phases not relevant in the following are absorbed into C . The point-spread function (PSF) given by $\text{somb}()$ is responsible for the non-perfect replication of the field. Rayleigh defined the resolution limit for distinguishing two points, imposed by the width of the PSF, to read

$$\Delta x_R = 1.22 \frac{\lambda s_o}{2R}$$

with the illumination wavelength λ [49]. The following light source and measurements show an narrower PSF and surpass this Rayleigh limit.

The Rayleigh resolution is valid for small R where the paraxial approximation applies and the resulting resolution $\Delta x_R \gg \lambda$. Object features smaller than the wavelength result in evanescent fields which are not transmitted through free-space and therefore are not available for imaging and measurement at a distance [3, 49]. While individual photon cannot carry this object information, their correlations can give access to it as seen in the following.

Two-Photon Illumination

The object is directly illuminated by the SPDC two-photon light source introduced in Sec. 3.1. The electric field of the crystal central plane Σ is replicated in the object plane Σ' , see Fig. 6.1. This is done by a 4-f image system with a near optimal PSF, i.e. we can assume a delta function like impulse response function. The electric field in the object plane

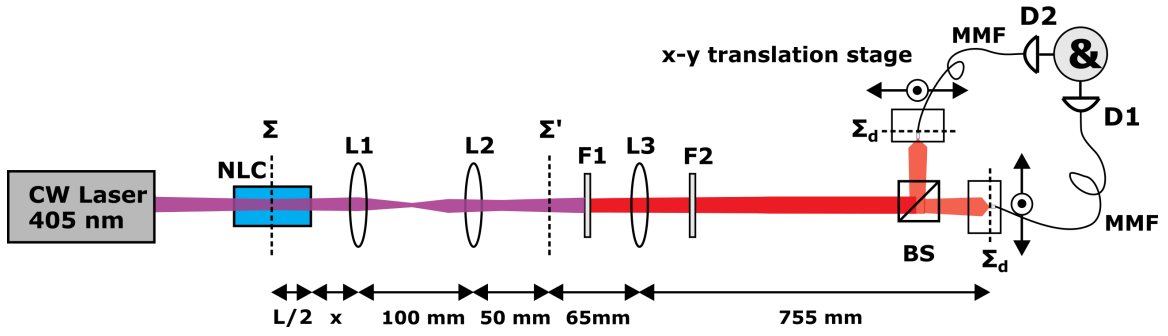


FIGURE 6.1: Two-photon imaging. Photon pairs are generated in SPDC in the NLC. A long-pass filter (F1) blocks the pump, the bandpass filter (F2) selects frequency-degenerate emission. The central crystal plane Σ is imaged (L1, L2) to the object plane Σ' where an object aperture is placed. In near-field imaging, the lens L3 of reduced radius produces a resolution limited image of Σ' in the detection plane Σ_d . For far-field imaging, L3 produces the far-field of object plane Σ' at the detectors. Two multi-mode fiber coupled detectors scan transverse positions and detect photon pairs in coincidence.

reads therefore

$$\hat{E}_o(\boldsymbol{\rho}, t) = A(\boldsymbol{\rho}) \int d^2 \boldsymbol{\rho}' h_F(\boldsymbol{\rho}, \boldsymbol{\rho}', z_0) \hat{E}(\boldsymbol{\rho}', t), \quad z_0 = -\frac{L}{2n(\omega_c)}, \quad (6.2)$$

with the free propagation h_F and the field operator $\hat{E}(\boldsymbol{\rho}, t)$ at the output plane of the crystal as used in Sec. 3.1. The result of Eq. (3.14) for z_0 is used for addressing the central plane involving the crystal length L and refractive index $n(\omega_c)$ at the central emission wavelength.

By appropriately spectral filtering of the collinear, frequency-degenerate emission, spatio-temporal factorization as discussed in Sec. 3.1.1 is assumed and we only consider temporally coincident correlation in the following. With Eq. (6.1), we yield in the image plane the spatial correlation function

$$G^{(2)}(\boldsymbol{\rho}_1, \boldsymbol{\rho}_2) = \left| C \int d^2 \boldsymbol{\rho}_o d^2 \boldsymbol{\rho}'_o A(\boldsymbol{\rho}_o) A(\boldsymbol{\rho}'_o) \Phi(\boldsymbol{\rho}_o, \boldsymbol{\rho}'_o) h(\boldsymbol{\rho}_1, \boldsymbol{\rho}_o) h(\boldsymbol{\rho}_2, \boldsymbol{\rho}'_o) \right|^2 \quad (6.3)$$

with the PSF

$$h(\boldsymbol{\rho}_i, \boldsymbol{\rho}_o) := \exp\left(-ik \frac{|\boldsymbol{\rho}_o|^2}{2s_o}\right) \text{somb}\left(\frac{Rk}{s_o} \left|\boldsymbol{\rho}_o + \frac{\boldsymbol{\rho}_i}{m}\right|\right) \quad (6.4)$$

and the two-photon correlation amplitude

$$\Phi(\boldsymbol{\rho}_s, \boldsymbol{\rho}_i) := \int d^2 \boldsymbol{q}_s d^2 \boldsymbol{q}_i H_F(\boldsymbol{q}_s, z_0) H_F(\boldsymbol{q}_i, z_0) \Lambda(\boldsymbol{q}_s, \boldsymbol{q}_i) e^{i\boldsymbol{q}_s \cdot \boldsymbol{\rho}_s + i\boldsymbol{q}_i \cdot \boldsymbol{\rho}_i} \quad (6.5)$$

with the two-photon wave function Λ given by Eq. (3.5) and free-space propagation transfer function H_F from Eq. (2.9). The light source is described by Φ , while the imaging system is characterized by h .

In the limit of a thin crystal, the correlation function $\Phi(\boldsymbol{\rho}_s, \boldsymbol{\rho}_i)$ becomes $\delta^{(2)}(\boldsymbol{\rho}_s - \boldsymbol{\rho}_i)$, i.e. photon pairs are perfectly correlated. Then, a resolution improvement is explicit in direct imaging by the measurement of

$$G^{(2)}(\boldsymbol{\rho}, \boldsymbol{\rho}) = \left| C \int d^2 \boldsymbol{\rho}_o A^2(\boldsymbol{\rho}_o) h^2(\boldsymbol{\rho}, \boldsymbol{\rho}_o) \right|^2$$

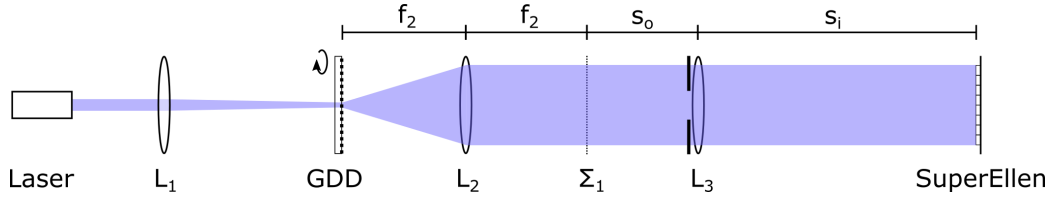


FIGURE 6.2: Thermal light imaging. The pseudo-thermal source uses a rotating ground glass disk (GDD) illuminated by a laser and produces a random speckle pattern. The disk's far-field plane Σ_1 , obtained by the use of L_2 , serves as object plane of the following imaging. In near-field imaging, the lens L_3 of reduced radius produces a resolution limited image of the object plane Σ_1 at the SuperEllen detector array. For far-field imaging, lens L_3 produces the far-field of the object plane Σ_1 at the detector.

as shown in [38]. In this limiting case and the measurement on the $G^{(2)}$ diagonal, resolution improvement is given by the squared PSF $h(\boldsymbol{\rho}, \boldsymbol{\rho}_o)$. Approximating it by a Gaussian, it can be shown to yield a $\sqrt{2}$ improvement [32, 39, 125]. Generally, sources of N entangled photons would show an advantage of \sqrt{N} [19]. In addition to this direct imaging result, applying a reconstruction algorithm on the full correlation function is expected to yield further improvements.

Entanglement of the photon pair is explicit due to the coherent integration in the squared modulus of Eq. (6.3). Multi-photon interference effects can occur. In contrast, for classically correlated pairs with spatial correlation given by the joint probability distribution $|\Phi(\boldsymbol{\rho}_s, \boldsymbol{\rho}_i)|^2$, we arrive at the correlation function

$$G^{(2)}(\boldsymbol{\rho}_1, \boldsymbol{\rho}_2) = \int d^2\boldsymbol{\rho}_o d^2\boldsymbol{\rho}'_o |A(\boldsymbol{\rho}_o)|^2 |A(\boldsymbol{\rho}'_o)|^2 |\Phi(\boldsymbol{\rho}_o, \boldsymbol{\rho}'_o)|^2 |h(\boldsymbol{\rho}_1, \boldsymbol{\rho}_o)|^2 |h(\boldsymbol{\rho}_2, \boldsymbol{\rho}'_o)|^2 \quad (6.6)$$

Here again, we have in the limit of a small correlation length a $\sqrt{2}$ improvement in resolution due to narrowing of the PSF by its squaring. This generalizes to \sqrt{N} for a classically correlated N -photon state [19, 34, 126].

Thermal Light Illumination

In this case, the object is illuminated by the pseudo-thermal light source introduced in Sec. 3.3 and shown in Fig. 6.2. Thermal light is fully characterized by its first-order correlation function given in Eq. (3.19). With the near-field imaging setup of Eq. (6.1), the bunching term $\Delta G^{(2)}$ of the second-order correlation function defined in Eq. (3.21) becomes in the detector plane

$$\Delta G^{(2)}(\boldsymbol{\rho}_1, \boldsymbol{\rho}_2) = \left| C \int d^2\boldsymbol{\rho}_o d^2\boldsymbol{\rho}'_o A^*(\boldsymbol{\rho}_o) A(\boldsymbol{\rho}'_o) \Gamma(\boldsymbol{\rho}_o, \boldsymbol{\rho}'_o) h^*(\boldsymbol{\rho}_1, \boldsymbol{\rho}_o) h(\boldsymbol{\rho}_2, \boldsymbol{\rho}'_o) \right|^2 \quad (6.7)$$

with the PSF $h(\boldsymbol{\rho}_i, \boldsymbol{\rho}_o)$ defined in Eq. (6.4) and the first-order correlation function

$$\Gamma(\boldsymbol{\rho}_1, \boldsymbol{\rho}_2) := G^{(1)}(\boldsymbol{\rho}_1, \boldsymbol{\rho}_2)$$

in the object plane. This result is in direct analogy to the two-photon correlation function of Eq. (6.3). The light source is characterized by the coherence function Γ and the imaging system by the impulse response function h . This result characterizes the thermal light source in the detector plane to every correlation order as discussed in Sec. 3.3.

For a homogeneous thermal source of vanishing correlation length l_c , $\Gamma(\mathbf{q}_1, \mathbf{q}_2)$ is well approximated by $\delta^{(2)}(\mathbf{q}_1 - \mathbf{q}_2)$ and the measurement of

$$\Delta G^{(2)}(\boldsymbol{\rho}, \boldsymbol{\rho}) = \left| C \int d^2 \boldsymbol{\rho}_o |A(\boldsymbol{\rho}_o)|^2 |h(\boldsymbol{\rho}, \boldsymbol{\rho}_o)|^2 \right|^2$$

can be considered as direct imaging. Again, the effective PSF is narrowed by its squaring, yielding a $\sqrt{2}$ resolution improvement in a Gaussian approximation. Note, that no second-order correlation measurement would be needed for this improvement in direct imaging. The intensity measurement already shows the exactly same signal due to $(G^{(1)}(\boldsymbol{\rho}))^2 = \Delta G^{(2)}(\boldsymbol{\rho}, \boldsymbol{\rho})$.

While these result are practically identical to the ones above discussed for the source of two-photon light, the main difference is the signal contrast. In the measurement of $G^{(2)}$, a background has to be subtracted in order to arrive at the here described $\Delta G^{(2)} = G^{(2)} - (G^{(1)})^2$, see Sec. 3.3. This influences noise of the acquired signal. Furthermore, in contrast to the above generalization to correlated N -photon sources where we can explicitly show the resolution scaling with \sqrt{N} , all correlations orders of thermal light can be expressed in products of $\Delta G^{(2)}$ and therefore only show the PSF at the power of two. Nevertheless, the information content in a full $G^{(N)}$ is expected to increase with N . Not only using the above direct imaging but applying a reconstruction algorithm on the full correlation function is expected to yield further improvements. This could be measured in terms of Fisher information for the reconstruction which is an ongoing work of IPNASB.

6.1.2 Far-Field Imaging

In Far-field imaging, the electric field with imprinted object features is not directly transmitted and measured, but essentially its Fourier transform. Signal processing then needs to invert this transformation in order to reconstruct the object. The measurement can either be lens-less with sufficient distance from the illuminated object, or with the single lens far-field imaging introduced in Sec. 2.1.5. Employing the latter, the electric field in the far-field plane

$$\hat{E}_i(\mathbf{q}, t) = C \int d^2 \boldsymbol{\rho}_o e^{i \mathbf{q} \cdot \boldsymbol{\rho}_o} \hat{E}_o(\boldsymbol{\rho}_o, t), \quad \mathbf{q} := \frac{k}{f} \boldsymbol{\rho}, \quad (6.8)$$

in terms of the field in the object plane \hat{E}_o , wave vector magnitude $k = 2\pi/\lambda$ and its transverse part \mathbf{q} . Constants and phases are absorbed in C .

In reconstruction of the object, the resolution limiting factor is in this case the accessible range of \mathbf{q} values. A realistic detector will only observe a finite range. The wavelength dependence is given by the detector position $\boldsymbol{\rho}$ to \mathbf{q} relation: Larger wave lengths λ , i.e. smaller k , allow for a smaller \mathbf{q} observation range given a fixed sensor size. A reduction of the lens aperture by an iris, as in near-field imaging, is not applied here because this can be shown to be of no relevance for the measurable \mathbf{q} range and thereby image resolution.

The ultimate limit of measurable wave vectors is the condition $|\mathbf{q}| \leq k$ because higher values are non-propagating evanescent fields not available at a distance. This restricts the spatial resolution attainable in a object reconstruction. The following schemes allow to go beyond

Two-Photon Illumination

The concrete experimental implementation is shown in Fig. 6.1. The lens L3 is replaced by a far-field lens in f-f configuration and therefore $s_o = s_i = f$. With the illuminating

field derived in Eq. (6.2) and the propagated field Eq. (6.8), we can express the correlation function in the far-field plane in the same as Eq. (6.3) with

$$G^{(2)}(\mathbf{q}_1, \mathbf{q}_2) = \left| C \int d^2\rho_o d^2\rho'_o A(\rho_o) A(\rho'_o) \Phi(\rho_o, \rho'_o) h(\mathbf{q}_1, \rho_o) h(\mathbf{q}_2, \rho'_o) \right|^2 \quad (6.9)$$

with two-photon correlation function Φ from Eq. (6.5) and the far-field impulse response function

$$h(\mathbf{q}, \boldsymbol{\rho}) := e^{i\mathbf{q}\cdot\boldsymbol{\rho}}. \quad (6.10)$$

This result can also be written in the form

$$G^{(2)}(\mathbf{q}_1, \mathbf{q}_2) = |(\tilde{A} \times \tilde{A}) * \Lambda(\mathbf{q}_1, \mathbf{q}_2)|^2$$

with the Cartesian product \times and convolution $*$ between the two-photon wave function $\Lambda(\mathbf{q}_s, \mathbf{q}_i)$ and the Fourier transform of the aperture function

$$\tilde{A}(\mathbf{q}) = \int d^2\rho A(\rho) e^{i\mathbf{q}\cdot\boldsymbol{\rho}}.$$

In the limit of a plane wave pump and a thin crystal, $\Lambda(\mathbf{q}_s, \mathbf{q}_i)$ becomes $\delta^{(2)}(\boldsymbol{\rho}_s + \boldsymbol{\rho}_i)$, see Sec. 3.1.1. It can be shown, that in this case

$$G^{(2)}(\mathbf{q}_1, \mathbf{q}_2) = |(\tilde{A} * \tilde{A})(\mathbf{q}_1 + \mathbf{q}_2)|^2 = \tilde{A}^2(\mathbf{q}_1 + \mathbf{q}_2) \quad (6.11)$$

with the Fourier transform \tilde{A}^2 of A^2 .

For the case of aperture functions of unit transmission amplitudes $A(\boldsymbol{\rho}) \in \{0, 1\}$, we have $\tilde{A}^2 = \tilde{A}$. The signal along the diagonal $\mathbf{q}_1 = \mathbf{q}_2$, i.e. spatially coincident detection, the correlation function

$$G^{(2)}(\mathbf{q}, \mathbf{q}) = \tilde{A}^2(2\mathbf{q}) = \tilde{A}^2\left(2\frac{2\pi}{\lambda f}\boldsymbol{\rho}\right).$$

Given a limited measurable $\boldsymbol{\rho}$ range, the measurement of this $G^{(2)}$ gives therefore access to transverse wave vectors of double magnitude in comparison to standard coherent illumination. Equally, the observed diffraction pattern would be yielded for coherent illumination of half the here used wavelength [17]. This is directly related to the two-photon interference effect observed in interferometer of Ch. 4. It can be shown that for a correlated N -photon source, an N -fold larger range can be observed. Therefore, the advantage of using this light source is the larger space of accessible transverse wave vectors of the object. A reconstruction algorithm thereby gets more information on the object features.

Using classically correlated light instead of entangled photon pairs would not yield the described far-field diffraction pattern. In the limit of small correlation length, the pattern would not contain any object information at all. Only the two-photon interference effect present thanks to entanglement can yield this effect. Nevertheless, classical techniques allow for the measurement of the broader wave vector range as discussed in the conclusion below.

Thermal Light Illumination

In the experimental setup of Fig. 6.2, far-field imaging is achieved with a lens L_3 of focal length f by using the distances $s_o = s_i = f$. Then, the first-order correlation function in the

far-field plane can be expressed in terms of the first-order correlation in the object plane by using the propagated field operator Eq. (6.8) and get

$$\Delta G^{(2)}(\mathbf{q}_1, \mathbf{q}_2) = \left| C \int d^2 \boldsymbol{\rho}_o d^2 \boldsymbol{\rho}'_o A^*(\boldsymbol{\rho}_o) A(\boldsymbol{\rho}'_o) \Gamma(\boldsymbol{\rho}_o, \boldsymbol{\rho}'_o) h^*(\boldsymbol{\rho}_1, \boldsymbol{\rho}_o) h(\boldsymbol{\rho}_2, \boldsymbol{\rho}'_o) \right|^2 \quad (6.12)$$

with the PSF $h(\mathbf{q}, \boldsymbol{\rho})$ defined in Eq. (6.10) and the first-order correlation function of the illumination $\Gamma(\boldsymbol{\rho}, \boldsymbol{\rho}') := G^{(1)}(\boldsymbol{\rho}, \boldsymbol{\rho}')$ in the object plane. This result can also be expressed with

$$\Delta G^{(2)}(\mathbf{q}_1, \mathbf{q}_2) = |((\tilde{A})^* \times \tilde{A}) * \tilde{\Gamma})(\mathbf{q}_1, \mathbf{q}_2)|^2$$

with the Cartesian product \times and convolution $*$ with the Fourier transforms of the object aperture $\tilde{A}(\mathbf{q})$. The first order-correlation function of the illumination in a plane wave basis is given by

$$\tilde{\Gamma}(\mathbf{q}_1, \mathbf{q}_2) := \langle \hat{E}^{(-)}(\mathbf{q}_1) \hat{E}^{(+)}(\mathbf{q}_2) \rangle = \int d^2 \boldsymbol{\rho}_1 d^2 \boldsymbol{\rho}_2 \Gamma(\boldsymbol{\rho}_1, \boldsymbol{\rho}_2) e^{i \mathbf{q}_1 \cdot \boldsymbol{\rho}_1 - i \mathbf{q}_2 \cdot \boldsymbol{\rho}_2}.$$

For a homogeneous thermal source of vanishing correlation length l_c , $\tilde{\Gamma}(\mathbf{q}_1, \mathbf{q}_2)$ is well approximated by $\delta^{(2)}(\mathbf{q}_1 - \mathbf{q}_2)$ and

$$\Delta G^{(2)}(\mathbf{q}_1, \mathbf{q}_2) = \left| (\tilde{A}^* * \tilde{A})(\mathbf{q}_2 - \mathbf{q}_1) \right|^2 = \left| (|\tilde{A}|^2)(\mathbf{q}_2 - \mathbf{q}_1) \right|^2.$$

with the Fourier transform of the aperture transmission $|A(\boldsymbol{\rho})|^2$.

For the case of aperture functions of unit transmission amplitudes $A(\boldsymbol{\rho}) \in \{0, 1\}$, we have $|\tilde{A}|^2 = \tilde{A}$. Along the anti-diagonal $\mathbf{q}_1 = -\mathbf{q}_2$, the correlation function yields

$$\Delta G^{(2)}(\mathbf{q}, -\mathbf{q}) = \left| (|\tilde{A}|^2)(2\mathbf{q}) \right|^2.$$

Again, as seen above with correlated photon pairs, the use of this light source allows to measure a twice broader \mathbf{q} spectrum in the correlation data. As remarked above for the thermal near-field case, signal contrast is the main difference to illumination with photon pairs. Furthermore, higher order correlation functions are given by products of $\Delta G^{(2)}$ and therefore do not show the same explicit scaling of observable \mathbf{q} spectrum width with correlation order N .

6.1.3 Object Reconstruction Algorithm

In addition to the above mentioned improvements due to photon correlation in direct imaging where no data processing takes place, a reconstruction algorithm applied on the full correlation function is expected to yield further improvements. The algorithm developed by IPNASB reconstructs the object features from this correlation data by using a model of the source, imaging and detection process. It will be published in a joint work, where it is applied to the here provided measurements [48]. The algorithm follows data pattern approach and can be applied to near- and far-field imaging as shown in the following.

The goal of the algorithm is to get a good estimate of the object aperture function $A(\boldsymbol{\rho})$ given the measurement $G^{(2)}(\boldsymbol{\rho}_1, \boldsymbol{\rho}_2)$. It is formulated as nonlinear optimization problem

where the difference between the measurement $G_{\text{meas.}}^{(2)}$ and model prediction $G_A^{(2)}$, under the assumption of an aperture $A(\boldsymbol{\rho})$, is minimized

$$\min_{A(\boldsymbol{\rho})} \sum_{\boldsymbol{\rho}_1, \boldsymbol{\rho}_2} \left(\frac{G_A^{(2)}(\boldsymbol{\rho}_1, \boldsymbol{\rho}_2) - G_{\text{meas.}}^{(2)}(\boldsymbol{\rho}_1, \boldsymbol{\rho}_2)}{\delta G^{(2)}(\boldsymbol{\rho}_1, \boldsymbol{\rho}_2)} \right)^2$$

with the estimate of the measurement error $\delta G^{(2)}(\boldsymbol{\rho}_i, \boldsymbol{\rho}_j)$. The aperture is decomposed

$$A(\boldsymbol{\rho}) = \sum_{\mu} x_{\mu} y_{\mu}(\boldsymbol{\rho})$$

into basis functions $y_{\mu}(\boldsymbol{\rho})$. A natural choice are pixels, i.e. quadratic regions of unit transmission amplitude. For all light sources and near- or far-field measurements, the common form of the correlation functions Eq. (6.3), Eq. (6.7), Eq. (6.9), and Eq. (6.12) can be exploited. These expressions can be written in the discrete form

$$G_A^{(2)}(\boldsymbol{\rho}_j, \boldsymbol{\rho}_k) = \left| \sum_{\mu, \nu} x_{\mu} x_{\nu} D_{\mu\nu}^{jk} \right|^2$$

with the finite number of detector locations $\boldsymbol{\rho}_j$. For the case of SPDC light, the constant is given by

$$D_{\mu\nu}^{jk} = C \int d^2 \boldsymbol{\rho}_o d^2 \boldsymbol{\rho}'_o y_{\mu}(\boldsymbol{\rho}_o) y_{\nu}(\boldsymbol{\rho}'_o) \Phi(\boldsymbol{\rho}_o, \boldsymbol{\rho}'_o) h(\boldsymbol{\rho}_j, \boldsymbol{\rho}_o) h(\boldsymbol{\rho}_k, \boldsymbol{\rho}'_o)$$

using the basis functions y_{μ} and the near- or far-field impulse response function h . The constant D can be formulated accordingly for thermal light imaging. As it does not depend on the object, it can be calculated and adapted in a calibration step prior to the measurement.

The nonlinear optimization is performed over the discrete variables x_{μ} . By taking into account symmetries of D , IPNASB was able to formulate the optimization in a efficient, iterative reconstruction algorithm. In addition to the above discussed advantages in the $\sqrt{2}$ narrower PSF of direct imaging, further improvements of resolution are expected for the reconstruction result: (i) As the probed object aperture occurs to its second power in the measurement signal, low contrast features show improved visibility. (ii) An analysis of the Fourier spectrum transmitted by the squared PSF of near-field imaging shows that it is effectively doubled. While these newly accessible values of transverse wave vector spectrum are suppressed, they are nevertheless measurable and the image can be reconstructed to double resolution similar to the far-field case [32, 125]. (iii) Given m detector position, the larger amount of m^2 values in a $G^{(2)}$ measurement in comparison to a $G^{(1)}$ with m values yields more constraints on the result of an object reconstruction algorithm. A Fisher information analysis of the object reconstruction process will allow the quantify the full resolution advantage from a statistical perspective.

6.2 Experimental Results

Imaging measurements with the above discussed light sources are here presented. Classical light sources at the same wavelength are used for resolution comparison and demonstration of the advantage. While imaging measurements are shown with a few object in the following, many more have been performed for the proper evaluation of the object reconstruction algorithm of IPNASB. Its preliminary reconstruction results are shown when available.

6.2.1 Near-Field Imaging

For near-field imaging, a single-lens setup is used. Resolution is artificially reduced by limiting the lens aperture with an iris of radius R . The system's PSF is thereby made broader as seen Eq. (6.4).

Two-Photon Illumination

The setup for illumination with correlated photon pairs is shown in Fig. 6.1. The SPDC light source is fully introduced in Sec. 3.1. The light is generated in the nonlinear crystal (NLC) whose temperature is set to 25°C. Its central plane is imaged in a 4-f lens systems (L1 and L2) to the object plane Σ' . Object apertures to be imaged are placed here. The lens L3 ($f = 60$ mm) is limited in its radius by a iris of radius R . It images the object plane Σ' to the detection plane Σ_d with a magnification of $m = 11.65$.

A beam splitter cube separates photon pairs to two different detectors. These are coupled to multi-mode fibers of 50 μm diameter whose bare fiber tips are on motorized x - y stages scanning the Σ_d plane. Detectors are single photon counters based on silicon avalanche diodes (Perkin Elmer SPCM-AGR-14). Detection events are timestamped with a time-to-digital converter (IDQ TDC id800) with 81 ps time resolution. The measurement of coincident pair events and the estimation of accidental events, as shown in Sec. 3.1.3, allow to determine the background corrected $G^{(2)}(\rho_1, \rho_2)$.

A sample object aperture, the USAF resolution target is used. The pattern with 31.25 μm slit width is used in the following. Correlation scans of the detectors are performed in one dimension across the object's slit pattern only. Fig. 6.3 shows the imaging result at different iris radii R . While panel (a) shows no resolution degradation but only the finite correlation length of the SPDC source, see also Sec. 3.1.2, the other panels clearly show the blurring due to widened PSF. The theoretical plot of panel (d) uses the imaging parameters of (b), the SPDC light source correlation width determined in Sec. 3.1.3, and the correlation function derived in Eq. (6.3).

In Fig. 6.4, the diagonals of Fig. 6.3(b) and (c) are compared to coherent illumination at the same wavelength of 810 nm by replacing the two-photon source with a laser. In Fig. 6.4(a), both light sources are able to resolve the slits, but SPDC shows higher visibility. With an imaging lens of smaller iris and broader PSF in panel (b), the individual slits are only resolved by two-photon light. These is expected due to the narrowing of the PSF discussed above. The theoretical prediction of Eq. (6.3) is shown together with the measurements.

Reconstruction results of IPNASB for our measurements with 1-D slit patterns are shown in Fig. 6.5. In contrast to the intensity signal in panel (d), panel (a) of the corresponding reconstructed image shows full visibility of the slits. In comparison to the indicated Rayleigh resolution (red lines), pixels of more than five times smaller size are possible to be reconstructed. This is a clear indication of imaging in a super-resolution regime.

Thermal Light Illumination

For near field imaging with thermal illumination, the setup of Fig. 6.2 is used. The light source is fully introduced and characterized in Sec. 3.3. A coherent laser beam at 405 nm is phase randomized using a rotating ground glass disk (GDD). Its far-field, obtained by lens L_2 ($f_2 = 75$ mm), is used for illuminating the object in plane Σ_1 . The resolution limited imaging is performed by lens L_3 with a mounted adjustable iris. Using the distance object and image distance $s_o = 232$ mm and $s_i = 455$ mm, a magnification of $m = 1.96$ is established. A correlation length of 35 μm is determined in Σ_1 , see Sec. 3.3.

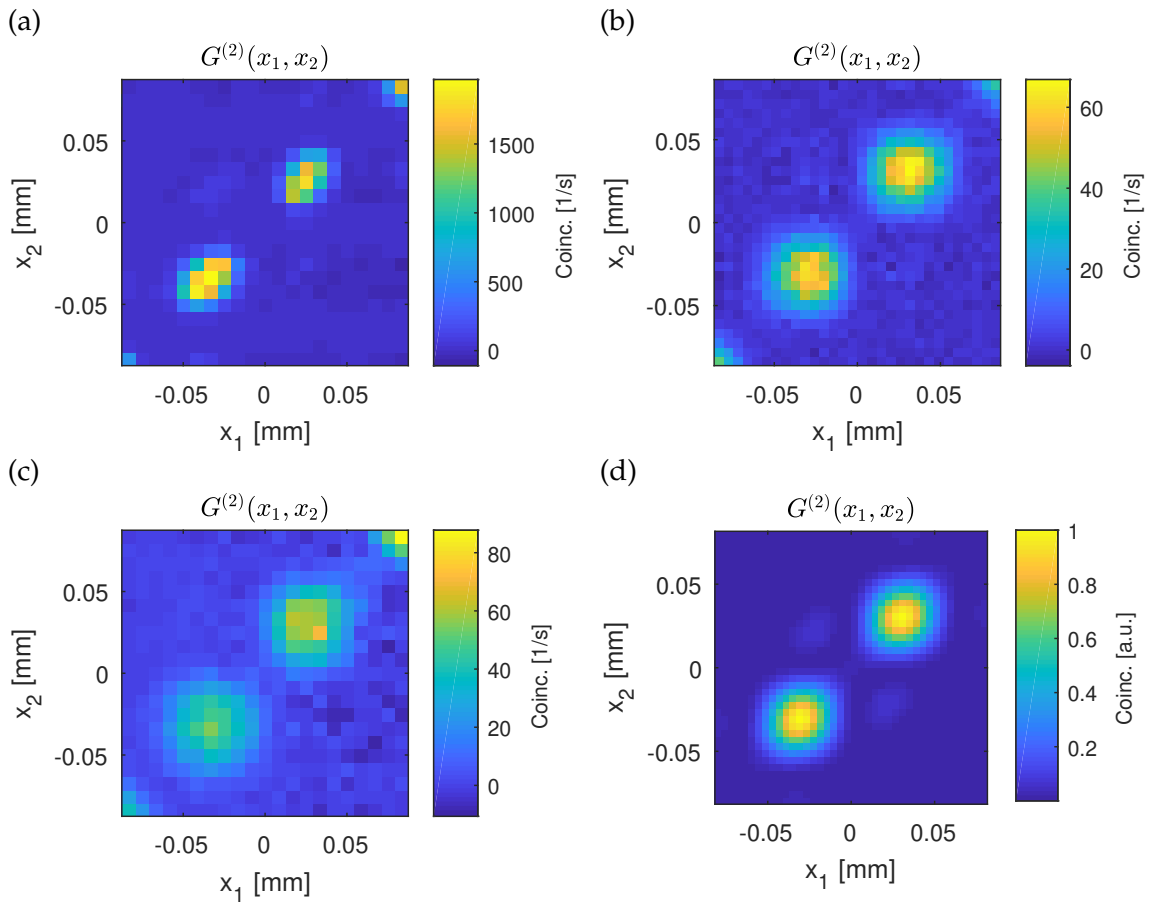


FIGURE 6.3: Near-field imaging of a double slit of $31.25 \mu\text{m}$ slit width using SPDC illumination. Only 1D correlation scans are performed. Rayleigh resolution is $5 \mu\text{m}$ (a), $32 \mu\text{m}$ (b, d) and $43 \mu\text{m}$ (c). The theoretical prediction for (b) is shown in (d).

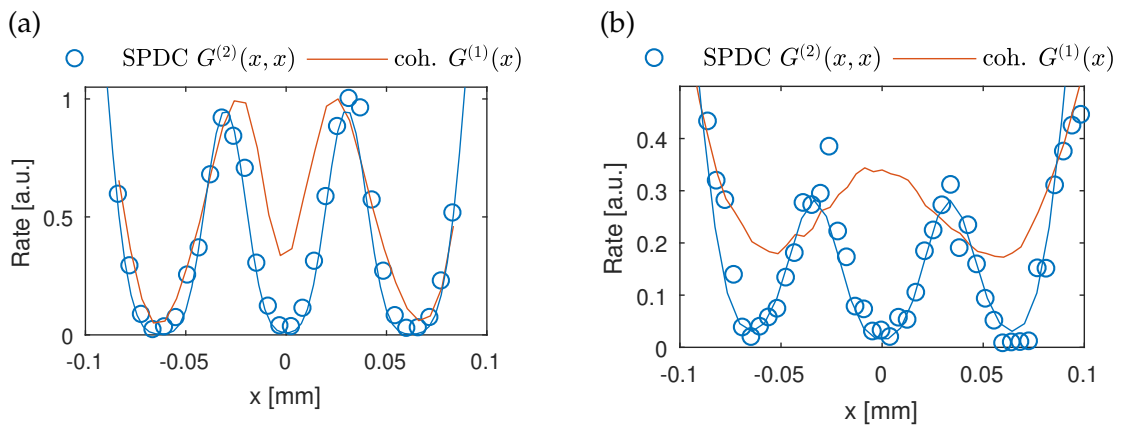


FIGURE 6.4: Near-field imaging of a 1D double slit of $31.25 \mu\text{m}$ slit width using SPDC and coherent illumination at 810 nm . The diagonal $G^{(2)}(x, x)$ is depicted for SPDC. Rayleigh resolution is $32 \mu\text{m}$ (a) and $43 \mu\text{m}$ (b). The two slits are only resolved by SPDC light in (b). Theory curves are shown for the SPDC measurements.

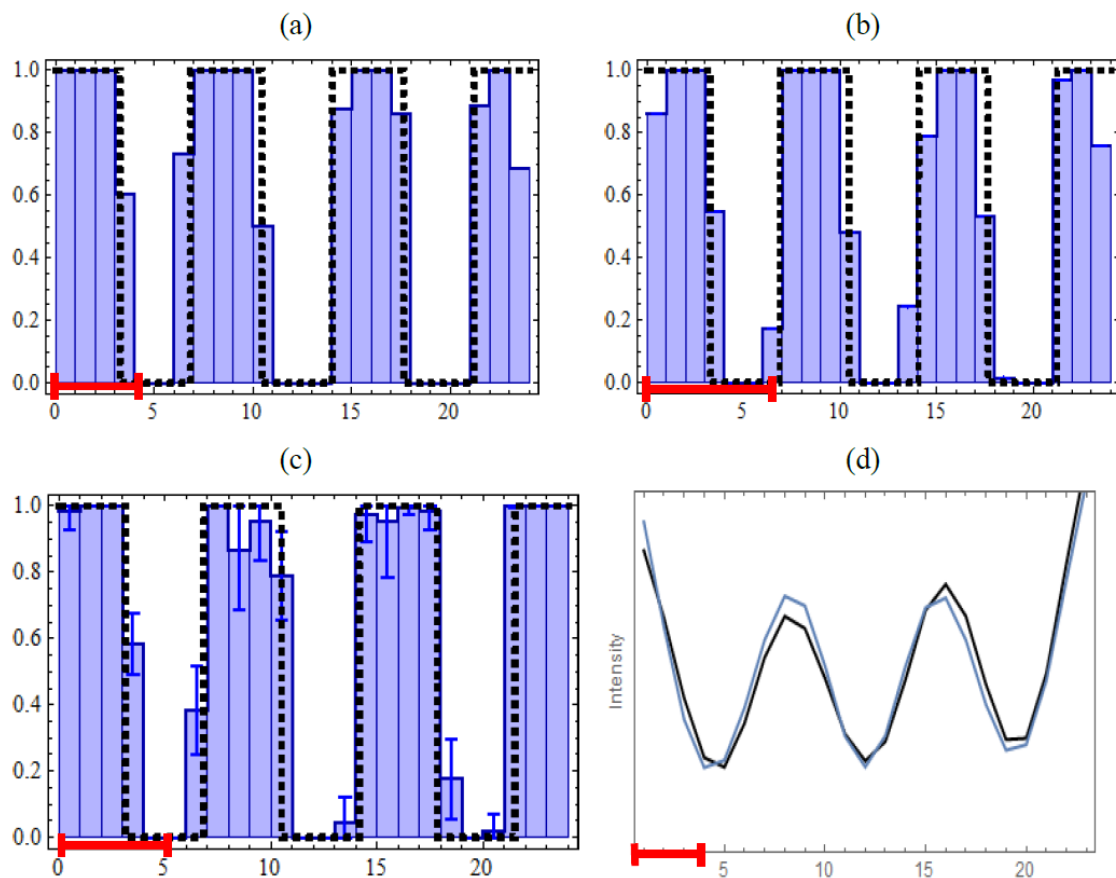


FIGURE 6.5: Reconstruction results from $G^{(2)}$ near-field measurements with SPDC illumination. The objects consist of 3 slits being $15.625 \mu\text{m}$ (a, b) and $31.25 \mu\text{m}$ (c) wide. One reconstructed pixel corresponds to $4.35 \mu\text{m}$ (a, b) and $8.51 \mu\text{m}$ (c) in the object plane. Rayleigh resolution is $13 \mu\text{m}$ (a,d), $21 \mu\text{m}$ (b) and $32 \mu\text{m}$ (c) indicated by the red lines. Bars show the reconstructed transmission function values. The dashed line corresponds to the expected object. Vertical error bars (c) show the estimated reconstruction error caused by statistical noise. The intensity distribution at the image plane for the object in (a) is shown in panel (d) for both detectors and corresponds to incoherent imaging. (Image courtesy of IPNASB)

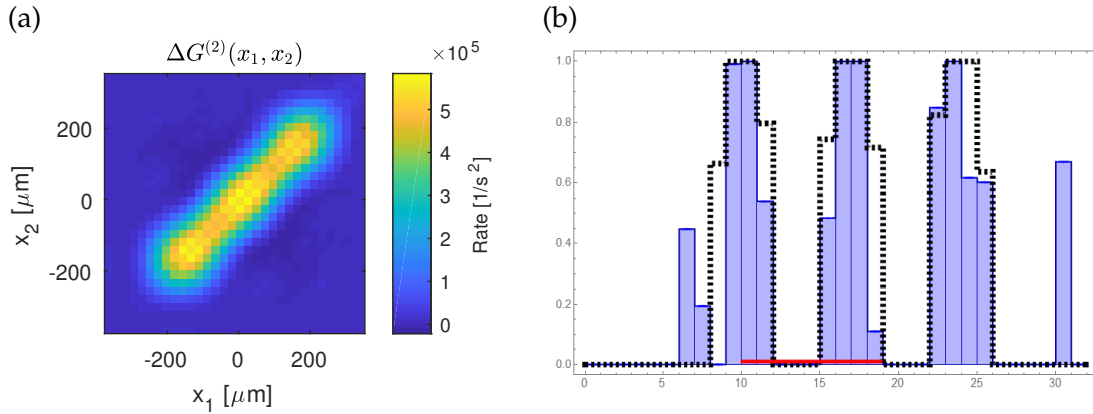


FIGURE 6.6: Near-field imaging of a triple-slit object with $79 \mu\text{m}$ slit width using thermal light illumination. The 1D second-order measurement (a) is used for object reconstruction in (b). Classical Rayleigh resolution is $140 \mu\text{m}$ indicated by the red line. (Image courtesy of IPNASB)

For light detection, the SuperEllen sensor array introduced in Sec. 5.2 is used. It is a 32×32 pixel array of single photon detectors of $44.67 \mu\text{m}$ pixel pitch. By employing the algorithm developed in Sec. 2.3.4, temporal coincident spatial correlation functions of high order can be measured.

A triple-slit pattern with $79 \mu\text{m}$ slit width is used in Fig. 6.6 as object. By using an iris of radius $R = 0.3 \text{ mm}$, the Rayleigh resolution of $190 \mu\text{m}$ does not allow the easy identification of three slits in the measurement in Fig. 6.6(a). The reconstruction in Fig. 6.6(b) successfully recovers the expected object features (dashed line).

An object aperture of digit 5 shape and a size of $275 \times 475 \mu\text{m}$ is used for imaging. Fig. 6.7 shows its measurement at different correlation orders. The uncorrelated background consisting of stray light and detector dark counts can be removed by the subtraction of $G^{(1)}$ at the according power. This is the reason why the image quality improves from panel (a), where no such subtraction can be performed, to the other higher-order measurements. Only correlation of pixels with itself, i.e. $G^{(N)}(\rho, \dots, \rho)$, are visualized for direct imaging illustration. As expected from theory, no increasing resolution with N is present in this case of thermal light. Note however, that the shown figures are cuts through high dimensional spaces available to a reconstruction algorithm.

Object reconstruction results for $G^{(2)}$ measurement at different PSF widths are shown in Fig. 6.8. Again, pixels smaller than the indicated Rayleigh resolution are successfully reconstructed and demonstrate the super-resolution regime. While data of higher order correlation is available as shown in Fig. 6.7, the algorithm of IPNASB is not yet ready to process these.

A direct comparison of imaging with a coherent, collimated laser beam and thermal light, both at the same wavelength of 405 nm , is shown in Fig. 6.9. The resolution advantage arising from the $\sqrt{2}$ improvement in PSF width as discussed in the theory section is clearly visible.

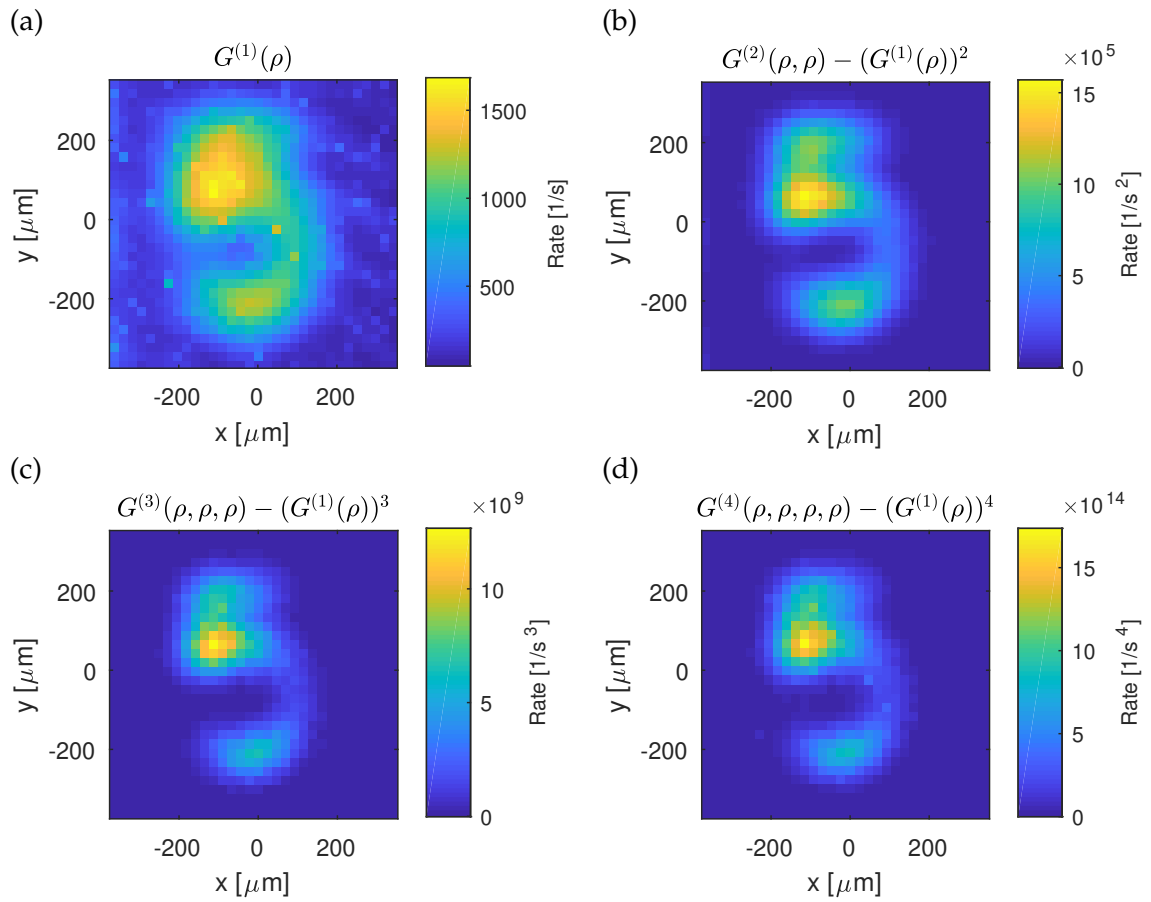


FIGURE 6.7: Near-field imaging with thermal light. Correlation orders $N = 1$ to 4 are shown of the same measurement with imaging lens iris diameter $R = 0.3$ mm corresponding to a Rayleigh resolution of $190 \mu\text{m}$. Only the pixel self-correlations, i.e. $\rho = \rho_1 = \dots = \rho_N$, are visualized. Coordinates units are defined in the object plane.

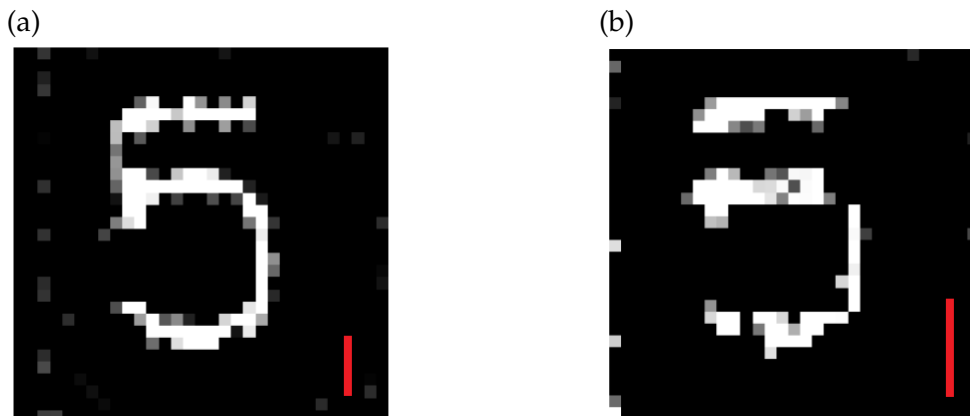


FIGURE 6.8: Reconstruction results for measured $G^{(2)}$ correlations using thermal illumination. One pixel corresponds to $22.7 \mu\text{m}$ in the object plane. Classical Rayleigh resolution is $114 \mu\text{m}$ (a) and $190 \mu\text{m}$ (b) indicated by the red line. Compare to the raw measurement of (b) in Fig. 6.7(b). (Image courtesy of IPNASB)

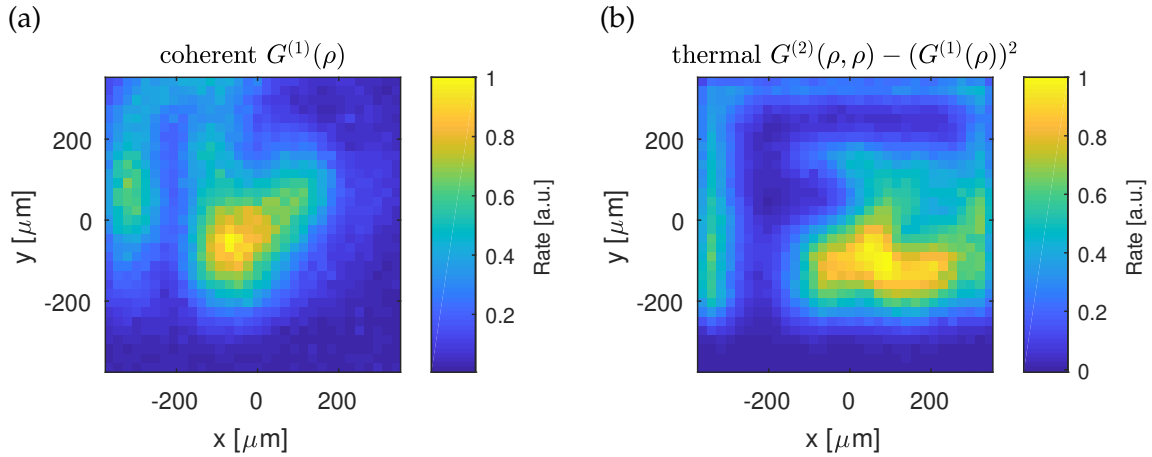


FIGURE 6.9: Near-field imaging with coherent (a) and thermal light (b) illumination at 405 nm. The same imaging lens iris radius with corresponding Rayleigh resolution of $140 \mu\text{m}$ is used.

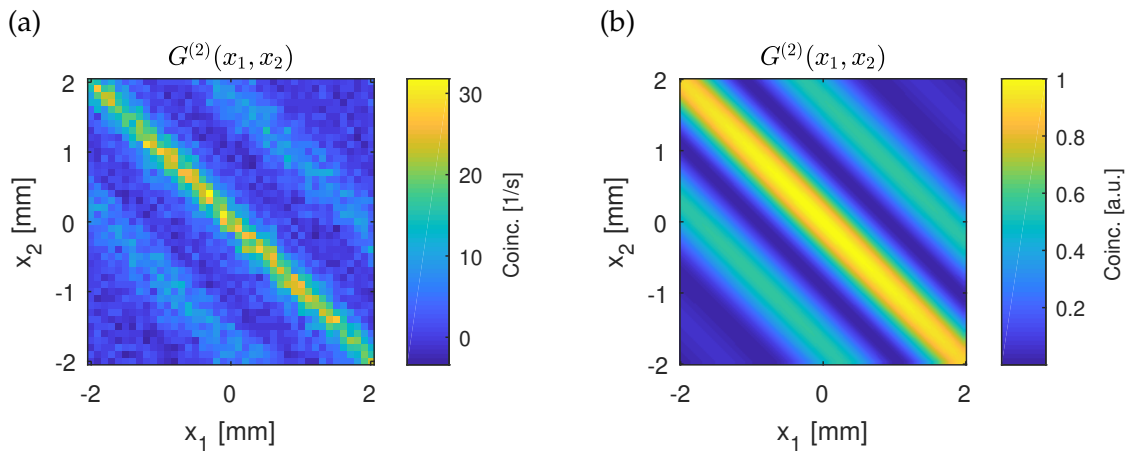


FIGURE 6.10: Far-field imaging of a double slit of $111 \mu\text{m}$ slit width using SPDC two-photon illumination in experiment (a) and theory (b). The correlation function is only measured in x direction transverse to the slit pattern while $y_1 = y_2 = 0$ is fixed on the optical axis.

6.2.2 Far-Field Imaging

In the far-field imaging modality, a lens is used to obtain the far-field diffraction pattern of the object. The iris for restricting the lens aperture is not used, i.e. fully open, as discussed in the theory section.

Two-Photon Illumination

In the far-field configuration, the setup of Fig. 6.1 is slightly adapted: Lens L3 is changed to focal length $f_3 = 500 \text{ mm}$ and the object and detector distances $s_o = s_i = f_3$ to establish the far-field, see Sec. 2.1.5. Otherwise, the same light source and measurement is used as for near-field imaging.

A measurement of the $G^{(2)}$ correlation function is shown in Fig. 6.10. A double slit aperture with $111 \mu\text{m}$ slit width is imaged and shows the diffraction pattern on the diagonal. The theory in panel (b) is calculated with Eq. (6.9). As the two-photon correlation length of $27.6 \mu\text{m}$ is much smaller than the slit width, the discussed limit of a thin is valid and we therefore have a correlation function given by Eq. (6.11) showing the anti-diagonal pattern.

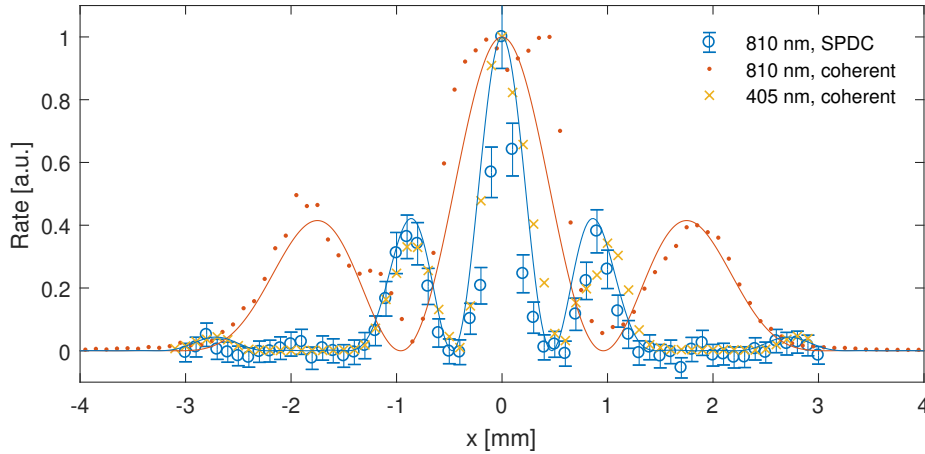


FIGURE 6.11: Far-field imaging of a double slit of $111 \mu\text{m}$ slit width using different light sources. Spatially coherent laser illumination at 810 and 405 nm is used and its intensity distribution shown. For SPDC two-photon illumination at 810 nm, the coincidence rate $G^{(2)}(x, x)$ (circles) is depicted with statistical 2σ errors. Theoretical curves for the classical sources are shown.

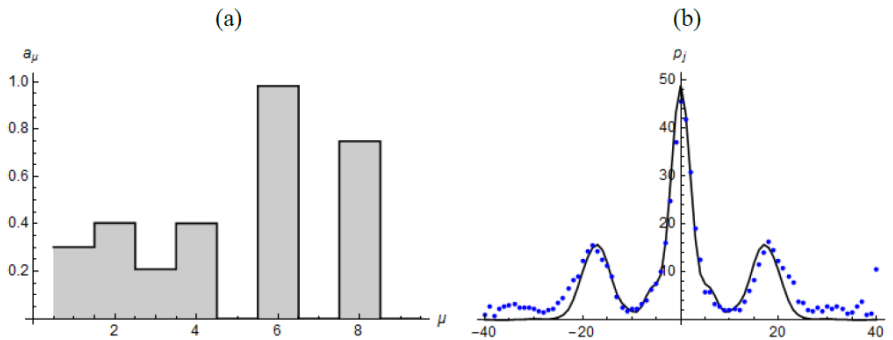


FIGURE 6.12: Reconstruction of the object (a) and the diagonal of a far-field $G^{(2)}$ measurement (b) with two-photon illumination. In (a), the used double slit is reconstructed in pixel 5 to 9. The measurement in (b) shows the diffraction pattern of this reconstructed object shape (line). (Image courtesy IPNASB)

Fig. 6.11 shows the far-field measurement of a double slit object using classical and two-photon illumination. Two-photon illumination shows the expected narrowing of the diffraction pattern corresponding to imaging at half the wavelength. A larger range of transverse wave vector information is available by using two-photon illumination. The theory curves show the diffraction pattern at the corresponding wavelength calculated using Eq. (6.8). The deviations of the measurement from theory are partially due to non-perfect object aperture, illumination wave fronts, and interference effects occurring in the object aperture carrier glass.

A preliminary reconstruction of a double-slit object is demonstrated in Fig. 6.12. While the main features of the double slit are clearly visible in pixels 5 to 9, some not expected artifacts occur for pixel 1 to 4. Non-perfect light source characteristics or not modeled aspects of the system seem to introduce these errors in reconstruction.

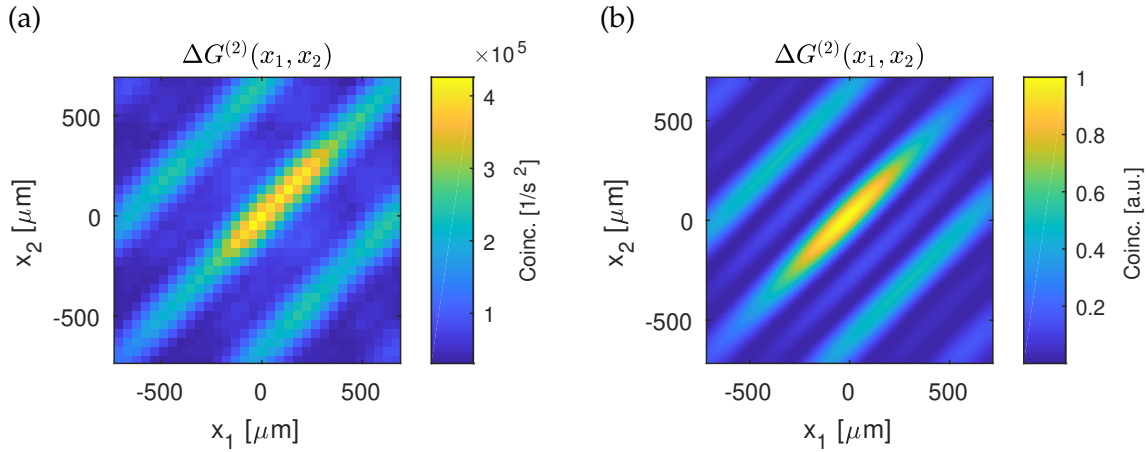


FIGURE 6.13: Far-field imaging of a triple slit of $62.5 \mu\text{m}$ slit width using thermal light in experiment (a) and theory (b). The second-order correlation function is only measured in x direction orthogonal to the slit pattern while $y_1 = y_2 = 0$ is fixed on the optical axis.

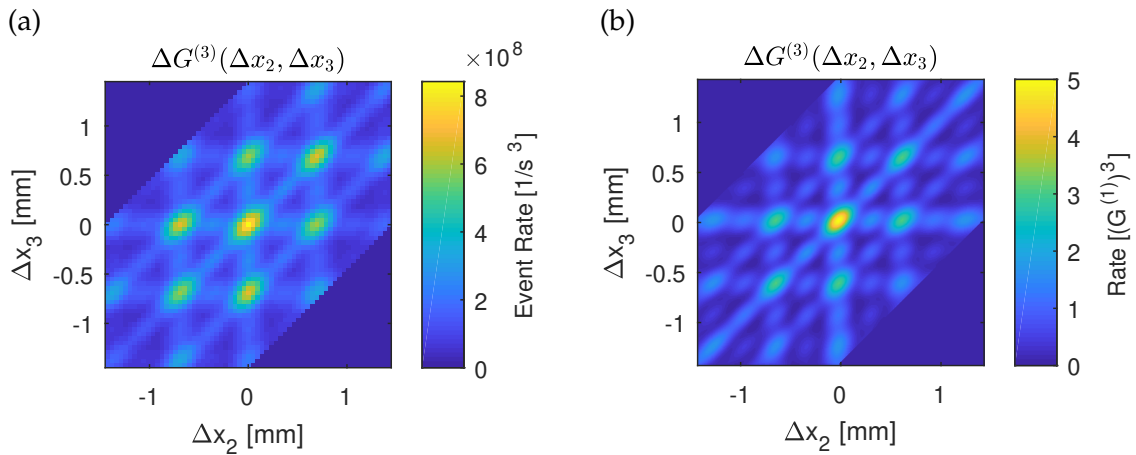


FIGURE 6.14: The third-order correlation $G^{(3)}$ for far-field imaging of a triple slit of $62.5 \mu\text{m}$ slit width using thermal light in experiment (a) and theory (b). Background is removed. Only the x direction orthogonal to the slit pattern is scanned while $y_1 = y_2 = y_3 = 0$. A projection of the $G^{(3)}(x_1, x_2, x_3)$ 3D space is shown using coordinates $\Delta x_2 = x_2 - x_1$ and $\Delta x_3 = x_3 - x_1$. Not measurable regions are visible.

Thermal Light Illumination

In the far-field configuration, the setup of Fig. 6.2 is slightly adapted: Lens L_3 is changed to focal length $f_3 = 200 \text{ mm}$ and the object and detector distances $s_o = s_i = f_3$ to establish the far-field, see Sec. 2.1.5. Otherwise, the same light source and measurement is used as for near-field imaging.

Fig. 6.13 shows the measured and theoretical $\Delta G^{(2)}$ for a triple slit object of $62.5 \mu\text{m}$ slit width. For theory, the correlation length $l_c = 35 \mu\text{m}$ determined in Sec. 3.3 and Eq. (6.12) is used. The very good agreement to theory shows that the same advantage as demonstrated in Fig. 6.11 for two-photon illumination is here realized with thermal light.

A projection of the third order correlation function of the far-field measurement with the same triple slit object is visualized in Fig. 6.14. The chosen projection plane has a normal vector $(1, 1, 1)$ in the (x_1, x_2, x_3) space. The coordinates $\Delta x_2 = x_2 - x_1$ and $\Delta x_3 =$

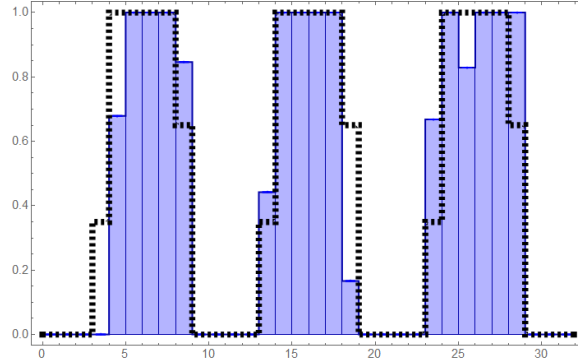


FIGURE 6.15: Reconstruction of the triple slit of $62.5 \mu\text{m}$ slit width from a far-field $G^{(3)}$ measurement using thermal light. The expected object (dashed line) is reconstructed in pixels of $13 \mu\text{m}$ width. (Image courtesy IPNASB)

$x_3 - x_1$ the projection. From the measured $G^{(3)}(\rho_1, \rho_2, \rho_3)$, we get the visualized quantity

$$\Delta G^{(3)}(\Delta x_2, \Delta x_3) := \sum_{\rho_1, \rho_2, \rho_3} [\Delta x_2 = x_2 - x_1 \wedge \Delta x_3 = x_3 - x_1 \wedge y_1 = y_2 = y_3 = 0] \left(G^{(3)}(\rho_1, \rho_2, \rho_3) - G^{(1)}(\rho_1)G^{(1)}(\rho_2)G^{(1)}(\rho_3) \right)$$

Here we used the Iverson bracket notation defined by: $[x] = 1$ if x is true, and $[x] = 0$ otherwise. Additional information beyond the second order correlation measurement is potentially expected in this structure. A reconstruction based on the full third-order correlation data is shown in Fig. 6.15. The triple-slit can be recovered with good agreement to the expected pattern (dashed line) while it can be shown, that the classical far-field measurement at the same wavelength would not allow for this detailed reconstruction.

6.3 Conclusion

We demonstrated in theory that the use of thermal and SPDC light for illumination brings advantages in terms of spatial resolution of imaging if higher order correlations are measured in the image plane. This was shown to be the case for optimal light source, i.e. with very small correlation length in the object plane, where the resolution improvement becomes explicit in the derived correlation functions available in a direct imaging scheme without data processing. In the near-field case, imaging with incoherent light shows the same resolution advantage of $\sqrt{2}$ as also shown for here used thermal and SPDC light by the narrowing of the effective PSF [19]. For far-field imaging, twice a broader transverse wave vector range is observable with both light sources.

Super-resolution object reconstruction was demonstrated in near- and far-field imaging. These results are promising and verified the developed algorithm with real measurement data. This allowed to spot before not modeled aspects like source inhomogeneities relevant for reconstruction. While the higher dimensionality of the correlation functions potentially carry more information than a simple intensity measurement, the ongoing Fisher information analysis performed by IPNASB will have to show the advantage of our approach over standard resolution improvement techniques, e.g. PSF deconvolution [37], by comparing it to their fundamental quantum limits imposed by noise [35, 36].

The experimental results agree to the theoretical predictions within expected errors. Only a minority of the performed experiments are shown. It is demonstrated that the experimental acquisition of correlation functions is feasible using the results of Sec. 2.3.

While for the thermal source the SuperEllen detector array is used, the low intensity of the SPDC source required the use of standard detectors with coupled scanning fibers. These show optimal detection efficiency (50% vs. 1%), optimal duty cycle (100% vs. 3%), and no crosstalk. The overhead due to scanning, which is avoided in SuperEllen, does not compensate for these drawbacks in second-order correlation measurements. Nevertheless, the exponentially increasing scanning time with correlation order N would put SuperEllen at an advantage already at moderate N . See also discussion in Ch. 5.

The SPDC two-photon illumination exhibits spatial entanglement, see Sec. 3.1. While this leads to the coherent integral in near-field imaging of Eq. (6.3), an almost identical expression is gained for classically correlated photon pairs in Eq. (6.6). It is not expected that this difference yields an advantage for object reconstruction. An arbitrary higher number of classically correlated photons can be produced by a randomly scanning focused beam of a classical light source. In this limit, the technique is related to standard scanning microscopy but where the scanning process is unknown and random. Measuring N th-order correlation functions, the resolution advantage is \sqrt{N} as implemented in [126]. In order to replace the time-consuming scanning, a non-Gaussian source of chaotic light is under investigation would allow to generate higher numbers of correlated photons.

In far-field imaging with entangled photons, it can be shown that a classical source emitting photon pairs in classically anti-correlated plane waves allows to measure a signal similar to Eq. (6.11) but with lower visibility. By replacing the random process of emission direction with a scanning direction plane wave illumination, exactly the same signal with not only two-fold but arbitrary larger observable wave vector spectrum is attainable while only requiring intensity measurements. This technique is successfully employed in Fourier ptychographic microscopy [127].

While entanglement is needed in the specific two-photon experiment to explain the far-field observation by multi-photon interference effects, the mentioned classical schemes in near- and far-field are equivalent alternatives and show that entanglement is not needed in order to gain the object information with the discussed improvements.

For application in microscopy, the scaling of the imaging resolution with light source parameters is of interest. If the physical advantages of narrowed PSF and broader wave vector spectrum, demonstrated above to exist for optimal light source, are shown to be of importance for object reconstruction, the following constraints have to be met: It can be shown that photon correlation length (coherence length for thermal light) in the object plane has to be smaller than the targeted resolution in order to achieve these advantages. For imaging with high resolution below the wavelength, the illumination with these correlation (coherence) lengths cannot be transmitted from a source to the object plane using a standard imaging system as these lengths would be increased to the system's resolution limit. An alternative is the generation of light directly in the object plane. Then, the illumination's evanescent field contribution needed for the sub-wavelength correlation or coherence length would allow to probe the object at this scale. Note, that for the analyzed low-resolution imaging systems with small lens apertures, the used scalar field and paraxial approximations are justified, see also assumptions in Sec. 2.1. For high numerical aperture lenses in microscopy, these break down. A vectorial field analysis has to show the advantages in this limit, as performed in [13] for other resolution enhancement techniques.

The scaling of direct imaging resolution with entangled photon number N is shown to be \sqrt{N} in near-field and N in far-field. Classically correlated photons show the same advantage in near-field and could provide resolution below the wavelength for high enough photon numbers N as a consequence of the narrowing of the PSF. Again, this only applies if sub-wavelength correlation lengths are realized in the object plane. Further enhancements

of statistical nature with a different scaling in N may be found for the object reconstruction. For thermal light, direct imaging in near- and far-field does not yield improvements at higher correlation order $N > 2$. Nevertheless, object reconstruction can potentially show a scaling in N which will be quantified by the ongoing Fisher information analysis.

The above reported \sqrt{N} resolution improvement for near-field imaging is at the so called standard quantum limit. As discussed, entanglement is not exploited and the same measurement results are available with classical sources. The scaling can be explained by a position averaging process and the central limit theorem of statistics, see also Sec. 7.6.4. While this is the case for the here described application in microscopy, i.e. the measurement of an object, the next chapter's goal of generating super-resolved structures of light will explicitly depend on spatial entanglement of photons.

Chapter 7

Super-Resolution Quantum Imaging at the Heisenberg Limit

Resolution improvements using quantum light is well-established in interferometric measurements where path-entangled photon states, called NOON-states, show phase sensitivity increased by the number of entangled photons N [13]. The observed multi-photon interference effects is characterized by λ/N , the de Broglie wavelength of the multi-photon system in terms of the individual photon wavelength λ . A classical light source would have to be at the de Broglie wavelength in order to reproduce the same fringe oscillation period. This N -fold improvement is termed Heisenberg limit. In contrast to the standard quantum limit with \sqrt{N} advantage, usually corresponding to a statistical averaging effect, the Heisenberg limit requires non-classical correlations to be achieved.

Ch. 6 showed near-field imaging with a spatial resolution improvement of $\sqrt{2}$ at the standard quantum limit using a two-photon source for illumination. As discussed, it is possible to show that classical light sources allow to gain the same resolution, even for higher photon numbers. The following work aims to exploit quantum entanglement of two-photon states to demonstrate super-resolution at the Heisenberg. In the given experimental conditions of a single-lens imaging system, it is possible to show that a classical source of light would not allow for the theoretically described and experimentally verified resolution.

To the best of our knowledge, this is the first quantum imaging experiment of object features with full visibility and spatial resolution at the Heisenberg limit. The general theoretical result demonstrates super-resolution for arbitrary photon number N and the corresponding resolution improvement. Furthermore, it allows to study the mechanism leading to the advantage and thereby unifies recent approaches to super-resolution imaging. While the experimental scheme for $N = 2$, intended as exemplary demonstration of the principle, may not have direct applications in imaging, it nevertheless shows the fundamental properties of quantum states of light which could be exploited in future work. The here presented approach demonstrates the generation of these quantum states which physically carry super-resolved structures at the Heisenberg limit. In contrast to schemes for resolution improvement in microscopy which allow to recover information only, the super-resolution is here physically realized. Thereby, this would allow for lithography at the Heisenberg limit in contrast to other schemes aiming at super-resolution.

7.1 Preface

The seminal work by Tsang introduced the method of optical centroid measurement (OCM) [42]. A N -photon state with wavelength λ of the individual photons is assumed. It is shown, that the centroid position of the photons X and the total transverse momentum K ,

defined by the single photon transverse positions ρ_k and wave vectors q_k with

$$\mathbf{X} := \frac{1}{N} \sum_{k=1}^N \rho_k, \quad \mathbf{K} := \sum_{k=1}^N q_k,$$

are conjugate variables. An imaging system limits the transmitted q spectrum by a finite lens aperture or by the condition $|q| < k = 2\pi/\lambda$ for propagating (non-evanescent) waves, see also Sec. 2.1.4. This transmission bandwidth limit reduces the spatial resolution and is imposed on every photon individually. Therefore, the total momentum \mathbf{K} can achieve N -times higher maximal values if all q_k are correlated appropriately. This N -fold enlarged \mathbf{K} spectrum allows the N -fold increased spatial resolution in transmission of the centroid position \mathbf{X} and corresponds to the Heisenberg limit.

The fact that the variables \mathbf{X} and \mathbf{K} are conjugates of each other is equivalent to the statement that a multi-photon wave function $\Lambda(\mathbf{X})$ in position basis is the Fourier transform of the corresponding wave function $\tilde{\Lambda}(\mathbf{K})$ in wave vector basis. With the remark above, an image encoded in the centroid distribution given by $\Lambda(\mathbf{X})$ has therefore access to Fourier components with N -fold higher magnitude than the transmission bandwidth of single photons would allow. This motivates the form of the quantum state given by $\Lambda(\mathbf{X})$ which is put forward as an ansatz in Eq. (7.2) below.

The following sections show the manuscript released on arXiv [47]. The here presented version features more experimental measurement results than the official manuscript.

Super-Resolution Quantum Imaging at the Heisenberg Limit

Manuel Unternährer,¹ Bänz Bessire,¹
Leonardo Gasparini,² Matteo Perenzoni,² and André Stefanov¹

¹*Institute of Applied Physics, University of Bern, 3012 Bern, Switzerland*

²*Fondazione Bruno Kessler FBK, 38122 Trento, Italy*

Abstract. Quantum imaging exploits the spatial correlations between photons to image object features with a higher resolution than a corresponding classical light source could achieve. Using a quantum correlated N -photon state, the method of optical centroid measurement (OCM) was shown to exhibit a resolution enhancement by improving the classical Rayleigh limit by a factor of $1/N$. In this work, the theory of OCM is formulated within the framework of an imaging formalism and is implemented in an exemplary experiment by means of a conventional entangled photon pair source. The expected resolution enhancement of a factor of two is demonstrated. The here presented experiment allows for producing arbitrary super-resolved spatial structures in the photon centroid in single-shot operation without scanning or iteration. Photon detection is performed with a newly developed integrated time-resolving detector array.

7.2 Introduction

In metrology, the optimal measurements of a parameter under restricted use of limited measurement resources are studied [13, 128, 129]. Using N independent particles for probing a sample, the parameter estimation error is improved by $1/\sqrt{N}$ beyond what can be achieved using a single particle, and is called standard quantum limit (SQL) [20]. It was shown that the best possible measurement strategy with N particles is by using quantum

correlated states. This leads to an $1/N$ improvement in estimation error [20], an optimum which is called Heisenberg limit (HL) [21]. In the case of an interferometric parameter estimation using photons, the multi-photon states at wavelength λ exhibit features described by the de Broglie wavelength λ/N [22]. In imaging, i.e., the transmission of object shape information to an image plane, the wavelength λ of the used illumination and the numerical aperture (NA) of the imaging system determine the image resolution through the Rayleigh resolution limit $1.22\lambda/\text{NA}$ [3]. Quantum imaging makes use of quantum states of light to go beyond this limit [12]. Schemes such as ghost imaging [11, 13] or thermal light imaging [11, 34] rely on classical correlations and therefore cannot achieve improvement beyond the SQL. It has to be noted that in a standard imaging setup, only changing the illumination to a spatially entangled light source, the SQL cannot be beaten [19, 32, 39, 126]. In order to reach the HL, specific schemes are to be designed. Using temporally shaped classical light and nonlinear multi-photon absorbers systems for detection, measurement at the HL was shown for interference fringes [130–132]. A scheme using monochromatic quantum light for super-resolution lithography was proposed in [133, 134] which iteratively builds up in principle arbitrary structures.

Despite these advances, no actual imaging of object features at the HL has been performed yet. One reason is the lack of N -photon transmitters. These are shown in [19] to allow for imaging at the HL but can be omitted by preparing a quantum state which would be fully transmitted by such a device, as realized in this work. Time-consuming scanning or iteration in generation of the optical states to build up image structures in the aforementioned schemes prevented their application. Our experimental implementation of the state generation operates in a single-shot mode. Moreover, quantum imaging was hindered by the low speed of correlations measurements using scanning single-pixel devices. A recently developed integrated sub-nanosecond time-resolving 2-D detector array allows for fast correlation measurements without scanning [46]. Furthermore, the detection efficiency is highly enhanced by the method of optical centroid measurement (OCM).

Tsang presented in [42] the OCM method and showed its ability to efficiently transmit the centroid position of a monochromatic, spatially entangled N -photon state beyond the Rayleigh diffraction limit. He theoretically showed that the resolution enhancement scales with $1/N$ corresponding to the HL where the de Broglie wavelength λ/N determines resolution. OCM was experimentally implemented in [40] for photon number $N = 2$ and in [41] for $N = 2$ to 4. Both groups demonstrate super-resolution at the HL by measuring oscillation periods of interference fringes of two plane waves.

In this work, the OCM method is used in an imaging setting where actual object features instead of interference fringes are observed. The OCM theory is derived in an imaging formalism. Moreover, coherent OCM imaging is implemented for photon number $N = 2$, where an experimental setup is presented which allows to generate an entangled biphoton state containing the super-resolved OCM image. In contrast to resolution enhancement techniques by image post-processing or correlation measurements in quantum microscopy [13], the here generated quantum state of light physically carries spatial structure surpassing the Rayleigh limit. As a distinctive property to previous works, this would allow for quantum lithography at the HL.

7.3 Theory

An object can be described by its transmission aperture function $A(\boldsymbol{\rho})$ in transverse position coordinates $\boldsymbol{\rho} = (x, y)$. For a monochromatic, spatially coherent and uniform light source at wavelength λ , the electric field after the object becomes $E(\boldsymbol{\rho}) \propto A(\boldsymbol{\rho})$. The goal of an imaging system is to reproduce the object field distribution in a distant plane where

it can be measured or exposes a film. For a general imaging system, the field intensity in the image plane reads

$$I(\boldsymbol{\rho}) = \left| \int d^2\rho' A(\boldsymbol{\rho}') h\left(\frac{\boldsymbol{\rho}}{m} - \boldsymbol{\rho}'\right) \right|^2 = \left| (A * h)\left(\frac{\boldsymbol{\rho}}{m}\right) \right|^2 \quad (7.1)$$

with magnification m and the point-spread function (PSF) $h(\boldsymbol{\rho})$ being specific to that system and used wavelength [3, 11]. A translation invariant PSF is assumed. Image resolution can be then defined by the width of the PSF and an optimal image is achieved with $h(\boldsymbol{\rho}) = \delta^{(2)}(\boldsymbol{\rho})$.

In order to transmit with an imaging system object features below the size of its PSF, i.e., the Rayleigh limit, Tsang proposed to replace the classical field distribution at the object plane by quantum correlated multi-photon states [42]. From these results, an explicit state can be constructed. For the case of a coherent image of the object $A(\boldsymbol{\rho})$ and N photons at wavelength λ , the OCM image state reads

$$|\Psi\rangle = \int d^2\rho_1 \dots d^2\rho_N A\left(\frac{\boldsymbol{\rho}_1 + \dots + \boldsymbol{\rho}_N}{N}\right) |\rho_1, \dots, \rho_N\rangle \quad (7.2)$$

in transverse positions of the photons $\boldsymbol{\rho}_1, \dots, \boldsymbol{\rho}_N$. Introducing new coordinates simplifies further analysis. The centroid position \mathbf{X} and the deviations $\boldsymbol{\zeta}_k$ are defined by

$$\mathbf{X} := \frac{1}{N} \sum_{k=1}^N \boldsymbol{\rho}_k, \quad \boldsymbol{\zeta}_k := \boldsymbol{\rho}_k - \mathbf{X}, \quad k \in \{1, \dots, N\}.$$

Due to $\sum_k \boldsymbol{\zeta}_k = 0$, the N -tuple $(\mathbf{X}, \boldsymbol{\zeta}_1, \dots, \boldsymbol{\zeta}_{N-1})$ forms a complete coordinate system. In these coordinates, the quantum state encodes the image in the centroid position \mathbf{X} . Notice the infinite extension of the state in all $\boldsymbol{\zeta}_k$ coordinates in this optimal case.

Propagating the electric field from the object plane through the imaging system, the N -photon detection probability density in the image plane is given by the N -th order correlation function [52]

$$G^{(N)}(\boldsymbol{\rho}_1, \dots, \boldsymbol{\rho}_N) = \left| \int d^2\rho'_1 \dots d^2\rho'_N A(\mathbf{X}') h\left(\frac{\boldsymbol{\rho}_1}{m} - \boldsymbol{\rho}'_1\right) \dots h\left(\frac{\boldsymbol{\rho}_N}{m} - \boldsymbol{\rho}'_N\right) \right|^2.$$

A change to the coordinates \mathbf{X} and $\boldsymbol{\zeta}_k$ with $k \in \{1, \dots, N-1\}$ leads to

$$G^{(N)}(\mathbf{X}, \boldsymbol{\zeta}_1, \dots, \boldsymbol{\zeta}_{N-1}) = \left| (A * H)\left(\frac{\mathbf{X}}{m}\right) \right|^2, \quad (7.3)$$

where the centroid PSF is given by the N -times repeated self-convolution

$$H(\mathbf{X}) = N^2 \underbrace{(h * \dots * h)}_{\times N}(\mathbf{X}) \quad (7.4)$$

and determines the resolution of the image in the centroid coordinate \mathbf{X} , see Sec. 7.6.1. As formally explicit in comparison to Eq. (7.1), the image is formed coherently. With an appropriate mixed state, an incoherent imaging variant is derived in Sec. 7.6.2. Summing $G^{(N)}$ over the $\boldsymbol{\zeta}_k$ coordinates in dependence of the \mathbf{X} coordinate yields the 2-D image.

In the following, we consider for the imaging system a single lens with a circular pupil of radius R determining its NA and Rayleigh resolution limit. The PSF is then given by a sombrero function $h(\boldsymbol{\rho}) = \text{somb}(2\pi R|\boldsymbol{\rho}|/s_o\lambda)$ with the distance s_o from the object plane to the lens [3, 11]. By assuming $s_o \gg |\boldsymbol{\rho}|^2/\lambda$ for $\boldsymbol{\rho}$ in the object and detector area, the phase $\exp(i\pi|\boldsymbol{\rho}|^2/\lambda s_o)$ appearing in the object plane for single lens imaging can be neglected. This establishes the translation invariance of the PSF. Using Eq. (7.4), it can be shown that

$$H(\mathbf{X}) = C \text{somb} \left(\frac{2\pi RN}{s_o\lambda} |\mathbf{X}| \right), \quad (7.5)$$

with an appropriate normalization constant C , see Sec. 7.6.1. The additional factor of N in the argument reduces the width of the PSF, a spatial resolution enhancement corresponding to a Heisenberg $1/N$ scaling in photon number N .

For discussing the mechanism of resolution enhancement, it is of value to determine the photon correlations in the plane of the lens pupil. Assuming s_o to be large, correlations in far-field can be considered. The OCM state of Eq. (7.2) in a far-field basis is given by

$$|\Psi\rangle = \int d^2\mathbf{q} \tilde{A}(N\mathbf{q}) |\mathbf{q}, \dots, \mathbf{q}\rangle \quad (7.6)$$

where $\tilde{A}(\mathbf{q})$ is the Fourier transform of $A(\boldsymbol{\rho})$ in the transverse wave vector coordinate \mathbf{q} . This coordinate can be related to a position in the pupil plane by $\boldsymbol{\rho} = (s_o\lambda/2\pi)\mathbf{q}$ in paraxial approximation [3]. Strong position correlation is therefore present at the pupil.

7.4 Experiment

Our exemplary experiment generates an OCM state for photon number $N = 2$. With a following low NA single lens imaging, its spatial resolution capability can be assessed and compared to theory and classical light sources. The optical setup for the preparation of the OCM state given in Eq. (7.2) with $N = 2$ is depicted in Fig. 7.1. An object aperture $A(\boldsymbol{\rho})$ is illuminated by a CW pump laser at 405 nm and 30 mW in the plane Σ'_o . A 4-f lens system, consisting of two lenses L_1 and L_2 of focal length $f = 50$ mm, images the object to the preparation output plane Σ_o . In the far-field plane between the lenses, a 5 mm long periodically poled KTiOPO₄ nonlinear crystal (NLC) generates photon pairs in type-0, frequency-degenerate, collinear spontaneous parametric down-conversion (SPDC). This emission is spectrally filtered by a bandpass filter (BP) transmitting $\lambda = 810 \pm 5$ nm.

Using the approximation of a thin crystal and a plane wave pump, the entangled biphoton state in the output plane Σ_o is derived in [52] and is given by Eq. (7.2) for $N = 2$. In the thick crystal case, it can be shown to read

$$|\Psi\rangle = \int d^2\boldsymbol{\rho}_1 d^2\boldsymbol{\rho}_2 A \left(-\frac{\boldsymbol{\rho}_1 + \boldsymbol{\rho}_2}{2} \right) \text{sinc} \left(\frac{\Delta k L}{2} \right) |\boldsymbol{\rho}_1, \boldsymbol{\rho}_2\rangle \quad (7.7)$$

with the NLC length L and wave vector mismatch $\Delta k(\mathbf{q}_1, \mathbf{q}_2)$ evaluated at $\mathbf{q}_k = (2\pi/\lambda f)\boldsymbol{\rho}_k$, $k \in \{1, 2\}$, see full derivation in Sec. 7.6.3. The mentioned infinite extension of the ideal OCM state in Eq. (7.2) is here restricted by the dependence of this phase-matching function on $\boldsymbol{\xi}_1 = (\boldsymbol{\rho}_1 - \boldsymbol{\rho}_2)/2$.

The resolution limited imaging is performed from Σ_o to the image plane Σ_i with the lens L_3 of 250 mm focal length at a distance $s_o = 355$ mm between Σ_o and the lens. With the given detector and object sizes, the assumption of a large s_o in the theory section is

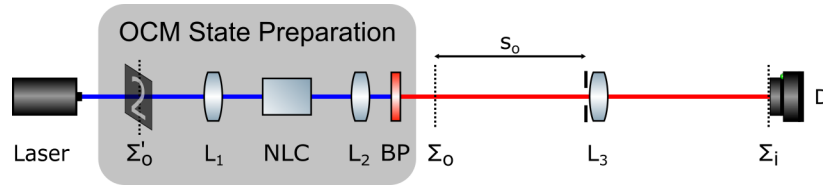


FIGURE 7.1: The optical setup consisting of OCM state preparation and single-lens imaging (right). A 405 nm laser source illuminates an object in the plane Σ'_0 . 4-f imaging from Σ'_0 to the output plane Σ_0 is performed by the lenses L_1 and L_2 . The non-linear crystal (NLC) in the central far-field plane produces photon pairs in SPDC. A bandpass filter (BP) transmits 810 nm. The actual imaging under investigation is performed by the lens L_3 from output plane Σ_0 to image plane Σ_i . L_3 is equipped with a circular pupil to reduce its NA and therefore the resolution of the imaging system. The 2-D detector array D measures spatial biphoton correlations.

valid. A magnification of $m = 2.4$ is measured. A circular pupil of radius $R = 1.38$ mm in front of the lens limits the NA.

For resolution comparison, the classical light sources are spatially coherent, monochromatic illumination at 405 nm and 810 nm, as well as spatially incoherent light at 810 nm. The former are implemented using collimated lasers, the latter by a halogen incandescent lamp spectrally filtered at 810 ± 5 nm. For imaging with classical light, the setup of Fig. 7.1 is used unaltered and allows comparison with otherwise identical parameters.

The newly developed detector used in the image plane Σ_i is an integrated, fully digital 32×32 pixel sensor array with single-photon sensitivity manufactured in CMOS technology [46]. The size of the pixel being smaller than the PSF of the optical system is thus not limiting the resolution. This device contains for every pixel a dedicated time-to-digital converter which timestamps the first detection event at 205 ps resolution in a frame of 45 ns duration. At an observation rate of 800 kHz, a measurement duty-cycle of 3.6% is achieved. The photon detection efficiency reaches 5% at 400 nm and 0.8% at 810 nm. Covering a sensitive region of 1.4×1.4 mm², the sensor is capable of efficiently measuring second-order correlation functions similarly to its predecessor presented in [43]. Despite these type of devices exist since 2009 [46], their use in quantum optics applications were limited by low fill-factor (1-5%). Only recently it was possible to achieve 19.48% allowing useful detection efficiencies [46]. For this work, a coincidence window of 1 ns is used where accidental events including all dark counts can be measured and removed.

In Fig. 7.2(a–e), a 200×300 μm object aperture is imaged at low NA values with different light sources. In the case of OCM, the measurement of the full second-order correlation function of Eq. (7.3) yields the image of Fig. 7.2(a) by summing over ξ_1 . This introduces a vignetting effect in the resulting image due to the finite sensor size which acquires a broader range of ξ_1 values in the image center than at the edges. It can be avoided by averaging instead of summing over the available ξ_1 values but leads to higher statistical noise at the edges, see Fig. 7.2(e). Because the image is encoded in the centroid position, the image can be reconstructed at half-pixel precision leading to 63×63 pixels images acquired by the 32×32 pixels sensor. In order to suppress detector crosstalk between adjacent pixels, only events with $|\xi_1| > 1$ pixel are considered. A measurement time of one hour is used for the high NA in Fig. 7.2(f), while ten hours is used at low NA in Fig. 7.2(a).

For a more objective comparison, cross-sections of a triple-slit object of $70 \mu\text{m}$ line width imaged at low NA are shown in Fig. 7.3. OCM imaging resolution surpasses coherent and incoherent light at 810 nm and shows practically identical resolution as 405 nm. Imaging a point of $25 \mu\text{m}$ Gaussian waist radius realized by focussing the pump laser and classical light sources in the object plane Σ'_0 , the PSF of the single lens imaging at low NA is

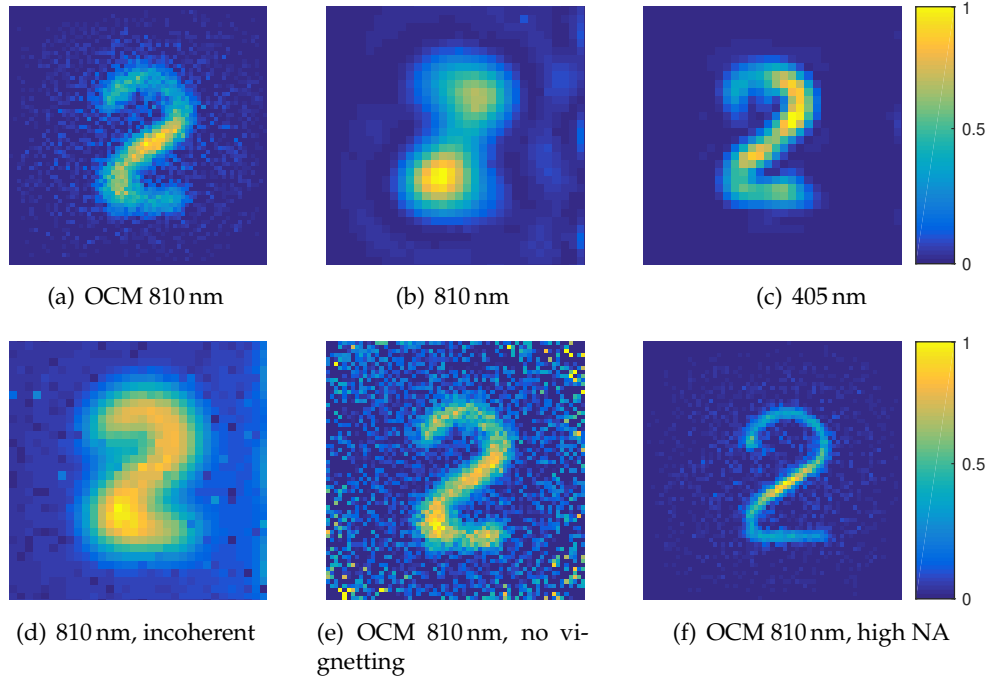


FIGURE 7.2: Imaging of an object using a single lens with different illumination light sources. Low NA is used in (a–e) to demonstrate the wavelength dependence of resolution. Spatially coherent laser illumination is used in (b) and (c). The region of $1.4 \times 1.4 \text{ mm}^2$ is acquired by a 32×32 pixels sensor. Biphoton OCM yields images at half-pixels and achieves a comparable image resolution at 810 nm as a coherent light at 405 nm. The vignetting effect in image (a) is removed in (e). For reference, an OCM image at high NA is shown in (f).

compared in Fig. 7.4. The theoretical curves for classical imaging are given by Eq. (7.1) and the classical PSF of Eq. (7.5) with $N = 1$. Classically correlated photons pairs of OCM type would produce a centroid PSF $|H(\mathbf{X})|^2 = (|h|^2 * |h|^2)(2\mathbf{X})$ derivable analogously to Eq. (7.4), see Sec. 7.6.4. This distribution is shown for comparison (dashed line) and scales at the SQL. This limit is clearly beaten by the OCM PSF and thereby verifies the quantum correlation nature of the enhancement.

With the full measurement of the correlation function in Eq. (7.3), spatial correlations of the OCM state can be analyzed. A double-slit of $200 \mu\text{m}$ line width is used as object. The OCM state shows in Fig. 7.5(a) position correlations along the x -direction orthogonal to the slits. This can be understood in terms of a 1-D version of Eq. (7.3) with $N = 2$, where the image is encoded in the centroid X (diagonal) and independence in ξ_1 (anti-diagonal) is present. Both inner slit edges and the central dark separation are visible, vignettted by the pump beam shape. Replacing the imaging lens by a far-field lens of 400 mm focal length placed in this distance in front of the detector, far-field correlations of Fig. 7.5(b) are measured. Strong position correlations are observed in agreement with Eq. (7.6). Furthermore, comparing the diagonal of this biphoton diffraction pattern to a measurement with coherent light at 405 nm in Fig. 7.5(c) yields almost identical results, confirming the theoretically predicted relevance of the twice smaller de Broglie wavelength. A related result was obtained in [17].

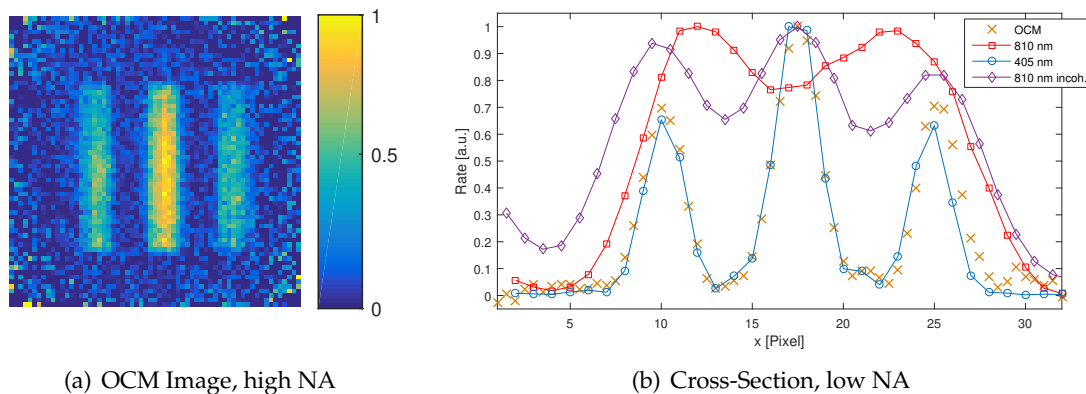


FIGURE 7.3: A triple-slit object of $70 \mu\text{m}$ line width (a) is used for resolution comparison. (b) shows cross-sections of images at low NA using biphoton OCM at 810 nm (orange crosses), spatially coherent illumination at 810 nm (red squares) and 405 nm (blue circles), and incoherent light at 810 nm (violet diamonds). OCM shows an advantage which is practically identical to the double resolution given with 405 nm.

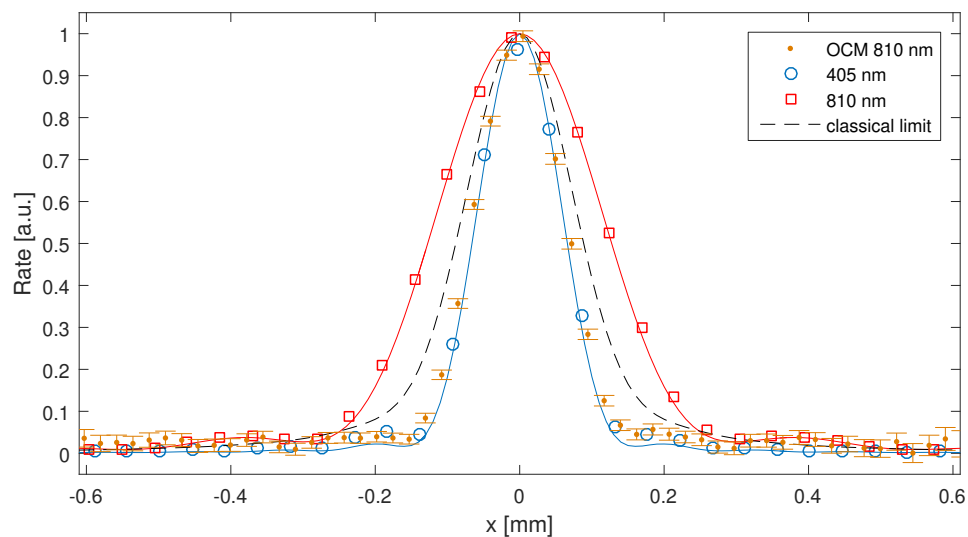


FIGURE 7.4: Projection of the PSF of low NA single lens imaging at different light sources. Measurements with coherent light at 810 nm (red squares) and 405 nm (blue circles) are shown with their theoretical curves. The biphoton OCM PSF at 810 nm (orange dots) closely agrees with 405 nm and confirms its doubled resolution. Statistical 2σ errors are shown. The OCM PSF surpasses a theoretical, SQL-scaling PSF of the centroid of two classically correlated photons at 810 nm (dashed line).

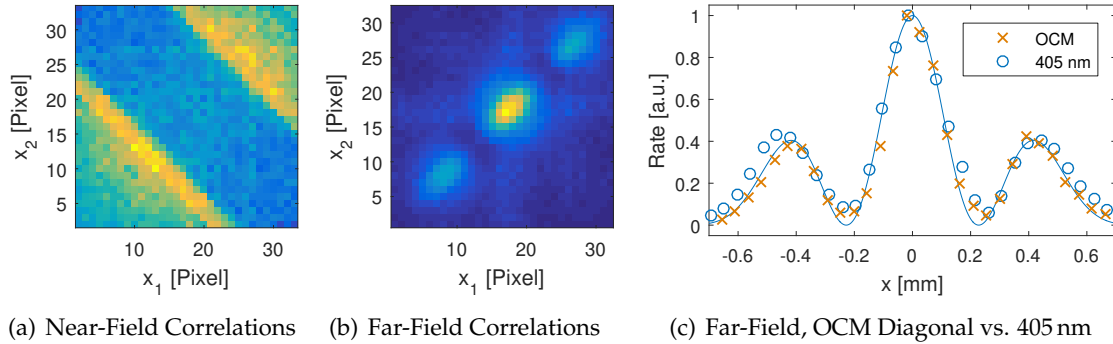


FIGURE 7.5: The biphoton OCM state of a double-slit is analyzed in near- and far-field for position-correlations in x -direction orthogonal to the lines. The high NA near-field measurement in (a) shows the image features on the diagonals and thereby in the centroid position. In far-field (b), strong correlation is observed. (c) shows the diagonal of this OCM diffraction pattern (orange crosses) and the expected narrowing down to the width produced with coherent light at 405 nm (blue circles). The theoretical curve for the latter is shown.

7.5 Discussion

The mechanism giving rise to the super-resolution can be understood by considering the far-field correlations of the OCM state. As evident in Eq. (7.6), it shows strong wave vector correlations or, equivalently, position correlations in the pupil plane. This situation can be regarded as a multi-mode NOON-state emanating from the lens and propagating to the image plane. As shown in [40, 41] for two-mode NOON states, this leads to N -times narrower multi-photon interference fringes in the image plane. The here presented multi-mode case allows to build up an image by the coherent superposition of such fringes of different directions and sizes.

With the current SPDC sources of entangled photons, the here presented method of generating the OCM state is the most efficient. To avoid the separation between state generation and imaging, a thin NLC could be placed directly at the imaging lens covering the full pupil area at the price, however, of lower efficiency. For reaching larger photon number N , higher order non-linear effects should be used [135].

Furthermore, the non-linearity needed to generate entanglement could in principle take place in the optical setup instead of the source. For instance, as previously mentioned, super-resolution can be achieved by using a spatially correlated light source for illuminating the object and using a N -photon transmitter (NPT) in front of the imaging lens [19]. Such devices would transmit spatially correlated N -photon states only, maintaining the N -photon coherence. Effectively, this filtering projects the incoming state to Eq. (7.6) or its incoherent imaging analogue and would therefore create an OCM state in the image plane. This general principle can be extended to an optical system of many lenses, where a NPT is placed at every lens. Intuitively, this mimics the propagation of a single photon of the de Broglie wavelength by forcing all N photons to stay together and tracing the same paths. As efficient NPT are yet not practically available, another approach was proposed in [11] for $N = 2$. The object is illuminated by spatially correlated biphoton light. Ultra-fast temporal quantum correlations of the pair is used through their relative time-of-arrival in the image plane to post-select on correlated positions on the lens pupil, where both photon take the same path, thus enabling resolution at the HL. It still has to be analyzed how temporal and spatial resolution are related and how to extend this scheme to higher N .

For an imaging system with a number of transmitted modes m [35, 36], the expected

dimension of the Hilbert space of a transmitted N -photon state is m^N . While this corresponds to the information, i.e. number of orthogonal states that could be conveyed, OCM imaging only uses Nm modes. The reason for this is given by the fact, that in the OCM result only the correlations in the centroid are relevant and all other degrees of freedom Ξ_k are neglected and traced out. This is a natural choice if lithography is targeted where a multi-photon absorber is sensitive to spatial coincident events and not to long range correlations. But from an information theoretic point of view, the larger Hilbert space allows in principle for even more transmitted information.

In conclusion, our theoretical and experimental results demonstrate the possibility to engineer quantum states of light which physically carry super-resolved spatial structure at the HL. This is investigated in low NA single-lens imaging, where spatial resolution is compared across different light sources. The OCM biphoton state shows an enhancement close to a factor of two corresponding to a Rayleigh resolution at its de Broglie wavelength. For high NA systems, where the classical resolution is mainly limited by the wavelength, or for higher photon number N , theory suggests the possibility to see sub-wavelength features. A full vectorial field analysis in contrast to the scalar approximations has yet to show the advantage in this limit.

The results presented here were made possible by the development of an integrated single-photon detector array; although the present device has non-optimal detection efficiency at the used wavelength. By optimizing the design and increasing the numbers of pixel, CMOS detectors will certainly be a key components of any future applications in the field of quantum imaging.

As elaborated by Tsang in [42] and shown here, the image acquisition efficiency of the OCM correlations is very high due to the fact that every N -photon event carries image information. In the case of an N -photon absorbing film in lithography, where only spatially coincident events ($\xi_k = 0$, $k \in \{1, \dots, N\}$) are registered, the image would be reproduced at N -fold resolution but at an efficiency which is expected to drop exponentially with N [19]. Efficiency can be gained by loosening the condition of strong correlation in far-field. An analysis of resolution and efficiency versus correlation length and photon number has yet to be performed.

The here developed theory is general and allows for different experimental realizations. As a concrete example, the presented biphoton experiment serves as a proof-of-concept, clearly agreeing to the theory and showing the advantage over classical light sources. Moreover, by unifying the understanding of recent results aiming at super-resolution at the HL, it might stimulate new paths of research.

7.6 Supplementary Material

This section provided together with the main manuscript of the last sections as supplementary material.

7.6.1 Derivation of the OCM Imaging Equation

This section provides a step-by-step derivation of Eq. (7.3) and (7.4). Starting from the N -th order correlation function in the image plane

$$G^{(N)}(\rho_1, \dots, \rho_N) = \left| \int d^2\rho'_1 \dots d^2\rho'_N A \left(\frac{\rho'_1 + \dots + \rho'_N}{N} \right) h \left(\frac{\rho_1}{m} - \rho'_1 \right) \dots h \left(\frac{\rho_N}{m} - \rho'_N \right) \right|^2,$$

where the simplification of setting the magnification to $m = 1$ does not limit the generality of the following result. A coordinate change to the centroid and deviation variables

$$\mathbf{X} = \frac{1}{N} \sum_{k=1}^N \boldsymbol{\rho}_k, \quad \boldsymbol{\zeta}_k = \boldsymbol{\rho}_k - \mathbf{X}, \quad k \in \{1, \dots, N\},$$

yields for the integral in the modulus

$$N^2 \int d^2 \mathbf{X}' d^2 \boldsymbol{\zeta}'_1 \dots d^2 \boldsymbol{\zeta}'_{N-1} A(\mathbf{X}') h(\mathbf{X} + \boldsymbol{\zeta}_1 - (\mathbf{X}' + \boldsymbol{\zeta}'_1)) \dots h(\mathbf{X} + \boldsymbol{\zeta}_N - (\mathbf{X}' + \boldsymbol{\zeta}'_N)).$$

The Jacobian determinant of this coordinate transformation can be readily shown to be $|\det J| = |\det J_x| \cdot |\det J_y| = N^2$ and is present as a prefactor. By a change of variables to $\boldsymbol{\zeta}''_k = \boldsymbol{\zeta}_k - \boldsymbol{\zeta}'_k$, we get

$$\int d^2 \mathbf{X}' A(\mathbf{X}') \left(N^2 \int d^2 \boldsymbol{\zeta}''_1 \dots d^2 \boldsymbol{\zeta}''_{N-1} h(\boldsymbol{\zeta}''_1 + \mathbf{X} - \mathbf{X}') \dots h(\boldsymbol{\zeta}''_N + \mathbf{X} - \mathbf{X}') \right).$$

The term in parentheses is a function $H(\mathbf{X} - \mathbf{X}')$ and serves as an effective OCM PSF. Therefore

$$H(\mathbf{X}) = N^2 \int d^2 \boldsymbol{\zeta}_1 h(\boldsymbol{\zeta}_1 + \mathbf{X}) \dots \int d^2 \boldsymbol{\zeta}_{N-1} h(\boldsymbol{\zeta}_{N-1} + \mathbf{X}) h(\boldsymbol{\zeta}_N + \mathbf{X}).$$

Due to $\sum_k \boldsymbol{\zeta}_k = 0$ we can infer $\boldsymbol{\zeta}_N = -\sum_{k=1}^{N-1} \boldsymbol{\zeta}_k$. By defining the notation $h^{*k} := (h * \dots * h)$ for the k -times repeated self-convolution of a function $h = h^{*1}$, we can deduce

$$\begin{aligned} H(\mathbf{X}) &= N^2 \int d^2 \boldsymbol{\zeta}_1 h(\boldsymbol{\zeta}_1 + \mathbf{X}) \dots \int d^2 \boldsymbol{\zeta}_{N-1} h(\boldsymbol{\zeta}_{N-1} + \mathbf{X}) h\left(\mathbf{X} - \sum_{k=1}^{N-1} \boldsymbol{\zeta}_k\right) \\ &= N^2 \int d^2 \boldsymbol{\zeta}_1 h(\boldsymbol{\zeta}_1 + \mathbf{X}) \dots \underbrace{\int d^2 \boldsymbol{\zeta}'_{N-1} h(\boldsymbol{\zeta}'_{N-1}) h\left(2\mathbf{X} - \sum_{k=1}^{N-2} \boldsymbol{\zeta}_k - \boldsymbol{\zeta}'_{N-1}\right)}_{h^{*2}(2\mathbf{X} - \sum_{k=1}^{N-2} \boldsymbol{\zeta}_k)} \\ &= N^2 \int d^2 \boldsymbol{\zeta}_1 h(\boldsymbol{\zeta}_1 + \mathbf{X}) \dots \int d^2 \boldsymbol{\zeta}_{N-2} h(\boldsymbol{\zeta}_{N-2} + \mathbf{X}) h^{*2}\left(2\mathbf{X} - \sum_{k=1}^{N-2} \boldsymbol{\zeta}_k\right) \\ &= \dots = N^2 \int d^2 \boldsymbol{\zeta}_1 h(\boldsymbol{\zeta}_1 + \mathbf{X}) h^{*(N-1)}((N-1)\mathbf{X} - \boldsymbol{\zeta}_1) \\ &= N^2 h^{*N}(N\mathbf{X}) \end{aligned} \tag{7.8}$$

This is the result of Eq. (7.4). The OCM PSF can be written as N -times repeated self-convolution of the PSF $h(\boldsymbol{\rho})$ of the optical system. For a general magnification factor m , we have therefore derived

$$G^{(N)}(\mathbf{X}, \boldsymbol{\zeta}_1, \dots, \boldsymbol{\zeta}_{N-1}) = \left| \int d^2 \mathbf{X}' A(\mathbf{X}') H\left(\frac{\mathbf{X}}{m} - \mathbf{X}'\right) \right|^2 = \left| (A * H)\left(\frac{\mathbf{X}}{m}\right) \right|^2.$$

For the single lens PSF $h(\boldsymbol{\rho}) = \text{somb}(2\pi R|\boldsymbol{\rho}|/s_o\lambda)$, the result of Eq. (7.8) yields

$$H(\mathbf{X}) = C \text{somb}\left(\frac{2\pi RN}{s_o\lambda} |\mathbf{X}|\right)$$

and can be understood in terms of a Fourier transform version of Eq. (7.8). With the Fourier transform $\tilde{h}(\mathbf{q})$ of $h(\boldsymbol{\rho})$ in transverse wave vector coordinates \mathbf{q} , Eq. (7.8) is equivalent to

$$H(\mathbf{X}) = \frac{N^2}{(2\pi)^2} \int d^2\mathbf{q} (\tilde{h}(\mathbf{q}))^N e^{iN\mathbf{q}\cdot\mathbf{X}}.$$

As $\tilde{h}(\mathbf{q})$ is given by the lens pupil function [3], any power of it is of unity transmission amplitude within its circular region. This results in a N -times narrower but otherwise equal PSF as for classical imaging. Note that for a Gaussian pupil function (apodization), the centroid PSF narrows only with $1/\sqrt{N}$, corresponding to the SQL.

7.6.2 Incoherent OCM Imaging

The OCM state of Eq. (7.2) with a sharp centroid position at location \mathbf{X}_0 can be gained by replacing $A(\boldsymbol{\rho}) \rightarrow A_x(\mathbf{X}) = \delta^{(2)}(\mathbf{X} - \mathbf{X}_0)$. This state shall be denoted by

$$|\Psi_{\mathbf{X}_0}\rangle = \int d^2\rho_1 \dots d^2\rho_N \delta^{(2)}\left(\frac{\rho_1 + \dots + \rho_N}{N} - \mathbf{X}_0\right) |\rho_1, \dots, \rho_N\rangle.$$

For an object aperture function $A(\boldsymbol{\rho})$, the mixed state given by the density operator

$$\hat{\rho} = \int d^2\mathbf{X} |A(\mathbf{X})|^2 |\Psi_{\mathbf{X}}\rangle \langle\Psi_{\mathbf{X}}|$$

contains an incoherent image. It is straightforward to show using the results of section 7.6.1 that with this mixed state as an input in plane Σ_o of setup in Fig. 7.1, the correlation function in Σ_i will read

$$G^{(N)}(\mathbf{X}, \boldsymbol{\xi}_1, \dots, \boldsymbol{\xi}_{N-1}) = \int d^2\mathbf{X}' \left| A(\mathbf{X}') H\left(\frac{\mathbf{X}}{m} - \mathbf{X}'\right) \right|^2 = (|A|^2 * |H|^2)\left(\frac{\mathbf{X}}{m}\right).$$

This is formally analogous to classical incoherent imaging. The image is formed point-by-point, no interferences can occur.

This imaging could be realized in our experimental implementation by focusing the pump beam in the object plane Σ'_o and randomly scanning over the aperture. This classical randomness would produce the mixed state described above. Tsang proposed in [42] such a scheme using a quantum “laser pointer” to build up an image incoherently at super-resolution. A disadvantage is that the single-shot property of the state generation would be lost in such an approach.

7.6.3 OCM State Generation using SPDC

This section derives Eq. (7.7), the biphoton state at the output plane of the state preparation. Assuming narrow-band pumping and fixed detection wavelengths realized by spectral filtering, the generated biphoton state at the central plane of the NLC reads

$$|\Psi\rangle = \int d^2\mathbf{q}_s d^2\mathbf{q}_i \tilde{E}_p(\mathbf{q}_s + \mathbf{q}_i) \operatorname{sinc}\left(\frac{\Delta k L}{2}\right) |\mathbf{q}_s, \omega_s\rangle |\mathbf{q}_i, \omega_i\rangle \quad (7.9)$$

in transverse wavevector coordinates \mathbf{q}_s and \mathbf{q}_i for the signal and idler photon at their corresponding angular frequencies ω_s and ω_i , and the pump field distribution $\tilde{E}_p(\mathbf{q})$ at angular frequency ω_p [58]. Energy conservation imposes $\omega_p = \omega_s + \omega_i$. The wavevector

mismatch

$$\Delta k = \sqrt{\left(\frac{\omega_s}{c}n(\omega_s)\right)^2 - \mathbf{q}_s^2} + \sqrt{\left(\frac{\omega_i}{c}n(\omega_i)\right)^2 - \mathbf{q}_i^2} - \sqrt{\left(\frac{\omega_s + \omega_i}{c}n(\omega_s + \omega_i)\right)^2 - (\mathbf{q}_s + \mathbf{q}_i)^2} + \frac{2\pi}{G}$$

where c is the speed of light and the refractive index $n(\omega)$ of the crystal is given by its temperature dependant Sellmeier equations. The NLC poling period G is fixed at its fabrication and is chosen to achieve $\Delta k = 0$ at the used wavelengths and for collinear emission $\mathbf{q} = 0$.

Let the function $E_o(\boldsymbol{\rho})$ define the electric field distribution of the monochromatic pump of angular frequency ω_p in the object plane Σ'_o of Fig. 7.1. Propagating it through the first lens of focal length f to the center of the crystal, the far-field plane relative to Σ'_o , the field distribution is given by $E_p(\boldsymbol{\rho}) = \tilde{E}_o(\omega_p \boldsymbol{\rho} / cf)$ with the Fourier transform $\tilde{E}_o(\mathbf{q}) = \int d\boldsymbol{\rho} E_o(\boldsymbol{\rho}) e^{-i\mathbf{q}\boldsymbol{\rho}}$ [3]. Therefore, this pump field incident on the NLC has a Fourier transform of

$$\tilde{E}_p(\mathbf{q}) = E_o\left(-\frac{cf}{\omega_p}\mathbf{q}\right) \quad (7.10)$$

and can be inserted in Eq. (7.9).

The SPDC state has to be propagated from the NLC through the lens of focal length f to the output plane Σ_o . The latter is the far-field plane relative to the NLC central plane. Plane waves of transversal wavevector \mathbf{q} emitted by the NLC are focused to a location $\boldsymbol{\rho} = \frac{cf}{\omega}\mathbf{q}$ [3]. Formally, the state propagation can be performed by the transformation $|\mathbf{q}, \omega\rangle \rightarrow |\frac{cf}{\omega}\mathbf{q} = \boldsymbol{\rho}, \omega\rangle$. Using Eq. (7.10) and Eq. (7.9), we get

$$|\Psi\rangle = \int d^2\boldsymbol{\rho}_s d^2\boldsymbol{\rho}_i E_o\left(-\frac{\omega_s\boldsymbol{\rho}_s + \omega_i\boldsymbol{\rho}_i}{\omega_s + \omega_i}\right) \text{sinc}\left(\frac{\Delta k L}{2}\right) |\boldsymbol{\rho}_s, \omega_s\rangle |\boldsymbol{\rho}_i, \omega_i\rangle \quad (7.11)$$

where Δk is evaluated at $\mathbf{q}_k = (\omega_k/cf)\boldsymbol{\rho}_k$, $k \in \{s, i\}$. For frequency degenerated emission with $\omega_s = \omega_i = \frac{1}{2}\omega_p$, the biphoton state in the preparation output plane Σ_o reads

$$|\Psi\rangle = \int d^2\boldsymbol{\rho}_s d^2\boldsymbol{\rho}_i E_o\left(-\frac{\boldsymbol{\rho}_s + \boldsymbol{\rho}_i}{2}\right) \text{sinc}\left(\frac{\Delta k L}{2}\right) |\boldsymbol{\rho}_s, \frac{1}{2}\omega_p\rangle |\boldsymbol{\rho}_i, \frac{1}{2}\omega_p\rangle.$$

Finally, uniformly illuminating an object aperture $A(\boldsymbol{\rho})$ in the plane Σ'_o yields $E_o(\boldsymbol{\rho}) = A(\boldsymbol{\rho})$.

Eq. (7.11) shows the necessity to filter for frequency degenerate emission in order to properly reconstruct the image with the centroid. Broadband emission could be conceived if the detection provides spectral information.

7.6.4 Standard Quantum Limit of Classically Correlated Photons

This section derives a centroid PSF for classically correlated photons with no entanglement and shows its behaviour at large photon number N . For simplicity, we set first $N = 2$. Assuming OCM-like correlations for a point object, in the object plane these are modelled by a classical, multi-variate probability density function

$$p_o(\boldsymbol{\rho}_1, \boldsymbol{\rho}_2) = \delta^{(2)}(\boldsymbol{\rho}_1 + \boldsymbol{\rho}_2).$$

Propagating the photons through the resolution limited imaging system, the process of blurring by the PSF can be described by adding a random variable N to their original positions in the object plane

$$\boldsymbol{\rho}_k \rightarrow \boldsymbol{\rho}_k + \mathbf{N}_k, \quad k \in \{1, 2\}.$$

As both photons are affected by the PSF independently, a separate random spread term is needed for each. Their probability density function is given by the PSF of the imaging system with $P_{N_k}(\mathbf{N}) = |h(\mathbf{N})|^2$. Using elementary statistics, we get for the probability density in the image plane

$$\begin{aligned} p_i(\boldsymbol{\rho}_1, \boldsymbol{\rho}_2) &= \int d^2\boldsymbol{\rho}'_1 d^2\boldsymbol{\rho}'_2 p_o(\boldsymbol{\rho}_1, \boldsymbol{\rho}_2) |h(\boldsymbol{\rho}_1 - \boldsymbol{\rho}'_1)|^2 |h(\boldsymbol{\rho}_2 - \boldsymbol{\rho}'_2)|^2 \\ &= (|h|^2 * |h|^2)(\boldsymbol{\rho}_1 + \boldsymbol{\rho}_2). \end{aligned}$$

This is formally equivalent to independent, incoherent imaging of the photons and therefore validates the statistical model assumed. Using $\boldsymbol{\rho}_- = \frac{1}{2}(\boldsymbol{\rho}_1 - \boldsymbol{\rho}_2)$, the centroid random variable \mathbf{X}_i in the image plane has a probability density function

$$P_{\mathbf{X}_i}(\mathbf{X}) = \int d^2\boldsymbol{\rho}_- p_i(\mathbf{X} + \boldsymbol{\rho}_-, \mathbf{X} - \boldsymbol{\rho}_-) = \int d^2\boldsymbol{\rho}_- (|h|^2 * |h|^2)(2\mathbf{X}) \propto (|h|^2 * |h|^2)(2\mathbf{X}).$$

Generalizing to a classically correlated N -photon state, one can use the fact that the centroid random variable in the image plane is

$$\mathbf{X}_i = \frac{1}{N} \left(\sum_{k=1}^N \boldsymbol{\rho}_k + \mathbf{N}_k \right).$$

With the OCM property $\sum_{k=1}^N \boldsymbol{\rho}_k = 0$ of a point object at the origin, we can conclude that the probability distribution of \mathbf{X}_i is given by the sum of N independent noise sources and reads

$$P_{\mathbf{X}_i}(\mathbf{X}) = (|h|^2)^{*N}(N\mathbf{X}) \quad (7.12)$$

using the self-convolution notation from Sec. 7.6.1. This is the PSF of classical OCM imaging and the optimum for any imaging using classically correlated photons.

Because the noise terms are independent, identically distributed random variables, we can apply the central limit theorem of probability theory. This says, that the probability density of Eq. (7.12) converges in the limit of large N to a normal distribution

$$P_{\mathbf{X}_i}(\mathbf{X}) \xrightarrow{N \rightarrow \infty} \frac{1}{\sqrt{2\pi\sigma^2/N}} e^{-\frac{\mathbf{X}^2}{2\sigma^2/N}}$$

with the standard deviation σ of the imaging system PSF $|h(\boldsymbol{\rho})|^2$. The asymptotic $1/\sqrt{N}$ decrease in width indicates a resolution enhancement at the SQL.

Chapter 8

Conclusion

In the thesis, we introduced a novel kind of light detector array with many potential applications (Chapter 5). Its capability to measure in parallel on hundreds of pixels with single photon sensitivity and sub-nanosecond time resolution distinguishes it from present detector solutions. In the quantum imaging experiments (Chapter 5, 6 and 7), it showed its advantage over scanning measurements by fast data acquisition in experiments. Real-time visualization of the signal considerably simplified setup alignment. The time resolution allowed to establish a short coincidence window and to thereby keep accidental events at a minimum. Due to the limited photon detection efficiency at the given source wavelength and moderate measurement duty cycle of the presented detectors, the advantage of parallel measurement nearly vanishes for low correlation order. Crosstalk does not allow to measure weak, spatially correlated sources. For a next-generation sensor with higher detection efficiency, these drawbacks have to be addressed in order to become a competitive tool for correlation measurement. Nevertheless, other applications than quantum imaging with less strict requirements on efficiency could already benefit from the very distinct features of the sensor.

The measurement of Glauber's correlation functions is theoretically worked out (Chapter 2) and implemented for these new detectors. Experimental results for well known sources validate the data processing (Chapter 4, 5 and 6). The theoretical results and algorithms are general and can also be used for future detector generations and thereby pave the way for their application in quantum experiments.

The super-resolution quantum imaging experiments successfully showed the theoretically expected improvements (Chapter 6). Preliminary results confirm the reconstruction algorithm which operates on measured higher-order correlation functions. However, a statistical analysis of this approach has yet to prove the superiority to standard reconstruction schemes. The scaling of the results to high-resolution microscopy applications is not straightforward and requires further investigation of appropriate light sources. As discussed, the weak quantum light sources do not show fundamental advantages and could be replaced by classical measurement and illumination techniques.

The theoretical and experimental results on quantum imaging at the Heisenberg limit allowed to investigate the mechanism of resolution improvement based on entanglement (Chapter 7). Furthermore, they unified the understanding of other recent works aiming for imaging at the HL. It showed the possibility to generate quantum states of light which carry spatial structure beyond the diffraction limit. In contrast to microscopy techniques for resolution improvement which are based on data post-processing, the here presented scheme physically realizes the super-resolved structure and would allow for quantum lithography at the HL.

Three different light sources were implemented and characterized (Chapter 3). They were used throughout this thesis for sensor test and in quantum experiments (Chapter 4, 5, 6 and 7). The documentation together with the appropriate measurement apparatus and

data evaluation software developed in this thesis makes them ready to be used for future experiments.

The results suggest a fundamental distinction between microscopy and lithography. The former has the goal to gain information about the structure of an object through the measurement of light. The amount of object information carried by light in microscopy is mainly a statistical question: Without noise, arbitrary resolution improvement would be attainable in reconstruction even with a classical light source [35, 36]. Quantum or correlated light sources might yield an advantage under the assumption of the restricted use of resources, e.g. the number of photons, as quantified in metrology. Whether this potentially better scaling in the number of resources is really relevant in practical applications is a different question as classical states of light are much more robust and easier to generate and detect.

In contrast to microscopy, a lithographic scheme requires a specific spatial structure of light with highest possible visibility, i.e. no background, for film exposure. This physical realization is diffraction limited: In a given imaging system, the finite number of spatial modes with sufficient transmission amplitudes fundamentally limit the complexity of the image structure, e.g. in terms of the number of distinct pixels which are possible to be exposed individually [35, 36]. As intuitively obvious, several independent photons allow by their modal correlation to encode more information than a single photon. Indeed, classically correlated multi-photon sources were here shown to yield arbitrary resolution improvement with full visibility at the SQL. Entanglement of multi-photon states is demonstrated to transmit super-resolved structures in photon correlations at full visibility and at the HL in Ch. 7. While thermal light would allow mimicking this result for two entangled photons [122], it only shows 50% visibility and does not generalize to higher photon numbers. Therefore, the benefit of using entangled states for lithography is the full visibility and the scaling at the HL.

As proposed in Ch. 7, the availability of N -photon transmitters (NPT) would allow using the OCM result in a microscopy application by using classically correlated N -photon state for illumination and an NPT in front of the imaging lens. Then, a centroid measurement or, with less efficiency, a spatial coincidence measurement would yield the HL super-resolved image. It is doubtful whether this apparent improvement really is advantageous in microscopy from a metrological perspective: The NPT filters the joint transverse wave vector spectrum for strong wave vector correlation and thereby makes the improved image information available in the simple centroid measurement. In an otherwise equal experiment but without an NPT, the same information, i.e. the same range of transverse wave vectors, is present in the joint electric field distribution in the image plane [32, 125]. In this case, we have therefore measurement access to the same and even to additional regions in the joint wave vector space of the photons. Using an appropriate measurement and computational methods for image reconstruction, a better image is achievable for a given number of emitted photons than with the centroid and NPTs! Entanglement, here generated by the NPT, seems again only to be beneficial for super-resolution lithography but not microscopy.

In which situations and for what measurements quantum light is superior to classical light is, in general, an open question. Many quantum experiments were later shown to be realizable with classical light. Nevertheless, some of these quantum inspired methods and techniques bring advantages and are used in applications. Thereby, quantum theory brings insights even into the classical domain. Following this path of research might turn out fruitful, even in the absence of pure quantum effects. Future work will have to show whether this proves true for super-resolution quantum microscopy.

Appendix A

Derivation of Sampling Space Volume

In the following, the analytic expression for the sampling space volume of the temporally coincident spatial correlation function, given in Eq. (2.42) and discussed in Sec. 2.3.4, is derived.

First, we calculate the sampling space volume in the time interval $t = 1, \dots, T$ only restricted by the measurable region

$$V_m(m^{(N)}, T) := \sum_{t_1=1}^T \cdots \sum_{t_N=1}^T \Theta_{\text{meas.}}(\mathbf{x}^{(N)})$$

as given in Eq. (2.41). The function indicating measurable space $\Theta_{\text{meas.}}$, defined in Eq. (2.37), yields 1 if all space-time points in $\mathbf{x}^{(N)}$ are different and vanishes otherwise.

Spatial multiplicities $m^{(N)}$ are given as input. Without loss of generality, we can assume that positions are ordered such that $\rho_1 = \dots = \rho_{m_1}$ for the first group of multiplicity m_1 and all the others following accordingly. By summing only over the space of t values which do not lead to a collision and to a vanishing $\Theta_{\text{meas.}}$, we can write

$$V_m(m^{(N)}, T) = \left(\sum_{t_1 \neq \dots \neq t_{m_1}}^T 1 \right) \left(\sum_{t_{m_1+1} \neq \dots \neq t_{m_1+m_2}}^T 1 \right) \dots$$

The individual sums are easily evaluated by elementary combinatorics: For the first group m_1 , the sum is given by the number of sorted arrangements of m_1 elements from the set $\{1, \dots, T\}$. As this is given by $T! / (T - m_1)!$, we can write the result of Eq. (2.41)

$$V_m(m^{(N)}, T) = \prod_{k=1}^N \frac{T!}{(T - m_k)!} = \prod_{k=1}^N \prod_{l=1}^{m_k} (T - l + 1). \quad (\text{A.1})$$

The full sampling space volume in a frame of duration T_F , the number of frames N_F , and using a coincidence window T_c is defined in Eq. (2.40) with

$$V(\mathbf{p}^{(N)}) = N_F \sum_{t_1=1}^{T_F} \cdots \sum_{t_N=1}^{T_F} \Theta_{T_c}(\mathbf{t}^{(N)}) \Theta_{\text{meas.}}(\mathbf{x}^{(N)})$$

The sum is over the space of T_F^N points is restricted by the measurable space given by $\Theta_{\text{meas.}}$ and further narrowed by the coincidence condition by Θ_{T_c} defined in Eq. (2.36).

An illustration of the temporal space for a second-order measurement for a single frame is shown in Fig. A.1. The total sampled space going into the coincidence signal is shown by colored squares. If the same position is considered, i.e. the same pixel and

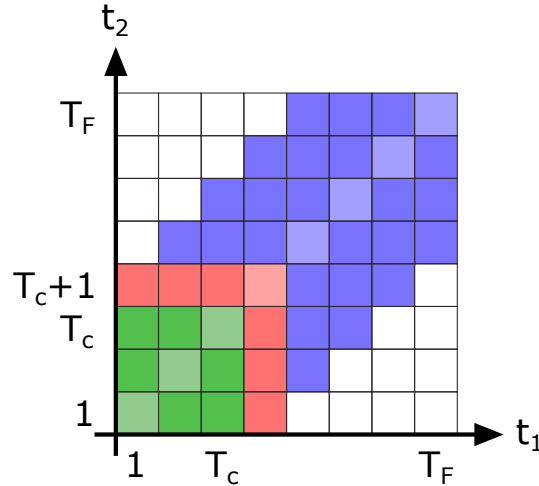


FIGURE A.1: Illustration of temporal space sampling in spatial second-order correlation using a coincidence window T_c . Time is measured in integer units and the frame duration is T_F . The sampling space volume is given by the colored squares. A subset of the total measurable space does not contribute due to the coincidence requirement imposed by Θ_{T_c} (white squares). In case of two identical pixels, the according spatial multiplicity $m = 2$ leads to non-measurable space on the diagonal (light colored squares).

therefore spatial multiplicity $m = 2$, $\Theta_{\text{meas.}}$ removes the diagonals (light colored squares). Furthermore, Θ_{T_c} removes temporal events with too large separation (white squares).

Independent of the multiplicity, the green space can be quantified with the result from above by $V_m(m^{(N)}, T_c)$. The red space is therefore given by

$$V_m(m^{(N)}, T_c + 1) - V_m(m^{(N)}, T_c).$$

Due to the fact that the blue area is a replication of the red area, we get for the blue area a volume of

$$(T_F - T_c - 1) \left(V_m(m^{(N)}, T_c + 1) - V_m(m^{(N)}, T_c) \right).$$

The total space of all colors is therefore

$$V_m(m^{(N)}, T_c) + (T_F - T_c) \left(V_m(m^{(N)}, T_c + 1) - V_m(m^{(N)}, T_c) \right)$$

and we can conclude

$$V(\mathbf{p}^{(N)}) = \left([T_F - T_c] V_m(m^{(N)}, T_c + 1) - [T_F - T_c - 1] V_m(m^{(N)}, T_c) \right) N_F \quad (\text{A.2})$$

by taking into account the number of frames N_F . This is the result of Eq. (2.40).

While this heuristic derivation only used a second-order correlation for illustration, one can convince oneself that the idea generalizes to higher orders with the according more difficult, higher-dimensional spaces. Even more, it generalizes to arbitrary spatial multiplicities. The validity can be checked by comparison to the numerical evaluation of the sum, which is feasible at low frame duration T_F and correlation order N , which successfully verified the expression.

Appendix B

Implementation of the Correlation Algorithm

The following program is a concrete implementation of the algorithm 1 in Sec. 2.3.4 for temporally coincident, spatial high-order correlation measurements. Its time-consuming measurement data processing part is implemented in C for better performance. Normalization with sampling space volume, symmetrization and analysis is done in Matlab. These programs are used for thermal light measurement in Sec. 3.3, Sec. 5.2.3, and Ch. 6. Similar programs are used for second-order correlation measurements of ultra-fast correlated quantum sources in all the other cases.

B.1 Measurement Data Correlation in C

This implementation in C results in a speed improvement of more than a factor of 50 in comparison to a similar Matlab version. Best performance is gained by setting compiler code generation optimization options to its highest value. No parallel processing is used, but can be easily incorporated by running this program on different data files in parallel and summing their outputs. SuperEllen's raw measurement data files are assumed as input, see Sec. 5.2.3. Its measurement frames are grouped in 64 consecutive frames. This group is called superframe where only the frame position (steps of $10\mu\text{s}$) is used for timing information because of the long correlation time of thermal light ($100\mu\text{s}$). The TDCs values are not considered. For simplicity, only one spatial coordinate provided by SuperEllen is used in the following program.

```
#include <iostream>
using namespace std;

#include <fstream>
#include <math.h>
#include <limits.h>
#include <stdlib.h>

#define Nmax          4          // maximal correlation order
#define Tcoinc        4          // coincidence window length
#define pixN          32         // number of pixels in array
#define N_SuperFrame  64         // frames per superframe

// global variables for algorithm
unsigned int *GNData;           // all correlation functions
long long GNsize = 0;           // size of GNData
short *PixelX, *PixelT;        // arrays of current superframe events
int eventN;                     // number of events in current superframe

// main program
int main(int argc, char** argv) {
```

```

initGNarray ();

int res = read_SE_file("RawData.bin", &frmCtr);

// write to output file
ofstream myfile("GNData.out", ios::binary | ios::out);
unsigned short header[] = {Nmax, 0, pixN, Tcoinc};
myfile.write((char*)header, sizeof(header));
myfile.write((char*)GNData, GNsize * sizeof(GNData[0]));
myfile.write((char*) &frmCtr, sizeof(frmCtr));
myfile.close ();

return 0; // succeeded
}

// initialize GNData array
void initGNarray() {
    GNsize = 0;
    long long pot = 1;
    for (int ii = 0; ii < Nmax; ii++) {
        GNsize += pixN * pot;
        pot *= pixN;
    }
    // allocate and initialize
    GNData = new unsigned int[GNsize];
    for (int i = 0; i < GNsize; i++) { GNData[i] = 0; }

    xs = new int[Nmax];
    ys = new int[Nmax];
}

// read file of SuperEllen raw measurment data , process frame by frame.
// return number of frames in pfrmCtr.
int read_SE_file(char* name, int* pfrmCtr) {
    char* buffer;
    long size;

    ifstream file(name, ifstream::binary | ifstream::in | ifstream::ate);
    size = file.tellg ();
    file.seekg(0, ifstream::beg);
    buffer = new char[size];
    file.read(buffer, size);
    file.close ();
    cout << "File_" << name << "_" << size/1024 << "_kB).";

    long frmCtr = 0;
    long byteCtr = 0;
    eventN = 0;

    PixelX = new short[pixN*pixN*N_SuperFrame]; // event positions
    PixelT = new short[pixN*pixN*N_SuperFrame]; // event times

    while (byteCtr < size) { // loop over frames
        int DetN;
        DetN = (int)buffer[byteCtr] +
            256 * (int)buffer[byteCtr+1]; // num. of detection events
        byteCtr += 2;

        // read all events , set time to frame ID
        for (int pixi = 0; pixi < DetN; pixi++) {
            PixelX[eventN] = buffer[byteCtr+1];
            PixelT[eventN] = frmCtr % N_SuperFrame;
            int dummy1 = buffer[byteCtr]; // omit Y position value

```

```

        int dummy2 = buffer[byteCtr+2]; // omit TDC value
        eventN++;
        byteCtr += 3;
    }

    frmCtr++;
    if ( (frmCtr % N_SuperFrame) == 0) { // superframe ready?
        if (UpdateGN() != 0) { // process superframe
            *pfrmCtr = frmCtr;
            return 1; // error encountered
        };
        eventN = 0; // reset for next superframe
    }
}

delete buffer;
delete PixelX;
delete PixelT;

*pfrmCtr = frmCtr; // return num. of frames
return 0; // ok, no error
}

// persistent variables to UpdateGN
short T1; // start of coinc. window
int *xs; // positions of current coinc. window

// updates GNData at order Ncurr using data from: PixelX, PixelT
int UpdateGN(int Ncurr, int starti){
    int found;
    int linearidx, NdxPowers, Nidx;
    unsigned short val;

    // calculate memory start index for current order Ncurr
    Nidx = 0;
    long long pot = 1;
    for (int ii = 0; ii < (Ncurr - 1); ii++) {
        Nidx += pixN * pot; // skip all lower orders
        pot *= pixN;
    }

    for (int ii=starti; ii < eventN; ii++) {
        if (Ncurr == 1) { T1 = PixelT[ii]; }
        if (PixelT[ii] - T1 > Tcoinc) { return 0; }

        xs[Ncurr-1] = PixelX[ii];

        // calculate array index
        linearidx = 0;
        NdxPowers = 1;
        for (int kk = 0; kk < Ncurr; kk++) {
            linearidx += xs[kk] * NdxPowers;
            NdxPowers *= pixN;
        }

        val = ++GNData[linearidx + Nidx]; // increment GN
        if (val == UINT_MAX) {
            cout << "_Overflow" << endl;
            return 1; // abort
        }

        if (Nmax > Ncurr) { // update higher order recursively
            if (UpdateGN(Ncurr+1, ii+1) != 0) {

```

```

        return 1; // abort if error
    }
}
return 0; // no error
}

```

B.2 Normalization and Symmetrization in Matlab

The following Matlab script reads the output data of the previous C program, symmetrizes the $G^{(N)}$ arrays in their indices, and normalizes by the sampling space volume using Eq. 2.42.

```

% read in correlation data file from C++ program above
fileId = fopen('GNData.out', 'r');
datatype = 'uint32';

% read header of file
header = fread(fileId, 4, 'uint16');
Nmax = header(1); % highest correlation order
pixN = header(3); % number of pixels
Tcoinc = header(4); % coincidence window length

% read correlation function GN and symmetrize
ArrSize = [1 pixN];
GNData = cell(Nmax,1);
for N = 1:Nmax
    GNcurr = fread(fileId, pixN^N, ['*' datatype]); % read G^(N)
    GNcurr = reshape(GNcurr, ArrSize);
    ArrSize = [ArrSize, pixN]; % for next order

    GNData{N} = zeros(size(GNcurr), datatype);
    pset = perms(2:N+1)'; % all permutations of indices orders
    for p = pset % symmetrize by reordering indices
        GNData{N} = GNData{N} + ...
            permute(GNcurr, [1 p(:)']);
    end
    GNData{N} = squeeze(GNData{N});
end
clear GNcurr;
frmNum = fread(fileId, 1, 'int32'); % number of frames
fclose(fileId);

% normalize correlation functions
for N = 1:Nmax
    V = Vcalc(N, pixN); % calc. sampling space volume of one frame
    V = frmNum/64 * V; % volume of all frames
    GNData{N} = double(GNData{N})./ double(V); % normalize
end

% show correlation data
G1 = GNData{1};
figure(1);
plot(G1);
title('G1');

```

```
G2 = GNData{2};  
G1 = G1(:);  
figure(2);  
imagesc(G2 - G1*G1. ');  
title('G2 - G1*G1');
```


Appendix C

Group Delay Dispersion Calculation with Zemax

A source of spatially single mode light is assumed in the following. If this mode propagates through a medium or a whole experimental setup, e.g. a block of glass, free-space or a prism-compressor, the corresponding transfer function introduces a wavelength dependent phase shift $\Phi(\omega)$ in the original electric field distribution [49]. This is given by

$$E(\omega) \rightarrow E(\omega) e^{-i\Phi(\omega)}.$$

Writing the phase in a Taylor series expansion around a center angular frequency ω_0

$$\Phi(\omega) = c_0 + c_1(\omega - \omega_0) + \frac{1}{2}c_2(\omega - \omega_0)^2 + \dots, \quad c_k = \left. \frac{d^k \Phi(\omega)}{d\omega^k} \right|_{\omega=\omega_0}.$$

The constants c_k are given by the derivatives and can be expressed in units of [fs^k]. While c_1 is the group delay introduced by the system, c_2 is the group delay dispersion (GDD).

For a piecewise homogenous system, the phase can be calculated by

$$\Phi(\omega) = \sum_i k_i(\omega) z_i = \sum_i k_0(\omega) n_i(\omega) z_i$$

with the wavelength dependent wave number $k_i(\omega)$ in the propagation medium i and the corresponding geometrical path length z_i . The wave number can be expressed in terms of the wave number in vacuum $k_0(\omega)$ and the medium's index of refraction $n_i(\omega)$. Therefore, we can write

$$\Phi(\omega) = \frac{2\pi}{\lambda} z_{opt}(\omega), \quad z_{opt}(\omega) := \sum_i n_i(\omega) z_i$$

with the defined effective optical path length $z_{opt}(\omega)$.

Zemax is capable of calculating $z_{opt}(\lambda)$ for an arbitrary optical setup with the Zemax operator OPTH. In addition to the refractive indices, its ray-tracing also correctly accounts for different geometrical path lengths introduced for instance by a prism compressor. It is straightforward to show, that the GDD

$$\frac{d^2 \Phi(\omega)}{d\omega^2} = \frac{\lambda^3}{2\pi c^2} \frac{d^2 z_{opt}(\lambda)}{d\lambda^2}.$$

and third-order dispersion

$$\frac{d^3 \Phi(\omega)}{d\omega^3} = -\frac{\lambda^4}{4\pi^2 c^3} \left(3 \frac{d^2 z_{opt}(\lambda)}{d\lambda^2} + \lambda \frac{d^3 z_{opt}(\lambda)}{d\lambda^3} \right).$$

For their cancellation, a optimization merit function which numerically approximates these

derivatives can be implemented. Any degree of freedom of a system can hereby be optimized for dispersion.

The following Zemax programming language (ZPL) macro calculates $z_{opt}(\lambda)$ over the specified wavelength range. An analysis of this data with a transformation from λ to ω and a following polynomial fit allows with the determination of the GDD and all higher-order dispersion coefficients c_k .

```
! calculates optical path length in wavelength range for dispersion calculation

! specify wavelength range [um]:
wlstart = 0.75
wlstop = 0.85
wlsteps = 100

! add new wavelength
wlnum = NWAV() + 1
NUMWAVE wlnum
UPDATE

PRINT "wavelength [um]  opt. pathlength z_opt[mm]"

FOR k = 0, wlsteps, 1
  actwl = wlstart + (wlstop - wlstart)/wlsteps * k
  WAVL wlnum = actwl
  UPDATE

  ! follow chief ray
  RAYTRACE 0, 0, 0, 0, wlnum
  zopt = OPTH(NSUR())

  FORMAT 13.12 EXP
  PRINT actwl, " ", zopt
NEXT

! remove wavelength
NUMWAVE wlnum-1
UPDATE
```


Appendix D

SuperEllen Technical Publication

In the following, the conference paper [46] appearing in the proceedings of the International Solid-State Circuits Conference (ISSCC) 2018 is reprinted:

A 32x32-pixels time-resolved single-photon image sensor with 44.64- μm pitch and 19.48% fill-factor with on-chip row/frame skipping features reaching 800 kHz observation rate for quantum physics applications

L. Gasparini,¹ M. Zarghami,¹ H. Xu,¹ L. Parmesan,¹ M. Moreno Garcia,¹
M. Unternährer,² B. Bessire,² A. Stefanov,² D. Stoppa¹ and M. Perenzoni¹

¹ *Fondazione Bruno Kessler FBK, 38122 Trento, Italy*

² *Institute of Applied Physics, University of Bern, 3012 Bern, Switzerland*

Entangled photons, beyond the classical physics understanding, show quantum correlations in some of their degrees of freedom. They find application in quantum computing, quantum key distribution, and super-resolution (i.e., beyond the diffraction limit) microscopy, but they are undistinguishable using conventional image sensors.

The optical process of spontaneous parametric down conversion (SPDC) occurring in a non-linear (NL) crystal pumped with an intense laser beam is a common way to generate pairs of photons that are spatially entangled. They show correlations in their emission location and anticorrelations in the direction of emission (momentum) and are generated simultaneously (<1 ps). Image sensors with high detection efficiency and time resolution are needed to detect both the photons and identify them as an entangled pair. [43] describes a first experiment that combines an SPDC source with a time-resolved single-photon imager.

This work presents a CMOS imager based on single-photon avalanche diodes (SPAD) with per-pixel time-to-digital converter (TDC) for the recording of the spatial correlation functions of a flux of entangled photons, with on-chip features to increase the duty cycle. The 32 \times 32-pixel array (1.69 \times 1.88 mm²), combining a 44.64- μm pitch with 19.48% fill-factor, was fabricated in a 150-nm 1P6M CMOS standard technology. A current-based mechanism requiring only 2 transistors per pixel exploits low photon rates to avoid reading empty frames, so allowing the sensor to open 50-ns-long observation windows at up to 800kHz. An additional transistor per pixel is used to sense the absence of SPAD activity in each row and reduce the readout time.

Fig.D.2 shows the pixel schematic and the applied waveforms. Initially, the SPAD is off ($V_{An} = V_{SPAD} - V_{3V3} < V_{Breakdown}$). Then, a 5-ns pulse on CHARGE drives V_{An} to 0 V, turning the SPAD on, and if it fires due to a photon or a dark count, a voltage step is observed at V_{An} . The signal propagates through the clamping transistor M4, separating

the 3.3 V and the 1.8 V domains. The NOR/NAND gates operate as a pulse generator triggering the START signal if the event occurs while $GATen = L$. The TDC has been designed to aggressively minimize its area ($402.7\mu\text{m}^2$). It is based on a 3-stage ring oscillator (RO), enabled by START. A sample and hold mechanism controlled by STOP stores the phase of the RO, which is then encoded into 2 bits (fine timestamp). At the same time, a 6-bit digital counter of RO periods produces a coarse timestamp.

Noise is mitigated in multiple ways: DISCHn turns off the SPAD at the end of the observation window to minimize afterpulsing, noisy SPADs are disabled through a programmable 1-bit SRAM, and no SPAD wells sharing scheme is used to recover fill-factor as in [121], as it negatively impacts crosstalk and the sensor modulation transfer function (MTF).

Fig. D.2 shows the overall sensor architecture. Full 1 kpixel readout is performed in $11.20\mu\text{s}$ streaming 8-bit digital data at 100 MHz. Additional circuitry is used to speed up the readout process by skipping empty rows (highlighted in blue in Fig. D.2). Each pixel in the i -th row shares a ROWEMPTY[i] net which is pulled-up when the pixels are reset. During the observation, the first firing pixel in the row sets the flag low through transistor M10 in Fig. D.1. At the end of the observation, the value of the flag is sampled in the row decoder and is provided at the output to speed up the readout process. E.g., 8 triggered pixels lead to a readout time $< 3.52\mu\text{s}$.

A second mechanism is implemented to skip entire frames when the total number of triggered pixels is below a user defined threshold. Each pixel in the array contains a tunable current source (M11 and M12 in Fig. D.1) sinking a current I_{SPAD} from a global TRIG_{int} net only when the pixel is triggered (highlighted in red in Fig. D.2). At the periphery of the array, replicas of the current source generate a reference current I_{th} that corresponds to the requested minimum number of triggered pixels and is subtracted to the global current $I_{SPADarray}$. The difference I_{Diff} is provided to a current comparator which outputs a logic '0' or a logic '1' if I_{Diff} is negative or positive, respectively. The value is then sampled in TRIG so that the external controller can skip the readout phase and start a new acquisition. When observing rare events (e.g., groups of 4 entangled photons), the observation rate approaches the limit of 800 kHz. The timing diagram of Fig. D.2 shows two consecutive acquisitions. The first frame is ignored due to an insufficient number of triggered pixels, while the second one is read out, skipping empty rows.

TDCs have been thoroughly characterized in terms of full scale variation, differential and integral nonlinearity (DNL, INL) over a 45 ns window for 64 pixels randomly distributed across the array. Results are shown in Fig. D.3. The TDC resolution is of 204.5 ± 2.7 ps. DNL is in the $-0.73.. + 0.77$ LSB range. All the INL plots lay in the $-0.93.. + 1.24$ LSB range.

The sensor accuracy has been measured for 64 equally-spaced pixels, with a pulsed 470 nm laser source with 70 ps FWHM. Fig. D.4 summarizes the results, including raw and calibrated data. Calibration includes DNL correction (bin oversampling and resizing) and offset compensation, caused by device mismatch and propagation of critical timing signals. The figure shows that the calibration procedure effectively recovers the increasing spread for longer delays. Single-photon timing precision is of 240 ps rms.

The sensor has been tested acquiring first- ($G^{(1)}(\rho)$) and second-order ($G^{(2)}(\rho_s, \rho_i)$) correlation functions of a flux of spatially entangled photons. Fig. D.5(top) shows a block diagram of the experimental setup. A NL crystal pumped with a 405-nm continuous wave laser generates entangled photon pairs at 810 nm. Being entangled, both photons exit the crystal with an angle, symmetric with respect to the propagation axis, so that their barycenter lays on the axis itself. To verify this property, the detector is placed in the far-field of the photons, thus measuring their direction of emission. A coincidence window of 5 TDC codes has been used to identify entangled photons. Fig. D.5(middle, right) shows

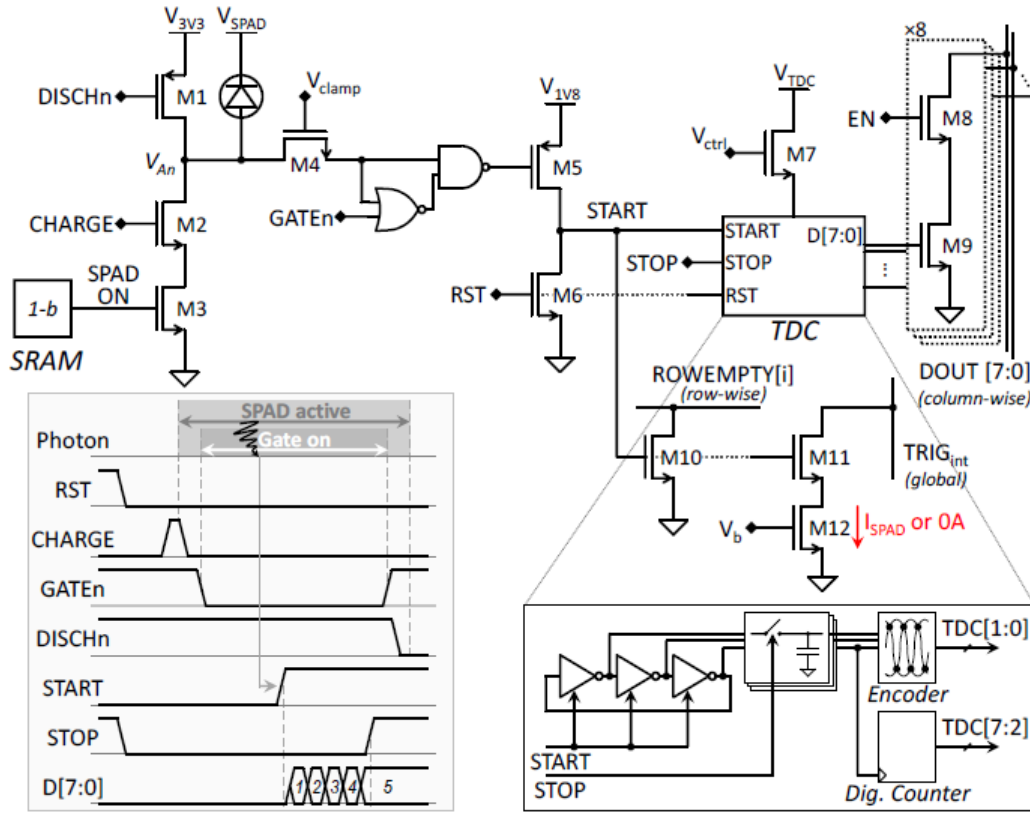


FIGURE D.1: Pixel high-level schematic with detailed inset for the TDC and timing diagram.

a model of the photon flux, with two photons of a pair, referred to as signal photon and idler photon, respectively. $G^{(1)}(\rho)$, where $\rho = (x_\rho, y_\rho)$ represents the photon position in the SPAD array, describes the spatial distribution of entangled photons. Fig. D.5(middle, left) shows the expected $G^{(1)}$, consisting of a circle, and the measured one. The circle is clearly visible, with hot spots due to dark counts and cold spots due to disabled SPADs. $G^{(2)}(\rho_s, \rho_i)$, where ρ_s, ρ_i represent the linearized coordinates ($\rho_{s,i} = 32x_\rho + y_\rho$) of the signal and idler photon, respectively, is obtained by building the 2D histogram of spatial coincidences for all possible pixel combinations. The expected measured function model in Fig. D.5(bottom) shows an anticorrelation pattern due to the entanglement. The obtained $G^{(2)}$ shows multiple antidiagonals: since the system is not ideal, given one photon detection, the other photon may fall in the anticorrelated pixel or in one of its neighbors. In linear coordinates, pixels in a column laying on adjacent rows become separated by 32 points. The measured histogram shows also correlation diagonals caused by crosstalk events, which are temporally coincident as entangled photons are.

In typical conditions, less than 8 SPADs trigger for each observation window and the sensor consumes 11.1 mW at 250kfps. Fig. D.6 summarizes the sensor performance and compares it with the state-of-the-art.

References: [43, 121, 136, 137]

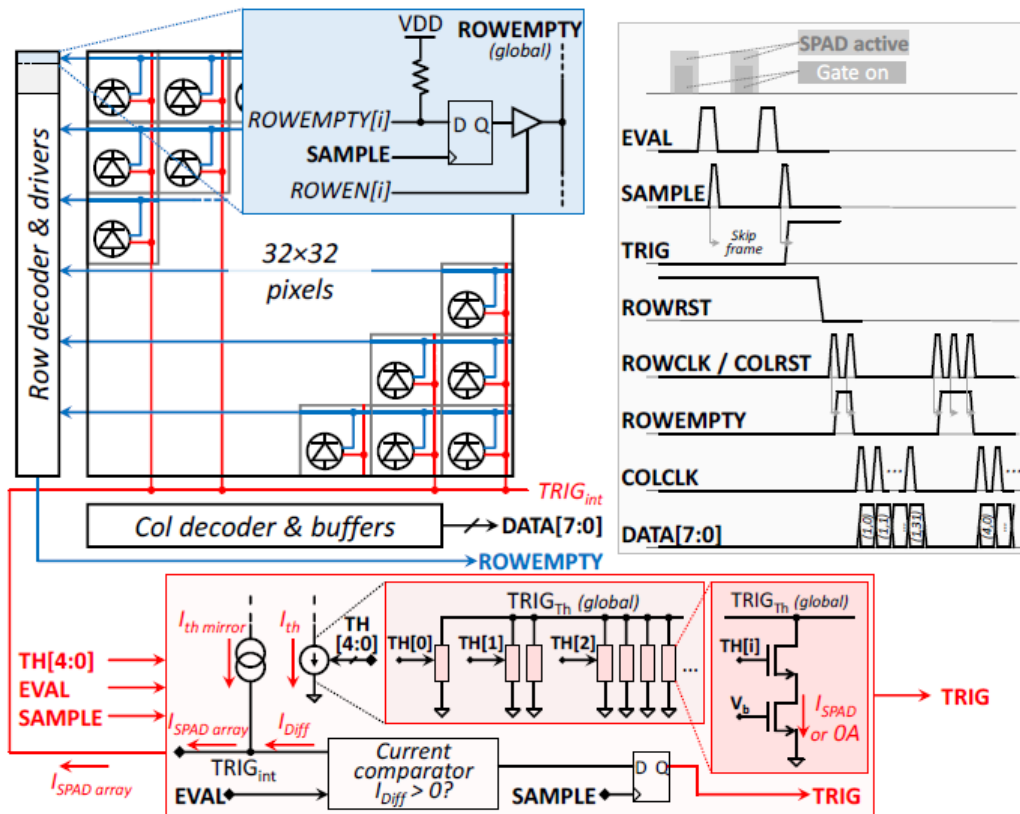


FIGURE D.2: Architecture of the imager and timing diagram. The frame and row skipping mechanisms are highlighted in red and blue, respectively. Externally driven/readable global signals are bold, while the italic names are for internal signals.

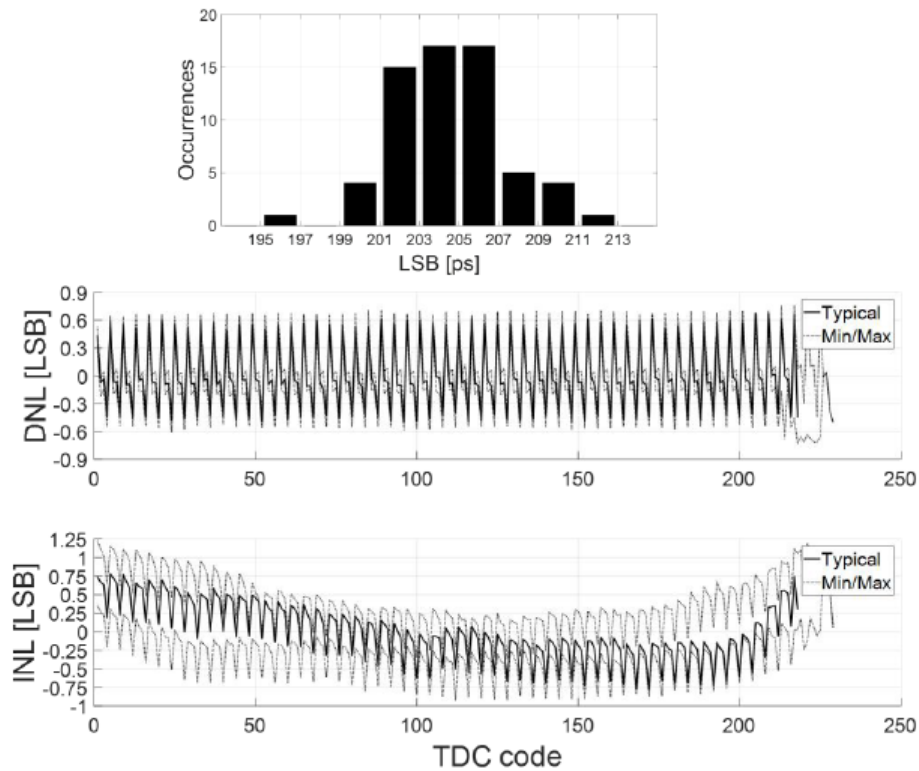


FIGURE D.3: TDC characterization including histogram of the resolution for 64 randomly distributed pixels, DNL and INL obtained from a code density test. Typical, maximum and minimum values are shown.

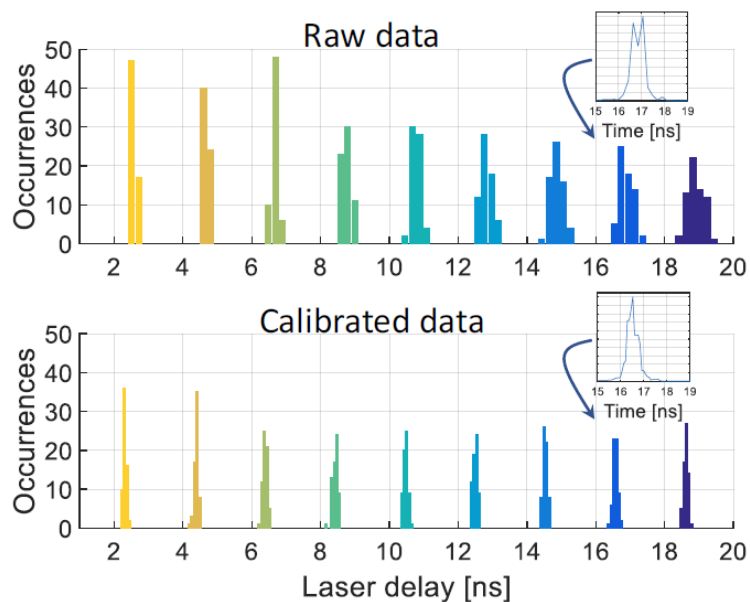


FIGURE D.4: Sensor accuracy (histograms of pixel mean values) sweeping a 470 nm 70 ps pulsed laser within a 16 ns time range in 9 steps of 2 ns. 64 pixels have been enabled at a time. Calibrated data means corrected for DNL and offset. The insets show the laser statistics for a given pixel.

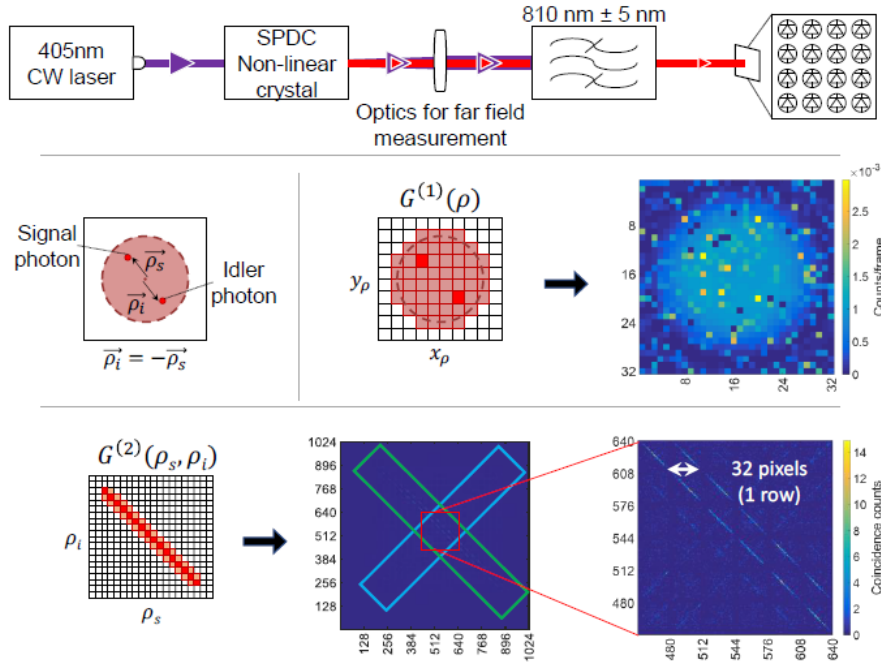


FIGURE D.5: Experimental setup (top) and measurements of the first- ($G^{(1)}$) and second-order ($G^{(2)}$) spatial correlation functions of a flux of entangled photon, including: model of the flux with expected and measured $G^{(1)}$ (middle), and expected and measured $G^{(2)}$, with zoom-in of the central region (bottom). Anticorrelated diagonals due to entangled photons and correlated diagonals due to crosstalk events are highlighted in green and sky-blue, respectively.

Parameter	This work	[136]	[137]	[121]
Year		2011	2014	2017
Architecture	TDC	TDC	TDC	TDC
Process	150nm	130nm	350nm	150nm
Pixel				
Pixel pitch (μm)	44.64	50	150	60
SPAD size (μm)	19.8	N.A.	30	N.A.
Pixel fill factor (%)	19.48	1	3.14	26.5
Sharing of SPAD well*	No	No	No	Yes
SPAD excess bias voltage (V)	3.0	0.73	6.0	3.0
SPAD DCR, median (Hz)	600	50	120	6800
TDC				
TDC area(μm^2)	402.7	N.A.	N.A.	N.A.
Range (ns)	52	55	360	16k
Time resolution / 1LSB (ps)	204.5 \pm 2.7	55	350	250
Depth (bit)	8	10	10	16
DNL (LSB)	-0.73..+0.77	-0.3..+0.3	\pm 0.02	-0.4..+0.5
INL (LSB)	-0.93..+1.24	-2.3..+1.7	\pm 0.10	-0.9..+1.2
Single-photon precision (ps)	240 (raw) 205 (after calibration)	170	254	N.A.
Chip				
Array size	32 \times 32	160 \times 128	32 \times 32	64 \times 64
Chip size (mm^2)	1.69 \times 1.88	11.0 \times 12.3	9 \times 9	4.4 \times 4.4
Max frame rate (fps)	80k (full readout) 250k (row skipping)**	250k (by design) 50 (demonstrated)	100k	17.9k
Max observation rate (Hz)	800k (frame skipping)	-	-	-
Power consumption (mW)	11.1 (row skipping)** 4.8 (frame skipping)	550	400	93.5

FIGURE D.6: Chip performance summary table. * Sharing of SPAD well reduces the dead area but negatively affects crosstalk and MTF. ** Values have been measured ensuring 8 detected photons in each frame, which is a worst-case condition for the quantum physics experiment described in Fig. D.5.

Bibliography

- [1] E. Abbe, "Beiträge zur Theorie des Mikroskops und der mikroskopischen Wahrnehmung", *Archiv für mikroskopische Anatomie* **9**, 413–418 (1873).
- [2] L. Rayleigh, "XV. on the theory of optical images, with special reference to the microscope", *The London, Edinburgh, and Dublin Philosophical Magazine and Journal of Science* **42**, 167–195 (1896).
- [3] J. Goodman, *Introduction to Fourier optics*, McGraw-Hill physical and quantum electronics series (W. H. Freeman, 2005).
- [4] R. Erni, M. D. Rossell, C. Kisielowski, and U. Dahmen, "Atomic-resolution imaging with a sub-50-pm electron probe", *Physical review letters* **102**, 096101 (2009).
- [5] *Scientific Background on the Nobel Prize in Chemistry 2014, Super-Resolved Fluorescence Microscopy*, https://www.nobelprize.org/nobel_prizes/chemistry/laureates/2014/advanced-chemistryprize2014.pdf, Accessed: 2018-03-10.
- [6] E. Betzig and J. K. Trautman, "Near-field optics: microscopy, spectroscopy, and surface modification beyond the diffraction limit", *Science* **257**, 189–195 (1992).
- [7] T. A. Klar, S. Jakobs, M. Dyba, A. Egner, and S. W. Hell, "Fluorescence microscopy with diffraction resolution barrier broken by stimulated emission", *Proceedings of the National Academy of Sciences* **97**, 8206–8210 (2000).
- [8] E. Betzig, G. H. Patterson, R. Sougrat, O. W. Lindwasser, S. Olenych, J. S. Bonifacino, M. W. Davidson, J. Lippincott-Schwartz, and H. F. Hess, "Imaging intracellular fluorescent proteins at nanometer resolution", *Science* **313**, 1642–1645 (2006).
- [9] M. J. Rust, M. Bates, and X. Zhuang, "Sub-diffraction-limit imaging by stochastic optical reconstruction microscopy (STORM)", *Nature methods* **3**, 793 (2006).
- [10] L. A. Lugiato, A. Gatti, and E. Brambilla, "Quantum imaging", *Journal of Optics B: Quantum and Semiclassical Optics* **4**, S176–S183 (2002).
- [11] Y. Shih, "Quantum Imaging", *IEEE Journal of Selected Topics in Quantum Electronics* **13**, 1016–1030 (2007).
- [12] M. Genovese, "Real applications of quantum imaging", *Journal of Optics* **18**, 073002 (2016).
- [13] D. Simon, G. Jaeger, and A. Sergienko, *Quantum metrology, imaging, and communication*, Quantum Science and Technology (Springer International Publishing, 2016).
- [14] M. J. Padgett and R. W. Boyd, "An introduction to ghost imaging: quantum and classical", *Philosophical Transactions of the Royal Society A: Mathematical, Physical and Engineering Sciences* **375**, 20160233 (2017).
- [15] J. C. Howell, R. S. Bennink, S. J. Bentley, and R. Boyd, "Realization of the einstein-podolsky-rosen paradox using momentum-and position-entangled photons from spontaneous parametric down conversion", *Physical Review Letters* **92**, 210403 (2004).
- [16] P.-a. Moreau, F. Devaux, and E. Lantz, "The Einstein-Podolsky-Rosen paradox in twin images", **2**, 1–5 (2014).

- [17] M. D'Angelo, M. V. Chekhova, and Y. Shih, "Two-photon diffraction and quantum lithography", *Physical Review Letters* **87**, 013602 (2001).
- [18] R. W. Boyd and J. P. Dowling, "Quantum lithography: Status of the field", *Quantum Information Processing* **11**, 891–901 (2012).
- [19] V. Giovannetti, S. Lloyd, L. Maccone, and J. H. Shapiro, "Sub-Rayleigh-diffraction-bound quantum imaging", *Physical Review A* **79**, 013827 (2009).
- [20] V. Giovannetti, S. Lloyd, and L. MacCone, "Quantum metrology", *Physical Review Letters* **96**, 13–16 (2006).
- [21] Z. Y. Ou, "Fundamental quantum limit in precision phase measurement", *Physical Review A* **55**, 2598–2609 (1997).
- [22] J. Jacobson, G. Björk, I. Chuang, and Y. Yamamoto, "Photonic de Broglie Waves", *Physical Review Letters* **74**, 4835–4838 (1995).
- [23] C. Thiel, T. Bastin, J. Martin, E. Solano, J. von Zanthier, and G. S. Agarwal, "Quantum imaging with incoherent photons", *Phys. Rev. Lett.* **99**, 133603 (2007).
- [24] D. Gatto Monticone, K. Katamadze, P. Traina, E. Moreva, J. Forneris, I. Ruo-Berchera, P. Olivero, I. P. Degiovanni, G. Brida, and M. Genovese, "Beating the abbe diffraction limit in confocal microscopy via nonclassical photon statistics", *Phys. Rev. Lett.* **113**, 143602 (2014).
- [25] C. Thiel, T. Bastin, J. Von Zanthier, and G. S. Agarwal, "Sub-Rayleigh quantum imaging using single-photon sources", *Physical Review A* **80**, 013820 (2009).
- [26] J.-L. Blanchet, F. Devaux, L. Furfaro, and E. Lantz, "Measurement of sub-shot-noise correlations of spatial fluctuations in the photon-counting regime", *Physical review letters* **101**, 233604 (2008).
- [27] L. Zhang, L. Neves, J. S. Lundeen, and I. A. Walmsley, "A characterization of the single-photon sensitivity of an electron multiplying charge-coupled device", *Journal of Physics B: Atomic, Molecular and Optical Physics* **42**, 114011 (2009).
- [28] M. P. Edgar, D. S. Tasca, F. Izdebski, R. E. Warburton, J. Leach, M. Agnew, G. S. Buller, R. W. Boyd, and M. J. Padgett, "Imaging high-dimensional spatial entanglement with a camera", *Nature communications* **3**, 984 (2012).
- [29] P.-A. Moreau, F. Devaux, and E. Lantz, "Einstein-podolsky-rosen paradox in twin images", *Physical review letters* **113**, 160401 (2014).
- [30] A. Avella, I Ruo-Berchera, I. P. Degiovanni, G. Brida, and M. Genovese, "Absolute calibration of an emccd camera by quantum correlation, linking photon counting to the analog regime", *Optics letters* **41**, 1841–1844 (2016).
- [31] R. J. Glauber, "The quantum theory of optical coherence", *Physical Review* **130**, 2529 (1963).
- [32] I. F. Santos, J. G. Aguirre-Gómez, and S. Pádua, "Comparing quantum imaging with classical second-order incoherent imaging", *Physical Review A* **77**, 043832 (2008).
- [33] T. Guerreiro, A. Martin, B. Sanguinetti, N. Bruno, H. Zbinden, and R. T. Thew, "High efficiency coupling of photon pairs in practice", *Optics Express* **21**, 27641 (2013).
- [34] J.-E. Oh, Y.-W. Cho, G. Scarcelli, and Y.-H. Kim, "Sub-Rayleigh imaging via speckle illumination", *Optics Letters* **38**, 682 (2013).
- [35] M. I. Kolobov and C. Fabre, "Quantum limits on optical resolution", *Physical Review Letters* **85**, 3789–3792 (2000).

- [36] V. N. Beskrovnyy and M. I. Kolobov, "Quantum limits of super-resolution in reconstruction of optical objects", *Physical Review A - Atomic, Molecular, and Optical Physics* **71**, 1–10 (2005).
- [37] J. G. McNally, T. Karpova, J. Cooper, and J. A. Conchello, "Three-dimensional imaging by deconvolution microscopy", *Methods* **19**, 373–385 (1999).
- [38] Y. Shih, *An introduction to quantum optics: photon and biphoton physics*, Series in Optics and Optoelectronics (CRC Press, 2011).
- [39] D.-Q. Xu, X.-B. Song, H.-G. Li, D.-J. Zhang, H.-B. Wang, J. Xiong, and K. Wang, "Experimental observation of sub-Rayleigh quantum imaging with a two-photon entangled source", *Applied Physics Letters* **106**, 171104 (2015).
- [40] H. Shin, K. W. C. Chan, H. J. Chang, and R. W. Boyd, "Quantum Spatial Superresolution by Optical Centroid Measurements", *Physical Review Letters* **107**, 083603 (2011).
- [41] L. A. Rozema, J. D. Bateman, D. H. Mahler, R. Okamoto, A. Feizpour, A. Hayat, and A. M. Steinberg, "Scalable Spatial Superresolution Using Entangled Photons", *Physical Review Letters* **112**, 223602 (2014).
- [42] M. Tsang, "Quantum Imaging beyond the Diffraction Limit by Optical Centroid Measurements", *Physical Review Letters* **102**, 253601 (2009).
- [43] M. Unternährer, B. Bessire, L. Gasparini, D. Stoppa, and A. Stefanov, "Coincidence detection of spatially correlated photon pairs with a monolithic time-resolving detector array", *Optics Express* **24**, 28829 (2016).
- [44] M. Unternährer, B. Bessire, L. Gasparini, M. Perenzoni, and A. Stefanov, "Coincidence detection of spatially correlated photon pairs with a novel type of monolithic time-resolving detector array", in 2017 european conference on lasers and electro-optics and european quantum electronics conference (2017), CD_10_1.
- [45] L. Gasparini, B. Bessire, M. Unternährer, A. Stefanov, D. Boiko, M. Perenzoni, and D. Stoppa, "Supertwin: towards 100kpixel cmos quantum image sensors for quantum optics applications", in Proc. SPIE, Vol. 10111 (2017), pp. 10111 –10111 –11.
- [46] L. Gasparini, M. Zarghami, H. Xu, L. Parmesan, M. M. Garcia, M. Unternährer, B. Bessire, A. Stefanov, D. Stoppa, and M. Perenzoni, "A 32x32-pixels time-resolved single-photon image sensor with 44.64- μm pitch and 19.48% fill-factor with on-chip row/frame skipping features reaching 800 khz observation rate for quantum physics applications", in International Solid-State Circuits Conference, ISSCC'18 (IEEE, 2018, in press).
- [47] M. Unternährer, B. Bessire, L. Gasparini, M. Perenzoni, and A. Stefanov, "Super-Resolution Quantum Imaging at the Heisenberg Limit", arXiv:1712.02200 [quant-ph], 1–10 (2017).
- [48] A. Mikhalychev, A. Sakovich, I. Karuseichyk, B. Bessire, M. Unternährer, A. Stefanov, and D. Mogilevtsev, "Piecewise tomography: optimizing reconstruction of multi-parameter systems", manuscript in preparation.
- [49] B. Saleh and M. Teich, *Fundamentals of photonics*, Wiley Series in Pure and Applied Optics (Wiley, 2013).
- [50] T. Feurer, *Lecture notes in modern optics*, 2009.
- [51] B. Bessire, "Shaped energy-time entangled two-photon states for quantum information", PhD thesis (University of Bern, 2013).

- [52] A. F. Abouraddy, B. E. a. Saleh, A. V. Sergienko, and M. C. Teich, "Entangled-photon Fourier optics", *Journal of the Optical Society of America B* **19**, 1174 (2002).
- [53] D. Griffiths, *Introduction to quantum mechanics* (Cambridge University Press, 2016).
- [54] R. Boyd, *Nonlinear optics* (Elsevier Science, 2003).
- [55] M. M. Fejer, G. A. Magel, D. H. Jundt, and R. L. Byer, "Quasi-phase-matched second harmonic generation: tuning and tolerances", *IEEE Journal of Quantum Electronics* **28**, 2631–2654 (1992).
- [56] L. Mandel and C. K. Hong, "Theory of parametric frequency down conversion of light", **31**, 2409–2418 (1985).
- [57] T. Keller and M. Rubin, "Theory of two-photon entanglement for spontaneous parametric down-conversion driven by a narrow pump pulse", *Physical Review A* **56**, 1534–1541 (1997).
- [58] C. H. Monken, P. H. S. Ribeiro, and S. Pádua, "Transfer of angular spectrum and image formation in spontaneous parametric down-conversion", *Physical Review A* **57**, 3123–3126 (1998).
- [59] S. Lerch, B. Bessire, C. Bernhard, T. Feurer, and A. Stefanov, "Tuning curve of type-0 spontaneous parametric down-conversion", *Journal of the Optical Society of America B* **30**, 953 (2013).
- [60] M. V. Pack, D. J. Armstrong, and A. V. Smith, "Measurement of the $\chi(2)$ tensors of KTiOPO₄, KTiOAsO₄, RbTiOPO₄, and RbTiOAsO₄ crystals", *Appl. Opt.* **43**, 3319–3323 (2004).
- [61] K. Kato and E. Takaoka, "Sellmeier and thermo-optic dispersion formulas for KTP", *Appl. Opt.* **41**, 5040–5044 (2002).
- [62] S. Emanuelli and A. Arie, "Temperature-dependent dispersion equations for KTiOPO₄ and KTiOAsO₄", *Applied optics* **42**, 6661–6665 (2003).
- [63] Z. Ou, J.-K. Rhee, and L. Wang, "Photon bunching and multiphoton interference in parametric down-conversion", *Physical Review A* **60**, 593–604 (1999).
- [64] A. J. H. Van Der Torren, S. C. Yorulmaz, J. J. Renema, M. P. Van Exter, and M. J. A. De Dood, "Spatially entangled four-photon states from a periodically poled potassium-titanyl-phosphate crystal", *Physical Review A* **85**, 013820 (2012).
- [65] S. Ç. Yorulmaz, "Beyond photon pairs", PhD thesis (Leiden University, 2014).
- [66] R. Loudon, *The quantum theory of light* (OUP Oxford, 2000).
- [67] H. D. Riedmatten, V. Scarani, I. Marcikic, A. Acín, W. Tittel, H. Zbinden, and N. Gisin, "Two independent photon pairs versus four-photon entangled states in parametric down conversion", *Journal of Modern Optics* **51**, 1637–1649 (2004).
- [68] M. V. Fedorov, Y. M. Mikhailova, and P. a. Volkov, "Gaussian modelling and Schmidt modes of SPDC biphoton states", *Journal of Physics B: Atomic, Molecular and Optical Physics* **42**, 175503 (2009).
- [69] L. Mandel and E. Wolf, *Optical coherence and quantum optics* (Cambridge University Press, 1995).
- [70] J. Liu and Y. Shih, "Nth-order coherence of thermal light", *Physical Review A* **79**, 023819 (2009).
- [71] W. Martienssen and E. Spiller, "Coherence and Fluctuations in Light Beams", *American Journal of Physics* **32**, 919–926 (1964).

- [72] T. Asakura, "Spatial coherence of laser light passed through rotating ground glass", *Opto-electronics* **2**, 115–123 (1970).
- [73] A. M. Zysk, F. T. Nguyen, A. L. Oldenburg, D. L. Marks, and S. A. Boppart, "Optical coherence tomography: a review of clinical development from bench to bedside", *Journal of biomedical optics* **12**, 051403 (2007).
- [74] A. F. Abouraddy, M. B. Nasr, B. E. A. Saleh, A. V. Sergienko, and M. C. Teich, "Quantum-optical coherence tomography with dispersion cancellation", *Physical Review A* **65**, 053817 (2002).
- [75] A. F. Abouraddy, M. B. Nasr, B. E. A. Saleh, A. V. Sergienko, and M. C. Teich, "Demonstration of the complementarity of one- and two-photon interference", *Physical Review A* **63**, 063803 (2001).
- [76] D. Lopez-Mago and L. Novotny, "Quantum-optical coherence tomography with collinear entangled photons", *Optics Letters* **37**, 4077 (2012).
- [77] D. Klyshko, "Combine EPR and two-slit experiments: interference of advanced waves", *Physics Letters A* **132**, 299–304 (1988).
- [78] J. Schneeloch and J. C. Howell, "Introduction to the transverse spatial correlations in spontaneous parametric down-conversion through the biphoton birth zone", *Journal of Optics* **18**, 053501 (2016).
- [79] S. P. Walborn, C. Monken, S Pádua, and P. S. Ribeiro, "Spatial correlations in parametric down-conversion", *Physics Reports* **495**, 87–139 (2010).
- [80] P. S. Ribeiro, S Pádua, J. M. Da Silva, and G. Barbosa, "Controlling the degree of visibility of young's fringes with photon coincidence measurements", *Physical Review A* **49**, 4176 (1994).
- [81] S. Walborn, M. T. Cunha, S Pádua, and C. Monken, "Double-slit quantum eraser", *Physical Review A* **65**, 033818 (2002).
- [82] G Brida, E Cagliero, G Falzetta, M Genovese, M Gramegna, and E Predazzi, "Biphoton double-slit experiment", *Physical Review A* **68**, 033803 (2003).
- [83] W. H. Peeters, J. J. Renema, and M. P. van Exter, "Engineering of two-photon spatial quantum correlations behind a double slit", *Physical Review A* **79**, 043817 (2009).
- [84] M. Reid, P. Drummond, W. Bowen, E. G. Cavalcanti, P. K. Lam, H. Bachor, U. L. Andersen, and G Leuchs, "Colloquium: the einstein-podolsky-rosen paradox: from concepts to applications", *Reviews of Modern Physics* **81**, 1727 (2009).
- [85] P.-A. Moreau, J. Mougín-Sisini, F. Devaux, and E. Lantz, "Realization of the purely spatial einstein-podolsky-rosen paradox in full-field images of spontaneous parametric down-conversion", *Physical Review A* **86**, 010101 (2012).
- [86] L. Lugiato, A Gatti, and E Brambilla, "Quantum imaging", *Journal of Optics B: Quantum and semiclassical optics* **4**, S176 (2002).
- [87] J. H. Shapiro and R. W. Boyd, "The physics of ghost imaging", *Quantum Information Processing* **11**, 949–993 (2012).
- [88] R. S. Aspden, D. S. Tasca, R. W. Boyd, and M. J. Padgett, "Epr-based ghost imaging using a single-photon-sensitive camera", *New Journal of Physics* **15**, 073032 (2013).
- [89] M. Genovese, "Real applications of quantum imaging", *J. Opt.* **18**, 073002 (2016).
- [90] L. Neves, G Lima, J. A. Gómez, C. Monken, C Saavedra, and S Pádua, "Generation of entangled states of qudits using twin photons", *Physical review letters* **94**, 100501 (2005).

- [91] A. Mair, A. Vaziri, G. Weihs, and A. Zeilinger, "Entanglement of the orbital angular momentum states of photons", *Nature* **412**, 313–316 (2001).
- [92] A. Vaziri, G. Weihs, and A. Zeilinger, "Experimental two-photon, three-dimensional entanglement for quantum communication", *Physical Review Letters* **89**, 240401 (2002).
- [93] E. Nagali, L. Sansoni, L. Marrucci, E. Santamato, and F. Sciarrino, "Experimental generation and characterization of single-photon hybrid ququarts based on polarization and orbital angular momentum encoding", *Physical Review A* **81**, 052317 (2010).
- [94] A. C. Dada, J. Leach, G. S. Buller, M. J. Padgett, and E. Andersson, "Experimental high-dimensional two-photon entanglement and violations of generalized bell inequalities", *Nature Physics* **7**, 677–680 (2011).
- [95] M. Agnew, J. Leach, M. McLaren, F. S. Roux, and R. W. Boyd, "Tomography of the quantum state of photons entangled in high dimensions", *Physical Review A* **84**, 062101 (2011).
- [96] N. K. Langford, R. B. Dalton, M. D. Harvey, J. L. O'Brien, G. J. Pryde, A. Gilchrist, S. D. Bartlett, and A. G. White, "Measuring entangled qutrits and their use for quantum bit commitment", *Physical Review Letters* **93**, 053601 (2004).
- [97] V. Salakhutdinov, E. Eliel, and W. Löffler, "Full-field quantum correlations of spatially entangled photons", *Physical Review Letters* **108**, 173604 (2012).
- [98] M. Krenn, M. Huber, R. Fickler, R. Lapkiewicz, S. Ramelow, and A. Zeilinger, "Generation and confirmation of a (100x100)-dimensional entangled quantum system", *Proceedings of the National Academy of Sciences* **111**, 6243–6247 (2014).
- [99] M. Almeida, S. Walborn, and P. S. Ribeiro, "Experimental investigation of quantum key distribution with position and momentum of photon pairs", *Physical Review A* **72**, 022313 (2005).
- [100] S. Walborn, D. Ether, R. de Matos Filho, and N. Zagury, "Quantum teleportation of the angular spectrum of a single-photon field", *Physical Review A* **76**, 033801 (2007).
- [101] D. C. Burnham and D. L. Weinberg, "Observation of simultaneity in parametric production of optical photon pairs", *Physical Review Letters* **25**, 84 (1970).
- [102] T. Pittman, Y. Shih, D. Strekalov, and A. Sergienko, "Optical imaging by means of two-photon quantum entanglement", *Physical Review A* **52**, R3429 (1995).
- [103] B. M. Jost, A. V. Sergienko, A. F. Abouraddy, B. E. Saleh, and M. C. Teich, "Spatial correlations of spontaneously down-converted photon pairs detected with a single-photon-sensitive ccd camera", *Optics Express* **3**, 81–88 (1998).
- [104] S. Oemrawsingh, W. Van Drunen, E. Eliel, and J. Woerdman, "Two-dimensional wave-vector correlations in spontaneous parametric downconversion explored with an intensified ccd camera", *JOSA B* **19**, 2391–2395 (2002).
- [105] H. D. L. Pires, C. H. Monken, and M. P. van Exter, "Direct measurement of transverse-mode entanglement in two-photon states", *Physical Review A* **80**, 022307 (2009).
- [106] R. Fickler, M. Krenn, R. Lapkiewicz, S. Ramelow, and A. Zeilinger, "Real-time imaging of quantum entanglement", *Scientific reports* **3** (2013).
- [107] R. S. Aspden, D. S. Tasca, A. Forbes, R. W. Boyd, and M. J. Padgett, "Experimental demonstration of klyshko's advanced-wave picture using a coincidence-count based, camera-enabled imaging system", *Journal of Modern Optics* **61**, 547–551 (2014).

- [108] P. A. Morris, R. S. Aspden, J. E. Bell, R. W. Boyd, and M. J. Padgett, "Imaging with a small number of photons", *Nature Communications* **6**, 5913 (2015).
- [109] F. Just, M. Filipenko, A. Cavanna, T. Michel, T. Gleixner, M. Taheri, J. Vallerga, M. Campbell, T. Tick, G. Anton, et al., "Detection of non-classical space-time correlations with a novel type of single-photon camera", *Optics Express* **22**, 17561–17572 (2014).
- [110] D. Boiko, N. Gunther, N Brauer, M Sergio, C Niclass, G. Beretta, and E Charbon, "A quantum imager for intensity correlated photons", *New Journal of Physics* **11**, 013001 (2009).
- [111] S. Burri, Y. Maruyama, X. Michalet, F. Regazzoni, C. Bruschini, and E. Charbon, "Architecture and applications of a high resolution gated spad image sensor", *Optics Express* **22**, 17573–17589 (2014).
- [112] N. Krstajić, J. Levitt, S. Poland, S. Ameer-Beg, and R. Henderson, "256x2 spad line sensor for time resolved fluorescence spectroscopy", *Optics Express* **23**, 5653–5669 (2015).
- [113] R. Lussana, F. Villa, A. Dalla Mora, D. Contini, A. Tosi, and F. Zappa, "Enhanced single-photon time-of-flight 3d ranging", *Optics Express* **23**, 24962–24973 (2015).
- [114] S. Jahromi, J.-P. Jansson, and J. Kostamovaara, "Solid-state 3d imaging using a 1nj/100ps laser diode transmitter and a single photon receiver matrix", *Optics Express* **24**, 21619–21632 (2016).
- [115] N. A. Dutton, I. Gyongy, L. Parmesan, S. Gnechchi, N. Calder, B. R. Rae, S. Pellegrini, L. A. Grant, and R. K. Henderson, "A spad-based QVGA image sensor for single-photon counting and quanta imaging", *IEEE Transactions on Electron Devices* **63**, 189–196 (2016).
- [116] L. H. Braga, L. Gasparini, L. Grant, R. K. Henderson, N. Massari, M. Perenzoni, D. Stoppa, and R. Walker, "A fully digital 8x16 SiPM array for PET applications with per-pixel TDCs and real-time energy output", *IEEE Journal of Solid-State Circuits* **49**, 301–314 (2014).
- [117] S. Emanuelli and A. Arie, "Temperature-dependent dispersion equations for KTiOPO_4 and KTiOAsO_4 ", *Applied optics* **42**, 6661–6665 (2003).
- [118] J. Richardson, R. Walker, L. Grant, D. Stoppa, F. Borghetti, E. Charbon, M. Gersbach, and R. K. Henderson, "A 32x32 50ps resolution 10 bit time to digital converter array in 130nm cmos for time correlated imaging", in *Custom integrated circuits conference, 2009. CICC'09 (IEEE, 2009)*, pp. 77–80.
- [119] Y. Zhou, J. Simon, J. Liu, and Y. Shih, "Third-order correlation function and ghost imaging of chaotic thermal light in the photon counting regime", *Physical Review A* **81**, 043831 (2010).
- [120] J.-Å. Larsson, "Loopholes in bell inequality tests of local realism", *Journal of Physics A: Mathematical and Theoretical* **47**, 424003 (2014).
- [121] M. Perenzoni, D. Perenzoni, and D. Stoppa, "A 64x64-pixels digital silicon photomultiplier direct TOF sensor with 100-mphotons/s/pixel background rejection and imaging/altimeter mode with 0.14% precision up to 6 km for spacecraft navigation and landing", *IEEE Journal of Solid-State Circuits* **52**, 151–160 (2017).
- [122] F. Ferri, D. Magatti, A. Gatti, M. Bache, E. Brambilla, and L. A. Lugiato, "High-resolution ghost image and ghost diffraction experiments with thermal light", *Physical Review Letters* **94**, 2–5 (2005).

- [123] A. Gatti, E. Brambilla, M. Bache, and L. A. Lugiato, "Ghost imaging with thermal light: Comparing entanglement and classical correlation", *Physical Review Letters* **93**, 1–4 (2004).
- [124] A. Valencia, G. Scarcelli, M. D'Angelo, and Y. Shih, "Two-Photon Imaging with Thermal Light", *Physical Review Letters* **94**, 063601 (2005).
- [125] I. Santos, M. Sagioro, C. Monken, and S. Pádua, "Resolution and apodization in images generated by twin photons", *Physical Review A* **67**, 033812 (2003).
- [126] F. Guerrieri, L. Maccone, F. N. C. Wong, J. H. Shapiro, S. Tisa, and F. Zappa, "Sub-Rayleigh Imaging via N-Photon Detection", *Physical Review Letters* **105**, 163602 (2010).
- [127] G. Zheng, R. Horstmeyer, and C. Yang, "Wide-field, high-resolution fourier ptychographic microscopy", *Nature photonics* **7**, 739 (2013).
- [128] K. T. Kapale, L. D. Didomenico, H. Lee, P. Kok, and J. P. Dowling, "Quantum interferometric sensors", in *Spie fourth international symposium on fluctuations and noise*, Vol. 6603, edited by L. Cohen (2007), p. 660316.
- [129] V. Giovannetti, S. Lloyd, and L. Maccone, "Advances in quantum metrology", *Nature Photonics* **5**, 222–229 (2011).
- [130] E. Yablonovitch and R. B. Vrijen, "Optical projection lithography at half the Rayleigh resolution limit by two-photon exposure", *Optical Engineering* **38**, edited by Y. Bar-Cohen and T. Wallmersperger, 334 (1999).
- [131] A. Pe'er, B. Dayan, M. Vucelja, Y. Silberberg, A. A. Friesem, Y. Silberberg, A. A. Friesem, Y. Silberberg, and A. A. Friesem, "Quantum lithography by coherent control of classical light pulses", *Optics Express* **12**, 6600–6605 (2004).
- [132] P. R. Hemmer, A. Muthukrishnan, M. O. Scully, and M. S. Zubairy, "Quantum Lithography with Classical Light", *Physical Review Letters* **96**, 163603 (2006).
- [133] A. N. Boto, P. Kok, D. S. Abrams, S. L. Braunstein, C. P. Williams, and J. P. Dowling, "Quantum Interferometric Optical Lithography: Exploiting Entanglement to Beat the Diffraction Limit", *Physical Review Letters* **85**, 2733–2736 (2000).
- [134] G. Björk, L. L. Sánchez-Soto, and J. Söderholm, "Entangled-state lithography: Tailoring any pattern with a single state", *Physical Review Letters* **86**, 4516–4519 (2001).
- [135] M. Corona, K. Garay-Palmett, and A. B. U'Ren, "Experimental proposal for the generation of entangled photon triplets by third-order spontaneous parametric down-conversion in optical fibers", *Optics Letters* **36**, 190 (2011).
- [136] C. Veerappan, J. Richardson, R. Walker, D.-U. Li, M. W. Fishburn, Y. Maruyama, D. Stoppa, F. Borghetti, M. Gersbach, R. K. Henderson, et al., "A 160×128 single-photon image sensor with on-pixel 55ps 10b time-to-digital converter", in *Solid-state circuits conference digest of technical papers (ISSCC) (IEEE, 2011)*, pp. 312–314.
- [137] F. Villa, R. Lussana, D. Bronzi, S. Tisa, A. Tosi, F. Zappa, A. Dalla Mora, D. Contini, D. Durini, S. Weyers, et al., "CMOS imager with 1024 SPADs and TDCs for single-photon timing and 3-d time-of-flight", *IEEE journal of selected topics in quantum electronics* **20**, 364–373 (2014).

Erklärung

gemäss Art. 28 Abs. 2 RSL 05

Name/Vorname: **Unternährer Manuel**

Matrikelnummer: **02-908-929**

Studiengang: **Physik**

Bachelor Master Dissertation

Titel der Arbeit: **On Quantum Imaging
with Time-Resolving Detector Arrays**

Leiter der Arbeit: **Prof. Dr. André Stefanov**

Ich erkläre hiermit, dass ich diese Arbeit selbständig verfasst und keine anderen als die angegebenen Quellen benutzt habe. Alle Stellen, die wörtlich oder sinngemäss aus Quellen entnommen wurden, habe ich als solche gekennzeichnet. Mir ist bekannt, dass andernfalls der Senat gemäss Artikel 36 Absatz 1 Buchstabe r des Gesetzes vom 5. September 1996 über die Universität zum Entzug des auf Grund dieser Arbeit verliehenen Titels berechtigt ist. Ich gewähre hiermit Einsicht in diese Arbeit.

Bern, 26. April 2018

Ort/Datum

Unterschrift

Curriculum Vitae

Personal Information

Name	Manuel Unternährer
Email	umanuel@gmail.com
Date of birth	November 13th, 1982
Nationality	Swiss

Education

2014-2018	PhD in Physics, University of Bern Thesis supervised by A. Stefanov, Institute of Applied Physics
2012-2014	Master of Science in Physics, University of Bern Thesis supervised by A. Stefanov, Institute of Applied Physics
2007-2011	Bachelor of Science in Physics, University of Bern Thesis supervised by Ch. Greub, Institute for Theoretical Physics
2005-2007	Eidg. Fähigkeitszeugnis als Elektroniker (Swiss Federal Diploma as Electronics Technician) Gewerblich-industrielles Bildungszentrum Zug
2000-2002	Maturität (high school), Kantonsschule Reussbühl

Work Experience

2009-2018	Teaching assistant in various physics lectures at the Institute for Theoretical Physics and the Institute of Applied Physics, University of Bern
2012	Internship as Physicist (July-September), Swiss Federal Institute of Metrology (METAS), Bern
2005-2007	Berufslehre Elektroniker, Siemens AG, Zug (Apprenticeship as Electronics Technician)